The Dissertation Committee for Shashvat Doorwar Certifies that this is the approved version of the following dissertation:

Understanding Unstable Immiscible Displacement in Porous Media

Committee:

Kishore K. Mohanty, Supervisor

Gary A. Pope

David DiCarlo

Chun Huh

Upali Weerasooriya

Carlos Hidrovo

Understanding Unstable Immiscible Displacement in Porous Media

by

Shashvat Doorwar, B.Tech.; M.Tech.

Dissertation

Presented to the Faculty of the Graduate School of

The University of Texas at Austin

in Partial Fulfillment

of the Requirements

for the Degree of

Doctor of Philosophy

The University of Texas at Austin

May 2015

Dedication

Dedicated to my family for their love and support throughout my life

Acknowledgements

I would like to extend my sincerest thanks to my supervisor, Dr. Kishore K. Mohanty for his constant support and encouragement throughout my stay at University of Texas at Austin. I greatly appreciate the freedom he granted me while pursuing this research, yet guiding me every time I went astray. I appreciate his humility and patience in answering all my questions. He has truly been and will always be an inspiration in professional and personal life. I also like to extend my thanks to my dissertation committee members; Dr. Pope, Dr. Weerasooriya, Dr. DiCarlo, Dr. Huh and Dr. Hidrovo for their guidance and their inputs in making this dissertation better.

My special thanks to Dr. Eric Dao and all my friends and research group members; Gaurav, Rahul, Himanshu, Luiz, Rubia, Peila, Chie, Sriram, Krishna, Robin, Ruth, Stephanie, Song-Yong, Prateek and Pinaki for all their help, especially in making every moment in the lab more enjoyable and memorable.

I would also like to acknowledge Ms. Barbara Messmore and Ms. Frankie Hart for every bit of their administrative support that usually goes unnoticed in such academic dissertations, Glen Baum for his keen insight and tips while designing experiments or arranging logistics, Gary Miscoe for constantly ensuring the safety of our labs, Daryl Nygaard at the CPE machine shop and Adam Kennedy at the glass workshop for their willingness to help and suggestions on improving my experiments.

Finally, I thank all my friends at Austin Pets Alive for welcoming me in their group, allowing me to spend time at their facility and for sharing some of the most memorable moments of my stay in Austin.

Understanding Unstable Immiscible Displacement in Porous Media

Shashvat Doorwar, PhD

The University of Texas at Austin, 2015

Supervisor: Kishore K. Mohanty

Our global heavy and viscous oil reserves are immense. 70% of our current global oils reserves are viscous or heavy. For an energy secure future, exploitation of heavy oil reserves is necessary to mitigate the impact of steadily declining conventional reserves. Though most viscous and heavy oils are produced by thermal stimulation, several cases do exist where thermal methods are neither technically feasible nor economically profitable. In such cases, non-thermal EOR methods have to be applied. Any displacement process at such high viscosity ratio will be influenced by viscous fingering. Polymers are typically added to the water to stabilize the displacement but for oils above a couple of 100 cp viscosity a stable displacement is not feasible. As unstable displacements are not very well understood, visualization along with experimentation is critical for understanding and modeling the process.

In this study, multi-scale experimental strategy was employed; experiments were conducted in cores at lab-scale to generate quantifiable data and were repeated in small micro-fluidic cells for visualization of the mechanism. Polymer flood as an alternative non-thermal process in a structurally complex carbonate formation was tested. In carbonates formations, thermal methods are not preferred as mineral dissolution and precipitation lead to formation damage. Effect of timing of polymer flood was studied in great details. Result from both the micromodels and core-floods indicate that for heavy

oils, unlike light oils, timing of polymer injection is not critical and a tertiary polymer flood at the completion of waterflood can also produce significant incremental oil. In some cases, tertiary polymer flood even out-performs a secondary polymer flood.

A major problem with modeling and predicting the performance of an unstable flood is largely due to our inability to accurately capture viscous fingering or its effects. Viscous fingering is a complex phenomenon and is dependent on several parameters such as injection rate, viscosity ratios, heterogeneity and dimensions. The micromodels were used to visualize the variation in flow pattern at different viscosity ratio and injection rates while core floods provided essential modeling data. Based on the results two new models were developed: a simplified network model that could accurately predict the viscous fingers for all viscosity ratios and a lumped model that capture the effect of viscous fingers at larger scales through pseudo-relative permeability functions. A dimensionless scaling parameter similar to the instability parameter of Peters and Flock (1981) was also developed that is useful in predicting the recoveries of all unstable displacement at various viscosity ratios, injection rate, permeability and width. The scaling parameter showed excellent fit with experimental data of over 60 experiments.

Table of Contents

List of Tables

List of Figures

CHAPTER 1: INTRODUCTION

1.1 MOTIVATION

With a steadily increasing world energy demand, concerns of climate change (global warming) and uncertainty in the energy supply chain, we are said to be living in the age of energy trilemma. A trilemma of achieving energy security, energy equality and environmental sustainability simultaneously (World Energy scenario, Oct 2013). Energy security implies the ability to satisfy the demand of energy consistently, over a long duration of time. Our energy security depends heavily on the supply of fossil fuel as more than 85% of the world's current energy needs are met through fossil fuels. In the current world scenario, where most countries have almost exhausted their light-conventional-oil reserves, sustaining energy security will require tapping into unexplored and unconventional sources of fossil fuels. Energy equality is the ability to transport this energy or fuel globally across borders, to the area of higher demand and less supply. While we strive to achieve this energy security and equality, it is important to make a conscious effort towards environmental sustainability. Of the three goals, energy security surely is the most important as without energy reserves, energy equality cannot be achieved.

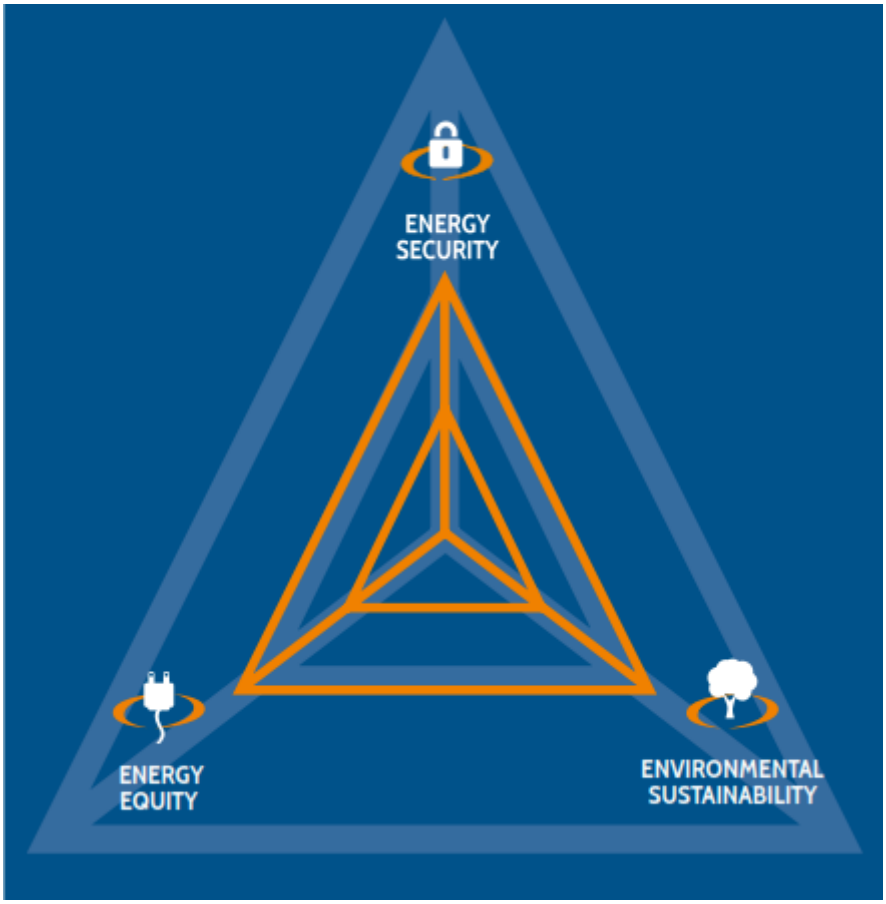

Figure 1.1: The energy trilemma as explained in World Energy Scenario (2013)

It is a known fact that our fossil fuel reserves are limited, non-renewable and certainly not all our resources are currently producible. M. King Hubbert's peak oil theory suggested that fossil fuel cannot be produced at an increasing rate for ever. The production will eventually achieve its maximum rate and then shall plummet into a fast eternal decline (Hubbert, 1956). Peak theory was based on the production trends of individual fields and some compensation was made for the new discovery of reserves. While historical data of oil production in USA and other countries initially matched the trend predicted by Hubbert's peak theory, it is now clear that there are multiple peaks and declines in any nation's production life cycle; not just one as suggested by the Peak Oil

theory. Hubbert's original prediction of peak oil production in 1970 hence proved to be premature. A primarily reason for this mismatch is that peak oil theory does not properly take into account the development of new production techniques, such as chemical enhanced oil recovery methods, exploitation of heavy oil reserves, directional drilling and shale oil production through fracturing.

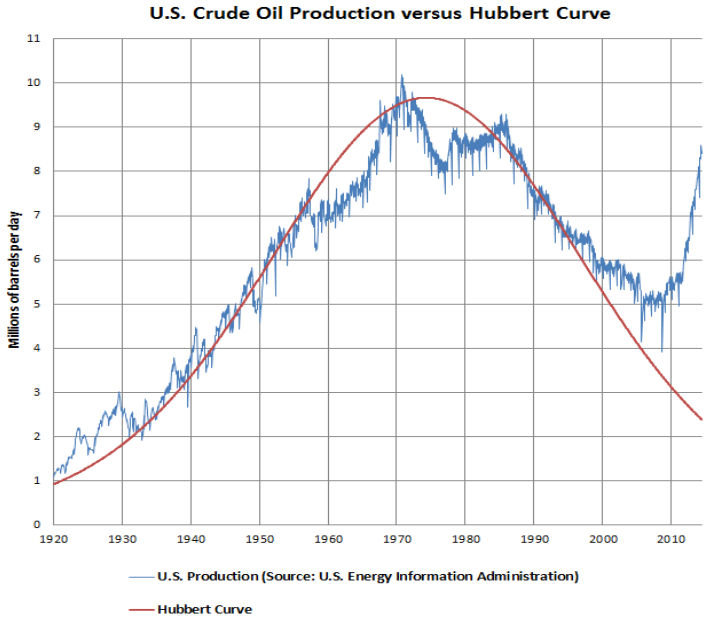

Figure 1.2: Hubbert's plot captures the initial trend in US oil production. It peaked and declined but the decline was not perpetual and the production boomed again in 2005.

Economics and oil prices play an important role too. If the prices are high, more reserves become profitable and hence producible. However, oil market prices are also controlled by several geo-political situations and are unpredictable. From engineering point of view, newer technologies have to be continually developed and improved for producing unconventional oils to maintain our energy sufficiency and to delay the inevitable decline after the new peak. Exploitation of heavy oil reserves will greatly help

in mitigating the impact of steady decline of conventional reserves. Our global heavy and viscous oil reserves are immense. 70% of our current global oils reserves is viscous or heavy. According to the Oilfield Review (Hussein *et al*., 2006) there is about six trillion barrel of heavy oil in the world and with the predicted depletion rate of the light oil reserves, in the next 40 years all oils companies will be dealing in heavy oils. Department of Energy (DOE) estimates that the United States heavy oil resource is about 100 billion barrels of OOIP. Around 80 billion barrels of this heavy oil is concentrated in the states of California, Alaska and Wyoming (DOE office of Petroleum Reserves-Strategic Unconventional Fuels, Jun 2007). Orinoco oil belt in Venezuela is one of the largest heavy oil sand traps and contains about 1.2 trillion barrels of oils in place.

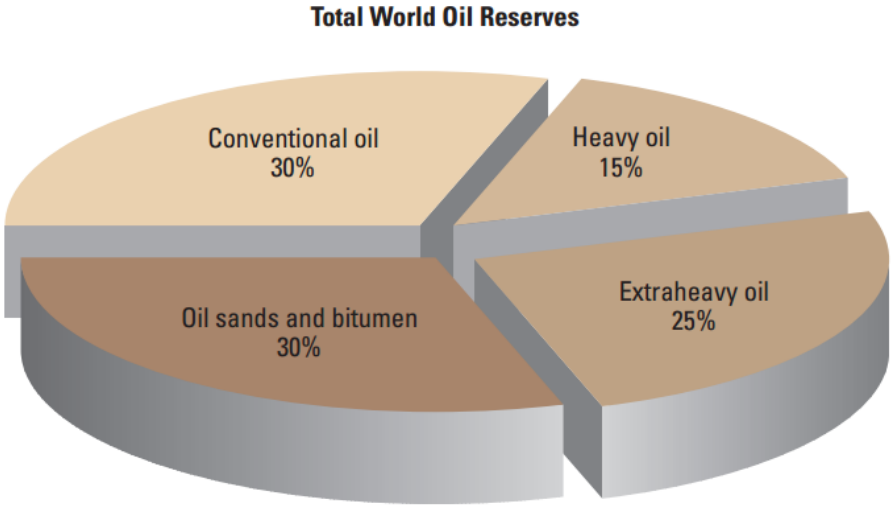

^ Total world oil reserves. Heavy oil, extraheavy oil and bitumen, make up about 70% of the world's total oil resources of 9 to 13 trillion bbl.

Figure1.3: 70% of our current global oil reserves is heavy, extra heavy or bituminous sand (Hussein *et al*., 2006)

Despite all the known heavy crude oil reserves, production remains a bigger challenge as much of the heavy oil is immobile. Due to its high viscosity, low gas oil

ratio, little gas cap and no aquifer drive (shallow reservoirs) the primary recovery is very little. Currently, most of the commercial heavy oil production is done using thermal methods like steam assisted gravity drainage (SAGD), cyclic steam stimulation (CSS) and steam injection. Despite the extensive use of thermal methods and enhancement in their performance with the introduction of directional well drilling, several oil reservoirs can still not be produced using thermal EOR techniques due to environmental, technical or economical reasons. For example, the north slope of Alaska contains about 20 billion barrels of viscous oil. These reservoirs are shallow and underlie a permafrost (Hallam *et al*. 1992) that may get destabilized if the reservoir is thermally stimulated. The proximity of the permafrost makes these reservoirs unsuitable candidates for thermal methods (Marques 2009; Peyton 1970; Wilson 1972, Kumar, 2012). Kumar 2012 suggested water flood followed by an alkali-surfactant or polymer followed by an alkali surfactant polymer flood as two alternative non-thermal methods for exploiting such reserves. Some reservoirs are highly laminated and do not have high vertical permeability which is a must for most thermal gravity drainage processes. Horizontal well- cyclic steam stimulation (HW-CSS) is uneconomical for a pay thickness of less than 8 m due to excessive heat loss to the over-burden and under-burden. A minimum pay thickness of 11m is required for breakeven HW-CSS (Chang, 2013). Broadly speaking, most of our thermal stimulation methods are high energy, high carbon impact methods which contradict our conscious effort towards environmental suitability.

While the heavy oils reserves in sand or sandstone reservoirs have been exploited to some extent, most of the heavy oil contained in carbonate reservoirs worldwide is largely untouched. It is estimated that the heterogeneous carbonates reservoirs contain about 1.6 trillion bbl in place (Briggs, 1988). One-third of this is approximated to be in middle-eastern reservoirs (Buza, 2008). Grosmont formation in Alberta-Canada contains

about 406 billion barrel of bituminous heavy oils in fractured carbonate reservoirs (Bryan and Kantzas, 2014).

Carbonate reservoirs are tough to produce due to their vuggy and highly fractured nature. For viscous oils, we clearly require a way to reduce mobility ratio, by either heating the oil or injecting a polymeric solution. Steam injection is expensive and channeling through fractures will cause a lot of steam and heat loss. Furthermore, carbonate reservoirs pose a danger of formation damage due to mineral dissolution at the injector and precipitation closer to the producer (Briggs *et al*., 1992). Other sophisticated chemical EOR methods have also proven to be challenging due to the structural complexity of the formation, high degree of hardness in the formation brine and dissolution of gypsum from the formation causing issues with surfactant adsorption and aqueous stability (Sharma *et al*., 2014, Southwick *et al*., 2014). An alternate simpler non-thermal method should be explored for viscous oils in carbonates such as a polymer flood. Polymers have been widely used in the petroleum industry to improve the sweep efficiency of a waterflood. In carbonates, waterflood sweep efficiency is expected to be poor because of the existing natural fractures that provide high permeability pathways to the producer. Although, perceived to be much simpler than other chemical EOR processes, polymer flooding is still not fully understood and modeled. The optimum timing to start a polymer flood is not clear. Some believe that secondary injection produces extra oil compared to tertiary (Wreath, 1989; Wang *et al*., 2000; Element *et al*., 2001, Huh and Pope, 2008) while others (Vermolen, *et al*., 2014, Fabbri, *et al*., 2014) have observed and reported conflicting results.

A major problem with modeling and predicting the performance of an unstable flood is largely due to our inability to model viscous fingering using conventional techniques. Therefore, it is also critical to develop better understanding of the viscous

fingering and modeling. Lenormand (1988) presented a three phase chart that predicts the three flow regimes: stable, capillary dominated and viscous fingering, depending on capillary number and viscosity ratio. For a light oil reservoir, the typical viscosity ratio is around 1 and the capillary number is thought to be of the order of 10^{-6} - 10^{-7}. The displacement is therefore capillary-driven. Most of our reservoir model and prediction theory are developed for capillary dominated region and work fairly accurately in this phase. The accuracy of these models and their predictions is compromised at high viscosity ratios, when the flow is outside of capillary controlled regime; in transition towards viscous fingering regime or in the viscous fingering regime. As discussed earlier, about 70% of our current global oil reserves lie outside of the capillary controlled region on the Lenormand's plot. Therefore, in today's world scenario it is critically important to understand the viscous fingering dominated flow.

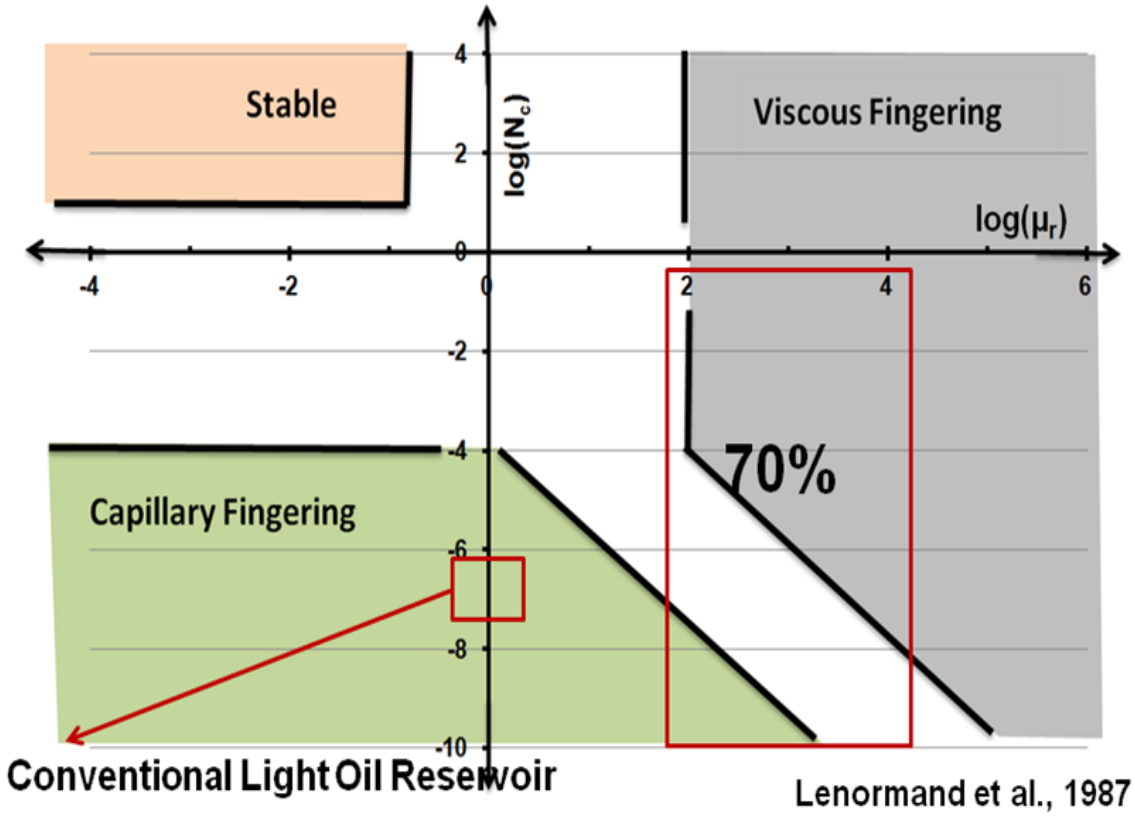

Figure 1.4: The three phase flow diagram as presented by Lenormand (1987)

1.2 Objective of the Research

The main objective of this research is to develop a better understanding of heavy oil recovery using non-thermal methods. Kumar *et al*. (2012) and Bryan and Katzas (2013, 2014) have recently suggested that ASP method can be applied for heavy oils with excellent recovery. We intend to extend this non-thermal approach to other viscous oil cases. While doing so we do realize that most of the complexity, uncertainty, and unpredictability in the viscous oil recovery is because of the unstable nature of the displacement. We intend to study this fingering phenomenon in detail and try to model viscous fingering. To accomplish this goal, an integrated micro-scale and macro-scale experimental approach is used in this study.

Major objectives of this research are listed below:

1. To evaluate the performance of polymer flooding for viscous oils in carbonates and to understand the sensitivity of the ultimate recovery with respect to timing of the polymer flood.
2. To understand and model viscous instability and fingering for all range of adverse viscosity ratios both at the core scale and pore scale.
3. Lastly, to use our experimental observation to develop a viscous fingering model usable at the reservoir scale.

1.3 DESCRIPTION OF THE CHAPTERS

The dissertation is organized into 6 specific chapters. Chapter 2 comprises of a detailed literature review of relevant published literature. The literature review is focused on heavy oils production techniques, viscous fingering theories and models, and some non-thermal/chemical EOR methods for heavy oils. Chapter 3 describes the materials used for experiments and the experimental protocols employed during the research. Micromodels are discussed in details in this chapter and the procedure of micromodel fabrication has been provided in Appendix A. Experimental results are discussed in Chapter 4. This chapter can be sub-divided into two sections: the first part focusing on experiments involving the study of viscous oils in heterogeneous carbonate reservoirs and the second part dealing with the fundamental study of viscous fingering. Both the sections contain experiments at micro-scale in micro-fluidic devices and at lab scale in laboratory core floods. Based on the results and observations made during the experiments discussed in Chapter 4, some mathematical models were derived and are discuss in Chapter 5. Chapter 5 also includes the results of all the simulations conducted based on the models developed. Lastly, the results are summarized and the major

conclusions of the research are presented in Chapter 6. Some recommendations for future directions of research in this field are also provided towards the end of Chapter 6.

CHAPTER 2: LITERATURE SURVEY

2.1 CRUDE OIL

2.1.1 Viscous and Heavy Oils

Crude oils consist of hydrocarbons of various molecular weight and other organic compounds that occur naturally in geological formations under the earth surface. Every crude goes through a different life cycle and has a different hydrocarbon source, called the kerogen. As a result, each crude oil differs from any other crude in terms of viscosity, density, chemical composition etc. In general, crude oils can be broadly classified as light oil and heavy oils. Light oils typically have API density of at least 22^{o}API and viscosity of less than 10 cp. Heavy oils can further be divided into 3 basic classes; heavy oils, extra heavy oils and natural bitumen. Heavy oils are crude oils with API density in between 10°API and 20°API gravity and viscosity in excess of 200 cp. Extra heavy oil have an API density of less than 10°API and high viscosity up to 10,000 cp. Lastly, natural bitumen is also called the oil sands and are immobile under reservoir conditions; they have a viscosity in excess of 10000 cp (Briggs *et al.*, 1988, Meyer *et al.* 2003).

It is believed that heavy oils must have once been light oils and got degraded to heavy oil due to natural weathering mechanisms. Two kind of natural weathering mechanisms are considered to be responsible for heavy oil formations, namely biodegradation and leaching. Bio-degradation takes places in low temperature reservoirs that are necessarily shallow. The shallow depth allows for the suitable temperature and climate for microbial growths. Microbe that are active around 80^{o}C, consume the lighter hydrocarbons decreasing the lighter less viscous components in the crude. This increases the viscosity and specific gravity of the crude. Leaching however occurs in a different environment. It is believed that sometimes under a certain reservoir pressure and

temperatures, the lighter crude ends can dissolve in ground water and leach away. This will increase the effective oil viscosity. Another theory of heavy oil formation involves a compromised seal which allows the gasses and light oil components to escape from the reservoir (Meyer *et al.*, 2003). Although leaching, leaking and bacterial degradation are slow processes, a considerable amount of mass loss occurs over a geological time scale. It is believed that the conventional crude oil reserve that degraded to form the current heavy oil deposits must has been 3 – 4 times larger than their current volume size.

Global heavy and viscous oil resource is immense. 70% of our current global oil reserves is viscous or heavy. According to the Oilfield Review (Hussein *et al.*, 2006) there is about six trillion barrel of heavy oil in the world and with the predicted depletion rate of the light oil reserves, in the next 40 years all oils companies will be dealing in heavy oils. Department of Energy (DOE) estimates that the United States heavy oil resource is about 100 billion barrels of OOIP. Around 80 billion barrels of this heavy oil is concentrated in the states of California, Alaska and Wyoming (DOE office of Petroleum Reserves-Strategic Unconventional Fuels, Jun 2007). Orinoco oil belt in Venezuela is one of the largest heavy oil sand traps containing about 1.2 trillion barrels of oils in place. It is believed that the total heavy oil reserves of Canada and Venezuela are more than the total proven reserves of conventional light oil in Saudi Arabia. From the economic perspective, the recoverable oil reserves are of more importance than the proven reserves. Out of all the heavy and viscous oil reserves, the estimated technically recoverable heavy oil and natural bitumen is 434 billion barrels and 651 billion barrels respectively. The expected recovery factor from these heavy and viscous oil reserves is usually low. Nonetheless the total recoverable oil from existing technologies is about equal to our remaining conventional (light) oil reserves. Meyer (2003) presented a list of all the known heavy and viscous oil reserves (Table 2.1). They estimated a maximum

recovery factor in best case to be about 32% and the minimum was about 9% OOIP. As our viscous and heavy oil reserves are immense any improvement on the existing technology that improves the recovery factor will greatly boost our technically recoverable oil reserves. It is therefore important to research heavy oil recovery for a secure energy future.

	Heavy Oil		Natural Bitumen	
Region	**Estimated Recovery Factor**	**Technically Recoverable Oil (BBO)**	**Estimated Recovery Factor**	**Technically Recoverable Oil (BBO)**
North America	0.19	35.3	0.32	530.9
South America	0.13	265.7	0.09	0.1
W Hemisphere	0.13	301.0	0.32	531.9
Africa	0.18	7.2	0.10	43.0
Europe	0.15	4.9	0.14	0.2
Middle East	0.12	78.2	0.10	0.0
Asia	0.14	29.6	0.16	42.8
Russia	0.13	13.4	0.13	33.7
E. Hemisphere	0.13	133.3	0.13	119.7
World		434.3		650.7

Table 2.1: Chart organized from the data presented in Meyer (2003) showing the distribution of heavy oil and natural bitumen around the world along with their estimated recovery factor and recoverable oil for each region.

2.1.2 Commercial Production Techniques

New technologies have emerged to enhance heavy oil production. Dusseault 2003, summarized technologies that are playing critical role in heavy oil production or will play a critical role in coming years. Heavy oils are generally produced using thermal methods that fall under the category of thermal enhanced oil recovery processes. The development of horizontal well technology has greatly enhanced the applicability and profitability of thermal gravity drainage processes like steam assisted gravity drainage (SAGD). Other methods include cold heavy oil production with sand (CHOPS), Cyclic Steam injection, vapor extraction (VAPEX), Toe-to-heel air injection (THAI) and open pit mining.

CHOPS: Cold Heavy oil Production with sand is non-thermal recovery process applied mostly in unconsolidated sands as a primary production method. In this process, screens or gravel packs are not used to prevent the sand from entering the well. It is in fact encouraged as a mean of near well bore productivity enhancement (Hussain, *et al.* 2006). It is believed that the sand production can enhance the productivity 10 times. Sand production improves the oil recovery in four major ways: Continuous sand movement decreases flow resistance, sand production improves near well bore permeability, it also prevents asphaltene deposition and plugging caused by fines, movement of sand helps in depressurization that leads to gas bubbling and generates a drive mechanism (Dusseault, 2003). CHOPS is one of the most widely used methods in Canada for viscous oil production and has now become fairly economical through technological advancements and better understanding of the process. Capital expenditure of CHOPS has been reduced to about $4/bbl. It should be noted that CHOPS requires naturally mobile oils, it cannot be applied on heavy oil reserves where the oil is immobile at reservoir conditions.

SAGD: Steam assisted gravity drainage is a thermal enhanced oil recovery process that is suitable for heavy oil reserves that are immobile at reservoir conditions. SAGD was introduced for the production of Canadian bitumen by Roger Butler and colleagues at Imperial Oil Company in early 1980s (Butler *et al.* 1981, 1981b, 1982). SAGD has benefitted the most from horizontal well drilling technology as it allows the steam to contact larger area of the reservoir, enhancing the heat exchange. One or two horizontal wells are drilled at the bottom of the oil rich formation and steam is injected in the wells. The steam heats up the formation and mobilizes the oil. The mobile oil drains downwards into the well as steam and heat diffuse into the formation. Sand production is not encouraged in this process as it will destabilize the well and shut it down.

Though SAGD involves heavy and viscous oils, the displacement is very stable as it is not a pressure driven process that initiates instabilities such as viscous fingering. Also the steam injection pressure is controlled so that it stays below the fracturing pressure. Dusseault (2001) believes that the SAGD process is not affected by the shale barriers in the formation because as the rocks are heated they undergo different degrees of expansion which leads to vertical fractures in the shale that act as conduits for steam.

SAGD is an effective method of production of extra heavy crude but certainly has some limitations. It cannot be applied in a reservoir which is highly laminated and has low vertical permeability. It is a high carbon foot print method. It cannot be applied in deep formations or in deep sea reservoirs because of excessive heat loss. There have been some examples of heavy oils reserves that are in close proximity of a permafrost. Using a thermal method in this reservoir will destabilize permafrost causing environmental concerns. SAGD is also limited by the pay thickness of the reservoirs. It is said to be suitable for reservoir thickness of about 15 – 20 m. Smaller pay will lead to excessive

heat losses to the over- and under- burden and complications in drilling two horizontal wells.

Pressure Pulse Technology: Pressure Pulse Technology (PPT) is a more recent invention and was introduced around late 1990s. PPT is based on the science that frequent large amplitude pressure pulses lead to enhanced fluid flowrates in porous media. This was found to be true for both single and multiphase flow (Davidson *et al.* 1999). During PPT, localized porosity dilation waves are sent through a fluid saturated porous media, this causes small expansion and contraction of the pores. This expansion and contraction generates a pulsating inflow and outflow through a pore throat which helps in unblocking plugged pore throats. It also enhances the overall flow, decreases capillary blockage and reduces viscous fingering, coning and channeling. PPT can also be applied in a light oil reservoir. Although this method is mostly still in laboratory phase it seems to be very promising. Figure 2.1 shows the images published by Davidson *et al.* (1999) of their lab-scale PPT experiment that show the decreases in viscous fingering during PPT.

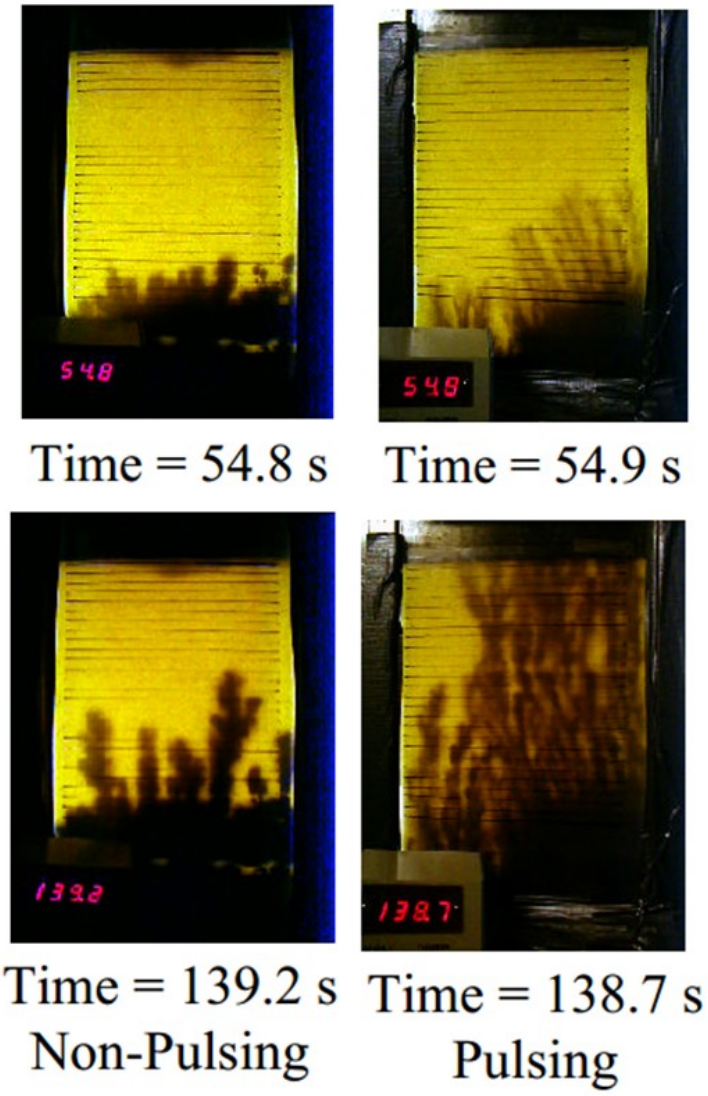

Figure 2.1: Images of pulsating and non-pulsating unstable displacement as presented by Davidson (1999). The images show that the displacement is more stable for pulsating case at both the time intervals.

Cyclic Steam Stimulation: Cyclic steam stimulation (CSS) was one of the first steam based oil recovery process and has been in field scale implementation since 1950s. Three main driving mechanisms that lead to improved oil recovery during CSS are viscosity

reduction, wettability alteration and gas expansion. Recent innovations such as addition of various chemicals in steam, directional drilling for horizontal wells and hydraulic fracturing has improved the average recovery factor for CSS from 15% to approximately 40%. CSS was more prevalent before the advent of SAGD as SAGD performs much better than CSS in terms of oil recovery. Alvarez (2013) indicated that while CSS produce about 10-20% of oil in place, SAGD can recover more than 60-70% oil in place. Cyclic steam injection process is performed in the huff and puff manner. Steam is injected first for a couple of days followed by a soak-in period of another couple of days. At the end of soak-in period, the hot oil and pressurized steam is produced. Once the production declines below economical rates, the steam cycle is started again.

Like any thermal method, efficiency of CSS is also restricted by the pay thickness of the reservoir. Chang (2013) performed a detailed analysis of Horizontal well- cyclic steam stimulation (HW-CSS) for different pay thickness and concluded that HW-CSS becomes uneconomical for a pay thickness of less than 8 m due to excessive heat loss to the over-burden and under-burden. A minimum pay thickness of 11 m is required for breakeven in HW-CSS. Pay thickness of 14 m leads to most efficient oil recovery. Pay thickness higher than 20 m lead to higher production but recovery cannot be classified as efficient because higher pay thickness have higher gravitational influence and steam rises to the upper section of the pay. Efficient oil recovery from thicker oil reservoirs therefore requires smaller well spacing.

VAPEX: Vapex or Vapor extraction is a process where instead of steam, a solvent or a mixture of solvents is used to mobilize oil. A benefit of Vapex is that it does not require steam generation. Solvent processes do not require energy expenditure to produce steam so they may have higher profitability potential. However, large scale implementation of

this process has not yet been carried out. VAPEX can also be coupled with cyclic steam injection or SAGD to enhance their performance. Several authors have looked into the prospect of incorporating heat with VAPEX process (Rezai *et al.* 2007; James *et al.* 2008). Role of asphaltene precipitation in Vapex was studied by Haghighat et al (2010). It is believe that the solvents cause the asphaltenes in the oil to precipitate that lead to in-situ upgrading of oils but asphaltene precipitation can plug some pores and cause formation damage, especially in near well bore regions.

THAI: Toe-to-heel air injection (THAI) is a form of in-situ combustion process that is relatively new and is thought to have great potential. Oil is ignited in the reservoir forming a front of fire moving from one end of the horizontal well (toe) to the other (heel). In-situ combustion breaks the heavy oil components and upgrades a part of heavy bitumen in the formation. Advantages of THAI are numerous; unlike water flood it does not require water, unlike steam injection it does not require burning fuel or steam generation and has lower green house gasses emission.

Most of the research on THAI or in-situ combustion processes has been conducted in University of Bath by the research group of Malcolm Greaves. Greaves *et al.* (1993) compared the efficiency of horizontal wells in-situ combustion processes vs. vertical wells. They conducted 3D experiments in semi-scaled models and concluded that the recovery was always higher for horizontal producer wells. This vertical injector and horizontal producer configuration later became popular as THAI. They also observed that the produced oil was upgraded by 7-10^{o}API. (Greaves *et al.*, 1996). Xia *et al.* (2002) found that the recovery from THAI is mostly independent of the formation thickness. The peak combustion front temperature does rises with thickness. However, these conclusions are based on laboratory experiments and the results may change at field scale. Greaves *et*

al. (2000) also proved through their laboratory experiments that the recovery of THAI is much higher than other IOR processes like SAGD etc. First pilot test of THAI was initiated in McMurray Formation of the Athabasca oil sands (Ayasse, 2005). Although not much has been published about the success of this pilot it is expected to produce 17-21% more than the expected bitumen production from SAGD.

2.1.3 Challenges with Heavy Oil Production

Compared to the conventional water flood or gas flood, production of viscous heavy oils is a challenge in itself. While new technologies like CHOPS, SAGD, CSS, VAPEX and THAI have made the production possible and economical; challenges still remain. There are cases where one of the above mentioned methods will cease to be uneconomical and therefore alternate methods need to be developed. Few reasons that render the conventional heavy oil production processes less effective are:

1. Thermal methods are not suitable for deep sea applications because of additional cost of steam generation and heat loss in the riser.
2. Thermal methods are not suitable for shallow reservoirs too. Especially the reservoirs close to a permafrost. Heat from the reservoirs may destabilize the permafrost and cause environmental concerns.
3. Effectiveness of most thermal methods also relies heavily on the horizontal drilling capability. It is believed that reservoirs with thickness less than 10 m are not good candidates for drilling two horizontal wells.
4. Thickness also affects thermal methods in other ways. If the reservoir is too thin, excessive heat loss to the over burden and under-burden occurs. In case of thick reservoirs there is a danger of steam or solvent coning upwards. Multiple wells might be a better alternative for thick reservoirs.

5. Thermal methods are associated with high carbon footprint, which can possibly lead to high taxes in some places for the operators. Most countries are resorting to stricter environmental and water regulations that mean extra cleanup and disposal cost. (McFadyen *et al.*, 2012)
6. Most thermal methods rely heavily on vertical permeability. Some reservoirs are highly stratified or laminated and the vertical permeability is low. The stratified layers may not even be in hydrodynamic contact with each other.
7. Lastly, One third of worlds heavy oils reservoirs are in carbonate formations. Steam or hot water injection in a carbonate formation will possibly cause formation damage. Minerals will dissolve at the high temperature end closer to the injector and precipitated out closer to the production well plugging up the formation. Also, steam channeling through the fractures will cause unstable heat propagation.

In Canada and Venezuela, several such reservoirs exist where conventional thermal or solvent techniques cannot be applied or are less favorable because of the above mentioned concerns. Alternate non-thermal EOR methods need to be developed for such reservoirs.

2.1.4 Alternate Non-Thermal EOR Methods

In cases where thermal or solvent based processes fail chemical EOR methods have the potential to recover the otherwise unrecoverable oil reserves. Polymer related chemical EOR processed like polymer flooding, surfactant polymer flooding or alkali-surfactant flooding were traditionally thought to be applicable for oils with viscosity around 200 cp only. Some recent studies have shown that ASP and polymer floods can be applied with significant recovery for oils as viscous as 10,000 cp. Use of alkali with heavy oils is very

beneficial as heavy oils typically have a high acid number and as a result in high in-situ soap generation that reduces the amount of surfactant required in the slug. Two main chemical EOR alternatives for heavy oils recovery are polymer flood and ASP floods.

Polymer Flood for Heavy Oils

Normal waterflooding under adverse viscosity/mobility ratios result in poor reservoir sweep and less oil recovery. As a method of enhanced oil recovery, polymers are typically added to water to reduce its mobility and result in a favorable viscosity ratio. Detling (1944), Aronofsky, 1952, Dyes *et.al.* (1952) and Barnes (1962) were one of the first researchers to study two phase displacement at adverse mobility ratios and propose the idea of viscosifying the injected water to stabilize the displacement. Pye (1964) and Sandiford (1964) introduced water soluble polymer for mobility control applications. A large number of laboratory, pilot and field studies have been conducted since then and to summarize them all is practically impossible. An excellent review was present in Chang (1978) and Needham and Doe (1987). During the early era, all polymer flooding was being considered only for moderately viscous oils. In recent years, high oil prices and new technologies like directional drilling and cheap availability of industrial grade polymers has initiated a shift towards polymer application in viscous and heavy oils reservoirs. Brooks *et al.* (1998), Levitt *et al.*(2011), T. Skauge *et al.*(2012), Clemens *et al.*(2013), Bondino *et al.*(2013) and T. Skauge *et al.*(2014) published a series of papers looking at the possibilities of polymer applicability for viscous and heavy oils. Delamaide (2014a) provided an excellent review of polymer flooding for viscous oils.

Field or Pilots of heavy oil polymer flood

Pelican lake field in Canada has been successfully flooding with polymer at the field scale. The reservoir was a low energy reservoir with very little solution gas and gas

cap. As a result the primary recovery was low and polymer pilots were initiated. To compensate for the high viscosity of the oil, wells were drilled at 50 m spacing and few were at 200 m apart. After a couple of unsuccessful pilots, polymer pilot worked and was implemented on the field scale. Operators estimate that the oil recovery due to polymer flood will be an additional 20-30% OOIP. Delamaide (2014a, 2014b).

Mooney Bluesky field in Canada with 300 cp oil has undergone a successful pilot polymer flood and plans to implement it at field scale are underway. The recovery is expected to increase about 20% OOIP. Another successful heavy oil polymer pilots in Canada is Seal Bluesky polymer flood conducted by Murphy Oil.

Outside of Canada, successful pilots have been completed in Oman and China (Marmul field and Bohai Bay, respectively). Marmul Field has medium viscous oils of about 90cp and Bohai Bay oil viscosity varies from 30 – 450 cp. (Moe Soe Let *et al.*, 2013, Denney, 2013, Jaspers *et al.* 2013, Kang *et al.* 2011). All known viscous oil polymer tests and their details are listed in Table 1 and 2 of Delamaide (2014a) (Table 2.2).

Project	Country	Status	Lithology
Pelican Lake	Canada	Full Field	Sandstone
Mooney	Canada	Pilot	Sandstone
Seal	Canada	Extended Pilot	Sandstone
Tambaredjo	Suriname	Pilot	Sandstone
Marmul	Oman	Full field	Sandstone
Bodo	Canada	Pilot	Sandstone
Suffield Caen	Canada	Pilot	Sandstone
El Corcobo	Argentina	Pilot	Sandstone
Bohai Bay	China	Full Field	Sandstone
Daidema	Argentina	Extended Pilot	Sandstone

Table 2.2: Chart showing the data of different polymer floods currently undergoing at pilot or field scale in various countries. (Data taken from Dilamaide (2014))

Polymer flood may have potential for viscous oils in fractured carbonate reservoirs too. There are no reported cases of field or pilot scale flood for viscous oils in carbonates and therefore this topic is either still un-researched or largely in the laboratory research phase and needs further investigation.

ASP for Heavy Oil

Alkali surfactant and polymer are used together in a synergetic combination in ASP EOR process. Alkali reacts with the acidic oil in-situ and generates soap. Alkalis also increase the pH of the system which changes the surface zeta-potential and reduced

surfactant adsorption on rocks surface in sandstones. Surfactant along with the in-situ generated soap helps in lowering the interfacial tension between oil and water. Polymer provides the mobility control for the displacement. The major enhanced recovery mechanism is the reduction of interfacial tension between oil and water that helps in mobilizing the capillary trapped oils. Reduction of interfacial tension leads to increase in capillary number and as a result a lower residual saturation can be achieved (Stegemeier, 1977; Lake, 1989).

Several ASP field tests for conventional oils have also confirmed that the residual oil can be displaced by the use of alkaline-surfactant-polymer system (Falls *et al.*, 1992; Reppert *et. al.*, 1990). In particular, the ASP field test in the Daqing field recovered about 20% additional OOIP after waterflooding (Shutang *et. al.*, 2010). The earliest idea of alkali application for heavy oil was suggested by Subknow (1942). They suggested injecting strong alkalis in bituminous sands to emulsify bitumen into water. The emulsification of course happens due to generation of soaps from organic acids in the bitumen. Jennigs *et.al.* (1974) conducted alkali flood on a moderately viscous oil of 187 cp and found that emulsification of the oil provided in-situ conformance control and resulted in high incremental oil recovery. Like polymer flooding, ASP was also developed for moderately viscous oils but lately due to new interest in heavy oils, ASP is also being considered for heavy oil reservoirs (Yang *et. al*. 2010; Bryan and Kantzas, 2007; Bryan and Kantzas, 2009; Shamekhi *et al.* 2013).

The boost in ASP research in heavy oils is also a result of development of new large hydrophobe surfactants that are specifically designed for heavy oils with high naphthenic content. Adkins *et.al*. (2010) and Liyange *et.al.* (2012) developed the novel surfactants as a substitute for high EACN crude oils suitable for high temperature and salinity environments. Kumar (2013) in his PhD dissertation developed ASP methods for

two different heavy oils: 330 cp and 10,000 cp. They used sodium bicarbonate alkali along with a commercially available non-ionic hydrophilic surfactant (TDA 30EO) to achieve optimum results. They reported significant increment in oil recovery for both the oils with their ASP formulation. For 10,000 cp oils they developed a new mechanism for enhanced recovery. As per the new mechanism, they injected water or polymer under secondary condition to form fingers. Alkali surfactant or alkali surfactant polymer was then injected in the medium and it flows along the water/polymer fingers that act as pseudo horizontal wells. The AS slug emulsifies oil along the walls of the finger and the fingers grow wider. Bryan and Kantzas (2009) proposed a different mechanism of improved oil recovery via AS injection in heavy oil (11,500 cp). They suggest that the improved recovery is caused by the oil in water emulsions that is generated in situ. The oil droplets in this emulsion may coalesce and plug up some pore throats. This plugging will redirect the flow of water and improve the sweep. Emulsification and entrapment along with interfacial tension reduction were believed to be the dominant mechanisms. Shamekhi *et al.* (2013) conducted several core flood experiments on 500 cp and 16000 cp oil to compare the recovery efficiencies of polymer and ASP floods. They concluded that even though addition of polymer improves oil recovery the over-all recovery increment is much higher for ASP floods. Hocine *et al.* (2014) conducted tertiary ASP slug injection in a 1400 cp oil saturated core that had been polymer flooded in the secondary mode. The surfactant formulation was designed to produce ultra low IFT and the experimental recovery was as high as 100% of remaining oil saturation depending on the slug size.

Field or Pilot scale ASP for Heavy Oils

In addition, to the laboratory research cited above. Some interesting ASP flood for heavy oils has been tried as pilots in Canada. Implementation of ASP process in field or pilot scale needs a lot more planning as alkalis usually precipitate the divalent ions and

therefore either water softening or a fresh water source is requires. Some authors are also working on alternate alkalis like ammonium hydroxide and sodium borosilicate for ASP application in hard brine (Sharma (2014), Southwick (2014)). Taber South Mannville B project by Husky oil and Suffield project by Cenovus are two ongoing projects of ASP floods in Canadian heavy oil reserves. The Taber South field has oil of about 150-50 cp and had already been successfully polymer flooded before the implementation of the ASP flood. The secondary polymer flood recovery was about 38% at the time of ASP initiation. The ASl slug comprised of 0.75% NaOH + 0.15% wt surfactant and 1200 ppm HPAM 3630s. ASP injection started in May 2006 and 0.34 PV of the ASP slug was injected and then it was chased by continuous polymer drive. The response was positive and production peaked from 300 bopd to 1800 bopd. Although the response was positive the project was plagued by scaling, plugging and injectivity issues that lead to high operational cost and work-overs. Overall the project was an economic success and reached a cumulative positive cash flow in less than 5 years. (McInnis *et al.*, 2013)

The Suffield project is a small block with a pay thickness of only 2.9 m but has high permeability (2000md) and porosity, making it a good candidate for non-thermal EOR. The block had been water flooded already and the recovery was only 10%. This is largely because of the high viscosity of the oil. (480-250cp). ASP injection was started at water cut of about 60% and oil rate of 100 bopd. However, the ASP injection did not improve the production and the recovery rate remained the same. The only argument for the success of this ASP flood is that the production should have steadily decreased in absence of ASP flooding. The prolonged constant recovery rate without improved WOR cannot be confidently attributed to the ASP injection. The overall response of the ASP injection in this case was not positive. (Delamaide, 2014b)

Other New Methods

Some new innovative EOR/IOR methods have been suggested in the recent literature. Taking advantage of the high acid number of the heavy oils Fortenberry et al. (2015) suggested a new chemical enhanced-oil-recovery (EOR) technology called alkali/co-solvent/polymer (ACP) flooding. They found that addition of low concentrations of certain inexpensive light co-solvents to alkaline polymer (AP) solutions dramatically improves the performance of Alkali-Polymer corefloods. The addition of co-solvent improves the phase behavior and produces low-viscosity micro-emulsions rather than viscous macro-emulsions. Taghavifar et al. (2014) suggested a hybrid scheme that involved some thermal and chemical EOR aspects. They proposed a mild heating of the reservoir by injecting a heated solution along with some chemical EOR slug (ACP/ASP) greatly enhances the performance. This process can be beneficial in a thin-shaley reservoir where steam injection is not efficient.

2.2 VISCOUS FINGERING IN POROUS MEDIA

2.2.1 Viscous Fingering in Immiscible Flows

Experiments and Theory

Study of immiscible displacement of oil by water in porous media has been a topic of interest for more than a century, as most secondary recovery processes require an immiscible displacement of oil by water or gas. Water flood, polymer flood, Gas or steam floods etc. are all examples of immiscible displacement in porous media. The oil targeted in these displacements is a naturally occurring hydrocarbon rich crude oil and very often have a viscosity much higher than that of water or the injected fluid. In cases, where the displacing fluid is less viscous than the fluid being displaced, the displacement is not stable and results in channeling of reservoir fluids leading to a poor recovery. This physical phenomenon of a high mobile phase channeling through a less mobile phase, has

been termed as viscous fingering in the petroleum engineering literature. The term viscous fingering was coined by Engelberts and Klinkenberg in 1951.

The research on understanding viscous fingering and predicting its occurrence started in early 1950s. Engelberts and Klinkenberg(1951), Van Meur(1957), Van Muer and Van der Poel(1958), Chouke *et al.*,(1959) de Haan,(1959) Hagoort(1974) and Peters and Flock(1981) made significant contribution to viscous fingering both in terms of it visualization and predictability. Engelberts and Klinkenberg (1951) published the results of laboratory floods in homogeneous unconsolidated sand packs at the mobility ratio of 24. They observed water channeling through the more viscous oil bypassing some area. This observation was consistent in most experiments with viscous oils and therefore they termed the process viscous fingering. Most of their experiments were conducted in homogeneous sandpacks and with 100% oil saturated porous medium i.e. without the presence of connate water saturation. Review of literature suggests that it was a common practice during that era (1950-1970) to ignore the presence of connate water saturation. It was later established that 100% oil saturated medium with no residual water is not a good representation of the reservoir conditions (Perkins and Johnston, 1969). Nonetheless, their experiments yielded important insights about viscous fingering. They observed that for light oil the displacement efficiently increases with increase in flow rate and the displacement is stable. However, for viscous oils, lower injection involved better recovery and sweep. Faster injection cause adverse fingering and increase residual. At intermediate rate they observed that the displacement was transitioning from a stable to unstable.

Van Muer (1957) conducted experiments in transparent three-dimensional porous media. They used cylindrical sand packs and 2 dimensional linear flow setup packed with pyrex glass beads and saturated it with an oil of same refractive index. Their experiments

yielded clear pictures of stable displacement at a viscosity ratio of 1 and viscous fingers at viscosity ratios of 80. While their experiments helped in clearly visualizing the growth of viscous fingers their experiments lacked the presence of connate water which makes the initial wettability state of the porous medium questionable. Also the experiments were conducted at rather high flowrates of about 1.67×10^{-2} cm/sec, equivalent to about 47 ft/day. Van Muer and Van der Poel (1958) published further new experiments in similar transparent porous media and developed a new theory for immiscible displacement in porous media highly dominated by viscous fingering. Their theory had several similarities with Buckley Leverett (1942) theory for stable displacement. The model assumes that the viscous fingers initiate at the inlet itself and grow in length over time while maintaining the same cross section. Furthermore, the water relative permeability curves for the finger growth region were assumed to be linear with respect with water saturation. The model, though very simple and ideal was a motivation for further studies on viscous fingering.

Viscous instabilities are said to arise due to perturbations in space or time. Perturbations in space may arise in form of perturbation in permeability. Even in the most homogeneous rocks, heterogeneities exist at the pore scale and lead to perturbation in the displacement front. However, for low viscosity and low flow rate, interfacial tension helps in stabilizing the interface and thereby dampening the growth of viscous fingers. Thus in order to predict the onset of viscous fingering in a particular system it is essential to understand the factors which could lead the interfacial instabilities to grow with time. Saffman and Taylor (1958) used Hele Shaw cell to study the growth of interfacial instabilities between two fluids. They found that interfacial tension acts as a dampening factor and prevents the growth of instabilities that are smaller than a critical size. Also, in

vertical displacements gravity tends to stabilize the perturbations if the heavier phase is injected from the bottom or the lighter phase is injected from the top.

Another systematic study on viscous fingering from a stability standpoint was conducted by Chuoke *et al.* (1959). They performed stability analysis on a planar interface between the two immiscible liquids being displaced at a constant rate and deduced the conditions that would promote viscous fingering and instability. They developed a critical wavelength λc, given by

$$\lambda_c = 2\pi\left[\frac{\sigma^*}{\left(\frac{\mu_2}{k_2}-\frac{\mu_1}{k_1}\right)(U-U_c)}\right]^{1/2} \text{ or } \lambda_c = C\left[\frac{\sigma}{\left(\frac{\mu_2}{k_2}-\frac{\mu_1}{k_1}\right)(U-U_c)}\right]^{1/2} \tag{2.1}$$

$$U_c = \frac{(\rho_2-\rho_1)\,g\cos\theta}{\left(\frac{\mu_2}{k_2}-\frac{\mu_2}{k_2}\right)} \tag{2.2}$$

Where 1 and 2 notation is used to distinguish the two liquids under consideration, μ, ρ and k are viscosity, density and effective permeability respectively. U is the superficial velocity (volumetric flow rate/area) and U_c is the critical superficial velocity, σ* is the effective interfacial tension in between the two fluids in a porous medium. Chouke's model assumes that the macroscopic curvature of the interface determines the interfacial forces and not the microscopic curvatures. This assumption is valid in a hele-shaw like models but not in a porous medium. C is Chouke's constant and is defined as $C = 2\pi\sqrt{3C^*}$ and $\sigma^* = C^*\sigma$. For parallel plates like in Hele-shaw model, σ* = σ. It is generally believed that if the system transverse dimensions are smaller than the critical finger wavelength the displacement will be quasi-stable i.e. the displacement will appear to be stable at the lab-scale but will be influenced by instabilities once the system

dimensions are larger than λ_c. A term called wavelength of maximum instability was also derived and was given by $\lambda_{max} = \sqrt{3}\lambda_c$. The model was verified against results of experiments in both parallel plate Hele-shaw model and unconsolidated porous media. The excellent match between the Chouke's model prediction and the Hele Shaw cell experiments was expected because the fundamental equation used to develop the model were mathematical representation of flow in between parallel plates. However, the model performed well in the porous media experiments as well. 25.40 and 190.45 were used as the values for Chouke's constant for oil-wet and water-wet media, respectively. Unlike the parallel plate experiments, the fingers observed here were not sinusoidal and the random orientation of the fingers made the measurement of the finger wavelength difficult. One drawback associated with the use of this model is the unknown variable σ* or C*. Haan (1959) also confirmed Chouke's theory through their displacement experiments without connate water. Although for a mild viscosity ratio of 25 the experiments proved the validity of Chouke's model in the absence of connate water. Haan (1959) studied the effect of the flow rate on the oil recovery by linear displacement experiments. At very low flow rates the capillary forces dominated the viscous forces and small immobile oil pockets were formed resulting in low oil recoveries. With increase in flow rates the size of the oil pockets decreased and the oil recovery increased accordingly. With still higher flow rates, the oil recoveries decreased again owing to viscous fingering. The number of fingers increased with flow rate, in accordance with the instability theory of Chouke or Saffman and Taylor.

Rachford (1964) was the first to question the applicability of a stability theory that is based on flow between parallel plates to flow in porous media in the presence of wetting fluid connate saturation. He presented his stability theory that was based on Buckley Leverett solution. A more holistic study of the topic was conducted by Perkins

and Johnston (1969). They conducted several experiments in system similar to Chouke's experimental setup. They observed a vast difference between the experiments with connate and without connate water and suggested that for experiments representing water-wet to mild wet medium, presence of connate water is must to capture the real physics. In the bead packs with connate water numerous water fingers developed at the inlet but were damped out and did not advance further into the model. This dampening of fingers was supposed to be caused by the presence of connate water in the porous media. Hagoort (1974) offered a new insight into the prevailing stability theories. He introduced the concept of shock mobility to replace the conventional end point mobility ratios. This implied that the stability of the front will be determined by the mobility of the two phases on the either side of the shock front rather than the conventional end point mobility ratios. He concluded that the shock mobility ratio is considerably lower than the end point mobility ratio; it is possible to have stable displacement in the porous media even when the end point mobility ratio is adverse.

Peters (1979) extended the existing Chouke's theory to predict the onset of instability in cylindrical and rectangular porous medium both with and without connate water saturation. They conducted 35 different experiments at 3 different viscosity ratio and different flow rates to study the onset of instability at different conditions. According to their new model the stability boundary in cylindrical core was given by an Instability number I_{sc} defined as,

$$I_{sc} = \frac{(M-1)(U-U_c)\mu_w D^2}{C^* \sigma K_{wr}} \leq 13.56 \tag{2.3}$$

where M is the mobility ratio, U and U_c are same as in Chouke's equation and D is the diameter of the core.

All the 35 experiments conducted in this study were conducted on a 2 in diameter sand packs. The length of the tube was varied but the diameter was not changed. However, the model does provide an option of dimensional scale up. An expression for rectangular system was also proposed. This expression was not experimentally tested.

$$\frac{(M-1)(U-U_c)\mu_w L_x^{\,2} L_y^{\,2}}{C^* \sigma K_{wr}\left(L_x^{\,2}+L_y^{\,2}\right)} \le 9.87 \qquad (2.4)$$

L_x and L_y are the dimension of the rectangular cross-section of the model and

Experimental observation suggested that the oil recovery decreases in the range 13.56 < Isc <1000. The expression has been tested by several other authors and has been proved to be a useful tool however, the wettability number or parameter C* remains ambiguous as in Chouke's model and varies from rock to rock. During this time, other authors such as Kloepfer (1975), Wilborg (1976) and Baird (1978) also conducted similar experiments to understand the trend of water flooding at different flow rates and high viscosity ratios. Like Peters work, these studies were also focused on only a couple of viscosity ratios and varied the flow rates to a large extent. This is understandable as during this era, there was neither an urgency for viscous oil research nor did the industry have much interest in producing oils with viscosity higher than just a couple of hundred centipoises. Most viscosity ratios discussed in these studies were in the range of 100-500. Also, most flow rates used by Peters, Kloepfer, Wilbrog and Baird were faster than the conventional 1 foot per day rate. This is not practical as typical flow rate in a viscous oil reservoir would be much smaller than one foot per day because of the injection pressure constraint. More recently, Tavassoli et al. (2014a, 2014b) and Lu et al. (2013, 2014) extended the stability theory to gravity stable surfactant flows. They performed stability analysis to develop a correlation for critical velocity of a gravity stable surfactant flood. Their analysis differed from a typical stability analysis because the formation of a viscous

micro-emulsion bank (typical of a surfactant process) between the oil bank and the surfactant slug creates two interfaces rather than just a single interface as in Chouke's or Peters's analysis.

Abrams (1975) presented data showing the influence of fluid viscosity, interfacial tension and flow rate on residual oil saturation. Although, he used only mildly viscous oil, he was the first to point out that residual oil saturation or recovery in a viscous system cannot be correctly represented by only capillary number or viscosity ratio and has to be a function of both capillary and viscous effect. They proposed a new dimensionless number based on their study and was given by,

$$\left(\frac{v_{\text{int}}\mu_w}{\sigma_{ow}}\right)\left(\frac{\mu_w}{\mu_o}\right)^{0.4} \tag{2.5}$$

where, v is the true interstitial velocity of water during a water flood and is defined by $\frac{Q}{A\phi(S_{oi}-S_{or})}$. Q is the volumetric flow rate (ml/sec), A is area (cm^2), ϕ is porosity, S_{oi} and S_{or} are initial oil saturation and residual saturation respectively.

Croissant (1968), found visually that the finger width can be scaled up with square root of time or square root of 1/injection rate. This implies that slower injection leads to fatter fingers. These observations were confirmed by Stokes *et.al.* (1986) and Pavone (1992). Stokes *et.al.* (1986) observed that the width of finger increased as the flow rate is decreased in a porous media. For a non-wetting fluid displacing a wetting fluid, fingers were found to be just a couple of pore wide and were much smaller than the observed finger width for imbibition. Pavone (1992) studied the viscous fingering process in porous media at different flow rate and viscosity ratios. They utilized a unique way of visualizing viscous fingering in a naturally occurring porous media. Unlike all his predecessors, who used artificially created transparent porous media; he conducted

experiments in a naturally occurring carbonate rock and used epoxy resin as the injected fluid. After breakthrough the core was heated to 120^{o}C which solidified the resin and then the core was put in a solution of hydrochloric acid. Hydrochloric acid dissolved the regions of the cores untouched with epoxy and the final finger shape and size were revealed (Figure 2.2). Pavone used oil up to 40,000 cp viscosity while the epoxy resin was about 40cp in viscosity. Their results scale up pretty well for the dimensionless number ΔN_c and μ_r. Where Nc was defined as ($N_{coil} - N_{cresin}$). On simulating the results of their experiments they concluded that the relative permeability of the injected epoxy was almost linear and the end point relative permeability decreased drastically with viscosity ratio. Oil relative permeability was also linear for stable displacement but changed shapes to become convex upwards towards for the most unstable case. Few criticism of Pavone's work are: he used cores that were initially 100% saturated with oil, although he claimed that the resin behaved very much like water in terms of IFT the dynamic capillary processes would have been slowed down owing it higher viscosity (40cp). Lastly, the process of dissolution of the core is a destructive process therefore the experiment has to be repeated on a different core each time.

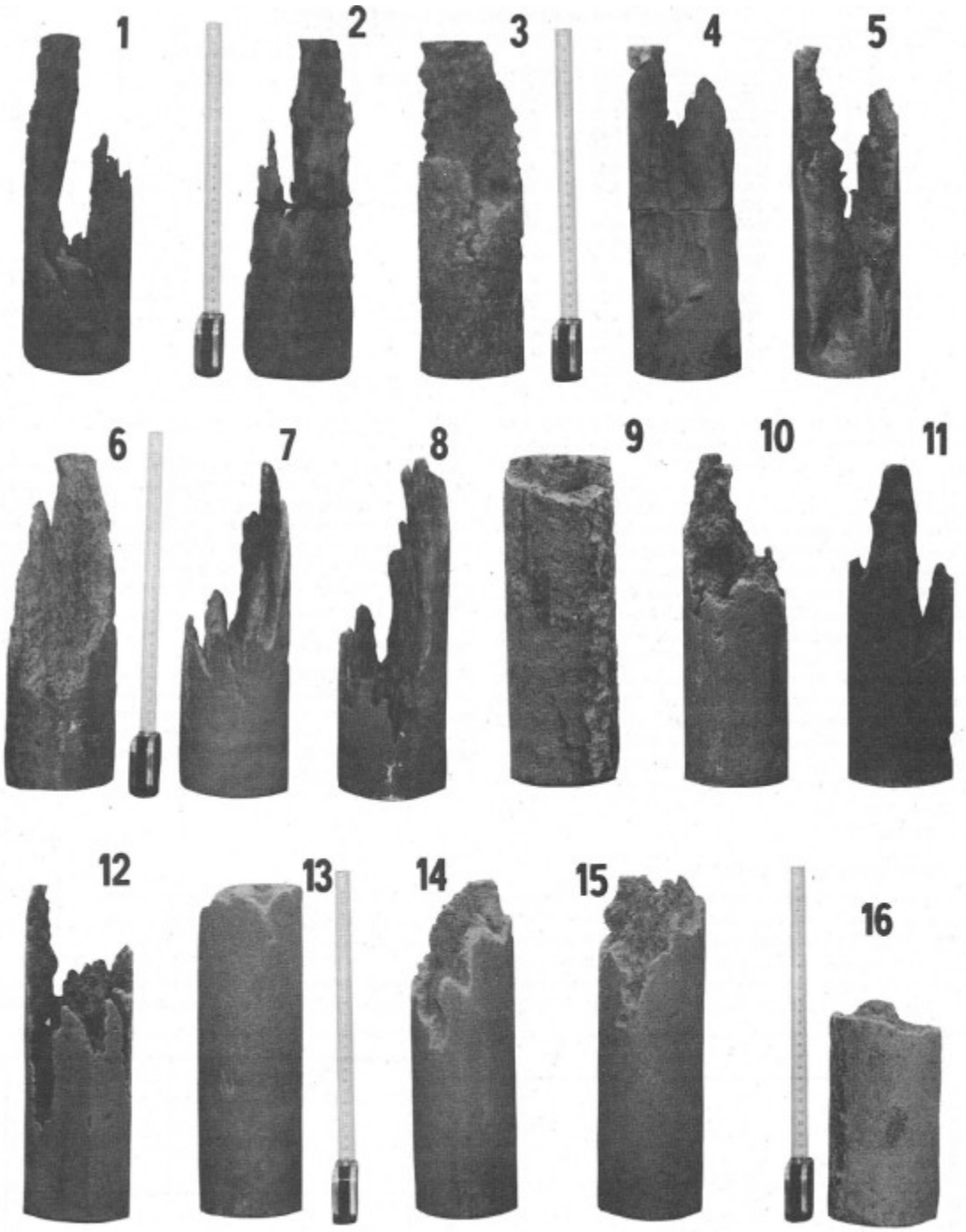

Figure 2.2: The molded fingers as observed by Pavone (1992) after dissolving the carbonate core in an acid solution. Viscous fingering can be clearly observed in these images.

Recently, the decline in conventional oil reserves has piqued the interest in exploiting unconventional heavy oil reserves. The industry is now looking to exploit reservoirs with oils up to 50,000 cp. Mai *et al.* (2009), Mai and Kantzas (2009) and Mai and Kantzas (2010) published a series of papers researching the effect of flowrate and oil viscosity on breakthrough and overall recovery. They also studied in detail the effects of low rate waterflooding in viscous oils and concluded that slower injection rate leads to higher oil recovery both in terms of breakthrough and ultimate recovery. This increase in recovery with decrease in flow rate has been attributed to the fact that slower injection allows more time for capillary equilibrium and hence water imbibes more. As a result, fingers are wider and recovery is higher. Bondino *et al.* (2011) and Skauge *et al.* (2012) have also published results of several unstable displacements in 2 dimensional Benthiemer slabs. They performed polymer and water floods, compared their efficiencies and used low energy X-Ray scanning technique to visualize the displacements. Even after years of research, viscous fingering and unstable displacements are not completely understood. The models to predict the instability limits and the knowledge to prevent these instabilities to occur exist. However, modeling these complicated flows is still a challenge, especially at the reservoir scale. Several researchers have attempted different approaches and suggested improvements to the existing models. The next section will be a review of the viscous fingering modeling and simulation.

2.2.2 Modeling Viscous Fingering

Viscous fingering as a fractal phenomenon

Fluid flow in porous media gives rise to several patterns and fronts depending on flowrate, viscosity and interfacial tension. Disorder in the pore size distribution causes

these fronts to display fractal properties. Lenormand (Lenormand and Zarcone (1985); Lenormand *et al.* (1988)) conducted micromodel studies at different viscosity ratios and flowrates to determine the flow regimes during two phase immiscible flow in porous media. Lenormand (1988) published his three regimes on viscosity ratio and capillary number plots that are expected to be stable, viscous dominant or capillary dominant.

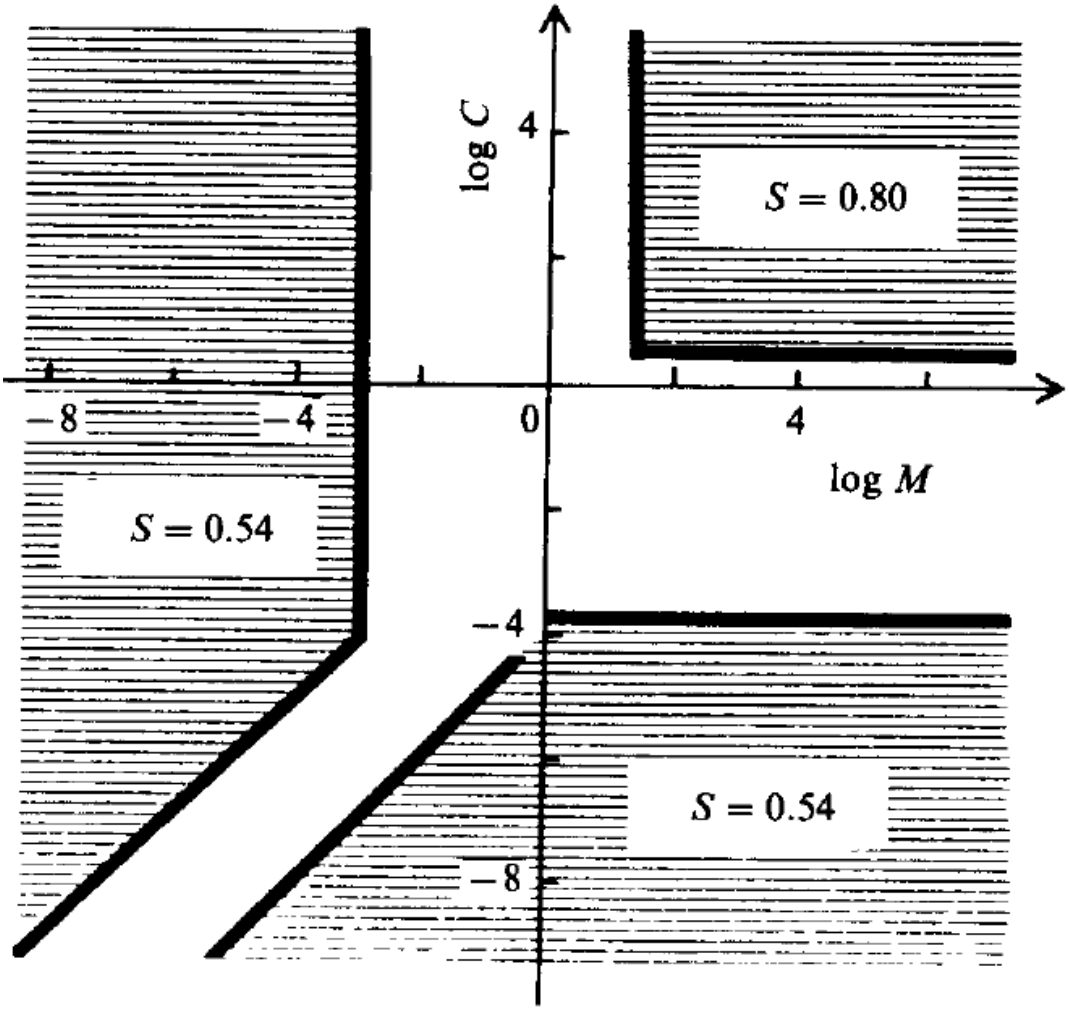

Figure 2.3: The phase diagram as presented by Lenormand and Zarcone (1988) shows the three possible displacement regimes in two phase flow.

Fractals occur in nature in a variety of systems (Mandelbrot, 1967; Meakin, 1988 etc.) when the randomizing effects dominate over the stabilizing effects. Fractals are described as self-similar objects; which means they are either exactly the same or nearly similar at different scales. Nittmann *et al.* (1985) conducted one of the earliest studies on the fractal nature of the viscous fingers in a Hele Shaw cell. They argued that in order to generate fractal structures, the stabilizing effects of interfacial tension should be minimized so that the random effects can dominate. To achieve this purpose, they filled the Hele Shaw cell with a viscous polymer solution and injected water into it. Their mathematical analysis showed that the viscous fingers formed could be analyzed using the concept of self-similarity or fractals. For this particular case the fractal dimension was found to be 1.40±0.04.

Growth of an invading fluid generates spatial structures that are fractal in disordered porous media. At high displacement rates or at very high viscosity ratios, the displacement front appears highly fractal (Chen and Wilkinson, 1985 and Maloy *et al.* 1985). These fractal structures closely resemble aggregates or patterns developed by diffusion limited aggregation (DLA) (Witten and Sanders, 1981; Witten and Meakin, 1983; Vicsek, 1984). DLA is the process by which particles undergoing a random walk due to Brownian motion cluster together to form aggregates of such particles. Paterson (1984) was the first to realize the analogy of the DLA aggregates with the two phase fluid flow in a porous media where one phase has a much larger viscosity than the other fluid. A limitation of DLA was its applicability at infinite viscosity ratios only. Also, apart from the appearance of the end products there is not much mathematical or physical similarity between flow in porous media and DLA. For example, in DLA a random walker is initiated at a certain distance away from the cluster and it moves towards the cluster. When the particle collides with the cluster it sticks to it. To visualize this in flow in

porous media or petroleum engineering terms, one has to image a chunk of produced oil coming in from the producer and flowing towards the injector. This is opposite to the natural flow direction of the fluids.

Maloy *et.al.* (1985) studied the radial displacement of immiscible fluids in a 2D random porous media. They also observed the fractal structure of the viscous fingers instead of the smooth broad fingers observed in the Hele Shaw cells. The fractal structures were found to have a dimension of 1.62+0.04 consistent with the results of a DLA simulation. Ferer *et.al.* (1995) employed the pore scale simulations to study the flow behavior of different viscosity fluids in a square lattice model. It was observed that in the limit of very large viscosity ratio (~10,000) the pore scale simulations indicated the fractal nature of the flow. However for finite viscosity ratios it was observed that although the flow was fractal at the initial stages it became compact (or linear) on a characteristic time scale that increases with the viscosity ratio.

Kucheryavskia and Belyaevb (2009), introduced sticking probability to change the structure of the DLA pattern qualitatively. Sticking probability is defined as 1/n, where n is the number of times a particle will have to arrive at a certain location before it can be allowed to stick to the aggregate. The resulting aggregates gave thicker DLA structures for smaller sticking probability.

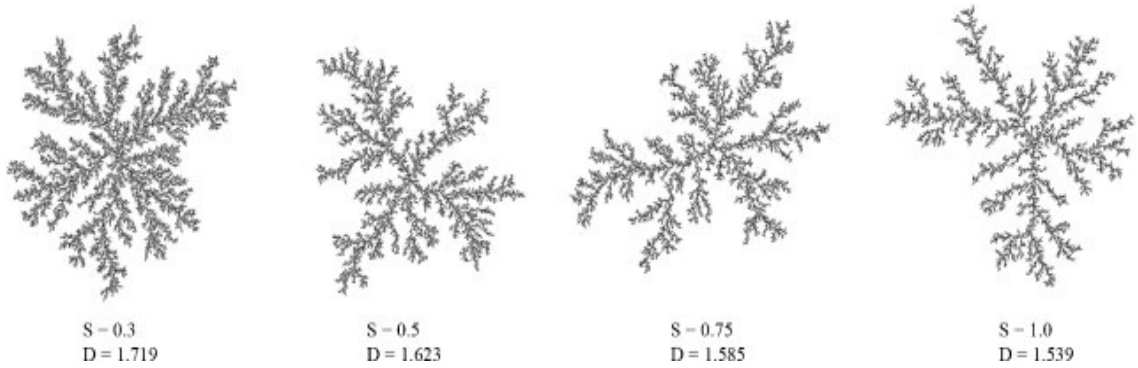

Figure 2.4: The effect of sticking probability on a normal DLA pattern as shown by Kucheryavskia and Belyaevb (2009); the pattern becomes thicker and the fractal dimension increases as the sticking probability decreases.

Fractal structures are also observed in invasion percolation (Lenormand, 1985; Wilkenson and Willemsen, 1983). Invasion percolation represents fluid invasion at low flowrates where capillary pressure is the most dominant force. This kind of flow typically occurs for light oil reservoirs at slow injection rates. A detailed discussion of invasion percolation has been avoided here to keep our focus on viscous forces or viscous dominated processes.

Among several objects in nature that exhibit fractal nature, dielectric breakdown or lightening strike is one of the physical phenomenon widely studied in physics. Dielectric Breakdown Model (DBM) was introduced for the modeling of dielectric discharge in insulators by Niemeyer *et al.* (1985) and later explained at molecular level by Pietronero and Wiesmann (1989). Due to conceptual and qualitative similarity between DLA, DBM and viscous fingering, DBM was also used as an analogy to unstable flows in porous media (Feder, 1985; Sheerwood, 1986). This model has so far

been mostly unappreciated in the field of petroleum engineering but it does have the potential to be useful to model flow in porous media.

Simple models to incorporate viscous fingering effects

It can be concluded from all the visual micromodel and bead pack experiments that the viscous fingering in a complex phenomenon and capturing it accurately will require a very detailed model. As a result, several simpler approaches have been suggested. The simplest of them is the use of pseudo relative permeability curves to lump the effects of all small perturbations into one. Theoretically, the relative permeabilities are supposed to be function of wettability, pore-structure and water saturation only. Relative permeabilities should not be a function of viscosity ratios, temperature or flow rates. This was proved experimentally by Sandberg (1956), Wilson (1965), Sufi (1982) and Miller (1985). They studied the effect of temperature on the relative permeability curves and found no dependence. Wilson, Sandberg and Miller (1985) however conducted experiments at very low mobility ratios (at room temperature) so all the experiments were stable.

Contradictions with respect to conventional theory became evident at higher viscosity ratios. Odeh (1958) conducted experiments on viscous oils up to 71 cp and was one of the first to report the viscosity dependence of relative permeability. This study used the steady state method with a short core of 3 cm length and 2.5 cm in diameter. Edmondson (1965), Davidson (1969), Poston (1970) conducted similar experiments and also observed that initial water saturation, residual oil saturation and end point relative permeabilities vary with temperature. Understanding the variation in relative permeability with temperature is of special interest for thermal extraction of heavy oils reserves. Maini (1985) studied the effect of temperature on heavy oil (16,500 cp at 23^{o}C)-water relative

permeability curves. They concluded that the heavy oil-water relative permeabilities are a function of temperature. They attributed this to three factors: decrease in absolute permeability, increase in initial water saturation and a shift towards water-wet conditions at higher temperature. Nakornthap and Evans (1986) developed an analytical theory to describe the variation of relative permeability with temperature. Their model was based on some questionable assumptions such as decrease in water absolute permeability with temperature and increase in water-wetness with increase in temperature. Lo and Mungan (1973) measured steady-state relative permeabilities at elevated temperatures. They observed that for both the water-wet and oil-wet systems, temperature affected relative permeabilities of both oil and water phase. However, no temperature effect was observed with tetradecane and water. The major difference in between the two set of experiments was that oil water viscosity ratio is very sensitive to temperature, but tetradecane-water viscosity ratio is mostly invariant with temperature. Therefore, they concluded that the viscosity ratio was responsible for the observed changes with temperature. Lo and Mungan (1973) did not explain how the viscosity ratio affects irreducible water saturations.

Kumar and Inouye (1994) used JBN analysis to obtain unsteady state relative permeability curves at different temperatures. They also concluded that the relative permeability data obtained at ambient conditions can be used at higher temperature as long as the viscosity ratio and wettability remains similar. Miller (1985) also pointed out that all the previous studies that showed a dependence on temperature were influenced by various degrees of instabilities. They confirmed that true relative permeability should be independent of temperature. In recent years, Akin *et al.* (1998), Wang *et al.* 2006 and Mosavat *et al.* (2013) have presented some results using viscous oils as high as 13,550 cp. Wang *et al.* (2006) conducted several systematic experiments to study the effect in

heavy oil/water relative permeability curves under ambient temperature conditions. They used oils of different viscosity range from 430 – 13,550 cp and experiments were conducted in silica sand packs. Their results show a clear dependence of relative permeability with viscosity ratio. It is important to understand how viscous fingering is affected by key displacement parameters and how fingering in turn affects the relative permeability.

There are conflicting evidences of variation of relative permeability with flow rate as well. Osoba *et al.* (1951) observed no dependence of relative permeability with injection rates. Sandberg *et al.* (1956) also studied the effect of flow rate and viscosity on two phase relative permeability and observed that the relative permeability is solely a function of saturation and wettability and is independent of flow rate and viscosity ratios. Here again the experiments were conducted in the stable displacement regime with viscosity ratios (μ_r) of 0.48 to 2.02. However, Sufi *et al.* (1982) reported that the flow rate of the injected phases affects the oil water relative permeability curves. The oil relative permeability increased slightly while the water relative permeability increased significantly with the flow rate.

Lefebvre de Prey (1973) studied the variation of relative permeability with respect to a dimensionless number ($\sigma/\mu v$). They kept the viscosity ratio between the two fluids constant and just varied the injection rate and the wettability. They found out that on increasing the viscosity of one phase, the relative permeability of the other phase declines. In general, they concluded that the two phase relative permeabilities are function of viscosity, velocity and wettability of the fluids involved. The most conclusive of all dynamic permeability measurement study was presented by Peters and Khataniar (1987). They studied the relative permeability variation with respect to the instability number (Eq. 2.2). Instability number is a function of mobility ratio and injection velocity

and hence it was clear that the observed affect with respect to viscosity ratio, temperature and flow rates is actually due to the change in the degree of instability of the flow. They compared dynamic relative permeability curves for different instability numbers and concluded that for smaller instability numbers the dynamic and steady state relative permeability curves are similar but as the instability number increases the curves move further away from the steady state curve.

It is important to understand how viscous fingering is affected by key displacement parameters and how fingering in turn affects the relative permeability. A model to predict the unstable pseudo-relative permeability curves as a function of viscosity ratios, flowrate or the instability number will be very useful for modeling the viscous oil displacement and especially for predicting thermal extraction of heavy oils. A part of this dissertation will be focused in development of one such model for pseudo relative permeabilities as a function of some scaling parameter.

It is not practical to account for viscous fingering in finite difference/finite element simulators because a typical finger size is much smaller than a typical computational cell and therefore cannot be represented on a numerical grid. There are many problems associated with simulating viscous fingering; some are a result of the complex physics of frontal instability, while others are mathematical in nature. Backed with the knowledge of the fractal and highly complex nature of viscous fingers several authors realized that it is more beneficial to talk about viscous fingering in terms of growth of cross-sectional averaged properties in time and space.

The early researchers realized that although it is important to understand the finger patterns and structures, it is not important to capture every individual finger at the reservoir scale. It would be desirable to have a model that captures the effect of viscous fingers without actually capturing the details. Skaugen (1985) was the first to understand

this averaging concept and used fractional flow theory to represent an unstable process. King and Scher (1985) extended the existing DLA theory to the finite viscosity regime and developed a DLA like random walker model for capturing both unstable miscible and immiscible processes. They started with the conventional form of Darcy's law and mass conservation equation and then converted it to represent the velocity of a constant saturation contour. The saturation contour velocity was then used as the probability of invasion for that particular grid. This probabilistic scheme generates the fluctuation essential of instability to occur. The probabilistic simulator was examined in detail by King (1987). Hughes and Murphy (1987) developed the concept of pseudo relative permeabilities that can be used to describe the average properties of the unstable immiscible flows. They developed a pseudo 1D equation for flow in porous media with properties averaged in the direction perpendicular to the direction of flow. This pseudo-1D equation lead to the development of pseudo relative permeability curves. The pseudo relative permeabilities are useful as they can be used directly in the conventional reservoir simulator without any other modification. Hughes and Murphy (1988) also presented a probabilistic simulator like King and Scher, which implicitly triggers an unstable flood when the mobility ratio is adverse. They used saturation as as a probability density function to determine the location of the invasion site.

Sigmund *et al.* (1988) conducted experiments in a glass bead pack and video graphed the displacement front at different flow rate at an adverse viscosity ratio of 40 cp. Their analysis was focused on wave-like features such as amplitude and frequency. Their experiments showed that unstable displacements result in a spectrum of viscous fingers and this spectrum is rate dependent. Faster injection leads to shorter wavelength fingers (high frequency) and slower injection leads to longer wavelength. The results

displayed that the RMS finger size for different rates of displacement increases linearly with time and were independent of the flow rate.

Araktingi and Orr (1993) introduced a particle tracking scheme to simulate viscous fingers a heterogeneous porous media and compared it with laboratory scale experiments. They determined that the permeability distribution and variance has a significant effect on the fingering pattern. Conventional simulators use low-order finite volume/difference methods and have significant numerical dispersion error due to large grid sizes. This tends to average or smear the perturbations that would trigger the instabilities and important information is lost. Riaz and Tchelepi (2006) developed a high order method to capture viscous fingering effects. Their model captures the instability due to competing viscous forces and gravitational forces. Mostaghimi *et al.* (2015) used unstructured control volume finite element (CVFE) method for simulating immiscible displacement viscous fingering. They used mesh optimization but generating unstructured coarse mesh in regions here high resolution is not required and the mesh is refined at the interface where the perturbations exist and high resolution is required to keep the interface details.

2.2.3 Viscous Fingering in Miscible Displacements

General Concepts

Instabilities or viscous fingering arise in two phase flow in porous media not just during immiscible displacements but also during miscible displacements. In fact miscible displacement in porous media is better researched than immiscible displacement. Miscible floods are recovery processes that involve injection of a low viscosity solvent which is generally a gas in its liquid state and under full miscibility conditions at the reservoir temperature and pressure. Liquefied gasses are generally much less viscous than

the reservoir crude and thus it tends to finger through the reservoir (Perkins *et.al,*. 1965). Also the oil contacted by the solvent become less viscous and would cause instability of the front. However when a solvent displaces a viscous oil significant instabilities may occur leading to the development of viscous fingering.

Simple models for miscible viscous fingering flows

Most of the models used to represent the fingering behavior of unstable immiscible displacement are inspired by existing models of miscible displacement therefore it is imperative to discuss briefly all the major miscible displacement models in the literature. The three well known models of miscible viscous fingering are Koval (1963), Todd-Longstaff (1972) and Fayers (1988).

Koval (1963) extended the 1D immiscible displacement fractional flow theory to capture the effect of miscible viscous fingering. They used the formula for frontal advance and the fractional flow equation and modified it to represent the miscible system. The relative permeabilities of two phase immiscible flow were replaced by straight lines relative permeabilities i.e. relative permeability of the phase being equal to the normalized saturation of the phase. They modified the fractional flow equation by introducing two constants H and E. H is the heterogeneity factor and E is the effective viscosity ratio. Both the heterogeneity factor and viscosity ratio can be clubbed into one constant 'K', which is now famously called the Koval factor. Fractional flow equation according to Koval theory can be written as,

$$Fs = \frac{1}{1+\left(\frac{1-\bar{S}_w}{\bar{S}_w}\right)\left(\frac{1}{H}\right)\left(\frac{1}{E}\right)} \tag{2.6}$$

A fourth order power law viscosity mixing model was used to determine the effective viscosity of the oil solvent mixture. Koval assumes the solvent concentration in

the mixed zone to be a fixed fraction equal to 0.22. The resulting fractional flow equation can then be used to predict the solvent breakthrough and cumulative recovery.

Another useful model for unstable miscible flow was presented in Todd and Longstaff (1972). They modified a three phase simulator to make it applicable for a miscible system. They critiqued Koval model for assuming a constant mixing ratio stating that in a real miscible displacement process solvent mixing in different ratios. They introduced a factor 'ω' that would vary from 0 to 1 and would represent the extent of dispersion of the solvent and the oil with respect to each other. Value of ω = 1 implies complete mixing and the mixture properties will be same as predicted by the mixing rule. On the other hand, ω = 0 implies negligible mixing and the two components viscosity and density is same as their individual pure state property. Todd-Longstaff model is still one of the most widely used miscible flooding models in the industry.

However, Fayers (1988) raised a question about the applicability of both the Koval model and the Todd and Longstaff model in two or three-dimensional systems. They argued that the viscous fingers are not continues in the transverse direction. Thus at any given cross section, the mobility or density are not the effective mobility or density due to the homogeneous mixing of oil and solvent. They could be drastically different between the inside and outside of the fingered region. Fayers also argues that both the Koval factor 'K' and Todd-Longstaff's 'ω' do not have any physical significance and cannot be well correlated to the actual fingering phenomenon. Fayers instead proposed a model where it was assumed that the fingers occupy a finite fraction of the total flowing cross section. They proposed a fingering function that represented the equivalent growing finger and can be represented by the expression, $a + bC_f^{\alpha}$, where 'a' is the size of the head of the finger, a+b = 1 for miscible floods (implying eventual 100% recovery), C_f is the normalized concentration of solvent and α is a growth exponent. The model assumes a

sharp transition between the leading edge of the finger and the bulk oil region. This model was shown to have the ability to reproduce the experimental observations of the miscible viscous fingering accurately. Fayers, Blunt and Christie (1992), compared the three viscous fingering models: Koval, Todd-Longstaff and Feyers models. The concluded that all three models performs equally well for simple 1D, linear and homogeneous cases but they differ in 2D systems. Todd-Longstaff and Fayer model were found to be superior for multi-dimensional systems and in capturing the effect of gravity. Blunt and Christie (1994) later modified the Todd-Longstaff model to predict the suppressed fingering in a multi-component flow process such as Water-Alternating-Gas (WAG). Recently, Jain *et al.* (2014) published a modified Koval theory for miscible floods in tertiary displacements. In doing so they relaxed the Koval assumption of single displacement front and modeled for two displacement front. The two displacement fronts model is more accurate because an oil bank is formed in the tertiary displacement processes and two fronts actually exist.

2.3 MICROMODELS AND MICRO-FLUIDICS

The conventionally used experimental techniques like core floods and sand pack flooding give us a good insight into the recovery trends and performance of a chemical flood but they do not provide any information about the process happening at the pore scale inside the porous media. Generally a hypothesis about the pore scale petrophysics is built based on the recovery trends and the pressure drop observed during a core flood. For unconventional and new chemical EOR processes or processes in complicated porous medium where conventional theoretical understanding does not apply an idea about pore scale petrophysics can be vital. However, visualizing inside a porous media is not easy. Based on best currently available techniques pore scale information can be obtained by sophisticated methods like micro-tomography and CT scanning. However, micro-

tomography can handle only a very small rock sample generally only a few millimeters in dimensions. It is often argued whether a few millimeter wide sample is a good representation of the actual reservoir. CT scanning and X-ray scanning can handle a larger sample of core but they do not have a very high resolution and therefore the information available is averaged over some depth and pore level details are lost in the process. If pore level details of the mechanism are to be studied, micromodels should be used along with a high resolution imaging device.

Micromodels are a simplified two-dimensional representation of a porous media. A pore network pattern is usually etched on to silicon or a glass plate by photographically printing an image of a pore network pattern on to a glass. This is followed by chemically etching the pattern onto the plate and then fusing it with another plain glass plate. Inlet and outlet ports permit transport of various fluid phases and solutes through the micromodel pore network. Visualization through the glass micromodels permits observations of pore-scale phenomena. Significant development and application of micromodel can be found in the fundamental oil and gas research. These include studies on wettability, viscous fingering, two and three-phase flow, and various enhanced-oil recovery techniques (Buckley, 1991; Wang, 2000; Buchgraber, 2011; Sharma, 2012; Bondino, 2013).

The first etched "capillary micromodel" was fabricated by Mattax and Kyte (1961). They coated a glass plate with wax and scribbled some lines on the wax coating to make the initial patterns. Lastly, the pattern was etched on the glass with hydrofluoric acid (HF). This approach was significantly improved by Davis and Jones (1968), they replaced the wax coating with a photosensitive material and a mask to produce the channels instead of scribbling with hands. This technique, similar to that used for making printed circuits in the electronics industry, permitted manufacturing of complex

micromodels with finer details. Their effort provided the basic method that has been used since then. Numerous modifications and additions to the fabrication technique were later contributed by McKellar and Wardlaw (1982), Chatzis (1982), Campbell (1983), Li and Wardlaw (1986), Conrad *et al.* (1992), and others. Wan *et al.* (1996) introduced a stepwise etching technique to introduce deeper etched heterogeneities in some sections of the micromodel. Some authors have suggested reactive ion etching as an alternative to wet etching using HF (Li *et al.*, 2000, Knizikevicius, 2009, Park *et al.*, 2005). RIE provides an advantage of anisotropic etching which produces channels that have sharp corners and edges unlike wet etching that produces smooth curved edges because of its isotropic etching nature. However, one drawback with RIE is that in comparison to wet etching with HF, it etches glass at very slow rates. REI is more suited for silica etching. It etches silica at a faster rate and can produce more detailed and finer etched pattern. The silica plates are then fused with a transparent plate of glass by a process called anodic bonding. The only drawback of using etched silica micromodels is opaque nature of silica which required reflective imaging and the contract in between oil and water is not great. Micromodels are extensively used in this work and more details are provided in the following chapters.

CHAPTER 3: MATERIALS AND METHODOLOGY

The chapter describes the materials, equipments and experimental methodology adopted in this research. A complete list of all the chemicals used is provided along with the composition of brines, types of oils and cores used. Experimental and analytical equipments have been described with emphasis on the important equipments.

3.1 MATERIALS

3.1.1 Brines

Two kinds of brines are typically encountered in a petroleum engineering application: formation brine and the injection brine. Formation brine is the connate brine that resides in an oil saturated reservoir in form of isolated blobs. Injection brine is the brine that is injected in the reservoir to displace oil during a secondary recovery process. Injection brine is usually sea brine, water from any other abundant water source or the produced water for a matured well. For most part of this study, 2% NaCl was used as formation brine and 4% NaCl was used as the injection brine. The experiments with viscous oils in carbonate reservoir were targeted to a specific reservoir and therefore specific formation brine and synthetic sea brine composition was selected. Table 3.1 provides the details of the brines used in carbonate study. All the salts were procured from fisher scientific.

Solution	Composition (ppm)	
Formation brine	NaCl	32000
	$CaCl_2$	12500
	$MgCl_2$	6700
	KCl	1200
Sea brine/Injection brine	NaCl	32000
	$CaCl_2$	1300
	$MgCl_2$	7200

Table 3.1: Brine compositions used in the study of polymer floods in carbonate rocks

3.1.2 Polymer

Polymers are added in water to reduce the mobility of the injected phase and improve the areal sweep efficiency of the displacement process. Hydrolyzed polyacrylamides (HPAM) are one of the most widely used polymers in the oil industry. HPAM was supplied from industrial provider SNF. They manufacture HPAM in two different molecular weight domains. A high molecular weight HPAM Flopaam^{TM} 3630S (MW=18 million Daltons) and a low molecular weight HPAM Flopaam 3330S (MW=8million Daltons). Low molecular weight 3330S HPAM is generally preferred for injection in tighter rocks owing to its small molecular size. Some heterogeneous rocks such as Silurian dolomites may have a higher effective permeability due to fractures and vugs but the matrix is generally tighter with tiny pores. HPAM 3330S was therefore a preferred choice for polymer flooding of viscous oil in carbonate reservoirs.

3.1.4 Oils

Two different crude oils and several different minerals oils were used for the experiments. The reservoir crude oils used had a viscosity of 10,000 (heavy oil A) and

200 cp (heavy oil B). The 200 cp crude oil is from a carbonate reservoir and was used for the study of polymer floods on heterogeneous reservoirs. The 10000 cp crude oil was diluted with toluene to obtain several different viscosity oils for micromodel experiments. For other more fundamental experiments mineral oils were used instead of crude oils. Table 3.2 provides the data of various crude and mineral oils used in the study. Viscosity measurements were made under standard laboratory conditions using TA instruments AR-G2 rheometer.

Oil	Viscosity (cP)	Types	Acid Number (mg KOH/g oil)
Heavy Oil A	~10,000	Crude Oil	3.55
Viscous Oil B	~200	Crude Oil	1.4
Mineral oils and mineral oil blends	~60	Synthetic Mineral oils	NA
	~560		
	~1440		
	~5200		
	~10500		

Table 3.2: List of oils used in the study along with their viscosities and Acid Number

3.1.4 Cores

Coreflood experiments are conducted on reservoir cores to mimic an oil reservoir under laboratory conditions. In the absence of reservoir cores, outcrop cores with similar mineralogy, permeability and porosity should be used. In this study, Berea and Boise, sandstone cores and Silurian Dolomite carbonate cores were used. Berea is fairly homogeneous sandstone with permeabilities in the range of 200-500 mD while Silurian dolomites are highly heterogeneous and are known to contain vugs and fractures.

Permeability of Silurian dolomite cores may vary a lot and can be anywhere within the range of 5mD to 2D. Like Berea, Boise is also fairly homogeneous and permeability is much higher, around 2-6 Darcy, probably due to larger grain sizes. The cores used for the experiments were 1.5 or 2 inches in diameter and 6 to 12 inches in length. Important properties of the cores such as porosity, permeability and wettability are provided in Table 3.3.

	Silurian Dolomite 1	Silurian Dolomite 2	Berea Sandstone	Silurian dolomite 3	Boise 1
Length	6 inch	12 inch	12 inch	12 inch	12 inch
Diameter	1.5 inch	1.5 inch	2 inch	1.5 inch	2 inch
Porosity	18.4 %	21.8%	19.4%	18.9%	29%
Permeability	180 mD	1000 mD	131 mD	730 mD	6000 mD
Aging	No	No	No	Yes	No

Table 3.3: List of the cores along with their major properties

3.1.5 Micromodels

Micro-fluidic devices or micromodels are simplified two-dimensional porous media and are often used as a surrogate to cores and sand packs to study flow in porous media. The micromodels allow visual observation of the displacement and are therefore widely used in the field of petroleum engineering to understand the complexity of flow in porous media. They can be classified based on the material of construction. Typically, glass, silicon or polydimethylsiloxane (PDMS) micromodels are used in laboratories. Glass and silica micromodels were extensively used during the experiments. The glass

micromodels were fabricated in-house. A detailed description of the fabrication procedure is provided in Appendix A.

Silicon Micromodel

The silicon micromodels were obtained from Stanford University. These micromodels had a 5 cm X 5 cm etched area with 25 μm etch depth. A simplified random grain pore pattern was etched on the silicon wafer. Figure 3.1 shows the image of the silica micromodel and a section of pore pattern etched on it. The micromodel has 4 entry ports: one set of diagonal ports is used for injection and production while the other set is sealed. A wide channel runs along two opposite edges to distribute the fluids effectively at the inlet and outlet. Silicon micromodels are etched using reactive ion etching (RIE) technique and the resulting channels are therefore sharp edged and have a uniform depth throughout. Glass micromodels are similar to silicon micromodels but the visualization and imaging is much better in glass micromodels. Glass micromodels are also sturdier and can handle the high pressure gradients required for injecting viscous oils.

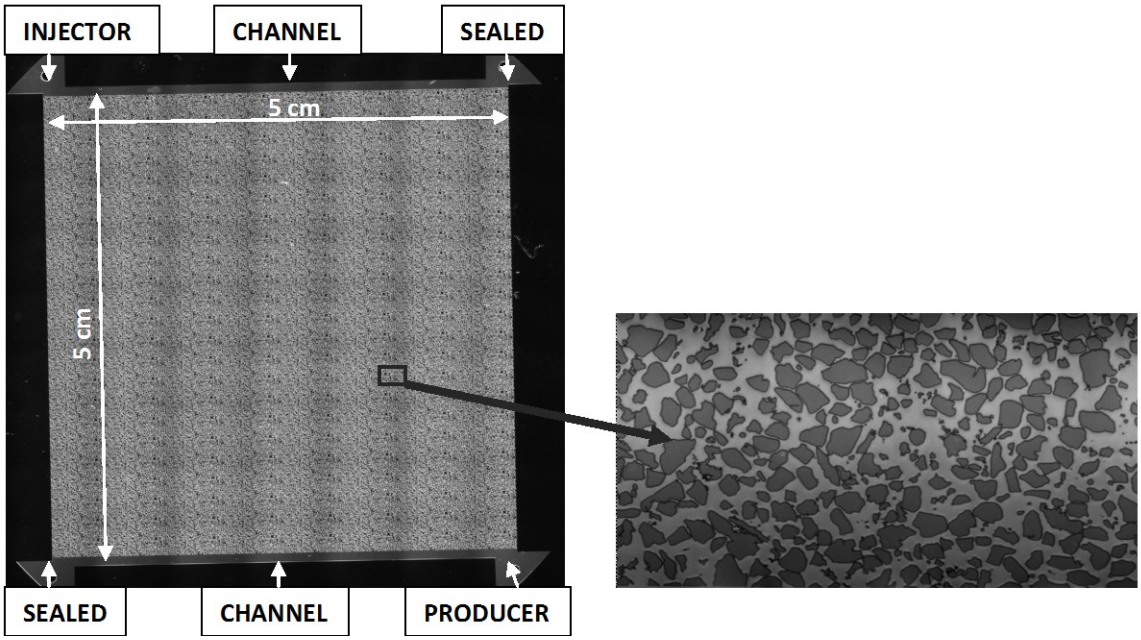

Figure 3.1: Silicon micromodel and an enlarged section with details of the pore structure

Glass micromodels

The glass micromodels used in this study were created in house using photolithography and wet etching. Glass micromodels enable excellent visualization and are sturdier. They can withstand the high pressure required to inject viscous oils. The pore pattern etched on the glass micromodels was similar to that on the silicon micromodels but the etching scheme was different. The glass micromodels were etched using the traditional wet-etching using hydrofluoric acid. Wet etching was preferred over RIE etching as RIE etching is very slow for glass and produced etch rates of about 1nm/min. Wet etching produced etch rates of about 1.3 μm/min with HF formulation used. While wet etching is the preferred method for etching glass, wet etching being isotropic in nature produces smooth round edges and curved channels in the finished product. Isotropic etching also leads to channel width higher than the pattern. For

example, a 10 μm channel on the mask will become 15μm wide and a 50 μm channel will be about 60 μm wide by the time an etch depth of 30-35 μm is achieved.

As these micromodels were fabricated in-house, they were frequently modified to suit different requirement and experimental conditions. Glass micromodels were produced in different shapes, sizes and different variations in same shape or size. A homogeneous standard micromodel was made with similar pore pattern as the silicon micromodel with 5 X 5 cm etched area. Figure 3.2 (a) and (b) shows the standard glass micromodels and its pore structure. These micromodels were etched to a constant over all depth of 30 microns. The micromodels of Figure 3.2 can be considered a good representation of homogeneous sandstone. To correctly represent a carbonate rock, heterogeneities must be included in the micromodel pore patterns to mimic the vugs and fractures typically present in a carbonate rock. This was achieved by a process called step-wise etching. After the first round of etching when the desired etch depth is achieved, a certain portion of the homogeneous micromodel was etched deeper to give it a high permeability in comparison to the rest of the etched area. Two kinds of heterogeneities were introduced, isolated and connected as shown in figure 3.3 (a) and (b). The micromodels of figure 3.3 were first etched to a depth of 35 μm and then only a certain section of the micromodel was subjected to a second round of etching. This etched the selected region to a depth of about 75 μm. The etch depths were verified using the Stylus Profilometer at the Centre of Nano and Molecular Science at University of Texas at Austin. A result of a scan of an area intercepted by a deeper etched region is shown in Figure 3.4.

Smaller micromodel with only 5 cm etched length could be influenced by entrance and end effects. To avoid end effect, longer micromodels were also fabricated with about 10 cm X 5 cm etch region. The pattern etched on these micromodels was

uniform and hexagonal beehive like pattern. Figure 3.5 shows a picture of a longer micromodel.

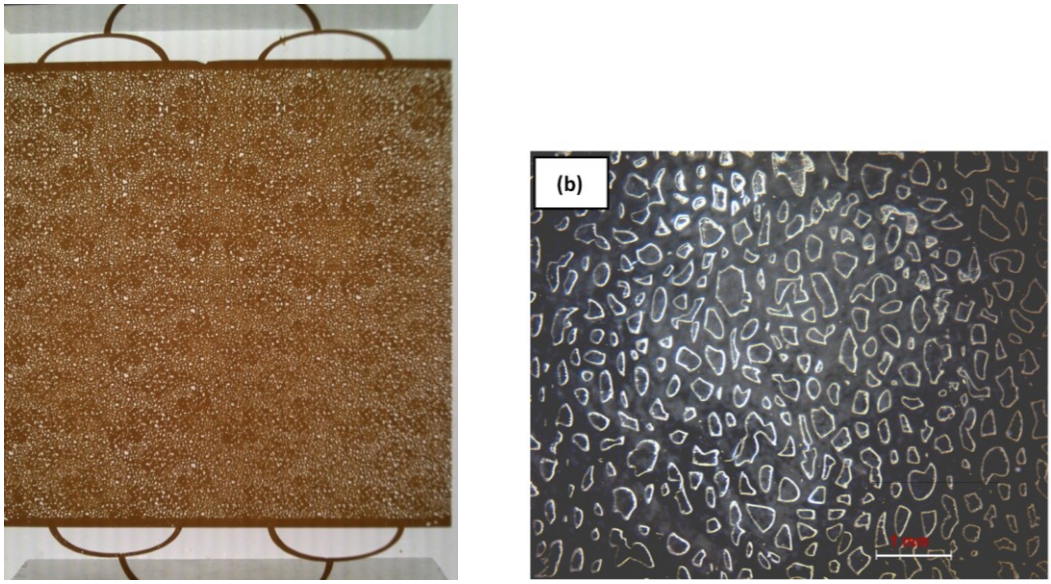

Figure 3.2: (a) Glass micromodel with a homogeneous random pore pattern etched on it, (b) Microscope image of a small section of the micromodel showing the pore pattern.

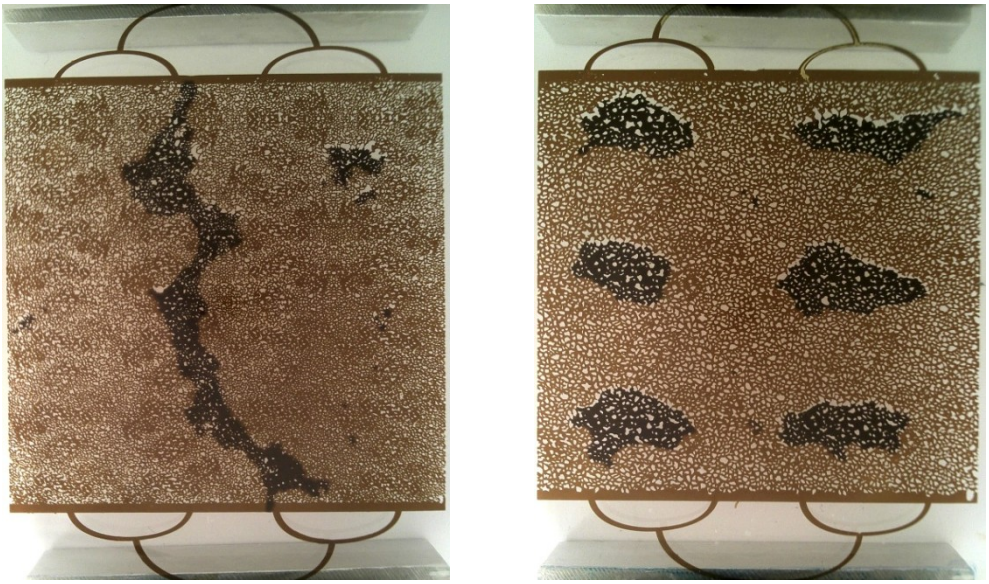

Figure 3.3: (a) A variation of glass micromodel with connected high permeability heterogeneity and (b) another variation of glass micromodel with isolated disconnected heterogeneities.

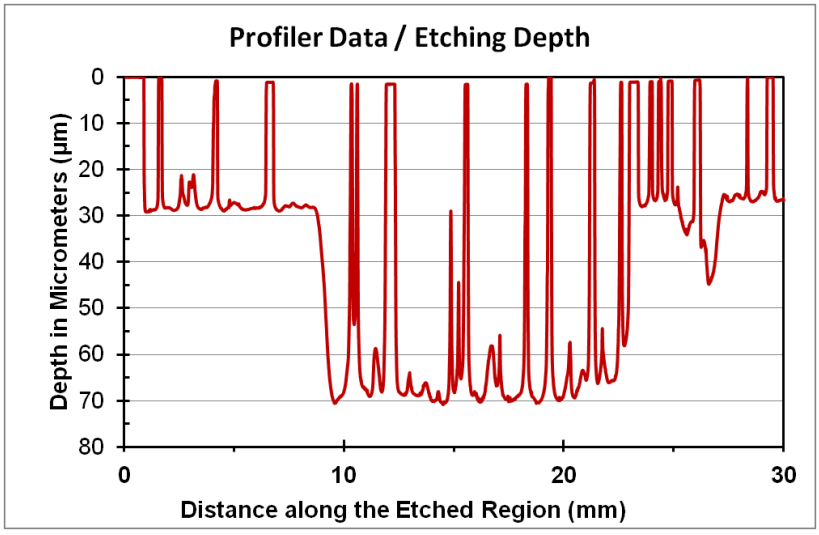

Figure 3.4: Surface profile data of a 3 cm section of the heterogeneous glass micromodel intercepted by a high permeability channel. The data was measured using a Stylus Profilometer.

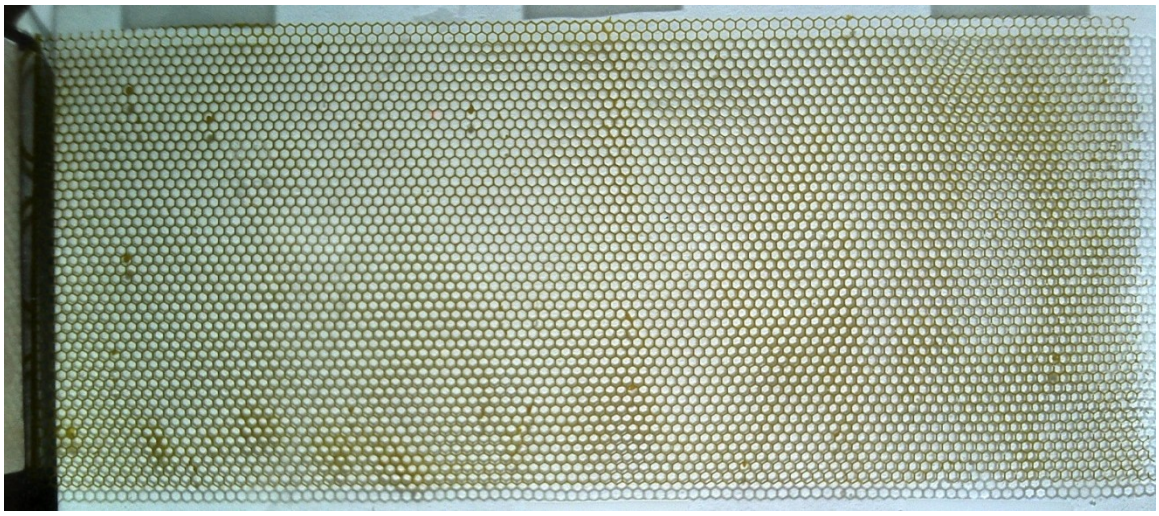

Figure 3.5: An image of an oil saturated long glass micromodel with regular hexagonal channel network.

To study the effect of wettability, some micromodels were rendered oil-wet by treating the pore walls with n-hexane-silane mixture (Salter and Mohanty, 1982). A dry micromodel was vacuumed and then saturated with a 6% by volume mixture of silane and n-hexane. After 20 mins, the silane solution was displaced with air and the micromodel was dried in an oven at 80^{o}C. Silane molecules are known to attach to silica and render it oil-wet. This was observed to be true in our micromodel as well.

Glass Micromodels vs. Silicon Micromodels

Both silicon and glass micromodels are equally effective and useful tool for pore level study. There are few pros and cons of each and depending on the need one may be better than the other. Table 3.4 provides a comparison between these two micromodels used in this study

Glass micromodel	Silicon micromodel
Excellent Imaging and visualization	Needs reflective microscopy for visualization
Sturdy and capable of withstanding high pressure	Fragile and break easily
Only fluoride based wet etching	Can be etched by both wet and dry etching
Contrast between oil and water is excellent. Also water with different dyes can be used	Dark color and opaque nature of silicon makes the oil and water hard to differentiate and dyes do not appear
Smooth rounded edges and curves channel floors	Sharp edges and sharp edge cross-section of the etched channels

Table 3.4: Relative comparison of glass and silicon micromodels

3.2 EXPERIMENTAL EQUIPMENT

3.2.1 Core Flood Setup

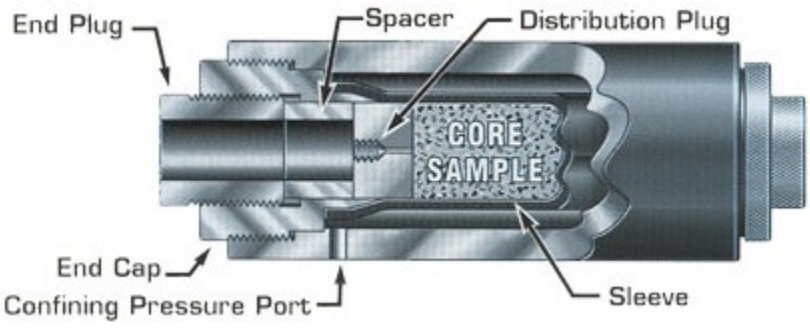

Figure 3.6: A standard Hassler type core holder (http://www.corelab.com/cli/core-holders/hassler-type-core-holders-rch-series)

Standard Hassler type core holders capable of holding 2” and 1.5” diameter cores were used for experiments. Hassler type core holders apply radial pressure on the core samples. These core holders are routinely used for core flooding experiments. The design allows easy removal of cores without the need of completely disassembling the core holder. After the confining pressure has been released, the end plugs and distribution plugs are unscrewed and the core sample is easily removed from the sleeve. The sleeve and end caps remain in place within the core holder. Spacers are used to accommodate undersized cores. The distribution plug is provided at the inlet and outlet to evenly distribute the fluids over the inlet face. The volume of all ports and flow lines (dead volume) should be kept sufficiently low. A complete core flooding setup consists of a pump to inject liquids at constant pressures or flow rates, an accumulator to store fluids, a pressure transducer to measure pressure data and a fraction collector to collect effluent samples.

Pumps

Teledyne ISCO 500D syringe pumps were used to pump the fluids into the desired experimental equipment. These pumps have a volume of about 500 ml and can withstand a pressure of 3750 psi. For brine flood the pumps injected the fluid directly into the sand pack whereas for the oil/polymer injection operations the pumps were used to inject the mineral oil into a glass accumulator. Figure 3.7 shows a picture of ISCO pump used for the experiments.

Figure 3.7: Teledyne ISCO 500D syringe pump
(http://www.isco.com/products/newsrelease.asp?Id=90)

Stainless Steel Accumulators

The stainless steel transfer cylinders commonly called accumulators were used in order to pump fluids such as oil and brine into the sand pack. Typically, the fluids that are viscous, corrosive or problematic to clean are used in accumulators and are not injected directly through the pump. Brines can directly be pumped through the ISCO pump but should not be stored for a long period to avoid corrosion. The accumulators were purchased from the Core Laboratories and have a capacity of 1 liter. They contain a floating piston which prevents the pumped and stored fluids from coming in contact with each other. In order to pump oil into the sand pack, the accumulators were mounted vertically and a mineral oil or

water was pumped into the accumulator on the other side. This pushes the piston and consequently the oil or polymer is pushed into the core.

Using polymer in a steel accumulator should be avoided because the presence of iron and oxygen rapidly degrades the polymer. Glass or poly acrylic accumulators were used for polymer and it was displaced by pumping mineral oil from the top. These plastic accumulators were constructed in the machine shop at Centre of Petroleum and Geosystems Engineering. Glass accumulators were bought from fisher scientific. Figure 3.8 shows the images of all the three accumulators used in the experiments.

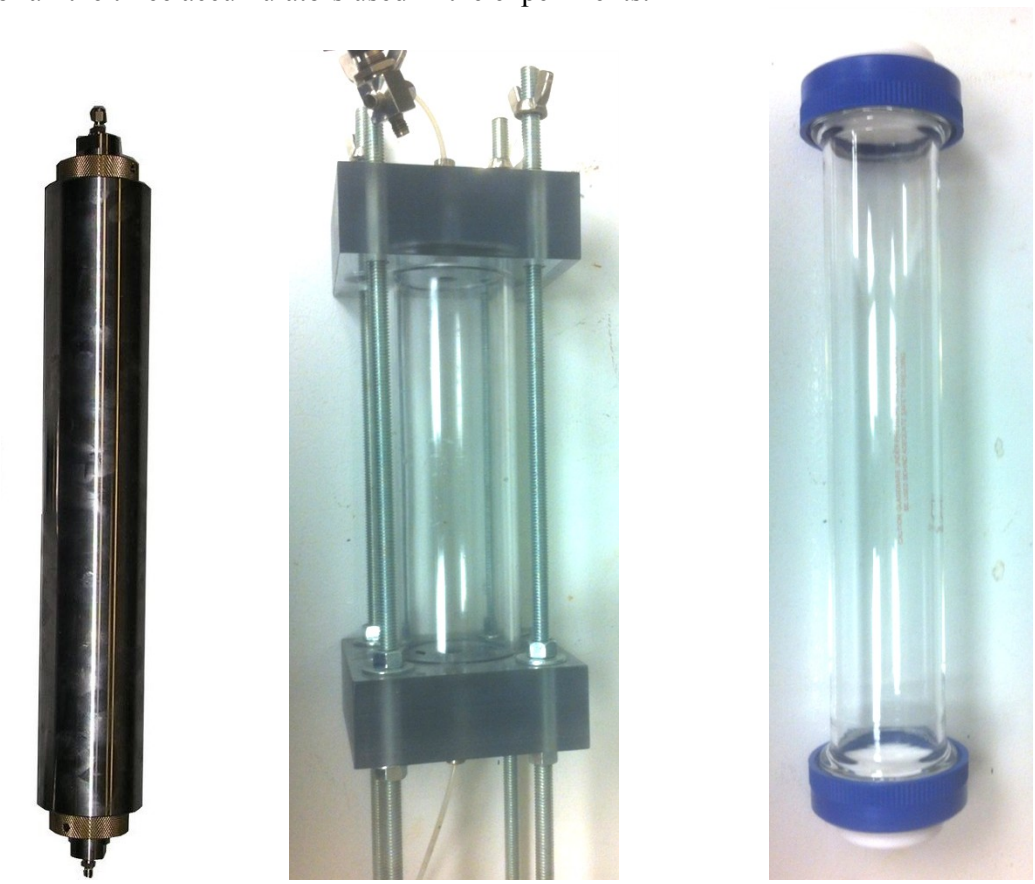

Figure 3.8: A steel accumulator, a plastic accumulator and a glass accumulator used during the study.

Pressure Transducers

Pressure transducers are used to record the differential pressure drop between two points of a flowing system. The transducers were purchased from Rosemount and Cole Parmer and were calibrated for different pressure ranges. The pressure transducers convert the exerted differential pressure into a voltage signal and transmit it to a Data Acquisition Card (DATAQ) where it is stored in a digital format on a computer. In order to convert the raw voltage data back into the pressure drop, a calibration curve is required. The calibration curve is a linear correlation between differential pressure drop and recorded voltage.

Fraction Collector

A Retriever 500 fraction collector (Figure 3.9) was used to collect the effluent samples from the coreflood experiments. A fractional collector can be programmed to collect fixed volume samples for a fixed interval of time. During the oil displacement experiments, a smaller sample size was selected until breakthrough. This gives a better idea of the actual water breakthrough time. After water breakthrough, oil cut decreases significantly so the sample size should be increased to collect measureable amount of oil in each tube. This practice reduces the error in measurement.

Figure 3.9: A sample collector or fractional collector used to collect effluent samples. (http://www.isco.com/products/products3.asp?PL=101603030)

3.2.2 Micro-Fluidic Setup

Micromodel experiments were conducted in the similar manner as the core floods. The micro-fluidic flow setup requires a flow cell that houses a micromodel, a syringe pump to inject fluids at very slow flow rates and an imaging device; a microscope or a camera. The equipments used are described below;

Flow Cell

Flow cell is an assembly that houses the micromodel or the micro fluidic device making a leak proof connection between the tubes and the ports of the micromodel. Silicon and glass micromodels both required a different flow cells specifically suited for their shape and other experimental constraints. Circular cage type flow cell was used for the silicon micromodel and a simple sliding connection flow cell was designed for glass micromodels.

1. Circular cage type flow cell

Figure 3.10 shows the unassembled cage type flow cell used for the silicon micromodel and Figure 3.11 shows a fully assembled flow cell holding a micromodel. The circular hole in the centre is the viewing hole that allowed the clear viewing of the micromodel. The six screws along the perimeter provide the pressure that holds the micromodel against the o-rings making a leak proof seal. 1/16 HLPC plastic tubing were used for connections. Few drawbacks of this assembly are that the setup is very bulky and uneven pressure from the peripheral screws can cause the thin silicon micromodel to crack. This assembly had a large dead volume (1 ml) in comparison to the micromodel pore volume (~60µl) because of the big O-rings used at the inlets.

Figure 3.10: The unassembled cage type flow cell used for silicon micromodel

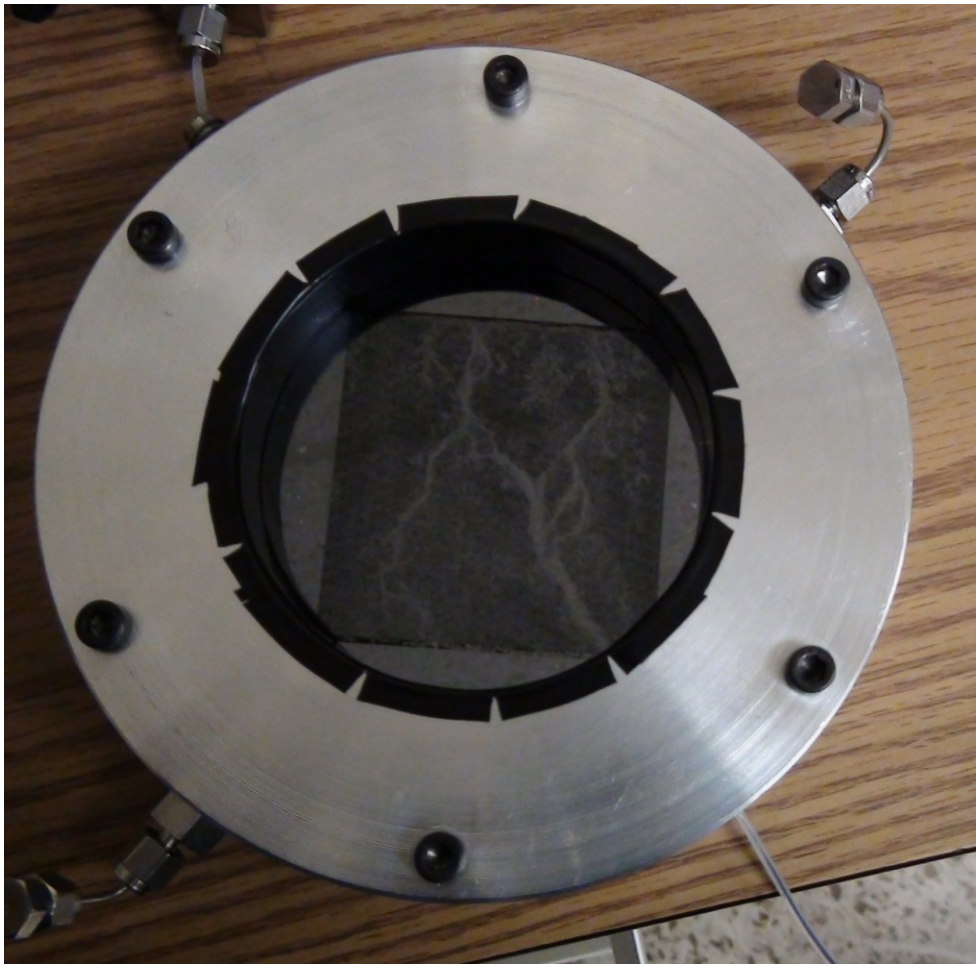

Figure 3.11: The assembled flow cell with a micromodel housed inside.

2. Sliding connection flow cell

Sliding connection flow cells were designed specifically for the glass micromodels and they were a significant improvement over the bulky aluminum flow cell both in terms of portability and dead volume. This flow cells is fairly simple to use and has a dead volume of only 30 micro liters. Figure 3.12 shows the picture of a sliding flow cell coupling and the figure 3.13 shows the complete flowing setup with both the end pieces. Tiny O-rings sit in between the glass and the HPLC connectors making a leak proof connection.

Figure 3.12: One of the sliding flow cell coupling with an HPLC adaptor and 1/16 tubing.

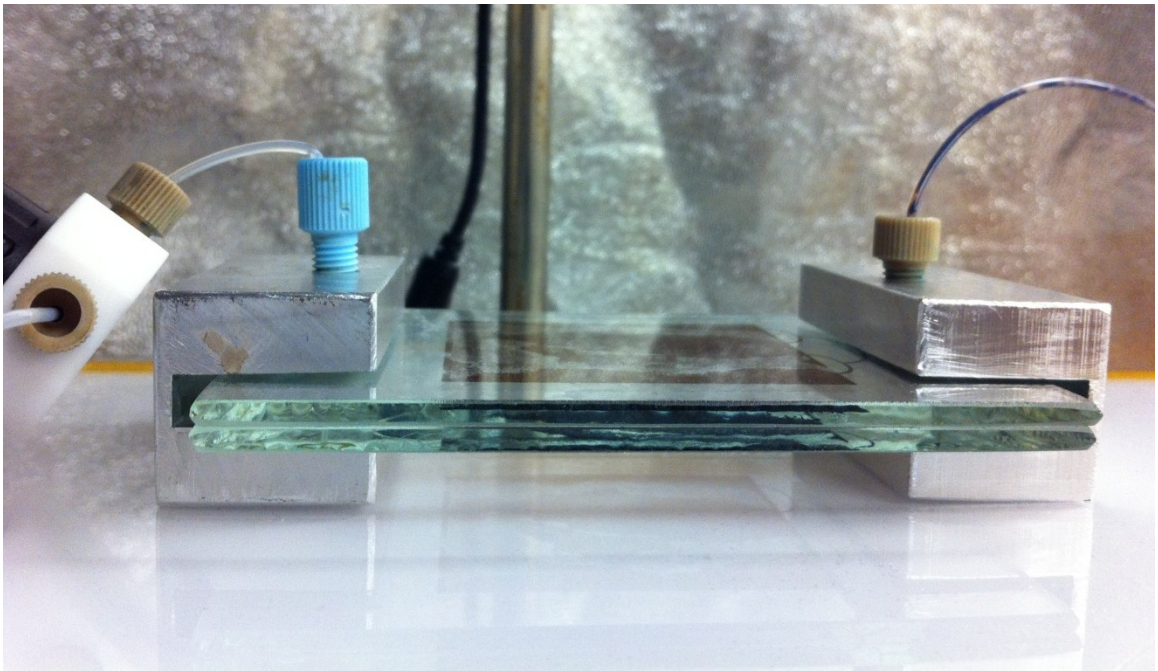

Figure 3.13: The complete flow assembly of the glass micromodel and sliding type flow cell

Syringe Pump

The 11 Elite Programmable Syringe Pump (Figure 3.14) from Harvard Apparatus was used for injecting fluids in the micromodels. These syringe pumps can handle syringes ranging from 0.5 ul to 60 ml (single syringe) and is capable of injecting fluids at rate as low as 1.28 pl/min. The pump can also be programmed for multiple infusion and withdrawal cycles. For the purpose of experiments, only the constant rate infusion feature was.

Figure 3.14: The 11 Elite Programmable Syringe Pump from Harvard Apparatus with infusion and withdrawal option (http://www.coulbourn.com/product_p/70-4504.htm)

Microscopes

Microscopes were used for inspection during micromodel fabrication phase and most importantly for visualization and imaging during the flow experiments. Two different microscopes were used:

1. ***Nikon Optiphot-2 microscope***

A Nikon Optiphot-2 microscope (Figure 3.15) with QImaging Micropublishing camera was used extensively during the micromodel fabrication process, especially

during the development of the mask. A high resolution scan of a Berea thin section core was used to generate a 2D connected pore pattern. This was later used to develop the mask for micromodel fabrication. This microscope has a higher magnification and captures higher resolution images. This microscope has two light sources and can be used for both transmitted light (glass micromodels) and reflected light microscopy (silicon micromodels). Owing to its high magnification, this microscope views only a tiny section of the micromodel. To view the whole area, several overlapping images can be clicked and stitched together using an image-stitching software (Fiji). Stitching yields a detailed and high resolution image of the object. This scheme is good for detailed imaging of a static system like a thin section of a rock but is not recommended for dynamic systems like a displacement experiment. For a dynamic system, a lower resolution camera with the ability to image a larger view area is recommended.

Figure 3.15: Nikon Optiphot-2 microscope, with two light sources and a remote controlled stage.

2. Supereye USB digital microscope

Supereye USB digital microscope is a simple hand-held portable microscope. It does not have a high resolution but allows a wider field of visualization. This microscope was used mostly with glass micromodel experiments. The micromodel had to be illuminated from behind to avoid the interference and noise due to shadows and light fluctuation in the laboratory. The image resolution of the microscope is 1600x1200 pixels. The microscope can be connected to a computer through a USB and its image acquisition software can be coupled with a freeware 'Mouse Auto-clicker' to capture images at regular intervals.

Figure 3.16: Handheld Supereye USB microscope
(http://www.supereyes.cc/product/show/query/11.html)

3.2.3 Analytical Instruments

Refractometer

Fisher Scientific™ Handheld Refractometers were used to measure salinity after a single phase tracer test. Refractometer gives a quick and accurate measure of brine salinity. Handheld refractometers are analog instruments for measuring a liquid's refractive index which can be related to the salinity (total dissolved solids, TDS). They work on the critical angle principle where lenses and prisms project a shadow line onto a small glass piece inside the instrument, which can then be viewed by the user through a magnifying eyepiece. A few drops of the sample are placed between a measuring prism and a small cover plate. When viewed through the eye-piece the shadow shifts depending on the salinity of the sample. Fisher Scientific™ Handheld Refractometers come with a view screen already calibrated with salinity values.

Figure 3.17: Handheld refractometer from Fisher Scientific used for salinity analysis (http://www.fishersci.com/ecomm/servlet/fsproductdetail_10652_639426__-1_0#)

Stylus Profilometer

Profilometers was used for measuring the depth of the etched channels before the fusing step during the micromodel fabrication. Dektak 6M stylus profilometers are used

to measure the unevenness or roughness of a surface. It can be used to quantify the microscopic features like depth of a channels and height of ridges on a particular surface. The stylus of the profiler is first zeroed on a smooth part of the surface and then moved laterally across the sample for a specified distance at a specified contact force. The profilometer measures small surface variations in height and depth as it is dragged along a surface. A Dektak 6M surface profilometer can measure features ranging from 50 nanometres to 1 millimetre. The radius of stylus tip ranges from 20 nanometres to 50 μm, and the data resolution is controlled by the scan speed and sampling rate.

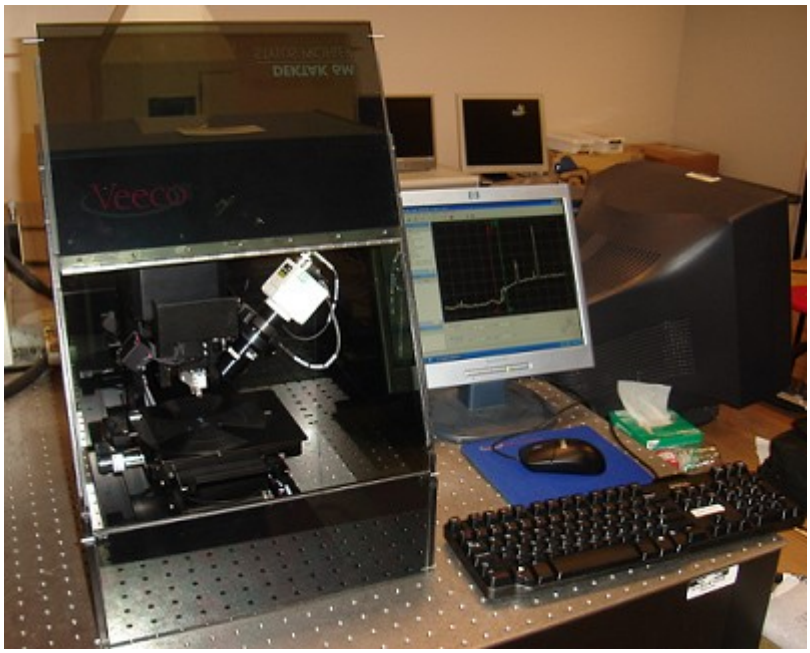

Figure 3.18: Dektak 6M stylus profilometer at The Centre of Nano and Molecular Science (http://www.cnm.utexas.edu/equipment/dektak-6m-stylus-profilometer/) Image from (http://www.cnm.utexas.edu/equipment/dektak-6m-stylus-profilometer/)

Rheometer

Bulk viscosity/rheology measurements were conducted using the AR-G2 rheometer (Figure 3.19) provided by TA instruments. A 2^{o} cone and plate geometry was used with the rheometer for viscosity measurements. Only 0.65 ml of sample volume is required for this geometry. In addition to viscosity, the instrument can also measure detailed rheology of the fluids. The instrument allows accurate measure of viscosity for torque as low as 0.2 μNm. It is important to understand the limitation in terms of torque and not confuse it with shear rate. Different liquids should have different shear rate pertaining to the torque of 0.2 μNm depending on their viscosity. As a result this machine is not very accurate for low shear rates and especially for low viscosity fluids. Figure 3.20 plots the values of viscosity vs shear rate for sample newtonian fluids of fixed viscosity. Figure 3.21 shows the same plot of viscosity against torque. It is clear that below the torque of 0.2 μNm the viscosity values are inaccurate and influenced by noise.

Figure 3.19: TA instruments AR-G2 rheometer
(http://www.tainstruments.com/product.aspx?id=43&n=1&siteid=11)

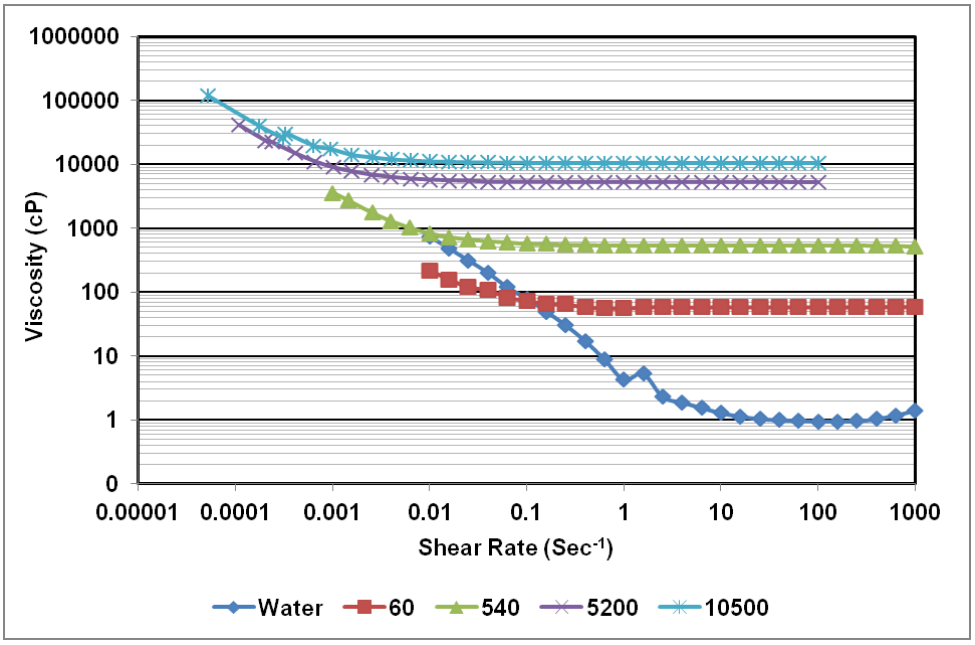

Figure 3.20: A plot of viscosity vs. shear rate for several Newtonian fluids as measured by the AR-G2 rheometer.

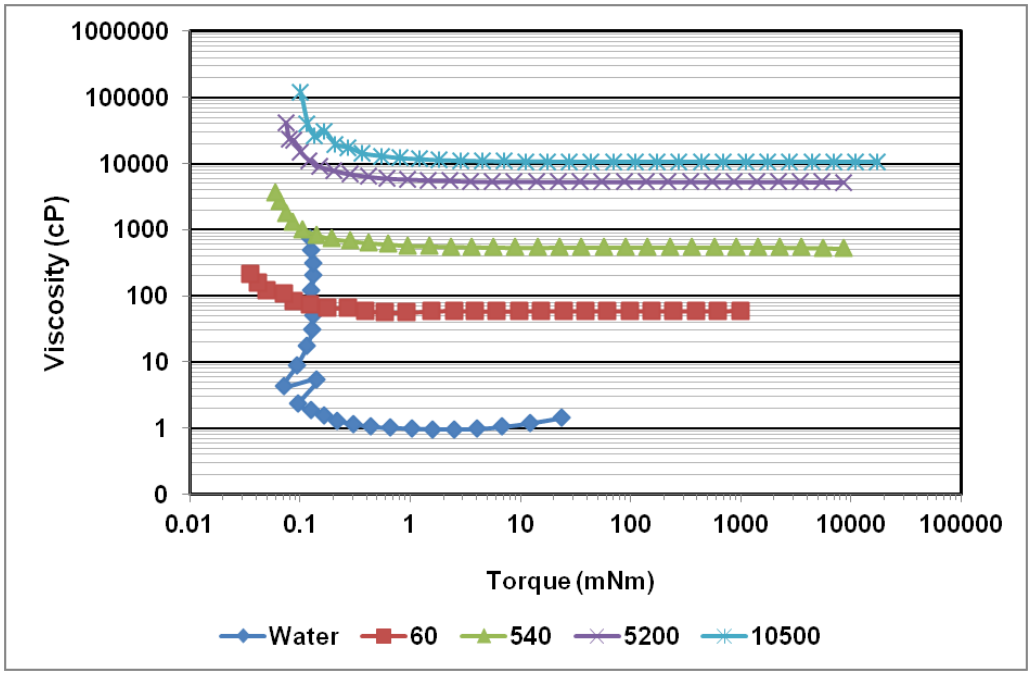

Figure 3.21: Measured viscosity plotted against torque

3.3 METHODOLOGY

3.3.1 Core Flood Experiments

A schematic of the core flood setup is described in Figure 3.22. Homogeneous Berea sandstone cores and heterogeneous Silurian dolomite carbonate cores were used in the experiments. The experimental procedure remains the same irrespective of the core type. Typical core flooding procedure requires the following steps.

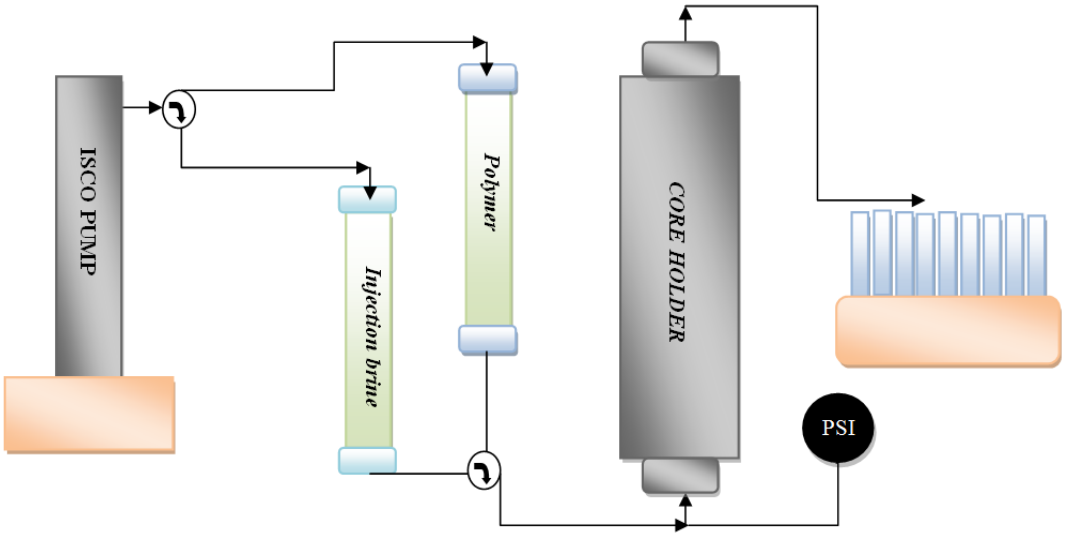

Figure 3.22: A schematic of a core flood experiment

Air permeability and porosity

Air permeability is a measured by injecting air from one side of the core while the other end is connected to an air flow meter. The air flow meter measures the volumetric flow rate while a differential pressure transducer should be used simultaneously to measure the differential pressure across the core. The pressure and flow rate data can then be used along with the Darcy's law for compressible fluids to estimate the air permeability of the system. Air permeability should be measure at low air flow rates, at higher flow rates the flow is turbulent and data does not follow equation 3.1. Air

permeability is usually higher than the experimentally observed water or brine permeability typically because of the clay swelling caused by brines.

$$Q = \frac{K_{air} A\left(P_{in}^2 - P_{std}^2\right)}{2\mu_{air} L P_{std}} \qquad 3.1$$

where, K_{air} is air permeability, P_{in} and P_{std} are the inlet and standard pressure (outlet/ambient) respectively. L is the length of the core and μ_{air} is the viscosity of the air.

Air porosity is usually measured using the Boyle's law. A vessel of known volume is first pressurized to a known pressure and then a valve is opened to allow the air to go into the core holder. The new pressure value is now noted and the experiment is repeated for several other values of initial pressure. The value of pore volume calculated from Boyle's Law includes the dead volume of the core holder and its connections, and should be subtracted accordingly.

Vacuuming

Core should be vacuumed thoroughly before injection of any liquid phase to avoid trapping air. The core is vacuumed using a vacuum pump until a steady pressure of about -14 psi is established on the far end of the core. The vacuuming is then stopped and the pressure is monitored for about an hour to ensure that the core can sustain a vacuum and there are no leaks. CO_2 is then injected from one end at a constant pressure to displace any remaining gas. The core is vacuumed again to remove CO_2. CO_2 is added owing to its high solubility in water. Any remaining CO_2 after vacuuming gets readily dissolved in water to give a 100% brine saturated core. After vacuuming, brine (2% NaCl) should be injected at a constant pressure and initial volume of the pump should be noted. Final volume of the pump should be noted when the whole system is pressurized to the

injection pressure and the pump injection rate is zero. Pump can then be stopped and the exit end of the core holder should be opened to the air. Some fluid will be ejected out and should be collected. The difference in between the pump's initial and final volume, minus the ejected liquid volume and the dead volume of the core holder should give another estimate about the pore volume of the core.

Brine permeability and tracer test

Brine permeability is measured by injecting brine in the core at different injection rates while measuring the pressure drop across the core. This data can then be used with Darcy's law to get the value of brine permeability. A tracer test is usually conducted to ascertain the uniform and homogeneous nature of the core. During a brine tracer test an injection brine of different concentration is injected in the core to displace the brine originally present and the effluents are collected at the outlet. Salinity of the effluent can then be analyzed and the trend gives another idea of the pore volume and homogeneity of the core. The tracer response that resembles a smooth 'S' shaped curve signifies a homogeneous core and while an early breakthrough and a long tapered tail is typical for a heterogeneous core.

Oil saturation

Once the permeability and porosity have been determined, oil is injected into the core from the top in a gravity stable manner. To achieve high oil saturation, oil is injected at a constant high pressure of about 200 – 500 psi depending on the viscosity of the oil. It should be noted that the overburden pressure on the sleeve of the core holder should always be at least 300 psi higher than the injection pressure. The connate water being drained out is collected to get an estimate of the initial oil saturation. Once the initial oil saturation has been established and the produced effluent is only oil the oil injection can be stopped.

It is desirable to have oil flowing through the core at 1ft/day equivalent flowrate before the water injection. The advantage of this step is that the pressure data during water flood is more accurate as the pressure starts from a realistic value and not zero. Also it gives a good idea of the oil relative permeability at connate water saturation.

Water flood/Polymer flood

Water flood or polymer flood are conducted at a flowrate equivalent to 1foot/day intrinsic frontal velocity. Typically about 2 pore volumes of the liquid is injected in the core, until the residual oil saturation is established. For unstable displacements, residual oil saturation cannot be achieved by injection of finite pore volumes of brine injection. In such cases, the displacement was stopped after the water cut exceeds 99%. Effluents were collected periodically using a fraction collector and the pressure drop across the core was recorded every second. After the waterflood, the cumulative oil recovery as a function of PVs injected was calculated. S_{orw} was calculated from the mass balance. From the pressure drop data an approximate value of end point water permeability at remaining oil saturation (krw_o) was determined.

3.3.2 Micromodel Experiments

Micromodel experiments are to be conducted in the similar manner as the core flood. Like core floods, it is important to confirm connectivity and to check for leaks. Connectivity can be checked just by pushing air through a syringe from the injection side of the flow cell and allowing it to bubble on the other side. Appearance of bubbles confirms that the injector and the producer port are aligned. To test for leaks, start with an empty syringe connected on the injected end and close the outlet value on the producer side. Withdraw the piston of the syringe to create a vacuum. If the piston goes back to its original place after withdrawing and holding it in place for few minutes, it indicates that the system is perfectly sealed. Now withdraw the piston again to draw a vacuum in the

system and switch the three-way valve in the other direction to begin injecting the brine. This will ensure 100% brine saturation and no trapped air. The outlet value can now be opened to allow brine flow. It is critical to have connate brine saturation to ensure a realistic wettability state of the micromodel. These steps do not change with different flow cells.

Micromodel experiments with cage type flow cell

Figure 3.23 shows the experimental setup used for this study. Injection of viscous oils (10,000 cp) into a silicon micromodel requires high pressure drop that may crack the micromodel. To avoid damage, oil injection was done in an oven heated to 80^{o}C. This reduces the oil viscosity and the pressure drops are lower. Once the micromodel is saturated with oil the flow cell was brought out of the oven and allowed to cool down. Water or polymer injection can then be initiated while the micromodel was being scanned under a microscope. These micromodels were used for study of viscous fingering at different viscosity ratios.

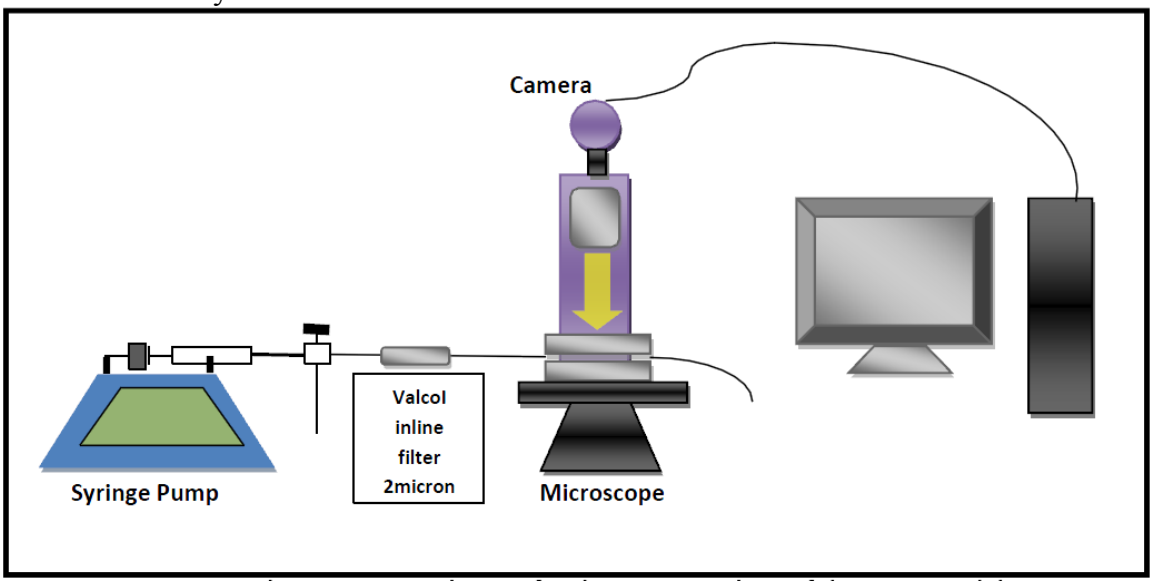

Figure 3.23: Schematic of the micromodel setup with the cage type flow cell

Micromodel experiments with Flow cell 2

Glass micromodels were used with the sliding connector flow cell. This system was used entirely for the study of viscous oils in carbonates. Some experiments were also conducted to study the effect of flow rates on viscous fingering and sweep. The experimental procedure was similar; the micromodels were first vacuumed and then saturated with brine. The brine was the displaced by the oil to achieve irreducible water saturation. The oil saturated micromodel was then directly observed using the Supereye USB microscope. Figure 3.24 shows the experimental setup for glass micromodel experiments.

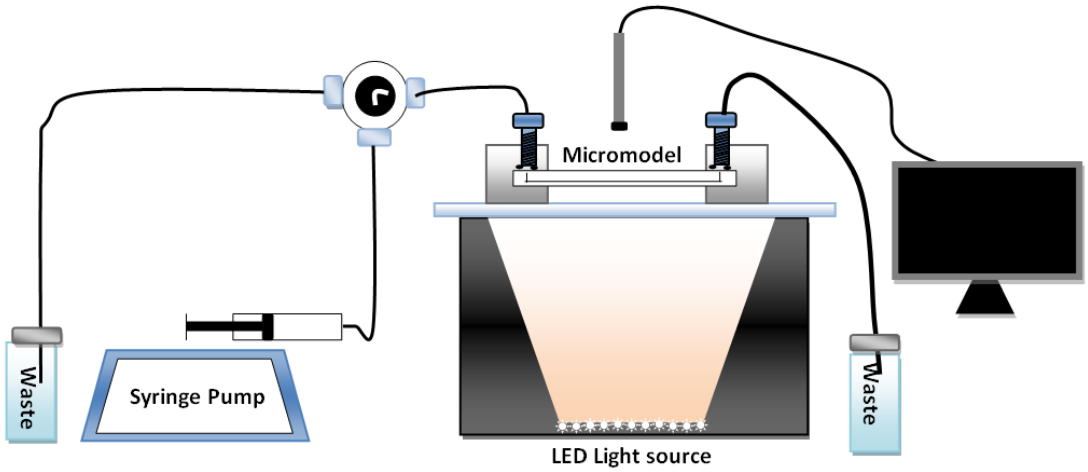

Figure 3.24: A schematic of the glass micromodel flow setup using sliding type flow cell.

CHAPTER 4: EXPERIMENTAL RESULTS AND DISCUSSION

The chapter discusses the results of all the experiments conducted in this research. The main objective of all the experiments conducted in the research is to better understand unstable displacements of viscous oils during non-thermal processes. The experiments can be categorized into two sections: (1) a study of polymer flooding for viscous oil in heterogeneous carbonates and, (2) understanding of unstable immiscible displacements. Several core floods and micromodel experiments were conducted for each section and have been discussed in details in this chapter.

4.1 TIMING OF POLYMER FLOOD FOR VISCOUS OILS IN CARBONATES

In viscous oil reservoirs, oil recovery from water flood is low due to viscous fingering. Polymers are typically used to decrease the mobility of the injected fluid, to stabilize an unstable displacement and increase the sweep. However, as the viscosity of oils increases it becomes increasingly difficult to attain close to unity mobility ratio even after adding polymer because of the injectivity and production constraints. For moderately viscous oils, it is easy to justify polymer floods as it is possible to predict recovery and thus optimize polymer concentration by combination of core floods, fractional flow predictions and reservoir simulations. In more viscous oils and in heterogeneous carbonates, though we may improve sweep and reduce viscous fingering with polymer, it is difficult to imagine completely eliminating viscous instabilities. Due to inherent viscous instabilities and uncertainty of the heterogeneities, prediction and optimization is a complex task for viscous oils in structurally complex reservoirs. Typically, for light oils, a tertiary polymer flood after a long waterflood does not result in an incremental oil recovery. Several papers in the literature also suggest that in

homogeneous sandstones (oil-wet or water-wet), a secondary polymer flood performs better than the tertiary polymer flood (Wreath, 1989 and Element et al., 2001) i.e., a secondary polymer flood can reduce residual oil saturation more than the tertiary. The visco-elastic rheology of the partially hydrolyzed polyacrylamide polymers has been attributed as the reason for this incremental recovery for both oil-wet (Wang et al., 2000) and water-wet (Huh and Pope, 2008) media. However, there are some publications that contradict this claim. Vermolen et al. (2014) published their finding on the effect of polymer visco-elasticity on the residual oil saturation. They conducted experiments at constant pressure with polymers that had the same viscosity but variable visco-elasticity. They concluded that the visco-elastic nature of the polymer has nothing to do with the improved S_{or} observed by the previous researchers. They also mentioned that the trends noticed by previous authors must have been due to the use of glycerol as a purely viscous fluid. They showed at the viscosity of glycerol is very sensitive to dilution and temperature and probably got diluted in the process.

Still the general consensus is that polymer flood provides better sweep and a polymer flood after extensive water flood is not beneficial. So the timing of the polymer flood is critical and a secondary polymer flood may even reduce the S_{or} of the rock. These opinions however do not seem to be consistent with the experiments on viscous oils. For viscous oils, a tertiary polymer flood can recover additional oil (Bondino et al. 2011) even after a high WOR has been established. Fabbri et al. (2014) also observed that tertiary polymer flood recovered oil even after extensive water flood; in fact, in their case the tertiary polymer recovery was much higher than the secondary recovery. Fabbri et al. (2014) did not provide a reason for a trend. From the recent published results about heavy oils, one may conclude that in viscous oil reservoirs, timing of a polymer floods may not

be an important parameter. Most researches have not provided a clear explanation or mechanism that causes such unexpected and unconventional recovery trends.

In such experiments, an insight into the pore scale displacement through visualization or scanning is critical in understanding the mechanism of incremental recovery. Recently, Skauge et al. (2012) used low energy X-ray scanning to study the displacement of the doped viscous oil by water in a 2D porous medium. However, because of the resolution of the X-ray systems and averaging over the depth, pore level details are lost in the process. If pore level details of the mechanism are to be studied, micromodels should be used along with a high resolution imaging system. Micromodels, owing to their simplified 2D nature and ability to visualize the displacement, have been used by several researchers to study pore-scale mechanisms in the field of petroleum engineering. The disadvantages of micromodels are the lower pore connectivity due to the 2D nature, smoothness of pore walls, small pore volumes and the absence of realistic minerals and clays. In some cases, micromodels can be enhanced to match important conditions, for example by depositing clays in the pore walls for low salinity studies (Bondino et al., 2013). To understand the core floods, a series of micromodel experiments were designed with two different micromodels. Micromodels help visualize the differences in the water and polymer displacement, the differences in the distribution of residual oils and the effect of heterogeneity and wettability on the flow dynamics.

4.1.1 List of Carbonate Coreflood and Micromodel Experiments

Carbonate Coreflood Experiments

In this study, lab scale experiments were conducted in core floods and investigation of the pore scale phenomenon were conducted using glass micromodels. Table 4.1 contains the list of the all the core flood experiments conducted in this study

and Table 4.2 consists of the micromodel experiments conducted in the study. The experiments in Table 4.1 were conducted in 4 different cores. For each core, a tertiary polymer flood and a secondary polymer flood is conducted for comparison.

Core Flood Experiments		
1	Secondary Water Flood and Tertiary Polymer flood	Silurian Dolomite 1
2	Secondary Polymer Flood	Silurian Dolomite 1
3	Secondary Water Flood and Tertiary Polymer flood (repeat of 1)	Silurian Dolomite 1
4	Secondary Water Flood and Tertiary Polymer flood	Silurian Dolomite 2
5	Secondary Polymer Flood	Silurian Dolomite 2
6	Secondary Water Flood and Tertiary Polymer flood	Berea Sandstone 1
7	Secondary Polymer Flood	Berea Sandstone 1
8	Secondary Water Flood and Tertiary Polymer flood (oilwet)	Silurian Dolomite 3
9	Secondary Polymer Flood (oilwet)	Silurian Dolomite 3
10	Secondary Polymer Flood at 5 times slower injection rate (oilwet)	Silurian Dolomite 3
11	Secondary Polymer Flood at half polymer concentration (oilwet)	Silurian Dolomite 3

Table 4.1: List of all the core flood experiments conducted for viscous oils in carbonates.

Micromodel Experiments

The micromodel experiments conducted in this study were complimentary to the core flood experiments. They can also be paired into secondary and tertiary polymer floods in similar micromodels. Three different forms of micromodels were used in this study. Table 4.2 shows the list of all the experiments conducted with micromodels

2D Micromodel Experiments		
a.	Secondary water flood and tertiary polymer flood in 200 cP oil	Water-wet, Micromodel A
b.	Secondary polymer flood in 200 cP oil	Water-wet, Micromodel A
c.	Secondary Water Flood and Tertiary Polymer flood in 200 cP oil	Water-wet, Micromodel B
d.	Secondary Polymer Flood in 200 cP oil	Water-wet, Micromodel B
e.	Secondary Water Flood and Tertiary Polymer flood in 200 cP oil	Oil-wet , Micromodel B
f.	Secondary Polymer Flood in 200 cP oil	Oil-wet, Micromodel B
g.	Secondary Water Flood and Tertiary Polymer flood in 200 cP oil	Oil-wet , Micromodel B
h.	Secondary Polymer Flood in 200 cP oil	Oil-wet, Micromodel B

Table 4.2: List of all the micromodel experiments conducted to mimic and justify the results of experiments of Table 4.1

A 200 cp oil (heavy oil B) was used in this study. The brine compositions are listed in Table 4.3. Synthetic sea brine was used as the injected brine for water flood and 4000 and 6000 ppm for HPAM 3330s polymer solution prepared in injection brine was used for polymer floods. 2000 ppm polymer was used for experiment 11. Figure 4.1 shows the viscosity of the polymer solutions at different concentrations as a function of the shear rate.

Solution	Composition (ppm)	
POLYMER (HPAM3330S)	6000ppm / 4000ppm	
Formation brine	NaCl	32000
	$CaCl_2$	12500
	$MgCl_2$	6700
	KCl	1200
Sea brine/Injection brine	NaCl	32000
	$CaCl_2$	1300
	$MgCl_2$	7200

Table 4.3: Compositions of brines used in the carbonate polymer floods study

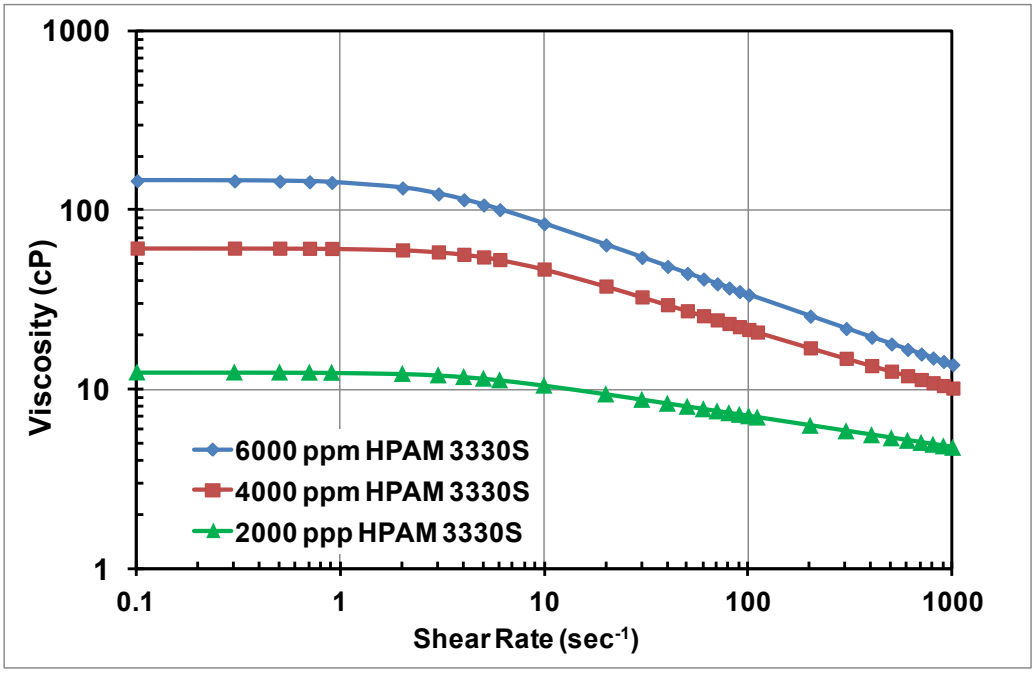

Figure 4.1: Plot showing the shear thinning rheology of the polymers used in the study

4.1.2 Carbonate Coreflood Results

Experiments 1, 2 and 3 were conducted on the same Silurian dolomite core, (Silurian Dolomite 1 from Table 3.3). Figure 4.2 shows the cumulative production profile of experiments 1, 2 and 3. In experiment 1, an about 1.8 pore volume of water was injected until no more oil was being produced. Water break-through occurred at 0.09 PV; oil recovery was 24% OOIP. Conventionally, for light to moderate viscous oils this would be called the irreducible water saturation and polymer flood at this stage would not be beneficial. A tertiary polymer flood with 4000 ppm polymer was conducted on the same core and it recovered about 10% (of OOIP) extra oil. Over all recovery was still low (~34% OOIP) suggesting a lot of bypassing and fingering in the system.

To compare the performance of a tertiary polymer flood with a secondary polymer flood. Experiment 2 was conducted on the same core after cleaning. After experiment 1, the core was flushed with about 10 pore volumes of water to remove the polymer. This was followed by 2 – 3 PV of 1000 ppm hypochlorite solution to remove the excess polymer. This was followed by injection of 3 PV of formation brine. The core was then re-saturated with oil and the initial oil saturation was same as that in experiment 1. In this case, oil recovery was better than that of the secondary water flood (experiment 1), but the polymer breakthrough was only slightly later, hinting that the early breakthrough is possibly dominated by heterogeneities in the core rather than just viscous fingering. Polymer breakthrough occurred at 0.13 PVs polymer injection. However, even after breakthrough the oil cuts remained much higher than those in the water flood. In terms of the cumulative oil recovery, experiment 1 (WF+PF) appeared to have performed slightly better than experiment 2 (secondary PF). This was unexpected and to verify, experiment 3 was conducted, which was essentially a repeat of experiment 1. Pressure drop of the experiment 1 and 2 are plotted against pore volume in Figure 4.3. We can see

that the pressure drop with polymer at residual oil saturation is higher than that of oil at connate water saturation. This means that these experiments are over-optimized therefore for experiments 4 onwards a 4000 ppm polymer concentration was used.

Waterflood of experiment 3 followed almost the same tread as that of experiment 1. In this case, polymer flood was started a bit earlier at about 1.5 PV. However, the overall recovery was again better than that in experiment 2 and about the same as that in experiment 1. Figure 4.2 shows that the tertiary polymer floods outperform secondary polymer floods in heterogeneous carbonate cores. To generalize the results, experiments 4 and 5 were conducted on a second core which had more than twice (about 76ml) the pore volume of the core 1.

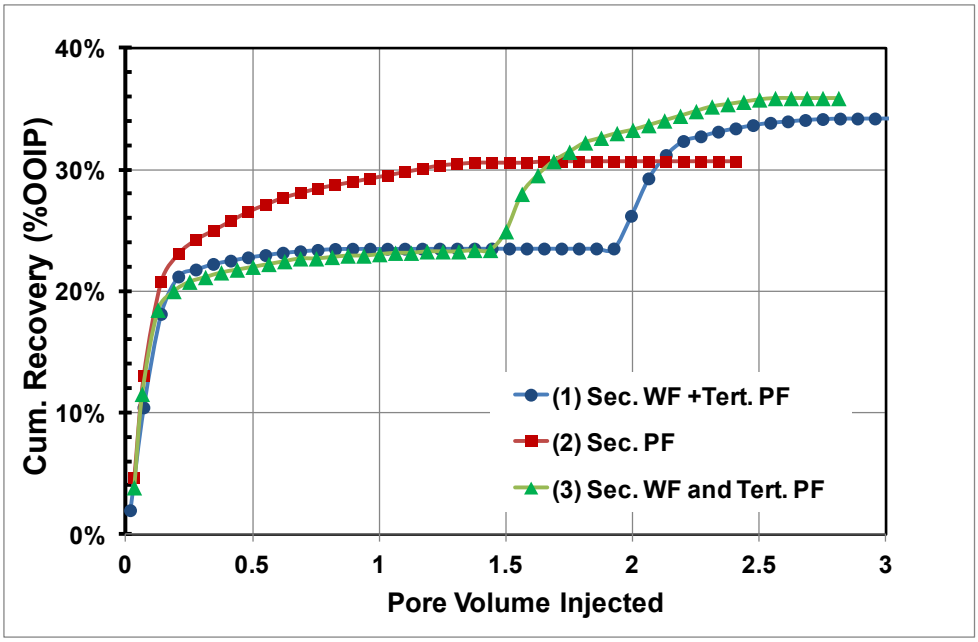

Figure 4.2: Cumulative oil recovery for experiments 1, 2 and 3

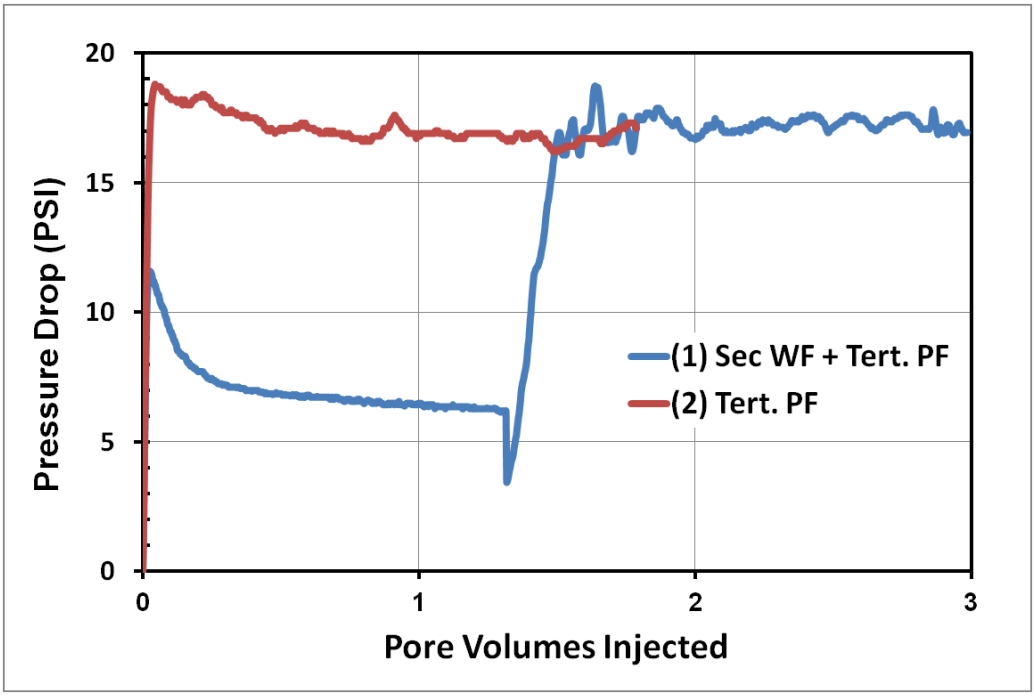

Figure 4.3: Pressure drop for experiments 1 and 2

Experiments 4 and 5 were conducted in a foot long core and the polymer solution used was only 4000 ppm of 3330s HPAM. This dolomite core was slightly fractured and vuggy and as a result the permeability was of the order of 1 Darcy (Figure 4.4). Similar secondary and tertiary polymer floods were conducted on this core. Figure 4.5 shows the cumulative oil recovery for experiments 4 and 5. The water broke through at about 0.09 PV and the oil recovery was about 32% OOIP at the end of the waterflood. The tertiary polymer flood recovered an additional 21% OOIP leading to a cumulative oil recovery of 53% in experiment 4. Cumulative oil recovery in the secondary polymer flood (experiment 5) was only 36% OOIP. In Figure 4.6, notice that the pressure drop during the polymer flood and the pressure drop for oil at connate water saturation is the same. This suggests that the polymer flood is conducted at an end point mobility ratio of 1. A

recovery of only 36% during a unit mobility flood is another indication of the high connected heterogeneity in the core.

Figure 4.4: A picture of the fracture along the core Silurian Dolomite 2.

From experiments 4 and 5, we can confirm that the tertiary polymer flood does perform better than the secondary polymer flood, even in a larger core. In this case about 17% extra oil was recovered and the difference in between the tertiary and secondary recoveries were significantly higher than that observed in previous experiments. Apart from the length of the core, the only obvious difference in the two cores was its heterogeneity. The core used in Experiment 4 and 5 was much more heterogeneous. The effectiveness of the tertiary polymer flood can be attributed to the heterogeneous nature of the dolomite. It appears that the tertiary polymer flood somehow performs better if the core is more heterogeneous (fractured and vuggy). Before concluding, it was prudent to repeat the same set of experiments on a homogenous Berea sandstone core.

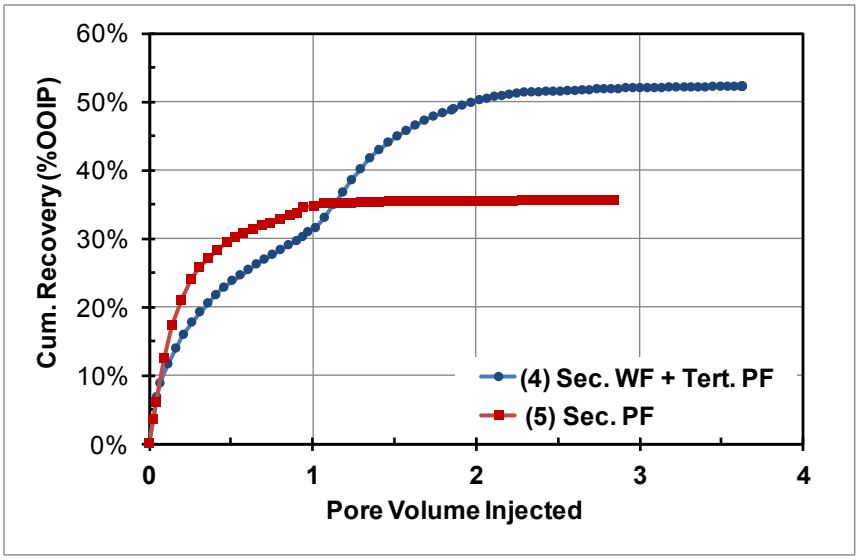

Figure 4.5: Cumulative oil recovery for experiments 4 and 5

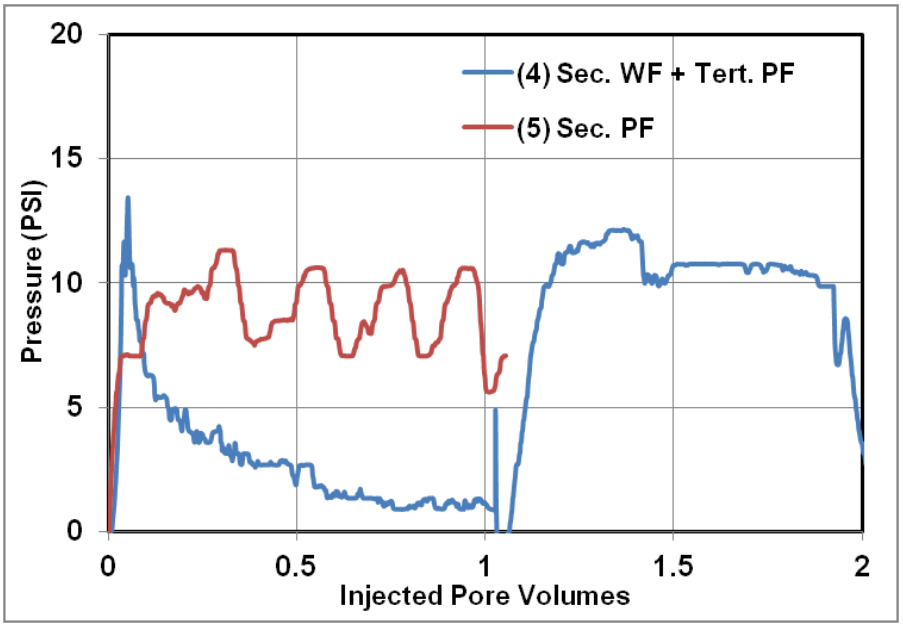

Figure 4.6: Pressure drop for the experiments 4 and 5.

Experiment 6 and 7 were conducted on a homogeneous Berea sandstone core. Figure 4.7 shows the production profile for experiments 6 and 7. Waterflood had a

recovery of 38% OOIP and the following tertiary polymer flood increased the cumulative recovery to about 47% OOIP. The secondary polymer flood recovered about 44% OOIP. It appears that in homogeneous Berea sandstone, the tertiary polymer flood performed almost as good as or only marginally better than the secondary polymer flood. The difference between the tertiary and secondary polymer floods recovery was much higher in the heterogeneous dolomite core. In the Berea core, the water break-through was at 0.15 PV and polymer break-through at 0.2 PV. For the heterogeneous dolomite core, water broke through at 0.09 PV and polymer at 0.13 PV. This suggests that in case of dolomite, the instabilities are highly influenced by the heterogeneities. In case of the Berea sandstone, it is fair to assume that the early break-through is only due to viscous fingering. Even in this case, tertiary polymer flood after secondary water flood did recover an extra 10% of the oil. This consistently observed incremental oil recovery in tertiary polymer floods is probably due to the mobile oil left behind by viscous instabilities and heterogeneities. This bypassed oil gets displaced by the larger pressure gradient of polymer flood. The bypassed regions are larger in heterogeneous cores so the tertiary jump is higher. Still the better performance of tertiary polymer flood over a secondary polymer flood could not be explained. It was thought that it could be a net result of the wettability and capillary interaction between the heterogeneities and viscous fingers. To verify the role of wettability, the next set of experiment was conducted on an oil-wet core.

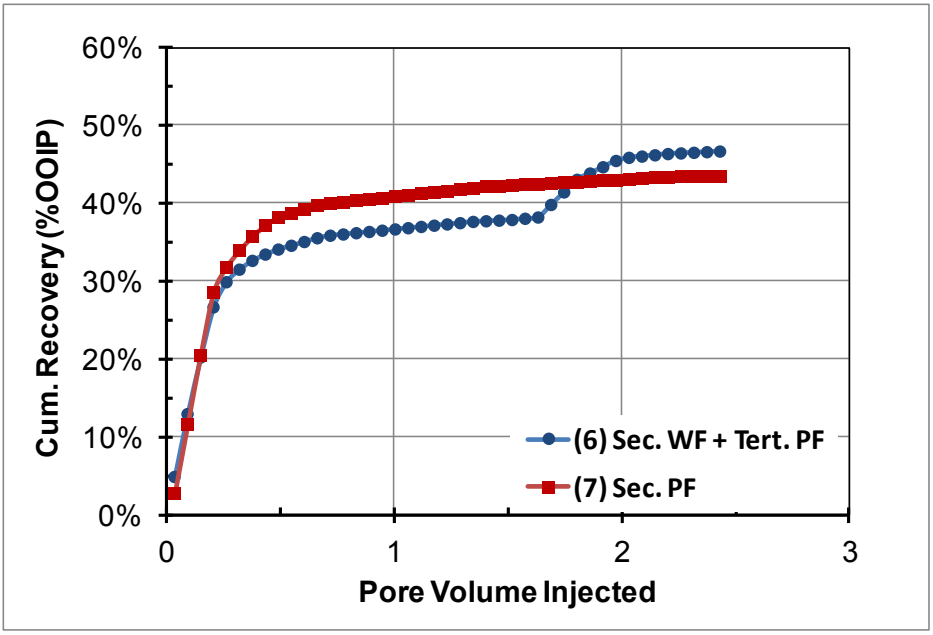

Figure 4.7: Cumulative oil recovery for experiments 6 and 7

Experiments 8 and 9 were performed on an oil-wet core. The Silurian dolomite core used for Exp. 4 and 5 was cleaned in a Dean Stark apparatus using chloroform and methanol. The core was then saturated with a reservoir oil that was known to render carbonate rocks oil-wet. It was then aged for about 50 days at 80^{o}C. Experiment 8 consisted of a water flood followed by a tertiary polymer flood. Experiment 9 was a secondary polymer flood in an oil-wet Silurian dolomite core. Figure 4.8 shows the picture of the water drop that beaded on the surface of the core and did not imbibe into the core for at least 30 mins. This suggests that the core was oil-wet. Figure 4.9 shows the oil recovery for experiments 8 and 9. The waterflood recovered about 30% OOIP and the tertiary polymer flood increased it to about 48% OOIP. The secondary polymer flood recovered about 44% OOIP. Again, the tertiary polymer flood recovers more oil than the secondary polymer flood, but the recovery trend looks very different. The tertiary oil recovery during for oil-wet case looks very gradual and slower.

Figure 4.10 compares the results of experiments 8 (oil-wet) and 4 (water-wet); as expected the waterflood oil recovery is slightly higher for the water-wet rock. The tertiary polymer flood oil recovery is also higher and faster for the water-wet rock (experiment 4) compared to the oil-wet rock (experiment 8). So clearly, wettability is a major player in the mechanism that leads to incremental extra recovery. One could hypothesize that this could be because of the spontaneous imbibition of water along the fingers and fractures. In both the water-wet and oil-wet cores, the water channels through the fractures and high permeability zones, but only in the case of the water-wet system, the water flowing along the fractures imbibes into the tighter matrix. This creates a counter-current imbibition and the oil is sucked out of the matrix into the flow channels. When polymer in injected, it drags this oil out of the channels and therefore the recovery is faster. For an oil-wet core or partially oil-wet core, there is little or no imbibition and therefore the recovery will be low and slower. When only polymer is injected, the displacement in the high permeability zones is better but the imbibition into the tighter zone would be slower. From the core flood experiments, we can conclude that viscous fingering, formation heterogeneity and surface wettability are three important parameters that should be studied in micromodel experiments.

Figure 4.8: Beaded water drop on the aged Silurian dolomite core

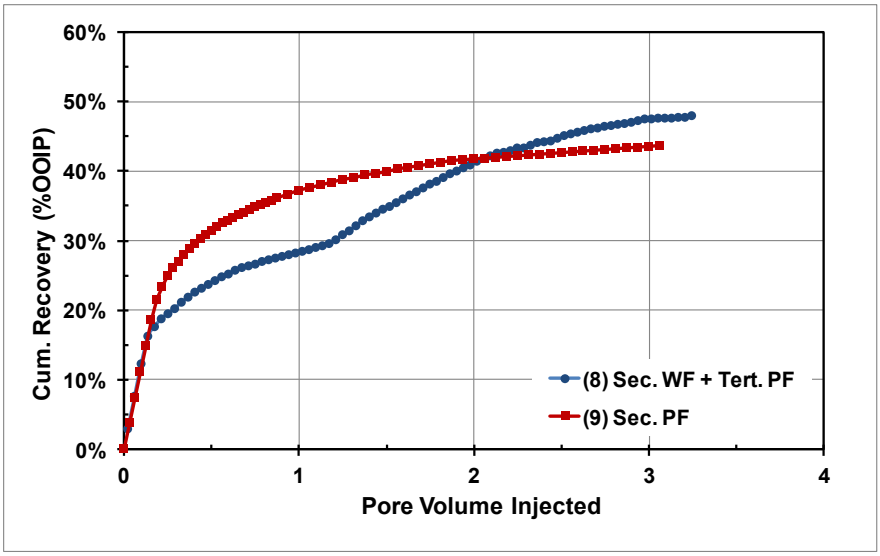

Figure 4.9: Cumulative oil recovery curves for experiments 8 and 9

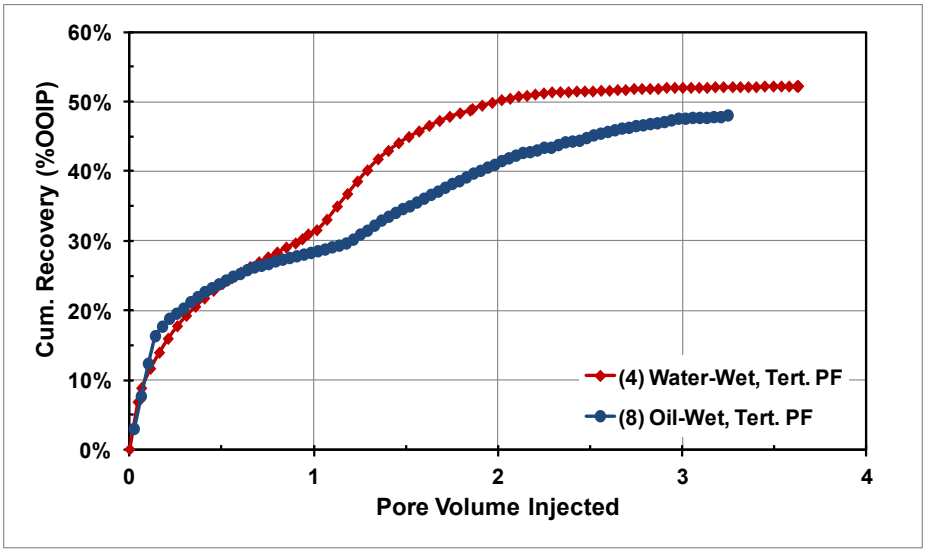

Figure 4.10: A comparison of cumulative oil recovery for a tertiary polymer flood in a water wet carbonate (experiment 4) and in oil wet carbonate (experiment 8)

Most of the coreflood experiments were conducted at 1 ft/day, a typical rate for light oils. The flow rates for viscous oils are smaller in fields because the viscous oil fields are shallow and the available pressure drop is limited. Experiment 10 was conducted to see the effect of flow-rate on secondary polymer floods. It was conducted at 5 times slower flow rate. Figure 4.11 compares the cumulative oil recovery for experiments 10 and 9 where the only difference is the flow rate. The reduction in the injection rate does not change the recovery significantly. This implies that the displacements at both 0.2 and 1 ft/day are stable. It could also mean that at the capillary number does not change significantly to affect the flow. In this case slower injection is not economical because we recover the same amount of oil but at 5 time slower rate.

Experiment 11 was conducted at a lower polymer concentration of 2000 ppm HPAM 3330s in sea brine. Lower polymer concentration leads to lower viscosity (10 cP at $10s^{-1}$). The oil recovery is significantly lower than that in experiment 9. This implies that the polymer flood is unstable and displacement is inefficient. Figure 4.11 shows the results of the experiments 9, 10 and 11.

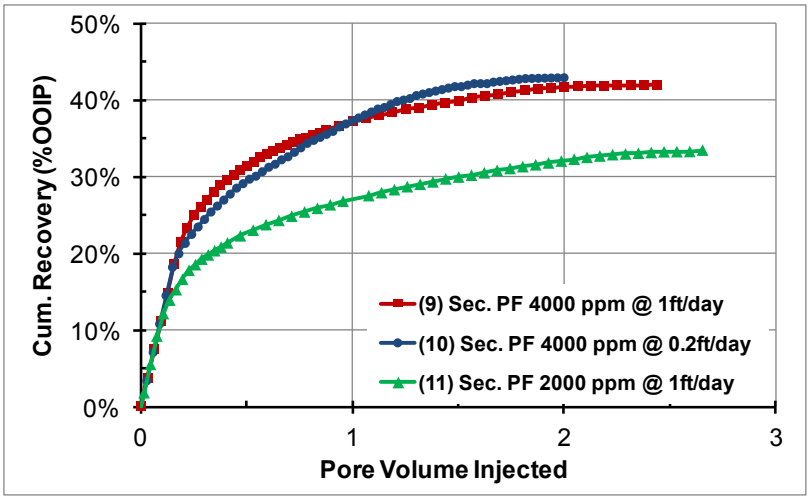

Figure 4.11: Cumulative oil recovery for experiments 9, 10 and 11

Imbibition test

As hypothesized above, imbibition plays an important role in modulating viscous finger width and shape. To study the effect of polymeric viscosity on imbibition rate the following complimentary experiment was conducted in two similar Berea cores plugs. The cores plugs were saturated with 200 cp oil and then one core was submerged in a solution of injection brine and other in a 4000 ppm HPAM polymeric solution. It was noticed that in the case of brine, oil starts oozing out almost instantaneously while for polymer solution, no significant oil is recovered in the first three hours. Figure 4.12(a) presents the image of brine and polymer imbibition cells 3 hours after the start of the experiment. Figure 4.12(b) presents a plot of oil recovery as a function of time; there is a clear lag between the polymer and brine recovery with the initial recovery in case of polymer about 4 times as slow as that for brine. Polymer does eventually recover the same amount of oil but in thrice the time. This simple experiment confirms that the addition of polymer does slow down the imbibition rate.

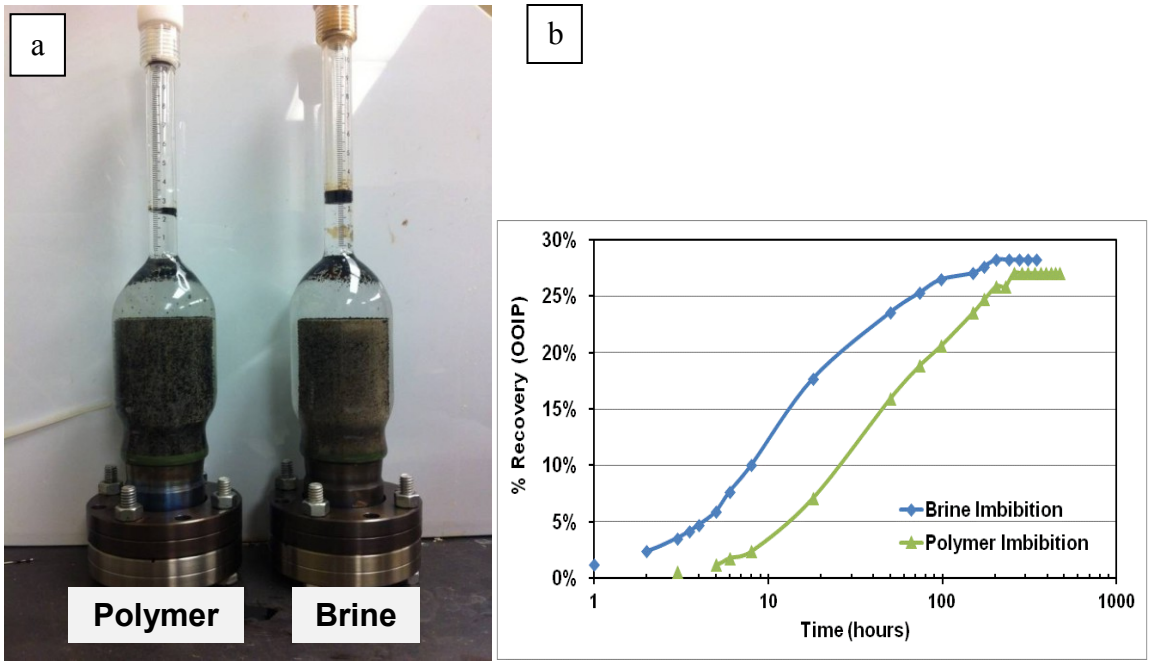

Figure 4.12 (a) A picture of oil saturated Berea cores in imbibition cell with polymer and brine. (b) Oil recovery for brine and polymer imbibition tests, both polymer and brine recover the same amount of oil, but brine recovers it 3 times faster

Carbonate Coreflood Summary

To summarize, the core experiments, tertiary polymer floods conducted after waterfloods (of a viscous) oil recovered a significant amount of additional oil in water-wet and oil-wet dolomite cores. Additional oil was also recovered in water-wet Berea cores, but to a lesser extent. It is hypothesized that this increase in oil recovery is due to viscous fingering and oil by-passing during the waterflood. Tertiary polymer flood recovery is higher than secondary polymer flood recovery because of the interplay between imbibition, fingering and heterogeneity. Micromodel study needs to be done to confirm and validate the mechanism for this incremental tertiary recovery. The oil recovery in secondary polymer floods decreased as the polymer viscosity decreased due

to increased viscous fingering. The secondary polymer flood, of course, recovered the oil faster than tertiary polymer floods. The oil recovery was lower and slower in oil-wet cores compared to water-wet cores of the same heterogeneity. Imbibition is minimal in oil-wet cores and slow in water-wet cores with polymeric solutions due to high viscosity. Imbibition rate is higher in waterflood than in polymer floods in water-wet rocks. Micromodel experiments were conducted to study the mechanism and the results are discussed in the following section. We hope that the visual investigation will provide a more mechanistic explanation of the unexpected trend in recovery.

4.1.3 Micromodel Experiment Results

Table 4.4 shows the list of all the experiments conducted with micromodels. The list is similar to the list of Table 4.2. Experiments 'a'-'f' were all conducted at an equivalent flow rate of about 12 ft/day and the corresponding capillary number values have been listed in Table 4.4. All the capillary numbers are in the range of 10^{-5} or less. All the experiments are complimentary to the secondary and tertiary polymer flooding experiments conducted in the carbonate cores.

List of Micromodel Experiments		
a.	Secondary water flood and tertiary polymer flood in 200 cP oil	Water-wet, Micromodel A
b.	Secondary polymer flood in 200 cP oil	Water-wet, Micromodel A
c.	Secondary Water Flood and Tertiary Polymer flood in 200 cP oil	Water-wet, Micromodel B
d.	Secondary Polymer Flood in 200 cP oil	Water-wet, Micromodel B
e.	Secondary Water Flood and Tertiary Polymer flood in 200 cP oil	Oil-wet , Micromodel B
f.	Secondary Polymer Flood in 200 cP oil	Oil-wet, Micromodel B

Table 4.4: List of micromodel experiments conducted to mimic and justify the results of core flood experiments of Table 4.1

The micromodel experiments were conducted in two kinds of micromodels. The normal homogeneous micromodels were modified to include heterogeneities and two types of heterogeneities were included; isolated and connected. Figure 4.13 (a) and (b) show the images of the two glass micromodels.

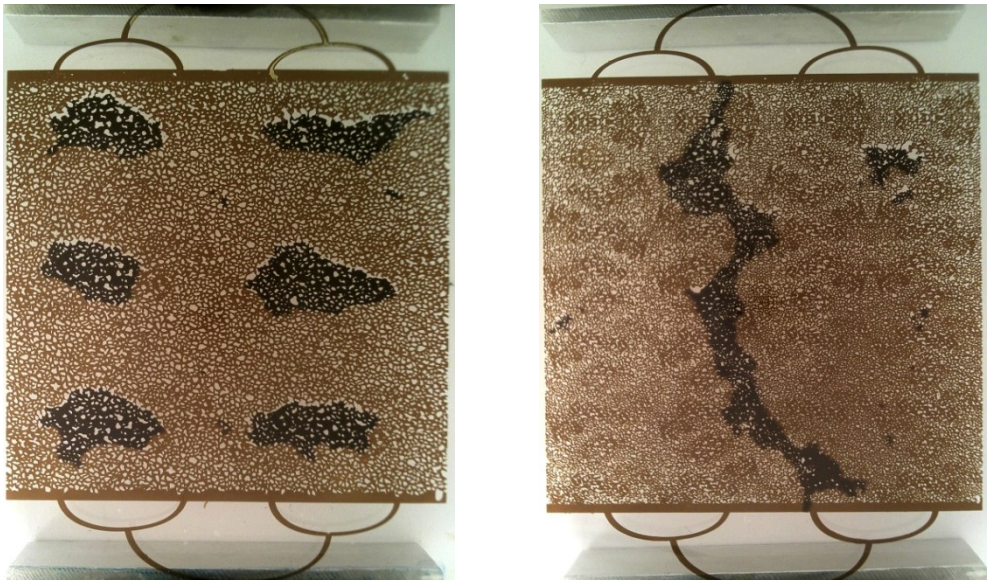

Figure 4.13(a): Glass micromodels with isolated or disconnected heterogeneities and (b) connected high permeability heterogeneity

Experiments (a) and (b) were conducted on a water-wet micromodel with isolated heterogeneities. Figure 4.14 shows the images at the initial state, the end of water flood, the end of tertiary polymer flood and the end of secondary polymer flood. We can see that the viscous fingers are initiated very early in the system, right at the inlet. This leaves behind a lot of connected and mobile oil at the end of water flood. Towards the end, even though the oil production went down to zero, we can visually see that oil saturation in the micromodels is definitely not at the irreducible oil saturation. When polymer is injected, pressure gradient is higher, the displacement front is stable and therefore it displaces most of the connected oil. It is also interesting to note that the smaller disconnected oil blobs were not displaced at all by the tertiary polymer flood. These small isolated oil blobs form the true residual of a porous media. The large connected oils pockets can still be displaced and produced. In the secondary polymer flood, the front is relatively stable from the beginning and leaves behind only tiny disconnected oil blobs. Visually it

appears that the secondary polymer flood performed better than the tertiary, but the image analysis suggests that the recoveries were about the same. This could be because the residual oil in case of secondary polymer flood is more dispersed and also in the deeper etched section of the micromodel. The difference in the depth of different sections of the micromodel was taken into account during the image analysis.

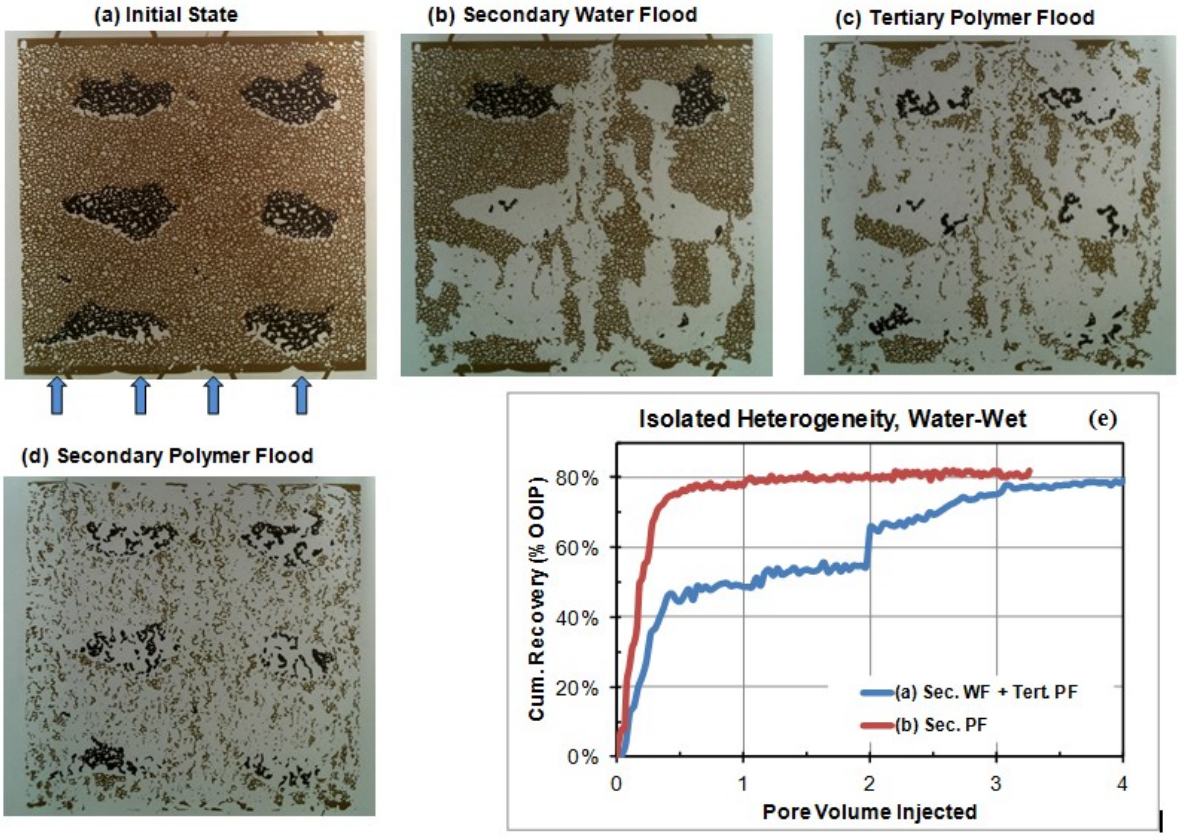

Figure 4.14: Displacements in water-wet micromodel A: (a) Image of the initial state of the micromodel, (b) Image after the end of water flood, (c) Image after the end of polymer flood, (d) Image after the end of secondary polymer flood, (e) Cumulative oil recovery obtained by image analysis.

Experiments c and d were conducted in a water-wet micromodel with connected heterogeneity. Figure 4.15 shows the images at the initial state, the end of water flood, the end of tertiary polymer flood, and the end of secondary polymer flood. We can see that during water flood, all of the injected water goes through the connected high permeability path, displaces all the oil in its path and does not even enter the matrix. However, it is interesting to see that towards the end of waterflood the whole high permeability region is re-saturated with oil while water has imbibed into the smaller pores of the matrix owing to its water-wet nature. Water then just flows along the walls of the fracture and the nearby matrix and does not displace the viscous oil. Water current cannot displace this viscous oil because the pressure head generated by water flow is not high enough. When polymer is injected, the pressure head increases, this displaces the oil in the channel while it also invades the matrix and displaces the oil from the unswept areas. So both the fracture and matrix are producing in this step. In case of the secondary polymer flood, polymer preferentially channels through the high permeability zone but it could invade the matrix as well. Recovery is faster and better than that of water flood alone but no evidence of oil re-saturation in the high permeability zone is observed. If the matrix was very tight, the polymer would not be able to invade; in that case the higher viscosity of polymer must slow down the imbibition. In this experiment we did not observe tertiary polymer flooding performing better in comparison to secondary, as seen in the corefloods. This could be because of the high permeability and connectivity of the low perm region in comparison to the actual dolomite rock. In an actual tight rock, some part of the matrix might be too compact to be invaded by the polymer and imbibition might just be the only way to reach this oil. This would also lead to higher recoveries in water-wet carbonate core-floods than in oil-wet carbonate core-floods.

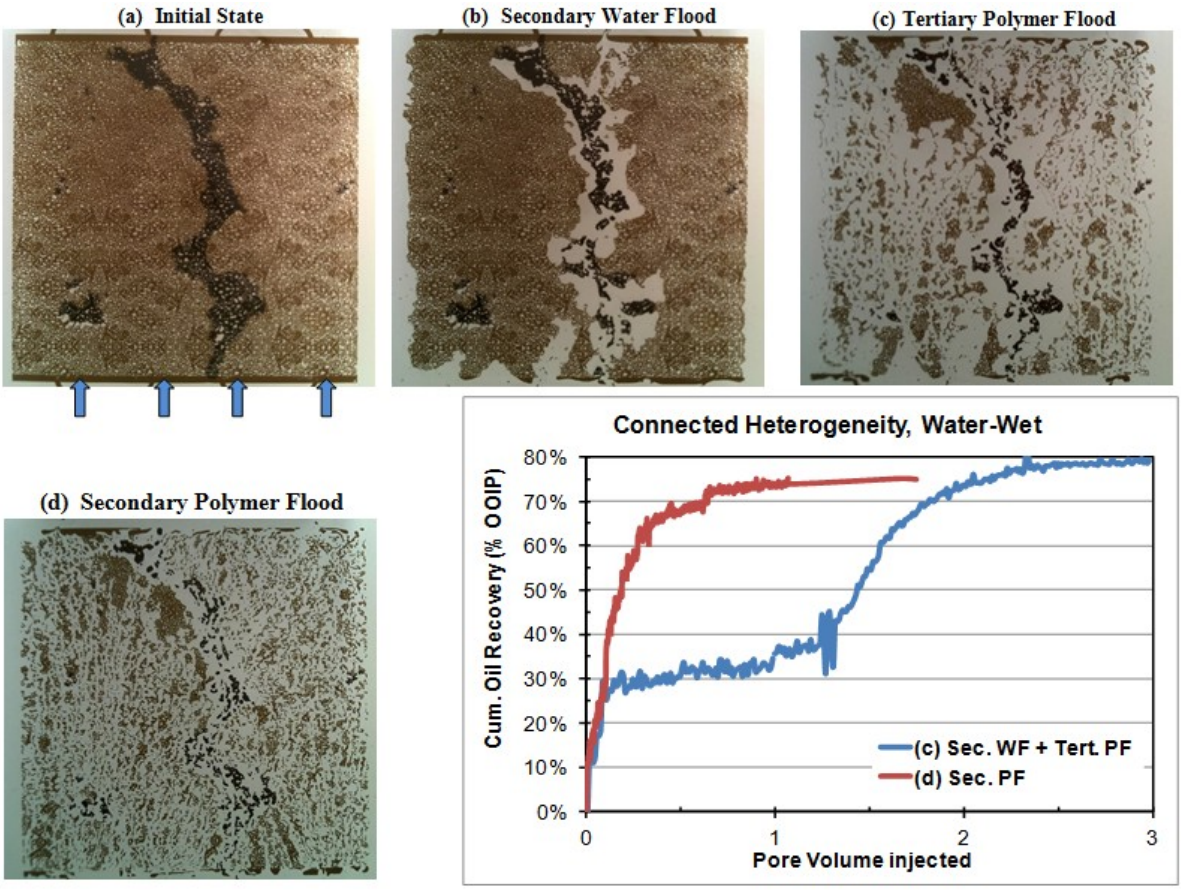

Figure 4.15: Displacements in water-wet micromodel B: (a) Image of the initial state of the micromodel, (b) Image after the end of water flood, (c) Image after the end of polymer flood, (d) Image after the end of secondary polymer flood, (e) Cumulative oil recovery obtained by image analysis.

To confirm that the observation of experiments (c) and (d) are influenced by water-wetness and imbibition, the next set of experiment were conducted on an oil-wet micromodel. To render the micromodel oil wet it was thoroughly cleaned after exp. (d) and then vacuum saturated with a n-hexane-silane mixture (Salter and Mohanty, 1982). The mixture is allowed to stand in the micromodel for 20 mins. Silane was then displaced

with hexane followed by air. Silane molecules attach themselves to quartz and silica render it oil-wet. This was observed to be true in our micromodel as well.

Experiments (e) and (f) were conducted in an oil-wet micromodel with connected heterogeneities. Figure 4.16 shows the images at the initial condition, the end of water flood, the end of tertiary polymer flood, and the end of secondary polymer flood. In this case as well, water initially channels through the high permeability region, but there was no imbibition along the walls of the channel. Brine flows through the channels and sits along its boundary with the matrix without imbibing. It is also interesting to compare the production profile of the tertiary polymer flood in experiments (c) and (e) (Figure 4.17). The recovery in the case of experiment (c) was much faster (water-wet case) than that in experiment (e) (oil-wet case), similar to our observation in the core flood experiments (Figure 4.10). This suggests that the slower recovery rate observed in tertiary polymer flood for an oil-wet core was because of the absence of oil in the high perm zone.

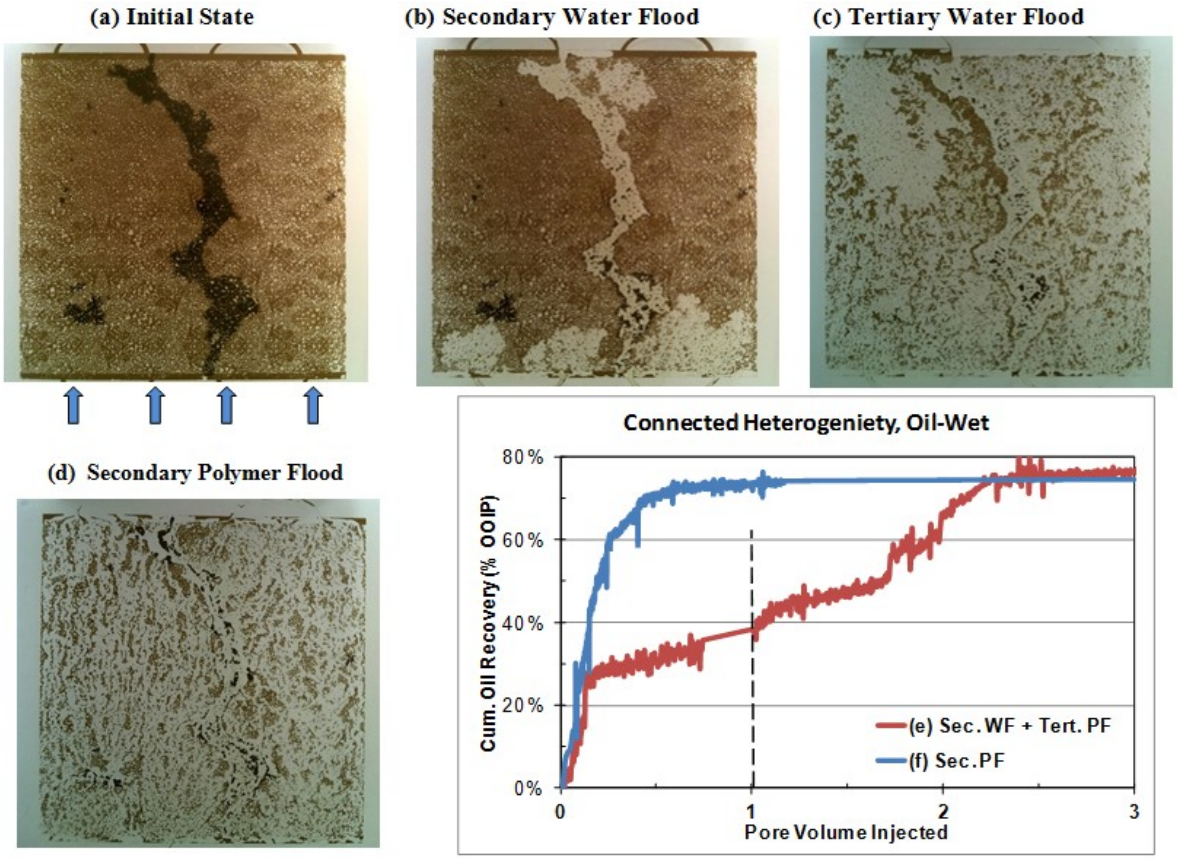

Figure 4.16: (a) Image of the initial state of the micromodel, (b) Image after the end of water flood, (c) Image after the end of polymer flood, (d) Image after the end of secondary polymer flood, (e) Cumulative oil recovery obtained by image analysis.

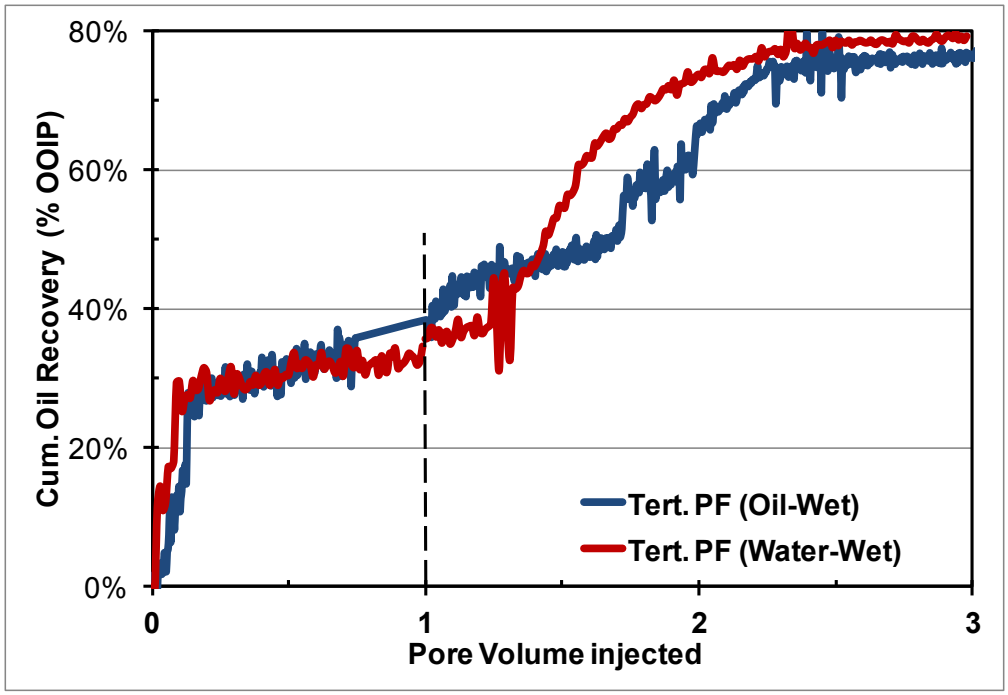

Figure 4.17: A comparison of the recovery profiles for oil-wet and water-wet micromodel experiments. The graph follows the same trend as observed during the core-floods (Figure 4.10)

Micromodel Summary

Micromodel experiments helped in confirming our hypothesis based on the core flood results and provided a more mechanistic explanation of the trend seen in the core floods. Micromodel experiments clearly showed that the bypassed viscous oil left after waterflood is mobile and can be recovered by polymer floods. This mobile oils accounts for the incremental tertiary recovery in each case (even for a homogeneous core). Micromodel also helped in visualizing the mechanism that lead to higher tertiary polymer recovery than secondary polymer recovery. The higher tertiary recovery was attributed to the imbibition of oil along the walls of the fingers or fractures into the flow channels in the water-wet media. When water is injected it channels through the fractures and breaks

through very early. However, owing to the water-wet nature of the matrix, water starts imbibing into the smaller pores. This creates a counter-current imbibition along the face of the fractures and the fractures are refueled with oil. However, the pressure gradient in the flowing water is not high enough to drag the oil out, so the oil just accumulates in the fracture until the polymer flood is initiated. When the polymer is introduced it displaces the connected mobile oil from the matrix (better sweep) and it also produces the imbibed oil from the fracture. Therefore, the tertiary polymer flood contacts more area and recovers oil due to improved sweep and imbibition along the fracture walls. During the secondary polymer flood, the imbibition is slower as the polymer is more viscous (as proved in the imbibition cell experiment) and therefore the recovery is less. A similar observation for higher recovery in tertiary polymer flood for a viscous oil system has been reported by Fabbri et al. (2014). They did not suggest a mechanism or reason for such an unexpected trend in oil recovery. The micromodel study has provided a possible mechanism that could eventually lead to modeling of this behavior. From the rate of recovery point of view, the oil is undoubtedly produced faster when the polymer is injected in the secondary mode (at a constant injection rate). Thus, in the context of this work, the timing of polymer flood or early initiation of polymer flood is not critical for viscous oil reservoirs.

4.2 VISCOUS FINGERING IN POROUS MEDIA

Viscous fingering is an important physical phenomenon that occurs during unstable displacements and is not very well captured in the numerical models and reservoir simulations. Viscous fingering is caused by frontal instability and is a function of fluid properties. Local fluctuations in permeability trigger frontal instability which may grow or damp out depending on the mobility of the two phases involved. It is not

very practical to account for viscous fingering in conventional finite difference or finite element simulators as the finger width is much smaller than the grid size. To capture these fingers, very fine grid parallel computing simulations could be performed, but these simulations are computationally expensive and also field data at this high resolution is not available adding to the uncertainty. Therefore, to history match these unstable displacement experiments using conventional simulators, relative permeability functions are generally modified to fit the production and pressure trends. It is important to understand the key parameters that affect the relative permeability in unstable displacements. A set of micromodel and core flood experiments were conducted in this part of this study to understand the effect of viscous fingering and its effect on two-phase relative permeability.

4.2.1 List of Micromodels Experiments and Corefloods

Micromodel Experiments

Nine micromodel experiments were conducted at different viscosity ratios and different flow rates. Table 4.5 has the list of all the micromodel experiments conducted in the study. Both glass and silicon micromodels were used in these experiments. All the different viscosity ratio experiments were conducted in silicon micromodels and all the variable flow rate experiments were conducted in glass micromodels. The switch to glass micromodel was due to their ability to withstand higher pressure gradients required while injecting or displacing heavy oils. Silicon micromodels were very fragile and cracked easily under high pressure. The procedure for micromodel experiments is described in Section 3.3.2.

#	Micromodel type	Viscosity Ratio	Flow rate ($Q/A\phi$)
1	Silicon Micromodel	$\mu_r = 0.005$	1ft/day
2	Silicon Micromodel	$\mu_r = 1$	1ft/day
3	Silicon Micromodel	$\mu_r = 200$	1ft/day
4	Silicon Micromodel	$\mu_r = 1000$	1ft/day
5	Silicon Micromodel	$\mu_r = 4000$	1ft/day
6	Silicon Micromodel	$\mu_r = 10000$	1ft/day
7	Glass Micromodel	$\mu_r = 10000$	1ft/day
8	Glass Micromodel	$\mu_r = 10000$	0.1 ft/day
9	Glass Micromodel	$\mu_r = 10000$	0.01 ft/day

Table 4.5: List of micromodel experiments conducted at different viscosity ratios and flow rates

Coreflooding Experiments

To complement the micromodel experiments and to confirm the effect of viscosity ratio and flow rate variation in a consolidated porous medium, eight core flood experiments were also conducted in this study. These experiments also provide quantitative data required for simulations and modeling purposes. All the 8 experiments were conducted on the same core sample cut out from a Boise outcrop sandstone block and are listed in Table 4.6. Procedure for core flood experiments is described in section 3.3.1.

#	Viscosity ratio	Flow rate ($v = Q/A\phi$)
1	$\mu_r = 1$	1 ft/day
2	$\mu_r = 60$	1 ft/day
3	$\mu_r = 560$	1 ft/day
4	$\mu_r = 1440$	1 ft/day
5	$\mu_r = 5200$	1 ft/day
6	$\mu_r = 10500$	1 ft/day
7	$\mu_r = 10500$	0.2 ft/day
8	$\mu_r = 10500$	0.05 ft/day

Table 4.6: List of core flood experiments conducted at different viscosity ratios and flowrates

4.2.2 Results of Micromodel Experiments

Results of the micromodel experiments 1-6 (in the silicon micromodels) are shown in Figure 4.18. At the stable viscosity ratios (μ_r=0.005 and 1), the displacement front is very stable and the flow pattern is similar in these two experiments. On a closer observation, it is evident that even the most stable macroscopic front looks perturbed at the microscopic scale (Figure 4.19). Thus, perturbation exists for all displacements. For stable system, the perturbation die or fade our faster because of the capillary effect of the pores. As the viscosity ratio increases the effect of capillary forces begin to subside, the perturbations take longer to fade and hence grow faster. Another important feature of immiscible displacement is the presence of residual oil saturation in the swept zone. There is always residual oil saturation behind the displacement front (Figure 4.19). Residual oil usually resides in form of disconnected isolated oil blobs.

As the viscosity increases, the macroscopic stable front starts breaking into fingers, water breakthrough occurs earlier and remaining oil saturation is higher. At the viscosity ratio of 200, the invaded region is less efficiently displaced and the front looks diffused. At the viscosity ratio of 1,000, the invaded region is even less efficiently displaced; the fingers are thinner and directed mostly in the flow direction. At the range of viscosity ratio of 4000 -10,000, finger width is only a few pores wide, and the displacement pattern resembles the fractal structures of diffusion-limited aggregation (DLA). Figure 4.20 shows the fractal behavior and fractal dimensions of the viscous finger formed at a viscosity ratio of 10000. A two-dimensional DLA structure is supposed to have a fractal dimension of 1.7. Maloy et al. (1985) in their 2D bead pack found the fractal dimension of the viscous fingers to be about 1.62±0.04. Daccord et al. (1986) mentioned that as the viscosity ratios tends to infinity the fractal dimension of the fingers will tend towards 1.7. In our system, the viscous finger at 10000 viscosity ratio has a consistent fractal dimension of 1.63±0.01. The self-similarity and repetitive nature of the fractal is also captured in Figure 4.20.

The separation in between the fingers is also observed to increase as the viscosity ratio increases; for μ_r = 10000 there is only one prominent finger growing, for μ_r = 4000 there are two contributing and competing fingers and for 200 and 1000 there are multiple fingers that smudge each other as they compete for growth in close proximity. Figure 4.21 shows the saturation profiles along the length of the micromodel for each case. The saturation profiles were measured by image analysis. As oil appears darker, the oil phase can be traced out using segmentation techniques. Once oil phase has been segmented out the saturation along the length can be determined by counting the number of dark sites along the length. From the data of Figure 4.21 an average value of

ultimate recovery can be estimated from the water saturation in the swept zone. Table 4.7 shows the data of recovery for each value of viscosity ratio.

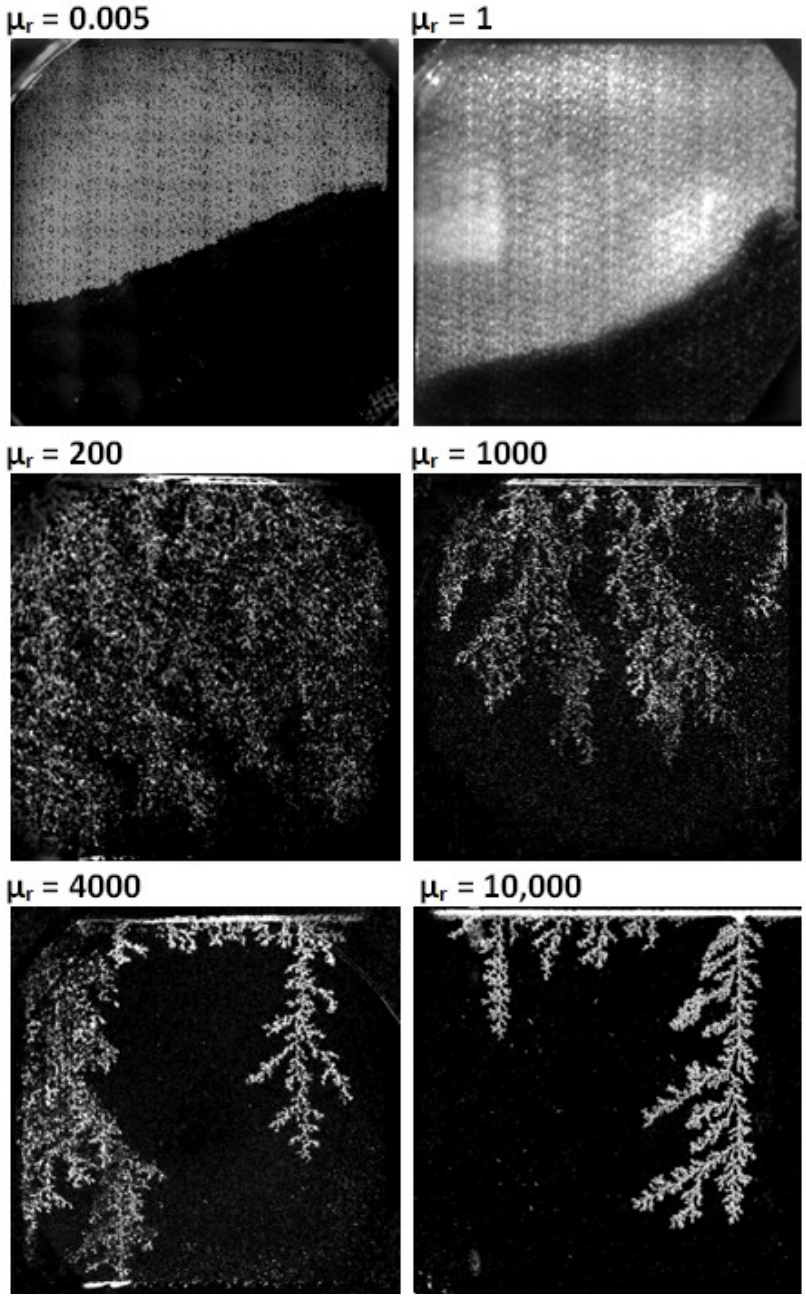

Figure 4.18: Displacement patterns generated in 2D silica micromodel while flooding at viscosity ratios of 0.005, 1, 200, 1000, 4000 and 10,000

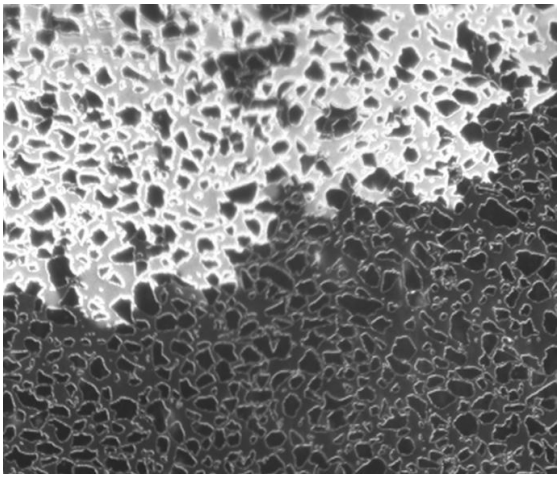

Figure 4.19: An expanded view of stable displacement with μ_r = 0.005 showing the trapped oil in the swept zone and the pore scale perturbations that exist in even the most stable displacement

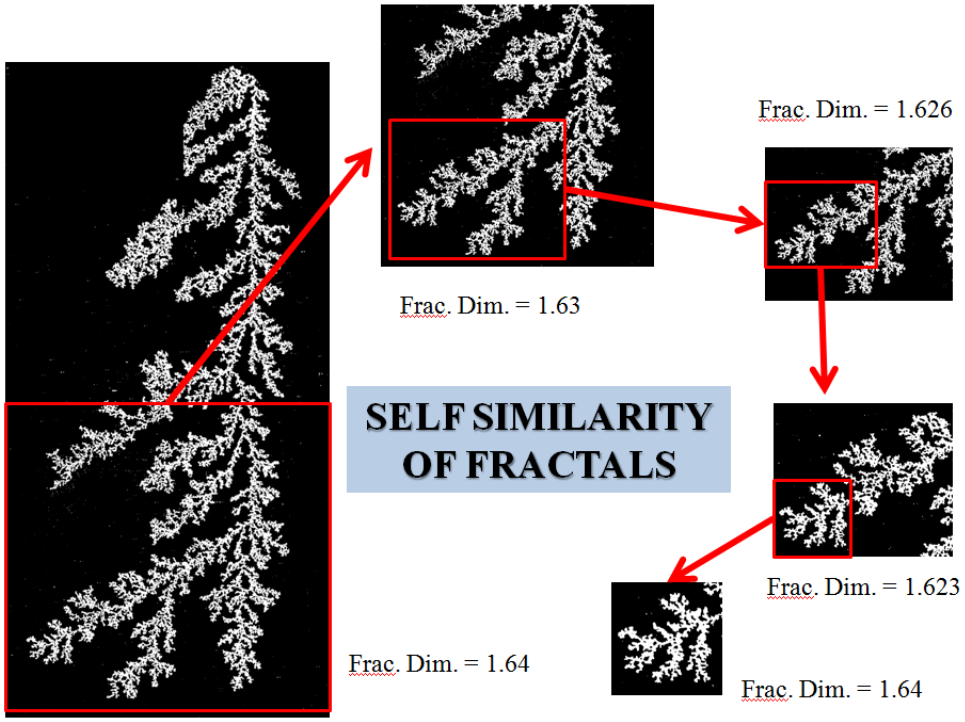

Figure 4.20: Viscous finger at viscosity ratio of 10000 shows fractal behavior with a fractal dimension of 1.62

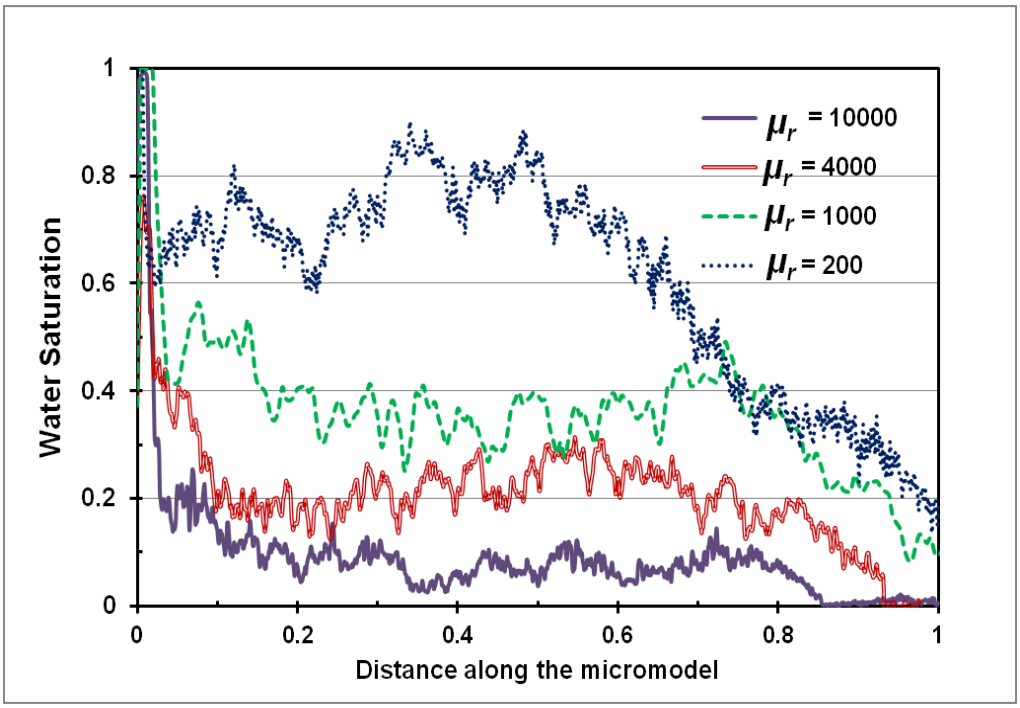

Figure 4.21: Saturation profile along the length of the micromodel at the time of break-through for $\mu_r = 200$ and above.

Viscosity Ratio, μ_r	Recovery Efficiency
1	0.8
200	0.65
1000	0.35
4000	0.2
10,000	0.08

Table 4.7: Estimated ultimate recovery efficiency and viscosity ratio data for micromodel experiments 1-6.

Figure 4.22 shows the result of experiments 7-9 performed in the glass micromodels. For this set of experiments, the viscosity ratio was kept constant at 10,000 while the injection rate was varied from 1ft/day to 1/100 ft.day . At 1 ft/day, the fingering

pattern is highly unstable and resembles the fractal structures of DLA or dielectric breakdown. As the injection velocity is decreased, fingers grow wider and the overall recovery is higher. Slower injection rates allow more time for water to imbibe into the pores around the fingers (driven by capillary pressure gradient) causing the resulting fingers to grow wider. From the trend in Figure 4.21, the flow may be stable and would resemble the unit viscosity ratio displacement at a very slow injection rate.

Figure 4.22: Snapshots of glass micromodel experiments showing the effect of flowrate on fingering pattern at a constant viscosity ratio of 10,000 cp

Micromodel Viscous Fingering Summary

Micromodel experiments shed important light on immiscible unstable displacement and how it is influenced by change in viscosity ratios and injection rate. Knowledge of fingering pattern and sweep at a certain viscosity ratio will help us better understand and predict the pseudo effects observed in the porous media. For example, when the flow is unstable, the injected fluid channels through only a thin section of the flow area. The area available for flow is thus smaller and therefore the observed pressure drops are higher. This will create an illusion of decrease in relative permeability. Such

experimentally measured relative permeabilities for unstable two phase displacements are reported to be different (lower) from expected (stable displacement) relative permeability curves (Akin et al. (1998), Wang et al. 2006 and Mosavat et al. (2013)). Similarly, if the viscosity ratio is held constant but the injection rate is reduced the injected brine will have longer time to imbibe. As a result the fingers will be wider and therefore the experimentally observed pressure drop/flow rate will be higher than that at a higher injection rate. This would give an impression of an increase of oil relative permeability.

Unstable immiscible displacement in porous media and its effects on the relative permeability curves is not very well understood. The series of coreflood experiments described in the following section are essentially a repetition of the micromodel experiments at different viscosity ratios and flow rates. The core flood experiments can provide us with measurable data in terms of pressure profile and recovery trends. This data can be used to model unstable displacements at the reservoir simulation scale based on our knowledge of viscous fingering via micromodel experiments.

4.2.3 Results of Unstable Corefloods

To complement the micromodel experiments and to confirm the effect of viscosity ratio and flowrate variation in a consolidated porous medium, eight core flood experiments were conducted in this study. All the 8 experiments were conducted on the same core sample cut out from a Boise outcrop sandstone block and are listed in Table 4.8. The core was 2 inches in diameter and 12 inches in length. The permeability and porosity of the core were measured to be 6 Darcy and 29% respectively. The high permeability of core enabled the used of viscous oils without causing extremely high pressure drops. Experiments 1 to 6 were conducted at six different viscosity ratios while the injection rate was kept constant at 0.125 ml/min, which is an equivalent of 1 ft/day in

the core. Experiments 6, 7 and 8 were conducted at a constant viscosity ratio of 10,500 but the injection rate was changed from 0.125 ml/min to 0.025 ml/min and 0.006 ml/min (equivalent of 0.2 ft/day and 0.05 ft/day), respectively.

#	Viscosity ratio (μ_r)	Flowrate, v ($Q/A\phi$)	Core	Brines
1	$\mu_r = 1$ 60 cp mineral oil 60 cp glycerol water	1 ft/d	• Boise Sandstone core, • 2 inch diameter, • 12 inch length, • 6 Darcy Permeability, • 29% porosity	• Injection Brine: 4% NaCl • Connate Brine: 2% NaCl
2	$\mu_r = 60$ 60 cp mineral oil 1 cp water	1 ft/d		
3	$\mu_r = 560$ 560 cp mineral oil 1 cp water	1 ft/d		
4	$\mu_r = 1440$ 1440 cp mineral oil 1 cp water	1 ft/d		
5	$\mu_r = 5200$ 5200 cp mineral oil 1 cp glycerol water	1 ft/d		
6	$\mu_r = 10500$ 10500 cp mineral oil 1 cp water	1 ft/d		
7	$\mu_r = 10500$ same as above	0.2 ft/d		
8	$\mu_r = 10500$ same as above	0.05 ft/d		

Table 4.8: List of core flood experiments at different viscosity ratios and flowrates.

Figure 4.23 shows the recovery trends for the experiments 1-5. Stable displacement at μ_r=1 recovers about 65% of oil. As the viscosity increases, the water

breakthrough occurs earlier and the recovery steadily falls to 50%, 37%, 29% and 23% for μ_r 60, 560, 1440 and 5200, respectively. Figure 4.24 shows the pressure trends for experiments 1 – 6. Most of the curves have a distinct monotonically decreasing nature with the exception of experiment 1, where the pressure rises because the end point mobility ratio is less than 1. Figure 4.25 shows the recovery trends for μ_r = 10,500 at three different flow rates. At 1ft/day injection rate, the recovery is about 21% and at slower injection rates of 1/5 ft/day and 1/20 ft/day recovery increases to about 24% and 27%, respectively. At slower injection rates, the breakthrough is delayed (as observed in the micromodel) and recovery increases. It is interesting to note that the recovery for experiment 7 is almost the same as in experiment 5 and recovery for experiment 8 is in between the recovery for experiments 5 and 4. It should be noted that in experiments 1 – 5 the initial oil saturation (before waterfloods) was different for different viscosity oils; therefore all the recoveries are reported in terms of % pore volume (PV). The pressure profiles for experiments 6-8 are shown in Figure 4.26. A summary of each core flood including viscosities of the fluids, initial and final saturations and recovery are listed in Table 4.9.

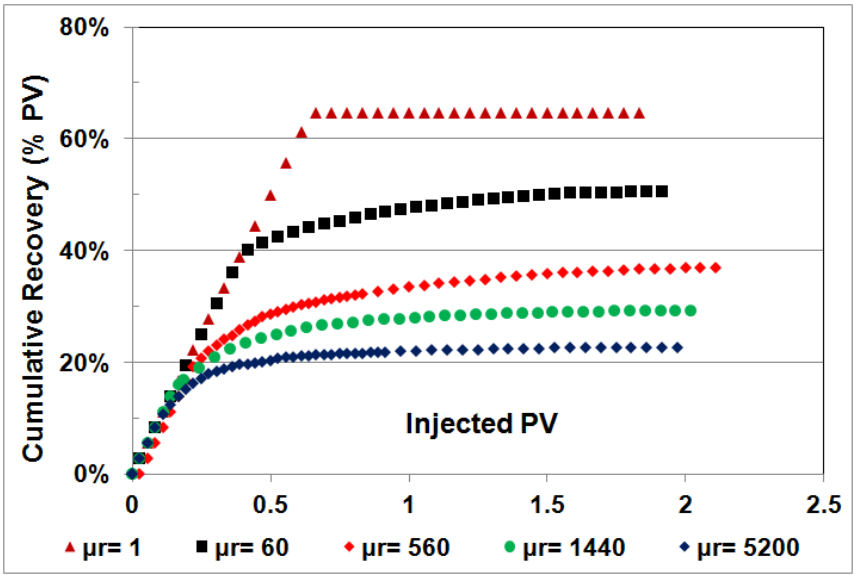

Figure 4.23: Cumulative oil recovery for experiments 1-5 at μr = 1, 60, 560, 1440 and 5200 and 1 ft/day injection rate.

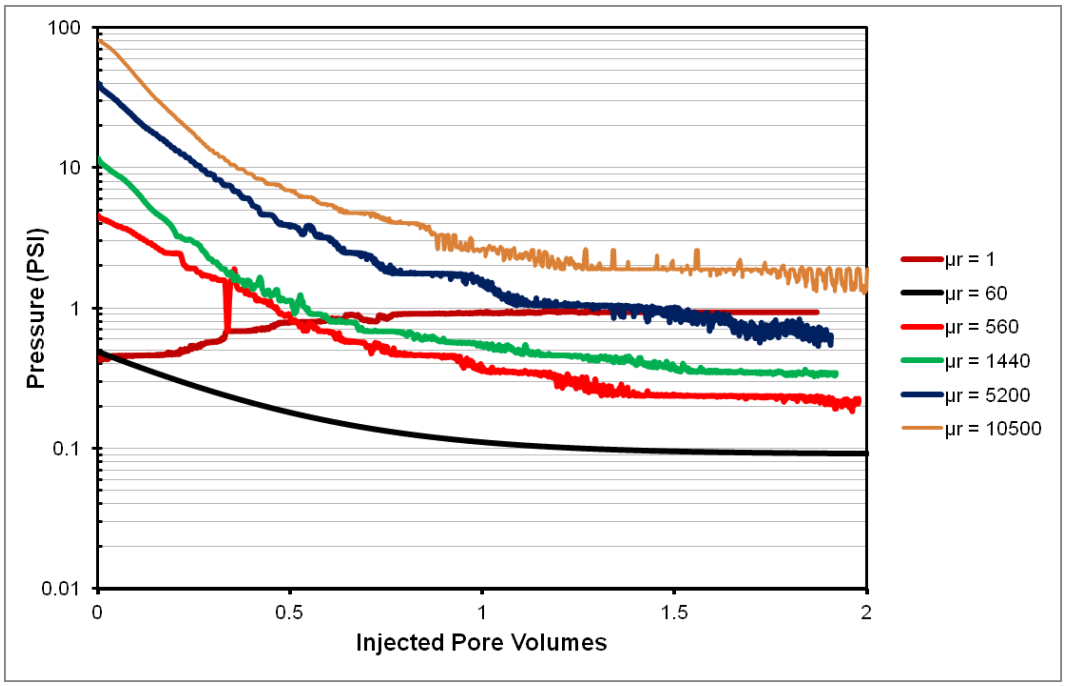

Figure 4.24: The pressure profiles of the experiments 1 to 6 at different viscosity ratios

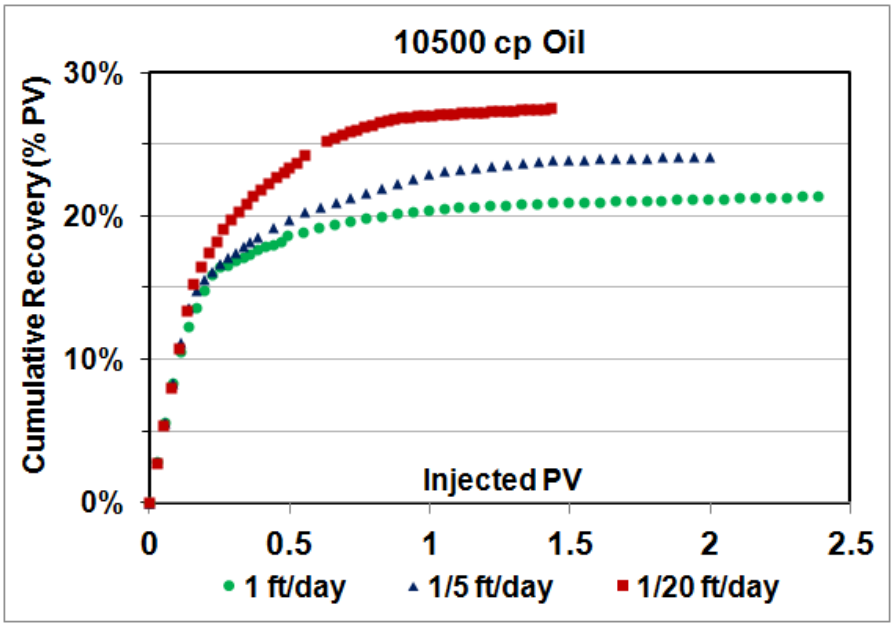

Figure 4.25: Cumulative oil recovery for experiments 6-8 at μ_r = 10000 and injection rate of 1, 0.2 and 0.05 ft/day

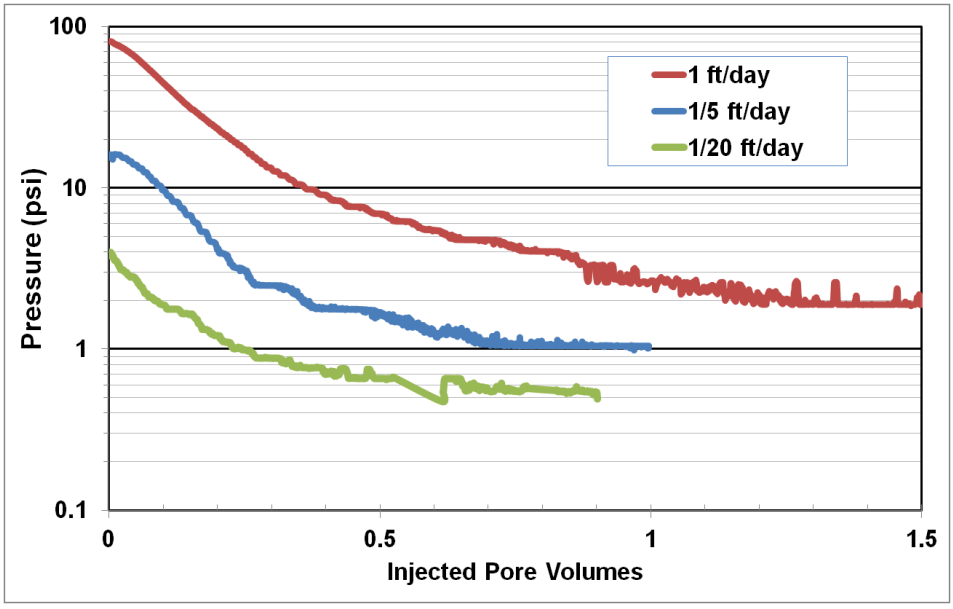

Figure 4.26: The pressure profiles of the experiments 6, 7 and 8 at different injection rates

Expt.	μ_w	μ_o	μ_r	S_{wi}	S_{wmax}	Recovery (%PV)
1	60	60	1	0.17	0.82	65
2	1	60	60	0.17	0.68	51
3	1	560	560	0.156	0.52	37
4	1	1440	1440	0.117	0.41	29
5	1	5200	5200	0.089	0.32	23
6	1	10500	10500	0.089	0.28	19
7	1	10500	10500	0.089	0.32	23
8	1	10500	10500	0.089	0.35	26

Table 4.9: List of viscosities of the fluids, initial and final saturation and recovery for each coreflood experiment

Exp	ρ_o	ρ_w	V	μ_w	μ_o	μ_r	N_c	N_{c_visc}	N_g	$N_{c\_visc}\mu_r$	$N_c\mu_r^2$	Breakthrough Recovery	Ultimate Recovery
1	0.9	1.2679	1	60	60	1	6.5E-6	6.5E-6	6.8E-7	6.5E-6	6.5E-6	64	65
2	0.9	1.06	1	1	60	60	1.1E-7	6.5E-6	2.9E-7	3.9E-4	3.9E-4	40	50
3	0.925	1.06	1	1	560	560	1.1E-7	6.1E-5	2.5E-7	3.4E-2	3.4E-2	20	37
4	0.94	1.06	1	1	1440	1440	1.1E-7	1.6E-4	2.2E-7	2.3E-1	2.3E-1	14	29
5	0.95	1.06	1	1	5200	5200	1.1E-7	5.6E-4	2.0E-7	2.9E+0	2.9E+0	12	23
6	0.95	1.06	1	1	10500	10500	1.1E-7	1.1E-3	2.0E-7	1.2E+1	1.2E+1	9	21
7	0.95	1.06	0.2	1	10500	10500	2.2E-8	2.3E-4	2.0E-7	2.4E+0	2.4E+0	13	24
8	0.95	1.06	0.05	1	10500	10500	5.4E-9	5.7E-5	2.0E-7	6.0E-1	6.0E-1	15	27

Table 4.10: List of calculated dimensionless numbers for each coreflood experiment along with breakthrough and ultimate recovery (%PV).

From the experimental results, it is clear that the overall recovery for viscous oil is a function of both viscosity ratios and injection rate and may not show a good correlation with either, individually. To compare the relation between the recoveries and viscosities or injection rates one could compare then against dimensionless numbers such as viscosity ratios and capillary number.

Before discussing the results, with respect to capillary number, it is important to clarify the definition of capillary number (*Nc*) used in this study. Capillary number is essentially a ratio of viscous forces over capillary forces and can be written as,

$$Nc = \frac{\left| \vec{K} \cdot \vec{\nabla} \psi \right|}{\sigma} \tag{4.1}$$

where $\vec{K}$ is the permeability tensor and $\vec{\nabla} \psi$ is the potential gradient vector and σ is the surface tension. For isotropic porous media, this equation can be simplified into,

$$N_c = \frac{K \Delta P}{\sigma L} \tag{4.2}$$

and by applying Darcy's law, one can further reduce equation 4.2 to,

$$Nc = \frac{v_{\text{int}} \mu}{\sigma} \tag{4.3}$$

where, v_{int} is the interstitial Darcy velocity. Either of the two definitions in eq. 4.2 or 4.3 are correct and can be used interchangeably as long as the viscosities of the two fluids involved remain comparable. At high viscosity ratios, the ΔP in equation 4.2 does not remain constant and drops sharply. As a result, capillary pressure is variable throughout the process. In equation 4.3, there are two complications; the viscosity of the fluid to be used and the definition of interstitial velocity. It is a general practice to use the viscosity of the injected fluid in eq. 4.3. However, it is more reasonable to use the viscosity of the most viscous phase irrespective of the injected fluid viscosity. Secondly, the actual value of interstitial velocity is not easy to estimate. The interstitial velocity in a water flood is given by,

$$v_{\text{int}} = \frac{Q}{A\phi(S_{oi} - S_{or})}. \tag{4.4}$$

However, the value of S_{oi}-S_{or} will change during the experiment and will also be affected by viscous fingering as shown in the micromodel experiments. To avoid such confusion, in this study we have consistently used the definition of *Nc* and interstitial velocity as shown in Figure 4.27

$$\text{Capillary number} = N_c = \frac{v_w \mu_w}{\sigma_{ow}}$$

$$v_w \text{ or } v = \frac{Q_w}{A\phi}$$

Figure 4.27: The definition of capillary number and interstitial velocity as used in this study.

Figure 4.28 and 4.29 show the recovery trends plotted against capillary number and viscosity ratio. There is clearly no trend with capillary number. For viscosity ratio, the data from constant injection rate experiments show a trend, but experiments with different flow rates do not fall on the same line. Based on the above discussion, a separate dimensionless number N_{c_visc}, called the modified capillary number was calculated and was defined as $v_w\mu_o/\sigma_{ow}$. Table 4.10 shows the calculated values of all the dimensionless numbers. The experimentally observed recoveries when plotted against N_{c_visc} (Figure 4.30) showed a better correlation with N_{c_visc} than N_c and μ_r, individually (Figure 4.28 and Figure 4.29). Even though the plot of Figure 4.30 should good relationship there is still some scatter and therefore it is clear that recovery will be correlated with a dimensionless number that is a combination of both capillary and viscous terms. At this point of time several combinations of dimensionless numbers were tried and best fit was observed for the product of N_{c_visc} and μ_r (Figure 4.31) . Recoveries for all the experiments when

plotted against $N_{c\_visc}\mu_r$ (Figure 4.29); fall on one straight line and show a good power law fit. This implies that if the viscosity of oil is used to define capillary number, the recovery data of Table 4.9 can be scalable with respect to the product of modified capillary number and viscosity ratio.

The term $N_{c\_visc}\mu_r$ can be expanded as,

$$N_{c\_visc}\mu_r = \left(\frac{v_w\mu_o}{\sigma_{ow}}\right)\left(\frac{\mu_o}{\mu_w}\right). \tag{4.5}$$

$N_{c\_visc}\mu_r$ can be represented in terms of only conventional capillary number, N_c and viscosity ratio, μ_r by simply multiplying and dividing by μ_w,

$$N_{c\_visc}\mu_r = \left(\frac{v_w\mu_o}{\sigma_{ow}}\right)\left(\frac{\mu_o}{\mu_w}\right)\times\left[\frac{\mu_w}{\mu_w}\right]. \tag{4.6}$$

Equation 4.6, can be rearranged to as

$$N_{c\_visc}\mu_r = \left(\frac{v_w\mu_w}{\sigma_{ow}}\right)\left(\frac{\mu_o}{\mu_w}\right)^2 = N_c\mu_r^2. \tag{4.7}$$

Thus, $N_{c\_visc}\mu_r$ becomes $N_c\mu_r^2$. To avoid confusion between the conventional form of capillary number and modified capillary number N_{c_visc}, $N_c\mu_r^2$ will be used instead of $N_{c\_visc}\mu_r$ from here on.

Typically, trapping number (not just the capillary number) is thought to influence the residual oil saturation in two phase flow. Trapping number is a vector sum of capillary number and Bond's number. Bond's number is a ratio of gravitational and capillary forces. Since all our experiments were conducted in gravity stable configuration, trapping number will be numerical sum of capillary and Bond's number. From the dimensionless numbers listed in Table 4.10, it can be observed that the value of the modified capillary number, N_{c_visc} is at least an order of magnitude higher than the

Bond's number. Therefore, Bond's number can be ignored in our experiments and only modified capillary number can be considered as the Trapping number (N_T). This may not be true for systems where the density difference between the injected and displaced phase is larger, such as gas floods. Therefore, one should be careful while applying this correlation for a system influenced by gravity.

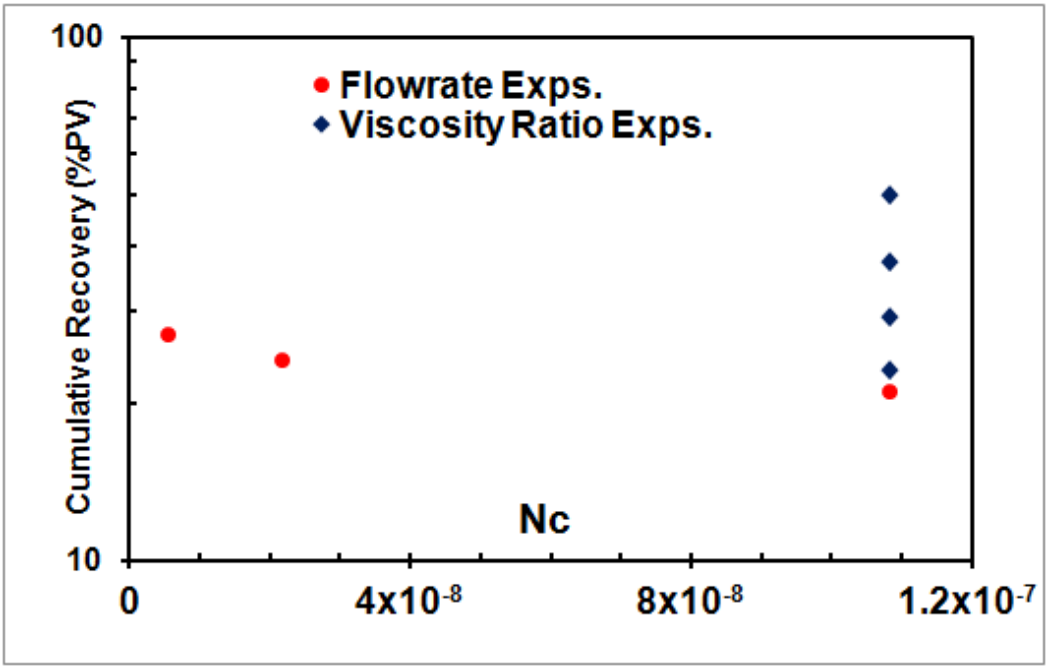

Figure 4.28: A plot showing no conclusive trend between experimental recoveries and capillary number

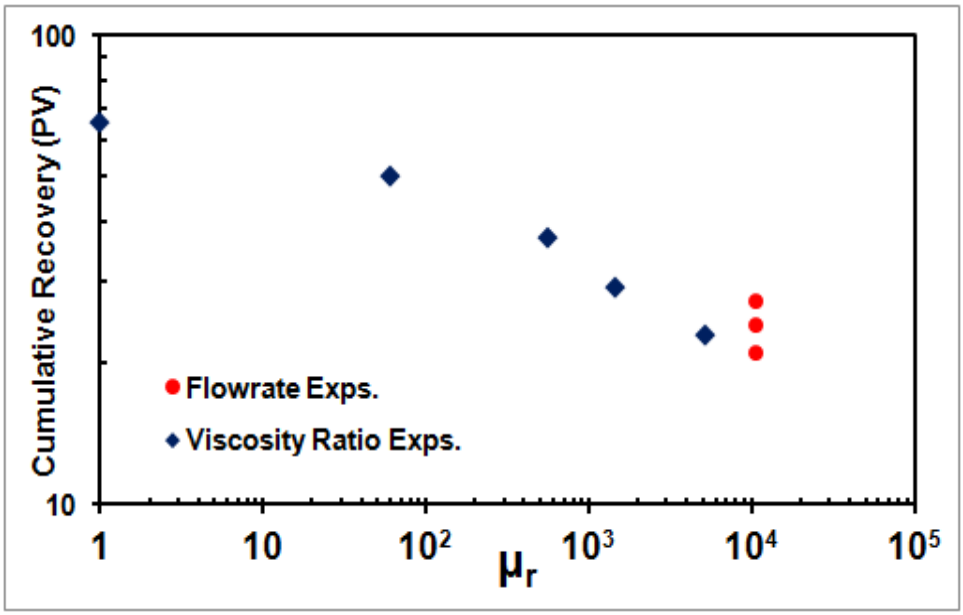

Figure 4.29: A plot showing no conclusive trend between experimental recoveries and viscosity ratio

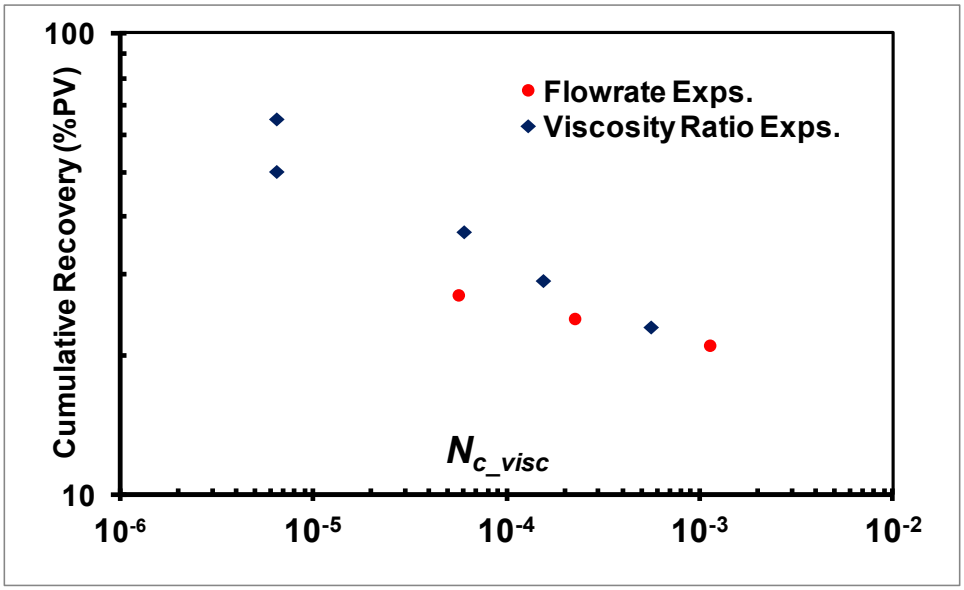

Figure 4.30: A plot showing a relatively better trend between experimental recoveries and modified viscosity ratio (N_{c_visc})

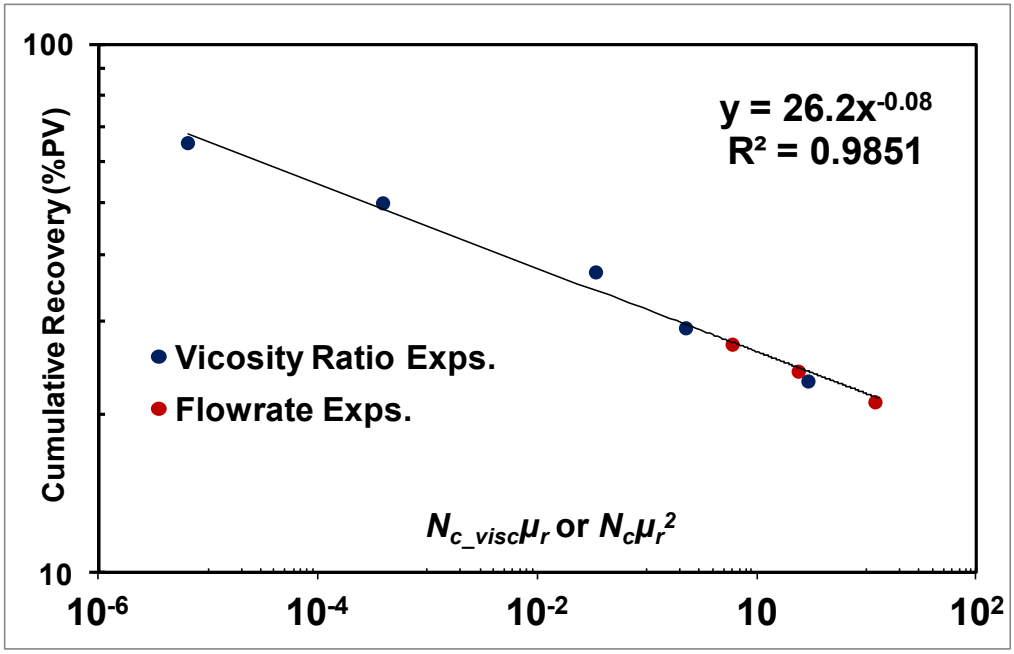

Figure 4.31: Experimental recovery vs. dimensionless number $N_c\mu_r^2$

Several other researchers who studied unstable displacement of viscous oils have conducted similar experiments at different viscosity ratios and flow rates. Baird (1978) conducted such experiments on sand packs for a 500 cp oil. Peters and Flock (1981) studied unstable displacement and correlated the breakthrough recoveries with the Instability number (I_{sc}). Mai (2008, 2009a 2009b) looked at the prospects of improving heavy oil recovery by low rate waterflooding. They published numerous results of low rate waterfloods conducted on oils of about 11000 cp. It would be interesting to see how these already published results compare with the results of the experiments conducted in this study. As Peters (1979) and Baird (1978) talked only about breakthrough recovery and the overall or ultimate recovery was not at all mentioned in their report; breakthrough recovery was chosen as the comparable parameter between all the results. Figure 4.32

shows that the breakthrough recoveries of experiments 1-8 also follow a power law relation with respect to $N_c\mu_r^2$.

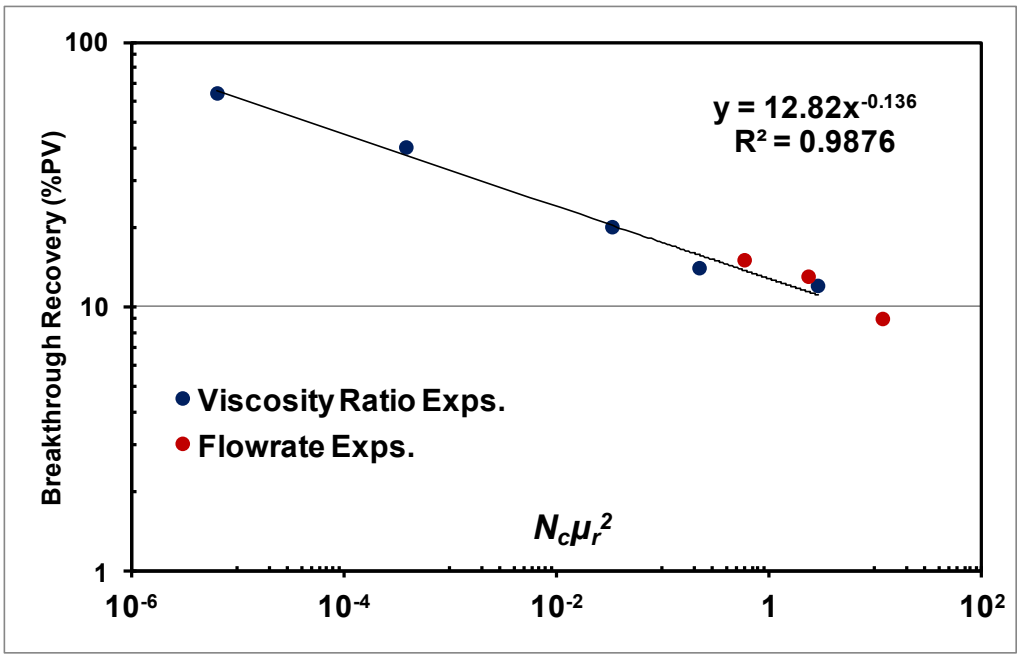

Figure 4.32: Plot of Breakthrough recovery vs. $N_c\mu_r^2$ for experiments 1-8.

Peters (1979) published results of about 35 unstable experiments; about half of them were conducted with 100% initial oil saturation and the other half had some connate water saturation. Only the results of the experiments with connate water saturation were used for comparison as all the experiments conducted in this study had some connate water saturation. Table 4.11, 4.12 and 4.13 shows the important experimental data from Baird (1978), Peters (1979) and Mai et al. (2008, 2009). As can be seen in Table 4.11, Baird (1978) focused on a viscosity ratio of 500 but varied the flowrate. Sand-packs of two different diameters (4.96 cm and 9.73 cm) were used and the permeability varied in the range of 9 – 12 Darcys.

L *(cm)*	D *(cm)*	Phi	K *(D)*	S_{wi}	V *(m/s)*	σ *(dyne/cm)*	μ_r	N_C	BT Recovery *(%PV)*	$N_C\mu_r^2$	$N_C\mu_r^2(D^2/K)$
107.15	4.96	36.5	15.4	9.8	3.55E-3	34.04	549.6	2.89E-8	24.55	8.74E-3	1.40E+6
107.95	4.96	36.9	17.3	11.26	1.40E-2	34.04	541.1	1.14E-7	21.45	3.35E-2	4.77E+6
108.61	4.96	36.7	16.4	11.45	2.26E-1	34.04	541.1	1.84E-6	17.45	5.39E-1	8.09E+7
107.73	4.96	37.2	13.75	12.5	4.17E-1	34.04	541.1	3.41E-6	14.83	9.97E-1	1.79E+8
107.75	4.96	36	8.43	11.44	1.15E+0	34.04	549.6	9.39E-6	14.42	2.84E+0	8.28E+8
107.31	4.92	36.1	7.56	10.58	2.91E-2	34.04	533	2.38E-7	23.13	6.76E-2	2.16E+7
107.72	4.96	36.8	8.54	11.86	7.88E-1	34.04	541.1	6.43E-6	14.25	1.88E+0	5.42E+8
106.92	4.96	38	16.72	12.46	6.81E-2	34.04	541.1	5.56E-7	18.3	1.63E-1	2.40E+7
107.81	4.92	35.5	8.66	9.7	2.22E-2	34.04	549.6	1.81E-7	21.47	5.48E-2	1.53E+7
107.42	9.73	37	16.46	10.2	3.63E-3	34.04	549.9	2.97E-8	14.43	8.97E-3	5.16E+6
107.34	9.73	37.1	18.28	10.8	1.45E-2	34.04	549.6	1.18E-7	22.31	3.57E-2	1.85E+7
107.01	9.73	37.4	11.33	11.73	2.16E-1	34.04	533	1.76E-6	13.42	5.00E-1	4.18E+8
107.17	9.73	36.2	10.39	10.34	4.16E-1	34.04	549.6	3.40E-6	13.33	1.03E+0	9.35E+8

Table 4.11: Experimental data of 13 unstable displacement experiments from Baird (1978) (M.Sc. Thesis)

Peters (1979) used two different viscosity ratios and a range of flow rates. The diameter of the sand pack was kept the same. Similarly, the data taken from Mai et al. (2008-2009) is from experiments at different flow rates and core diameters; all conducted at the same adverse viscosity ratio. The results of experiments 1-8 described in this chapter along with the data from Table 4.11-13 provide recovery data for a wide spectrum of viscosity ratios, flow rates, diameters, length of tube and permeability. It will be interesting to compare the published data with respect to the $N_c\mu_r^2$ correlation developed in this chapter.

L *(cm)*	D *(cm)*	Phi	K *(D)*	S_{wi}	V *(m/s)*	σ *(dyne/cm)*	μ_r	Nc	BT Recovery *(%PV)*	$N_c\mu_r^2$	$N_c\mu_r^2(D^2/K)$
22.9	4.8	38.98	16.43	11.2	9.85E-7	24.3	102	4.05E-8	38.74	4.22E-4	5.91E+4
23.6	4.8	36.37	18.36	8.66	8.45E-6	24.3	102	3.48E-7	38.25	3.62E-3	4.54E+5
112.8	4.8	38.38	21.89	9.18	4.00E-6	24.3	102	1.65E-7	39.67	1.71E-3	1.80E+5
23.7	4.8	38.94	18.93	11.34	6.31E-5	24.3	102	2.60E-6	31.31	2.70E-2	3.29E+6
110.5	4.8	38.91	20.5	10.83	1.97E-5	24.3	102	8.12E-7	35.94	8.45E-3	9.50E+5
110	4.8	37.61	21.91	10.48	4.08E-5	24.3	102	1.68E-6	36.79	1.75E-2	1.84E+6
23.6	4.8	37.49	14.19	15.26	1.97E-4	24.3	102	8.09E-6	25.76	8.42E-2	1.37E+7
116.1	4.8	34.66	18.28	8.32	7.09E-5	24.3	102	2.92E-6	29.54	3.04E-2	3.83E+6
113	4.8	39.62	22.99	8.61	7.75E-5	24.3	102	3.19E-6	28.23	3.32E-2	3.33E+6
115.9	4.8	35.85	19.22	12.53	1.03E-4	24.3	102	4.23E-6	30.34	4.40E-2	5.28E+6
22.8	4.8	37.52	16.23	11.2	4.58E-4	24.3	102	1.89E-5	21.26	1.96E-1	2.79E+7
110.4	4.8	37.42	20.85	10	1.97E-4	24.3	102	8.11E-6	24.13	8.43E-2	9.32E+6
115.9	4.8	37.8	18.54	9.29	1.95E-4	24.3	102	8.03E-6	30.15	8.35E-2	1.04E+7
110	4.8	38.11	22.5	8.91	3.22E-4	24.3	102	1.33E-5	26.07	1.38E-1	1.41E+7
112.8	4.8	35.48	22.72	9.92	4.85E-4	24.3	102	2.00E-5	23.42	2.08E-1	2.10E+7
23.4	4.8	34.61	14.51	11.03	4.44E-6	26.4	302	1.68E-7	32.04	1.53E-2	2.43E+6
23.6	4.8	38.6	20.87	10.15	7.96E-5	26.4	302	3.01E-6	20.03	2.75E-1	3.03E+7
23.7	4.8	35.44	12.11	12.02	4.85E-4	26.4	302	1.84E-5	10.49	1.68E+0	3.19E+8

Table 4.12: Experimental data of 18 unstable displacement experiments from Peters (1979) (PhD Dissertation)

L (cm)	D (cm)	Phi	K (D)	S_{wi}	V (m/s)	σ (dyne/cm)	μ_r	N_c	BT Recovery (%PV)	$N_c\mu_r^2$	$N_c\mu_r^2(D^2/K)$
17.2	3.81	36.61	2.76	10.33	1.33E-5	-	11500	1.62E-7	9.48	2.15E+1	1.13E+10
16.95	3.81	35.57	2.79	10.61	6.85E-6	-	11500	8.12E-8	10.75	1.07E+1	5.59E+9
17.55	3.81	35.51	2.79	10.34	6.87E-7	-	11500	8.12E-9	8.94	1.07E+0	5.59E+8
16.95	3.81	35.81	2.58	11.17	6.81E-6	-	11500	8.12E-8	8.37	1.07E+1	6.04E+9
114.8	8.89	34.80	3.86	8.13	1.23E-7	-	11500	3.84E-9	15.62	5.08E-1	1.04E+9
9.27	2.54	45.70	10	9.02	4.88E-6	-	11500	1.53E-7	11.83	2.02E+1	1.30E+9
21.1	3.63	45.00	9.05	10.27	4.39E-6	-	11500	1.37E-7	8.08	1.81E+1	2.64E+9
53.2	2.6	41.20	0.79	6.76	5.93E-6	-	11500	1.85E-7	6.53	2.45E+1	2.10E+10
53.2	2.6	41.20	0.77	4.90	1.05E-6	-	11500	3.28E-8	7.61	4.34E+0	3.81E+9
53.2	2.6	41.20	0.78	5.21	5.23E-7	-	11500	1.63E-8	9.48	2.16E+0	1.87E+9

Table 4.13: Experimental data of 10 unstable displacement experiments from various publications of Mai et al. (2008-09), BT Recovery is the breakthrough recovery.

The values of $N_c\mu_r^2$ corresponding to very experiment from the literature is listed in the respective Tables. Figure 4.33 shows the breakthrough recoveries of all the 41 different experiments reported in Table 4.11-4.13 plotted along with the experimentally measured breakthrough recoveries for the 8 experiments conducted in this study. The published data and our experimental data show a reasonable match with $N_c\mu_r^2$ despite the wide range of core diameters, permeability, flow rates, viscosity ratios and length. The published data compared here is also known to show good correlation with the instability number of Peters and Flock (1981). The instability number is defined as

$$I_{sc} = \frac{(M-1)(v-v_c)\phi\mu_w D^2}{C^*\sigma K_{wr}}, \tag{4.8}$$

where M is the mobility ratio $\left(\frac{K_{wr}\mu_o}{K_{or}\mu_w}\right)$, D is the diameter, μ_w is the viscosity of water, C* is the wettability number, σ is interfacial tension and K_{wr} is the water relative permeability. V_c is the critical velocity and is defined as $v_c = \frac{K_{wr}(\rho_w - \rho_o)g\cos\alpha}{\mu_w\phi(M-1)}$.

At high mobility ratios (M>>1) and small density difference ($M-1 \to M$ and $V - V_c \to V$), the instability number I_{sc} can be reduced to

$$I_{sc} = \left(\frac{K_{wr}\mu_o}{K_{or}\mu_w}\right)\frac{(v)\phi\mu_w D^2}{C^*\sigma K_{wr}}; \tag{4.9}$$

This can be further simplified to

$$I_{sc} = \left(\frac{\mu_o}{\mu_w}\right)\frac{(v)\phi\mu_w}{C^*\sigma}\left(\frac{D^2}{K_{or}}\right). \tag{4.10}$$

If μ_w in the numerator of I_{sc} is replaced by μ_o, the equation 4.10 will reduce to

$$I_{sc} = \left(\frac{\mu_o}{\mu_w}\right)\frac{\phi(v)\mu_o}{C^*\sigma}\left(\frac{D^2}{K_{or}}\right). \tag{4.11}$$

Multiplying and dividing by μ_w and rearranging will reduce equation 4.11 to

$$I_{sc} = \phi\left(\frac{\mu_o}{\mu_w}\right)\frac{(v)\mu_o}{C^*\sigma}\left(\frac{D^2}{K_{or}}\right)\left(\frac{\mu_w}{\mu_w}\right) = \mu_r^2 N_c\left(\frac{D^2}{K_{or}}\right)\left(\frac{1}{C*}\right)\phi \tag{4.12}$$

This explains why the published data shows good correlation with both $N_c\mu_r^2$ and Instability number (I_{sc}). In fact, we can include the dimensional scaling term in $N_c\mu_r^2$ to include the effect of diameter and permeability. Since, k_{or} is generally equal to 1. We can approximate K_{or} as the absolute permeability K. The new scaling function will now be,

$$\mu_r^2 N_c\left(\frac{D^2}{K}\right) \tag{4.13}$$

All the 41 experiments of Table 4.11-4.13 and the data of experiments 1-8 when plotted against the new scaling parameter, $\mu_r^2 N_c\left(D^2 / K\right)$ show an even better fit with much less scatter. Figure 4.34 shows the breakthrough recovery of experiments 1-8 and 41 experiments from published literature plotted against $\mu_r^2 N_c\left(D^2 / K\right)$.

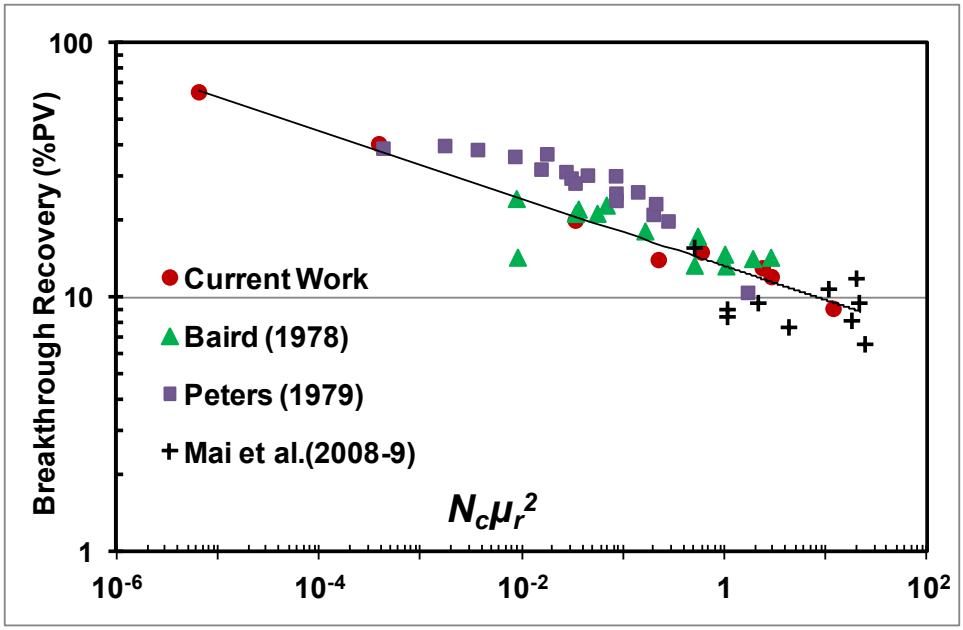

Figure 4.33: Plots of breakthrough recoveries of Exp. 1-8 and 41 different experiments from the literature plotted against $N_c\mu_r^2$

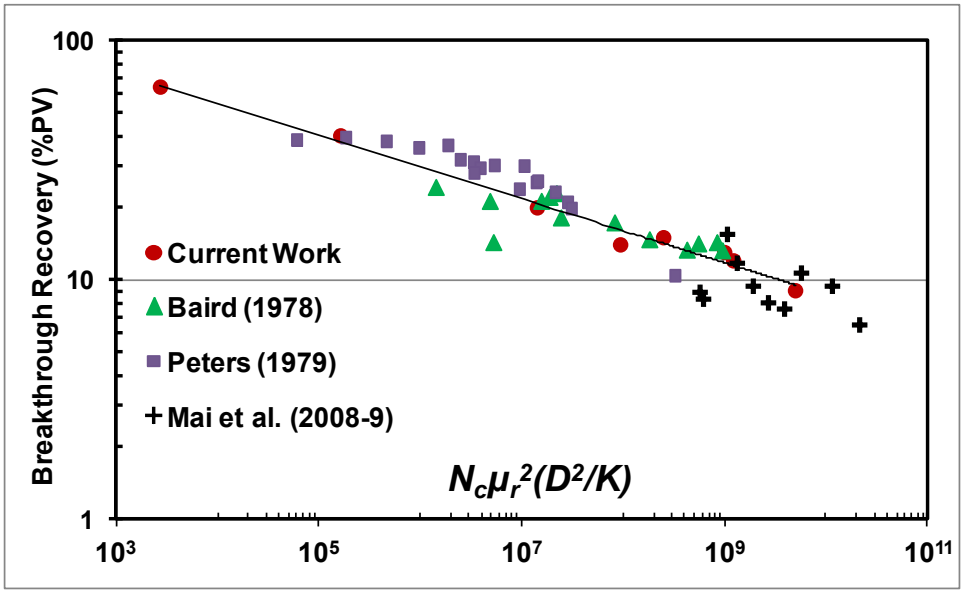

Figure 4.34: Plots of breakthrough recoveries of Exp. 1-8 and 41 different experiments from the literature plotted against $\mu_r^2 N_c \left(D^2 / K\right)$

Having compared the breakthrough recoveries and overall recoveries of experiments 1-8 with respect to $N_c\mu_r^2$ or $\mu_r^2 N_c\left(D^2/K\right)$, it is only fair to do a similar comparison with respect to the classical instability number. The values of Instability number corresponding to experiments 1-8 are listed in Table 4.14. As these experiments were conducted vertically the generic form of instability number (Eq. 4.4) was used. As claimed during the derivation of Eq. 4.9, the value of V_c in Table 4.14 is almost negligible for mobility ratios much greater than 1. Figure 4.35 shows a plot of breakthrough recovery versus instability number. The breakthrough recoveries of experiments with different viscosity ratio show a decent trend with the instability number but the slow injection rate experiments show a slightly different trend. From Table 4.14 we can confirm that the value of instability number is almost same for experiment number 8 and 3 but the breakthrough recoveries are not the same (20% and 15%). This is because the instability number does not capture the fact that the effect of viscosity ratio is of an order of magnitude higher than the effect of capillary number. Instead it gives equal weight to both the capillary and viscous terms. Instability number is more suitable to predict the breakthrough recovery trend with different injection rate for a given viscosity ratios or mobility ratios. As can be seen in Figure 4 of Peters and Flock (1981), each viscosity ratio has its own recovery trend (Figure 4.36) however, for our $\mu_r^2 N_c\left(D^2/K\right)$ correlation all the viscosity ratios and flow rates converge onto one trend-line. A mechanistic explanation of $N_c\mu_r^2$ has been provided in Appendix B using a pore doublet model.

#	$\Delta\rho$	V (ft/day)	μ_r	k_{rw}	M	v (m/s)	v_c (m/s)	R_{bt} (%PV)	$I_{sc} = \frac{(M-1)(V-V_c)\mu_w D^2}{C^* \sigma K_{wr}}$
1	0.37	1	1	0.5	0.5	3.47E-6	-6.13E-08	64	-2760.58
2	0.16	1	60	0.1	6	3.47E-6	3.2E-08	40	2239.728
3	0.13	1	560	0.06	33.6	3.47E-6	2.48E-09	20	24547.19
4	0.12	1	1440	0.035	50.4	3.47E-6	8.5E-10	14	63796.79
5	0.11	1	5200	0.011	57.2	3.47E-6	2.15E-10	12	230973.9
6	0.11	1	10500	0.007	73.5	3.47E-6	1.06E-10	9	468244.8
7	0.11	0.2	10500	0.007	73.5	6.94E-7	1.06E-10	13	93637.5
8	0.11	0.05	10500	0.007	73.5	1.74E-7	1.06E-10	15	23398.63

Table 4.14: Data of coreflood experiments 1-8 required to calculate the instability number along with the calculated instability number. R_{bt} is the breakthrough recovery.

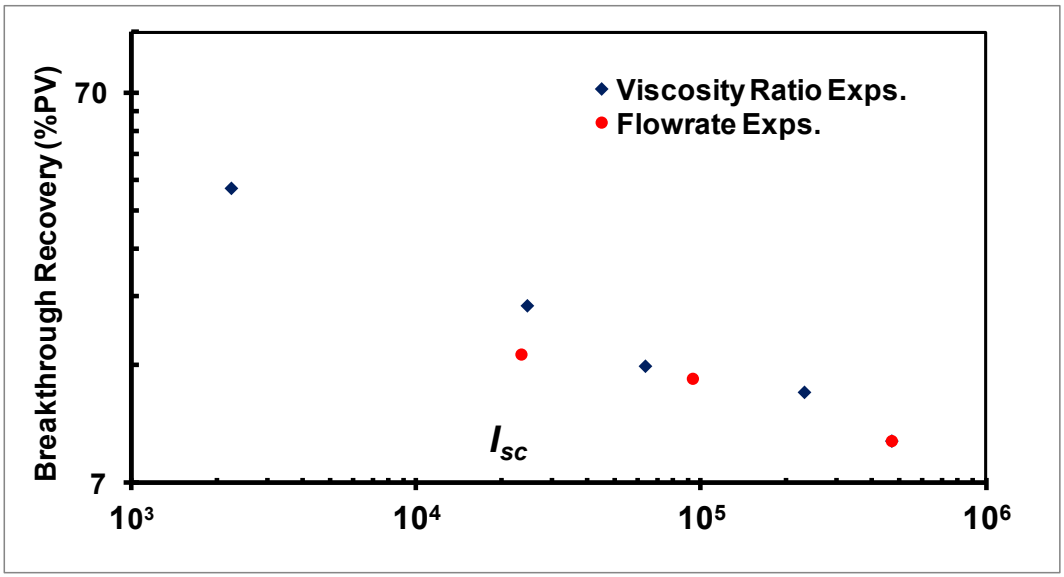

Figure 4.35: Plot of breakthrough recoveries of coreflood experiment 1-8 plotted against instability number.

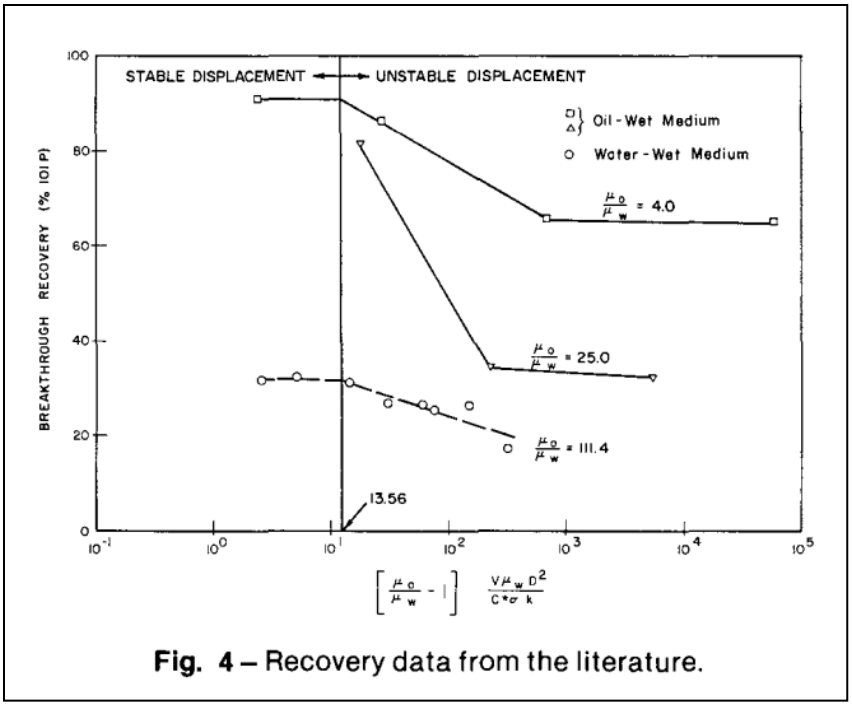

Fig. 4 – Recovery data from the literature.

Figure 4.36: A chart presented in Peters (1981) showing three different trend lines for three different viscosity ratios.

From the published data provide in Table 4.11 – 4.13, a value of instability number can be calculated for each of the 41 experiments. Table 4.15 shows the breakthrough recovery and instability number for this data. The breakthrough recovery and the instability number data of all the 49 experiments (41 from literature and 8 from this study) were plotted on the same chart as shown in Figure 4.37. The scatter in the data is much higher than that observed with, $\mu_r^2 N_c \left(D^2 / K\right)$ in Figure 4.34. The instability number does provide the luxury of the unknown wettability parameter, C*. In Figure 4.37, one can manipulate the value of C* in each case to make all the dataset coincide. To avoid this, wettability number (C*) is ignored or assumed to be 1 for each case. All the data (from literature and current study) used for this comparison was measured on relatively similar high permeability and water-wet system. Thus, the variation in between

the wettability parameter C* should not be high enough to influence the overall trend. For water-wet systems, C* value is usually around 300.

On closer analysis, Figure 4.37 clearly shows that the instability number predicts a separate recovery trend for each viscosity/mobility ratio. The wide range of data presented in Figure 4.36, orients itself in a layered manner with the top-most layer consisting of data corresponding to viscosity ratio of 100 (Peters, 1979), followed by the Baird's data at a viscosity ratio of 500 and Mai's data at the bottom corresponding to viscosity ratio of 11500. The recovery trend for Experiment 1-8, which were conducted on a wider viscosity ratio range, passes through all the three layers. Figure 4.38 explicitly illustrates the layered nature of Figure 4.36. In Figure 4.39, the plots of breakthrough recoveries versus instability number and breakthrough recoveries versus $\mu_r^2 N_c \left(D^2 / K\right)$ are presented side by side for better comparison. As mentioned earlier, the new correlation $\mu_r^2 N_c \left(D^2 / K\right)$, shows a better fit with all the data and the value of correlation coefficients improves from $R^2 = 0.53$ to about 0.9.

Baird (1978)		Peters (1979)		Mai (2008-09)	
Breakthrough Recovery *(%PV)*	***I_{sc}***	**Breakthrough Recovery *(%PV)***	***I_{sc}***	**Breakthrough Recovery *(%PV)***	***I_{sc}***
24.55	2.54E+3	38.74	5.74E+2	9.48	9.82E+5
21.45	8.80E+3	38.25	4.41E+3	10.75	4.86E+5
17.45	1.49E+5	39.67	1.75E+3	8.94	4.86E+4
14.83	3.29E+5	31.31	3.19E+4	8.37	5.25E+5
14.42	1.50E+6	35.94	9.22E+3	15.62	9.05E+4
23.13	4.05E+4	36.79	1.78E+4	11.83	1.13E+5
14.25	1.00E+6	25.76	1.33E+5	8.08	2.30E+5
18.3	4.42E+4	29.54	3.71E+4	6.53	1.82E+6
21.47	2.78E+4	28.23	3.23E+4	7.61	3.31E+5
14.43	9.37E+3	30.34	5.12E+4	9.48	1.63E+5
22.31	3.36E+4	21.26	2.71E+5		
13.42	7.83E+5	24.13	9.05E+4		
13.33	1.70E+6	30.15	1.01E+5		
		26.07	1.37E+5		
		23.42	2.04E+5		
		32.04	8.03E+3		
		20.03	1.00E+5		
		10.49	1.05E+6		

Table 4.15: Experimental breakthrough recovery and the calculated instability number for the data set of all the 41 experiments taken from literature, C* was assumed to be 1.

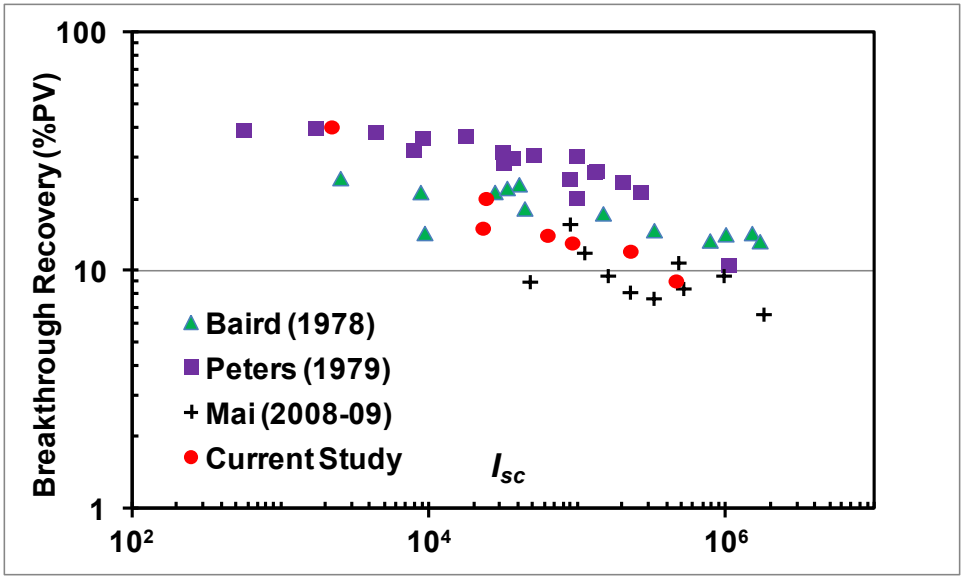

Figure 4.37: Plot of experimental breakthrough recovery vs. instability number for the current study and the experiments from published data.

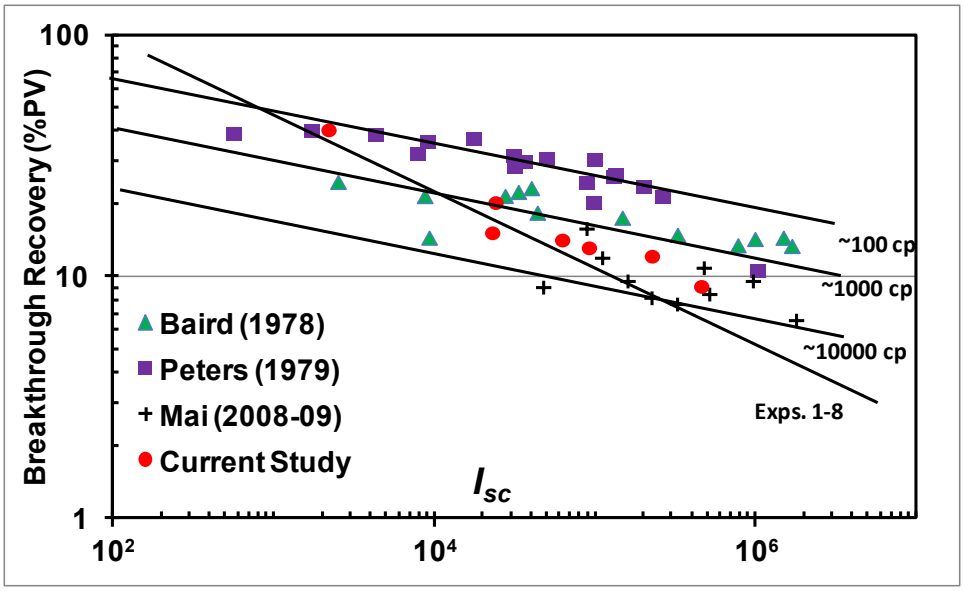

Figure 4.38: An illustration of layered nature of the plot of experimental breakthrough recovery vs. instability number in Figure 4.35.

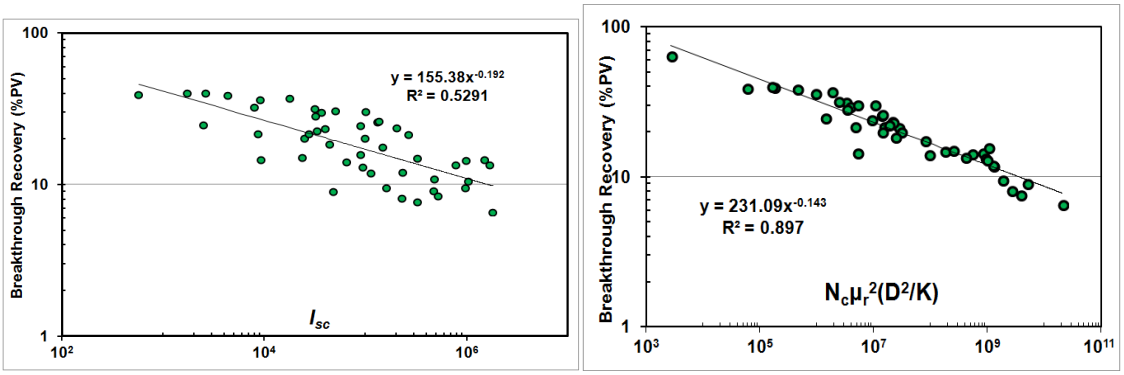

Figure 4.39: Plots of breakthrough recovery with $\mu_r^2 N_c \left(D^2 / K\right)$ and I_{sc} presented side by side along with the correlation factor.

Additional data

As shown in the previous section, the dimensionless number $\mu_r^2 N_c \left(D^2 / K\right)$ proved to be a good criterion for predicting and scaling of the breakthrough recoveries of the water flood. To compare the correlation with some polymer floods conducted on viscous oils, experimental results of Kumar (2013) and Koh (2015) were used. Kumar (2013) conducted a set of water flood and polymer flood for 330cp and 10000 cp oils. Koh (2015) conducted several different water floods and polymer floods on oils with a wide range of viscosity ratios. The data extracted from the dissertation is listed in Table 4.16; polymer floods are denoted by PF and the viscosity of the polymer is taken at the approximate shear rate predicted by the authors for their cores/sandpacks.

		D(cm)	K(Darcy)	v (ft/day)	μ_w	μ_o	μ_r	N_c	$N_C\mu_r^2(D^2/K)$	R_{bt} *(%PV)*
Koh (2015)	WF	2.54	7.9	13	0.48	80	166.7	6.77E-07	1.54E+08	14
	PF	2.54	7.9	1	16	80	5.0	1.74E-06	3.54E+05	45
	WF	4.8	6.65	14	0.48	120	250.0	7.29E-07	1.58E+09	17
	PF	4.8	6.65	1	28	120	4.3	3.04E-06	1.93E+06	43
	WF	2.54	7.31	14	0.48	250	520.8	7.29E-07	1.75E+09	17
	PF	2.54	7.31	1	90	250	2.8	9.77E-06	6.65E+05	27
	WF	3.81	0.227	3.3	0.57	72	126.3	2.04E-07	2.08E+09	16
	WF	3.81	0.022	5.6	0.51	8	15.7	3.10E-07	5.03E+08	24
	WF	3.81	6.08	5	0.66	1050	1590.9	3.58E-07	2.16E+10	8
	PF	3.81	2.3	1	14.4	3.5	0.2	1.56E-06	5.83E+03	50
	WF	3.81	2.2	1	0.44	3.5	8.0	4.77E-08	1.99E+05	29
	PF	3.81	2.2	1	13.8	3.5	0.3	1.50E-06	6.36E+03	45
	WF	2.54	6.913	5	0.66	1230	1863.6	3.58E-07	1.16E+10	6
	WF	3.81	4.916	5	0.66	1111	1683.3	3.58E-07	3.00E+10	6
	WF	3.81	5.319	5	0.66	1290	1954.5	3.58E-07	3.73E+10	7
Kumar (2013)	WF	1.68	28.56	1	0.98	10000	10204.1	1.06E-07	1.09E+10	8
	PF	1.397	24.18	1	100	10000	100.0	1.09E-05	8.76E+07	21
	WF	1.7018	22.6	1	1	330	330.0	1.09E-07	1.51E+07	30
	PF	1.7018	26.17	1	1100	330	0.3	1.19E-04	1.19E+04	55

Table 4.16: Data of water flood and polymer flood extracted from Kumar (2013) and Koh (2015).

Data from the 19 experiments listed in Table 4.16 when plotted on the data of the previous 49 data points, show a good match as well. Figure 4.40 shows the previous 49 data points along with the data points from Kumar (3013) and Koh (2015). Polymer floods can be compared separately in Figure 4.41. Both the polymer flood and water flood data for all the 68 experiments show good correlation with respect to the scaling number, $\mu_r^2 N_c \left(D^2 / K\right)$.

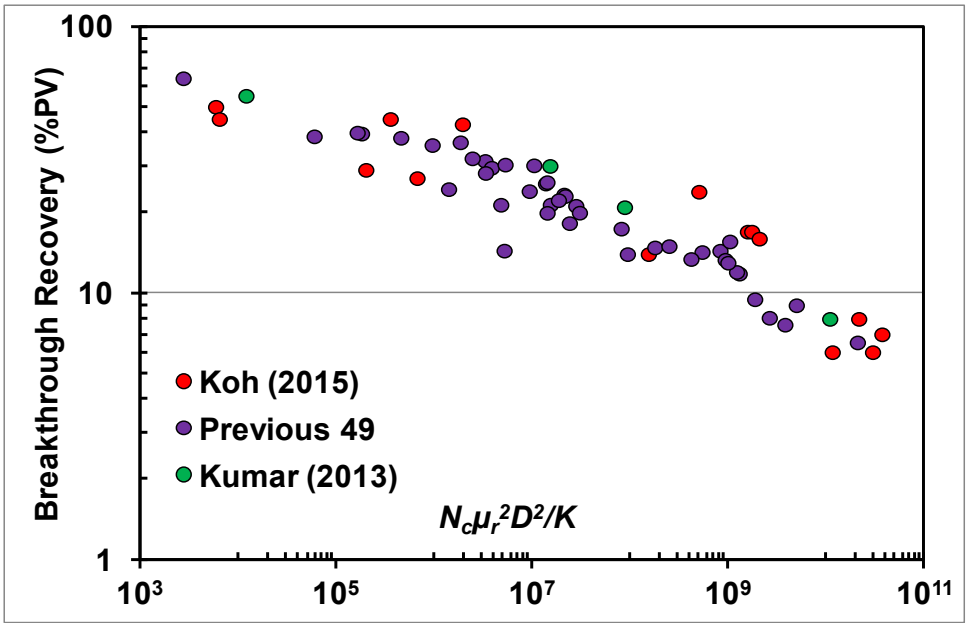

Figure 4.40: Plot of experimental results of Kumar (2013) and Koh (2015) with the previous 49 data points wrt. $\mu_r^2 N_c \left(D^2 / K\right)$.

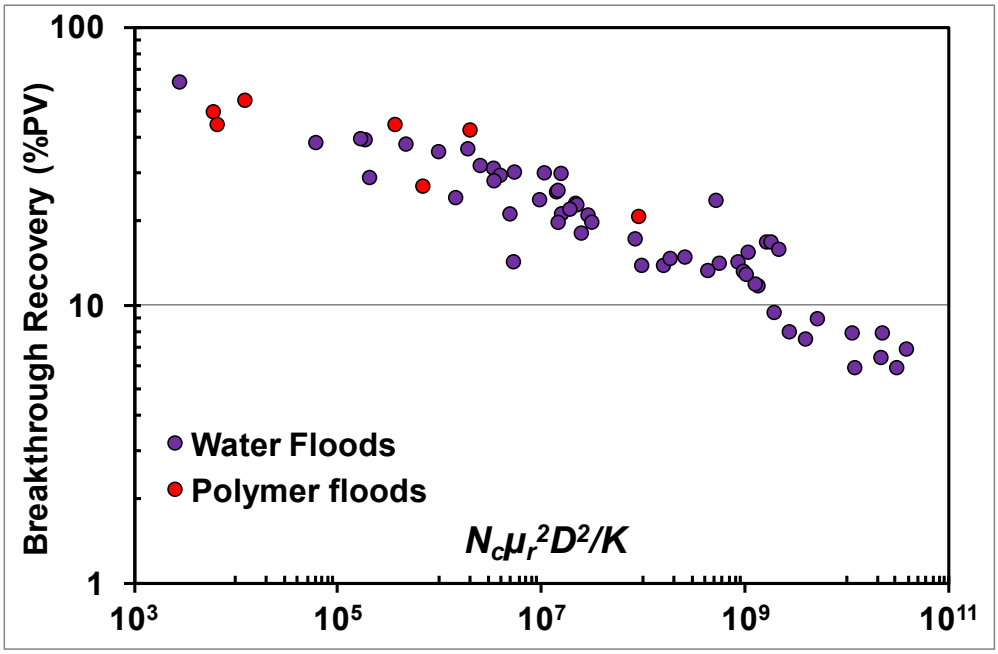

Figure 4.41: Plot showing the breakthrough recoveries of all the 61 water flood experiments and 7 polymer flood experiments.

Summary of Unstable Corefloods

From these experiments, it can be concluded that in the unstable regime, two-phase oil-water flow in porous media has a significant dependence on both flowrate and viscosity ratio. A new correlation connecting both viscosity ratio and capillary number was developed as $\mu_r^2 N_c \left(D^2 / K\right)$. The new correlation shows good match for both ultimate recovery and breakthrough recovery. The breakthrough recovery trend was not just observed for the 8 experiments conducted in this research but also for the 68 other water flood and polymer flood experiments published in the literature. The correlation is comparable to the instability number of Peters and Flock (1981) but shows better correlation for the same data set. Therefore, $\mu_r^2 N_c \left(D^2 / K\right)$ can be a useful dimensionless scaling parameter to predict the ultimate and breakthrough recovery for unstable displacement. Another advantage of $\mu_r^2 N_c \left(D^2 / K\right)$ is that is based on the all the known parameters and do not requires experimental data like end point relative permeability or a hypothetical wettability number. Although, the scaling parameter was derived purely empirically, a mechanistic explanation can be provided by considering the competition between time scales of imbibition and viscous flows rather than the competition of the forces involved (see Appendix – B).

From simulation point of view, the micromodel experiments have shown that most fingers are only a few pores wide and would require very fine grid simulations to be captured explicitly. Capturing such detailed fingering could be possible at the core scale, but at a field or pilot scale this would prove to be computationally very expensive. Also, at the field scale it is not critical to capture every finger in detail. At larger scale, an averaged model that mimics the trend with a large grid size will be much faster and technically more desirable. In the next chapter, two new models have been discussed:

(1) a simplified pore network model that is capable of capturing the detailed fingering pattern for all viscosity ratios at the micromodel scale and

(2) an averaging scheme called the lumped finger model that helps in capturing the effect of these fingers at larger scale without the need of computationally expensive fine grid simulations were proposed.

CHAPTER 5: MODELING AND SIMULATIONS

Modeling of the experimental results is critical for prediction and up-scaling. In this chapter, results of the experiments discussed in Chapter 4 have been modeled and simulated. A novel yet simple pore network model was developed to simulate the fingering pattern observed during the micromodel experiments. The simulations were compared to the experiments and a generalized correlation was developed. The knowledge from pore network model was then used to develop a lumped fingering model to simulate effects of viscous fingering at a larger scale. The lumped model ignores the details at the finger scale, but captures the effect of viscous fingering on relative permeability at the larger scale. The lumped model was then used to simulate the results of coreflood experiments listed in Table 4.8 of Chapter 4.

5.1 PORE NETWORK MODEL

5.1.1 Introduction to Network Models

Modeling unstable displacements in porous media has always been a challenge. The difficulty with capturing instability arises due to the use of large grid blocks (much larger than viscous fingers) and the large numerical dispersion/grid orientation error associated with most conventional finite difference simulation techniques. Felgueroso and Juanes (2008) pointed out an inadequacy in Richard's law while studying fingering in water seepage through dry soil. They introduced local and non-local energy terms in the Richard's equation to better predict the channeling of water in unsaturated porous media. Some authors have suggested stochastic or probabilistic methods for simulation of viscous fingers (Hughes and Murphy, 1987, 1988). For modeling instabilities, stochastic and probabilistic methods generally perform better as they have an inherent randomness

and perturbations that incites instabilities that may grow or dampen depending on the probabilistic scheme.

Most probabilistic or randomness based models were developed or were inspired by observations at molecular or pore–scale, but the analogies have been extended to larger scales as well. One of such examples is Diffusion Limited Aggregation (DLA). DLA was introduced by Written and Sanders (1983) as a random walk model to describe formation of aggregates in nature. DLA mimics the process where particles (molecular scale) undergoing random Brownian motion cluster together to form aggregates. Such aggregates occur naturally in several processes such as electro-deposition, formation of clouds and snowflakes, mineral deposition, dielectric breakdown. Similar patterns have also been observed on larger scales like river flow patterns, mountain range formation and viscous fingering in porous medium. Patterson (1984) observed that DLA produced structures that resemble viscous fingers in the limit of infinite viscosity ratio. A limitation of DLA was its applicability only in the infinite viscosity ratio. As an alternative some investigators introduced a sticking probability in DLA to make the structure of the fingers qualitatively different. The width of the fingers became wider as the sticking probability was decreased, but even for very low sticking probability the model fails to predict the displacement patterns expected at low viscosity ratios.

Another mathematical model that produces patterns similar to DLA was introduced by Niemeyer et al. (1984) for modeling dielectric breakdown (DBM) in gases. Due to conceptual and qualitative similarity between DLA, DBM and viscous fingering, DBM is used here as an analogy for unstable flows in porous media (Maloy et al., 1985, Sheerwood et al., 1986). The dielectric breakdown and immiscible flow in porous media have a great degree of similarities. Therefore, a clear understanding of the dielectric breakdown may help us in better understanding and modeling of viscous unstable flow in

porous media. In this research, the existing DBM was modified to develop a new simplified pore network model that is capable of predicting viscous fingering for finite viscosity ratios. At low viscosity ratios, a stable, uniform Buckley-Leverett type displacement front is obtained. At adverse, yet finite viscosity ratios, instabilities arise and grow with time. At very adverse viscosity ratio limits, the model produces DLA type fractal fingers.

5.1.2 Dielectric Breakdown Model (DBM)

The dielectric breakdown model as proposed by Niemeyer et al (1984) and the various similarities between dielectric breakdown and flow in porous media are listed in this section. Niemeyer et al. (1984) developed a stochastic model to simulate discharge patterns of dielectric breakdown. They assumed that the growth probability is influenced by the local electric field rather than just the absolute potential. In this model, the domain is divided into grids (consisting of sites and bonds) and the central site is assumed as one of the electrodes. The other electrode is modeled as a circle at a large enough distance, so the pattern grows radially outwards. At each step, the electrical potential is calculated by solving the discretized Laplace equation (equation 5.1). The boundary condition $\phi = 0$ is maintained at the central electrode and $\phi = 1$ at the external circle.

$$\nabla^2 \emptyset = 0. \tag{5.1}$$

The discrete forms of Eq. 5.1 can be written as

2D:

$$\emptyset_{i,j} = \frac{1}{4}\left(\emptyset_{i-1,j} + \emptyset_{i+1,j} + \emptyset_{i,j-1} + \emptyset_{i,j+1}\right) \tag{5.2}$$

3D:

$$\emptyset_{i,j,k} = \frac{1}{6}\left(\emptyset_{i-1,j,k} + \emptyset_{i+1,j,k} + \emptyset_{i,j-1,k} + \emptyset_{i,j+1,k} + \emptyset_{i,j,k-1} + \emptyset_{i,j,k+1}\right). \tag{5.3}$$

Using equation 5.2 or 5.3, the new potential is calculated based on the boundary conditions. At the first time step, owing to symmetry, the potential of all the sites next to the central electrode are the same. Therefore, the first invaded cell is always chosen randomly. The invaded cell becomes a part of the central electrode and is assigned a potential of $\phi = 0$. This newly added site distorts the symmetry and the potential field also gets distorted. The new potential field is calculated using equation 5.2 iteratively. At each step, one site is added adjacent to an occupied site on the discharge pattern depending on its probability. The probability of invasion or the growth probability of sites adjacent to the invaded grids is calculated using equation 5.4. The denominator of the equation is the sum of all the neighboring sites and η is a parameter of the system. The purpose of η is to introduce non-linearity in the system. The probability of growth should be proportional to the potential but it may not always be linearly related. A probability P(*ij* → *i'j'*) is associated with the transport of electron from an occupied site (*ij*) at the edge of the discharged region to an adjacent site (*i'j'*).

$$P(ij \rightarrow i'j') = \frac{(\emptyset_{i'j'})^{\eta}}{\Sigma(\emptyset_{i'j'})^{\eta}} \quad . \tag{5.4}$$

The calculated probability of each site is then multiplied by a random number between 0 and 1 to introduce randomness in the system. The site with the maximum probability is chosen as the new invaded site. The use of probability and the invasion of one site at a time is a major difference in between the DBM and a conventional continuum based simulator. In a conventional simulator, the potentials are calculated over the whole grid and all the neighboring sites are invaded by an amount proportional to their potential. This fades all the fluctuations/perturbations that are caused due to small scale heterogeneities and might develop into viscous fingers.

The process of invasion and re-calculation of probability is repeated until the discharge pattern hits the external electrode. Niemeyer et al. (1984) focused their work on a particular case with η =1. Parameter η =1 implies that the growth probability is proportional to local potential field. The computed patterns for η =1 yielded the same fractal dimension as experimental discharge image. Figure 5.1 shows the picture of the experimental and simulated dielectric breakdown as presented by Niemeyer et al. (1984).

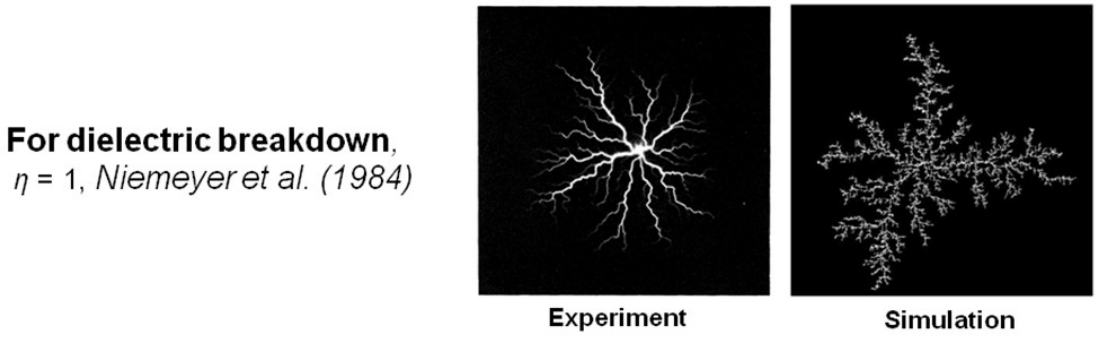

Figure 5.1: Experimental and simulated dielectric breakdown from Niemeyer et al (1984) for η =1.

Pietronero et al. (1988) explained the origin of the stochastic nature and the power-law dependence of the model through ionization of gas molecules and propagation of electrons (Figure 5.2a). They describe that the process of discharge propagation requires ionization which occurs only above a minimum excitation potential. Ionization creates electrons that move along the field and make collisions with other molecules. These collisions can lead to generation of new electrons and propagate the discharge further or could result in the absorption of the electron, causing a branch of electric discharge to fade out (Figure 5.2a). The elastic collision is also a probability, where an

electron simply bounces of a molecule without adding a new electron or getting adsorbed. The elastic collision is not of great interest in the DBM context.

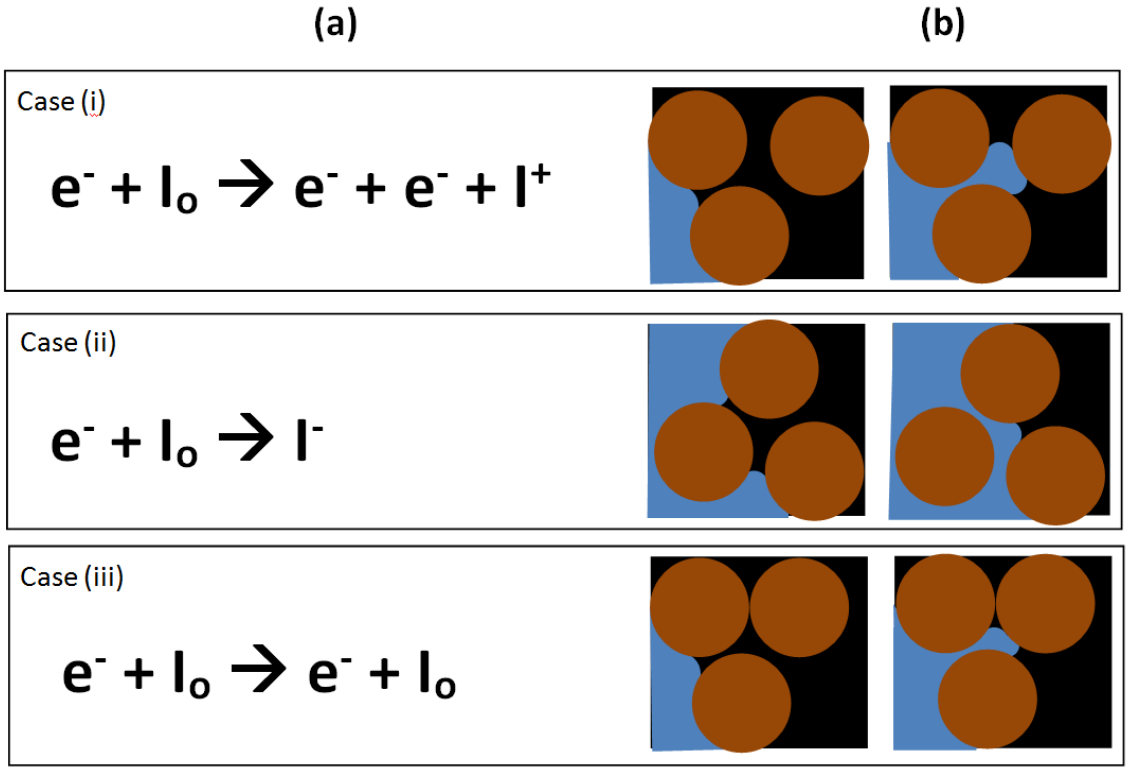

Figure 5.2: (a) Schematic showing the three possibilities of electron propagation during dielectric breakdown as described by Pietronero et al. (1988) and (b) some analogous case for a meniscus movement in a porous medium

Figure 5.2(b) shows the similarity in between pore scale interface propagation during drainage to electron propagation during electrical discharge. As in ionization, the meniscus invades one pore throat when the pressure is above the invasion capillary pressure of the throat. This meniscus can make a jump through a pore throat (Haines jump) and then branch into two menisci after crossing the adjacent pore body. This leads to generation of a new meniscus (case i). Two menisci can merge into one meniscus at a

pore body, causing a loss of meniscus (case ii). Lastly, a meniscus can make a Haines jump without adding a new meniscus (case iii). Pietronero et al. (1988) proposed that the relationship between the local electric field and growth probability for a breakdown is linear ($\eta = 1$) because it depends on the velocity of electrons from one point to the other and the subsequent electron discharge occurs spontaneously. For a porous medium, the flow of the fluid is definitely proportional to the pressure gradient, but each pore throat has a different invasion pressure and adds resistance to the flow. The flow also depends on the viscosities of the fluids and the wettability of the pore walls. Therefore, the relationship should be non-linear. In DBM for $\eta = 0$, the probability becomes unity for every case and therefore the growth probability is same all over the interface. The interface will therefore grow with an integral fractal dimension of 2. As the parameter η is varied, the simulated patterns changes from a uniform 2 dimensional structure at $\eta = 0$ to a complex structure with fractal dimension at $\eta = 1$. This observation is analogous to two-phase immiscible displacements in porous media where the displacement fronts change from being stable (D = 2) at smaller viscosity ratios ($\mu_r < 1$) to unstable, fractal-like at very high viscosity ratios, as shown in Figure 4.20 We intend to introduce the effect of finite viscosity ratio through the parameter 'η' in our extended dielectric breakdown model. Other similarities between viscous fingering and dielectric breakdown are listed below;

- Like dielectric breakdown, viscous fingers at high viscosity ratios also display fractal nature.
- In both the processes, particles flow from high potentials to low potentials along a path of least resistance. Dielectric breakdown is essentially just an extreme case of viscous fingering, where high mobility particles (electrons) are discharged into a medium that offers infinite resistivity (air).

- Dielectric discharge would not occurs below a certain potential called the critical excitation potential (E_c) and a non-wetting phase would not enters a pore throat below the critical capillary pressure (P_c).
- Like dielectric breakdown, viscous fingering also has a higher growth probability at the tip (Niemeyer et al., 1984).
- It is known that the region in between two fingers gets screened off and very little invasion could occur in this region. This phenomenon can be compared to Faraday's screening effect, where a conductive cage creates a region inside it where electric potential gets totally screened (Niemeyer et al., 1984).

5.1.3 Extended DBM

Considering all the theoretical and mathematical similarities in between DBM and the flow in porous medium, an extension of DBM can be suggested. For two-phase, immiscible, incompressible displacement in homogeneous porous media, the pressure field is described by the following equations (Lake, 1989),

$$\nabla^2 P_w = 0; P_{w1} = P_{injection} \text{ and } P_{w2} = P_{interface} \quad (5.5)$$

$$\nabla^2 P_o = 0; P_{o1} = P_{interface} \text{ and } P_{o2} = P_{outlet} \quad (5.6)$$

where P_w is the pressure in the water phase, $P_{injection}$ is the pressure at the injector, $P_{interface}$ is the pressure at the oil-water interface, P_o is the pressure in oil phase and P_{outlet} is the pressure at the outlet. In equation 5.5 and 5.6, by assuming that the pressure of water phase and oil phase at the interface are same ($P_{w2}= P_{o1}= P_{interface)}$ the capillary pressure is ignored. Even with this assumption, this set of equation is not easy to solve as the pressure at the interface and the location of the interface are both variable and unknown at each time step. If we ignore the pressure drop in the injected fluid/water phase and

only solve for the pressure gradient in the displaced phase, the only remaining equation is,

$$\nabla^2 P_o = 0;\ P_{o1} = P_{interface} \text{ and } P_{o2} = P_{outlet} \tag{5.7}$$

It is evident that Eq. 5.7 is similar to Eq. 5.1, i.e., the pressure field in viscous oil phase is similar to the potential field in the uninvaded region of DBM. To normalize the boundary conditions in between zero and one, a pseudo potential term can be defined ($\bar{\emptyset}_o$) as,

$$\bar{\phi}_o = \frac{P_o(t) - P_{interface}}{P_{outlet} - P_{\text{int}erface}}; \tag{5.8}$$

This converts Eq. 5.7 to

$$\nabla^2 \bar{\phi}_o = 0;\ \bar{\phi}_{o1} = 0 \text{ and } \bar{\phi}_{o2} = 1 \tag{5.9}$$

As $P_{interface}$ is a variable that changes at every time-step, $\bar{\phi}_{o1} = 0$ and $\bar{\phi}_{o2} = 1$ are the normalized constant pressure boundary conditions at a particular time step at the injector and producer respectively. The potential field in the displaced fluid is calculated by iteratively solving the equation and the boundary conditions shown in Eq. 5.9. The process is repeated for each grid and iterated until the values do not change beyond a certain assigned value of tolerance ($<10^{-4}$). The model is also tested for a smaller value of tolerance (10^{-7}), this slows down the simulation considerably and does not change the results qualitatively. After the iterations converge and the new potential field is calculated, Eq. 5.4 is used to assign a probability of growth to each grid in the vicinity of the interface. This probability is multiplied with a random number to account for local fluctuations in pore throats. The jump with the highest probability is executed and the process is repeated again. While using Eq. 5.4, different values of η were used. The value of the power exponent η is changed from 1 to values less than one to generate variety of different patterns corresponding to different viscosity ratios.

To understand the rationale behind the use of power exponent η to mimic the changes in viscosity ratio consider a flat interface of 100 neighboring sites with the boundary conditions of eq. 5.9. In such a system, invasion of the central site will change the potential field and hence growth probability around it. Figure 5.3 shows the change in growth probability distribution along the interface caused by the invasion of one particle for different values of η (or μ_r). For η = 1; the growth probability is highest around the center (initial perturbation) and hence the tip grows faster. As the value of η decreases the growth probability distribution curve flattens and the probability of growth is almost uniform for $\eta = 10^{-4}$. This suggests that the effects of perturbation are less pronounced for smaller values of η and therefore the perturbations fades out.

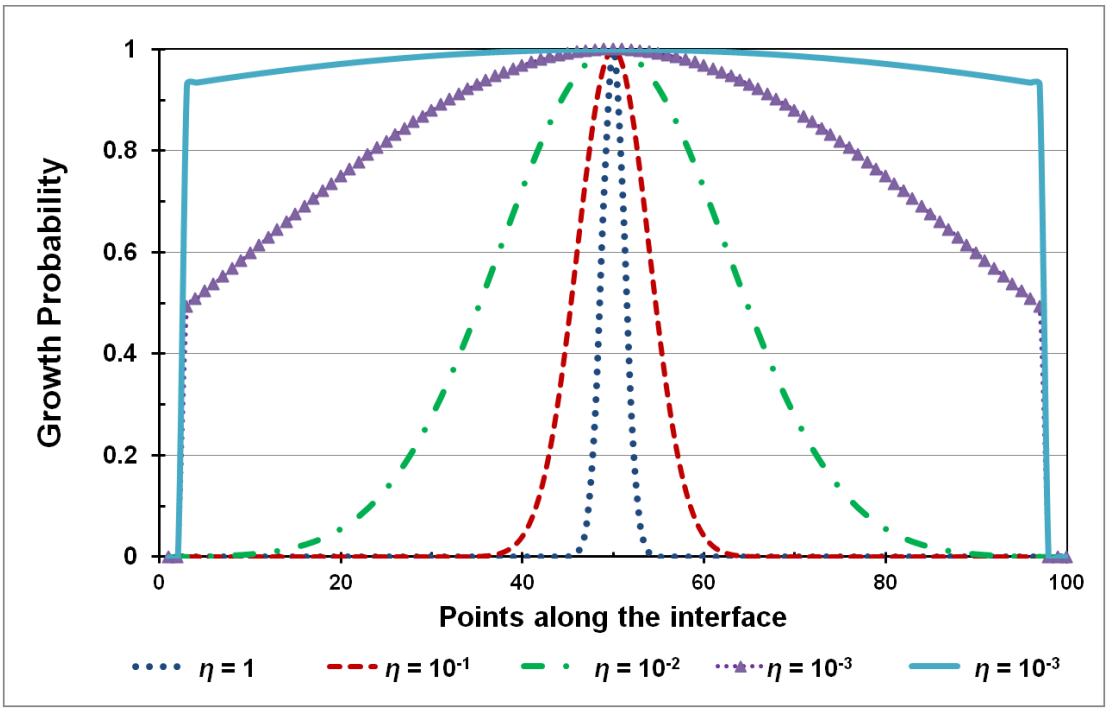

Figure 5.3: A plot of growth probability distribution along a flat interface with a small perturbation at the centre for different values η (or μ_r)

It is well known that two-phase, immiscible flow in porous media is influenced by both capillary and viscous effects. It is interesting to add that even though the capillary forces are not explicitly accounted for in the model, the multiplication of a random number implicitly bring in the effect of capillary forces for smaller values of η (low viscosity ratios, where capillary effects are important). The small value of power exponent η (say 10^{-4}) when applied to the calculated probability based on potential, evens out the differences in growth probability and the invaded grid is selected randomly or based on the pore throat distribution. For example, consider two grids with growth probability of $P_1 = 0.9$ $P_2 = 0.7$ and two cases with $\eta = 0.0001$ and $\eta = 0.1$. For $\eta = 0.0001$ after applying the power exponent $P_1 = 0.9998$ and $P_2 = 0.9996$, in this case randomness dictates the invading grid. For $\eta = 0.1$, $P_1 = 0.989$ $P_2 = 0.964$ in this case, both randomization and potential are important. The model does not take into account capillary pressure and pore-size distribution explicitly for the sake of simplicity of the model. It assumes a homogeneous permeability and pore size (away from the interface). Near the finger-tip, it accounts for the variability of the pore throats through the use of a random number. In general, this model is more suited for processes where capillary forces are not dominant either due to the wettability of the system or due to the high viscosity of the fluids involved.

5.1.4 SIMULATIONS

Extended dielectric break down model was used to simulate the results of the micromodel experiments listed in Table 4.5 and Figure 4.19. The simulator was coded entirely in Java using the open source interface called Easy Java Simulator (EJS). To match the experimental setup, the model was applied to a rectangular domain. A flow potential of $\bar{\phi}_w = 0$ (water) is specified for all the sites at the inlet. The sites at the

producer are assigned a flow potential of $\overline{\phi}_o = 1$ (oil). The grids between the inlet and the outlet can be assigned some intermediate value in the beginning and their actual values are computed while solving the Laplace equation. Each grid (or site) represents a pore body and each connection between grids (or bond) represents a pore throat connecting pore bodies. So each pore body is connected to 4 pore throats in 2D and 6 throats in 3D systems. The pore volume is associated with pore bodies and flow resistance is assigned with pore throats. 2D and 3D simulation were conducted, the results of the 2D simulator were compared to the micromodel result and 3D simulations were compared to some published results from literature.

2D Simulations

To mimic the results of micromodel experiments at different viscosity ratios, extended DBM simulations were run on a 100 X 100 X 1 grid system. The model parameter η was varied to attain fingering pattern similar to experimental figures. Using the micromodel experiments as a base case, a correlation between experimental parameter viscosity ratios μ_r and model parameter η could be developed. The results of the 2D network model simulations are shown in Figure 5.4 (a)-(b). Figure 5.4 (a) shows the displacement patterns generated and Figure 5.4 (b) shows the corresponding saturation profile averaged in the direction perpendicular to the flow.

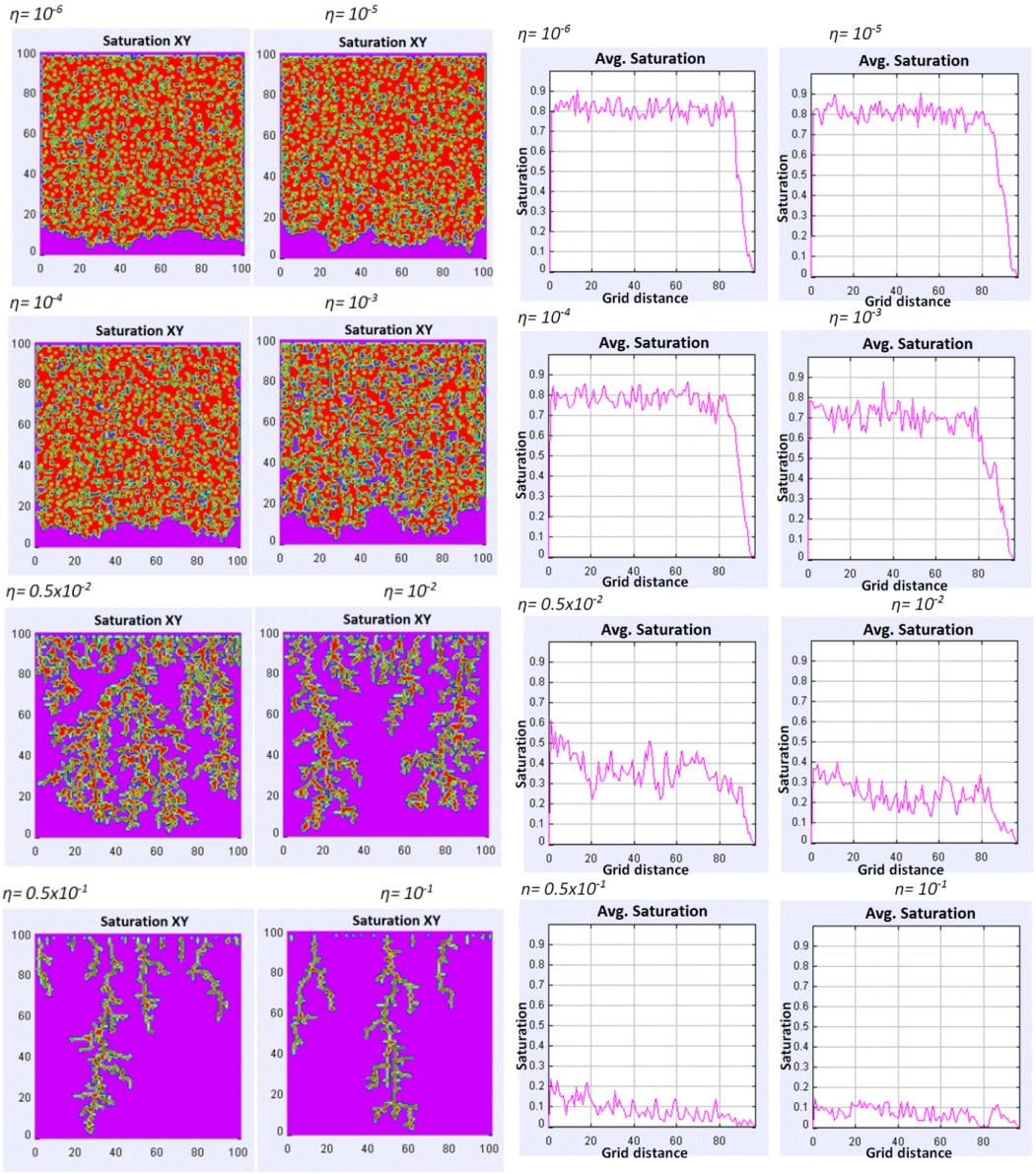

Figure 5.4 (a) Water/oil distribution in 2D simulations for different values of parameter η, (b) plot of water saturation along the length of the matrix at the time of breakthrough. Saturation XY is the phase distribution in XY plain and Avg. Saturation is the average across the width.

The 2D simulation captures most of the features of the 2D micromodel experiments. There is always some remaining oil in the swept zones, even for the smallest value of η (the most stable case) and the interface has pore scale perturbations that lead to this residual. Figure 5.5 shows a comparison of the expanded sections of a stable micromodel displacement at μ_r = 0.005 and simulations at $\eta = 10^{-6}$; the perturbations at the interface and the capillary trapped oil in the swept zone is captured accurately by the model. As the viscosity ratio is increased, the remaining oil saturation and the separation between the fingers increase as observed in the micromodels experiments. At η between (10^{-6}-10^{-4}) (low viscosity ratio), the displacement is stable and the swept area has a displacement efficiency of 80% (20% remaining). As the value of η is increased, the stable front starts to break into thick fingers and the remaining oil saturation (S_{or}) in the swept area increases. When the value of η is increased further, thin fingers that start to resemble DLA-like fractals appear. Figure 5.6 presents a plot of recovery efficiency (1-S_{or}) vs. η for the 2D simulations. For smaller values of η ($\eta < 10^{-4}$) all patterns converge into a stable displacement; for values close to 1 and above ($\eta \sim 1$) the patterns approach DLA like fractals.

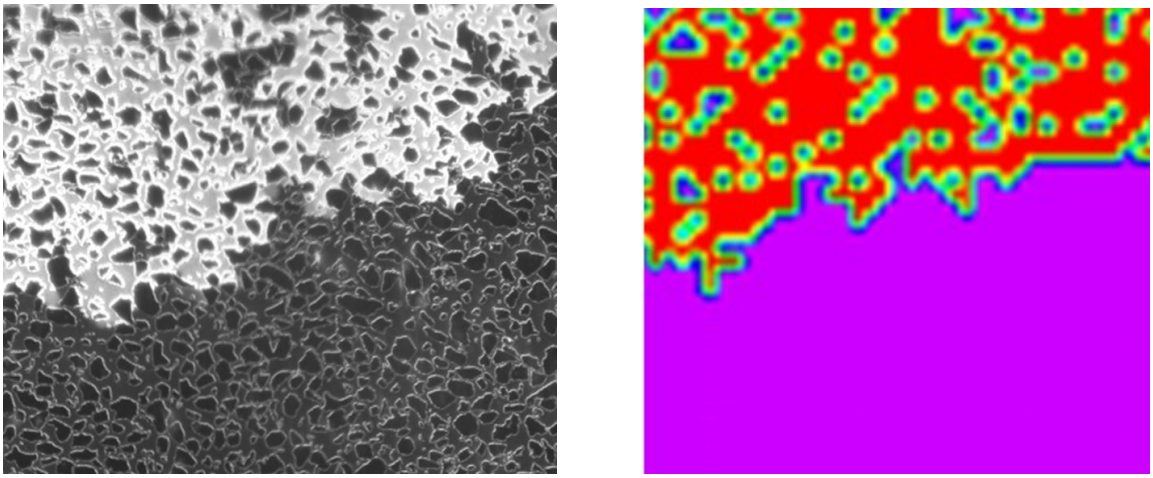

Figure 5.5: A comparison of the experimental 2D micromodel result and simulation at μ_r = 0.005 and η=10^{-6}, respectively; pink color (lower half) indicates the oil phase, red (top, speckled portion) is the water phase with trapped oil.

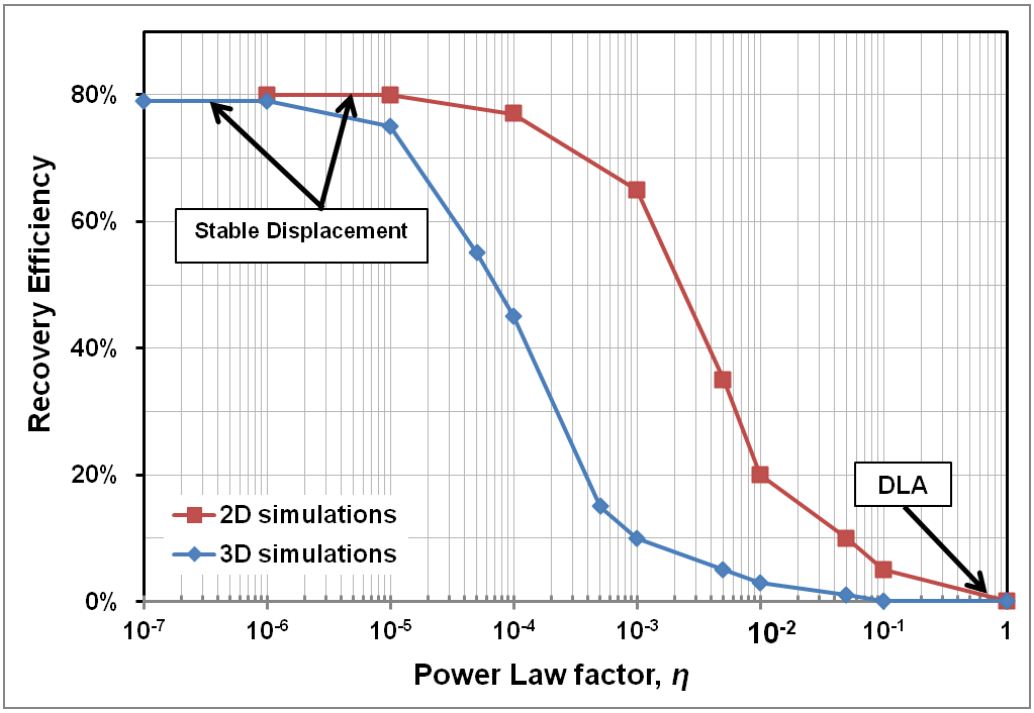

Figure 5.6: A plot of recovery efficiency vs. power law factor (η) for 2D and 3D simulations

Based on the recovery efficiency in the flooded zone (shown in Figure 5.4 (b)), a graphical correlation between η and recovery efficiency can be established. Also, from the micromodel experiments of Figure 4.19 and the chart of Figure 4.21, a correlation in between the viscosity ratio and recovery efficiency can be obtained. By combining the micromodel experiments and the simulations, a correlation in between η and viscosity ratio can be developed. Table 5.1 shows the recovery efficiency, viscosity ratio of the micromodel experiments and the corresponding value of parameter η that yielded similar recovery efficiency. The data of Table 5.1 can also be plotted in Figure 5.7 to show the relation between η and viscosity ratio (μ_r) for 2D simulations. The data shows a good power-law correlation between parameter η and μ_r and can be expressed as,

$$\eta = 10^{-5}\mu_r^{0.8775} \tag{5.10}$$

An existing model in the literature (Sherwood and Nittmann, 1986) presented a similar model for unstable displacement. This model is also probabilistic; the resulting interface is always perturbed. The perturbations grow into fingers, but the invaded region in this model is always 100% swept. 100% recovery is not practical in any immiscible displacements. In our model, the recovery efficiency never goes beyond 80% for all finite values of η. Randomness of the interface may sometime cause the two neighboring menisci to merge and trap the oil in the process. Once isolated, these blobs cannot be displaced in the simulation because the invading phase is assigned a boundary condition of $\Phi = 0$. As a result, an isolated blob is totally shielded by an externally applied potential field. When the Laplacian is solved iteratively for sites on the isolated island, the potential becomes zero and therefore, for all finite values of η, once isolated any oil blob cannot be displaced. Only for $\eta = 0$, the probability of these blobs along with every point

on the interface is one ($0^0 = 1$); so the islands are still created, but they disappear with time. This is not realistic and hence the case for $\eta = 0$ was not simulated.

Viscosity Ratio, μ_r	Recovery Efficiency	η
1	0.8	0.00001
200	0.65	0.001
1000	0.35	0.005
4000	0.2	0.01
10,000	0.08	0.04

Table 5.1: Recovery efficiency and viscosity ratio data from the experiment along with the matching value of η

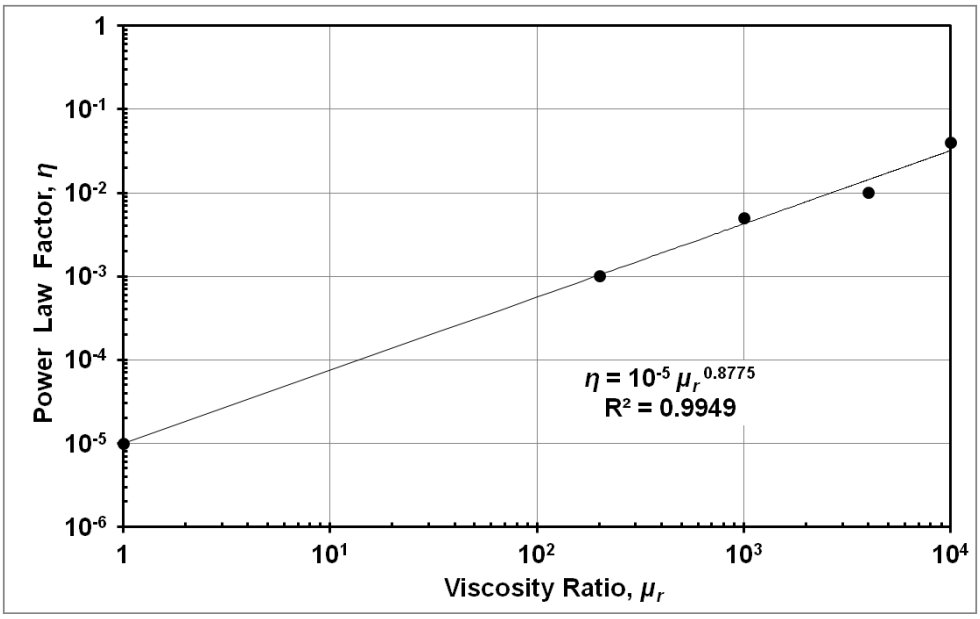

Figure 5.7: Relation between η and viscosity ratios based on the 2D micromodel experimental results.

3D simulations

The three-dimensional simulations were conducted on a 100 X 100 X 15 grid system and Eq. 5.3 was used for solving the Laplacian for a 3D system. Recently, Bondino et al.

(2011) and Skauge et al. (2012) have published results of X-ray scans of viscous fingers in a 12 inch x 12 inch x 1 inch Bentheimer slab. These images were used as a qualitative reference for our simulations in the absence of 3D experimental data. Figure 5.8 (a) show the saturation profile at breakthrough as generated by the simulation and Figure 5.8 (b) show the averaged saturation along the length. The saturation profile for 3D experiments has fewer fluctuations because of the averaging in the z-direction.

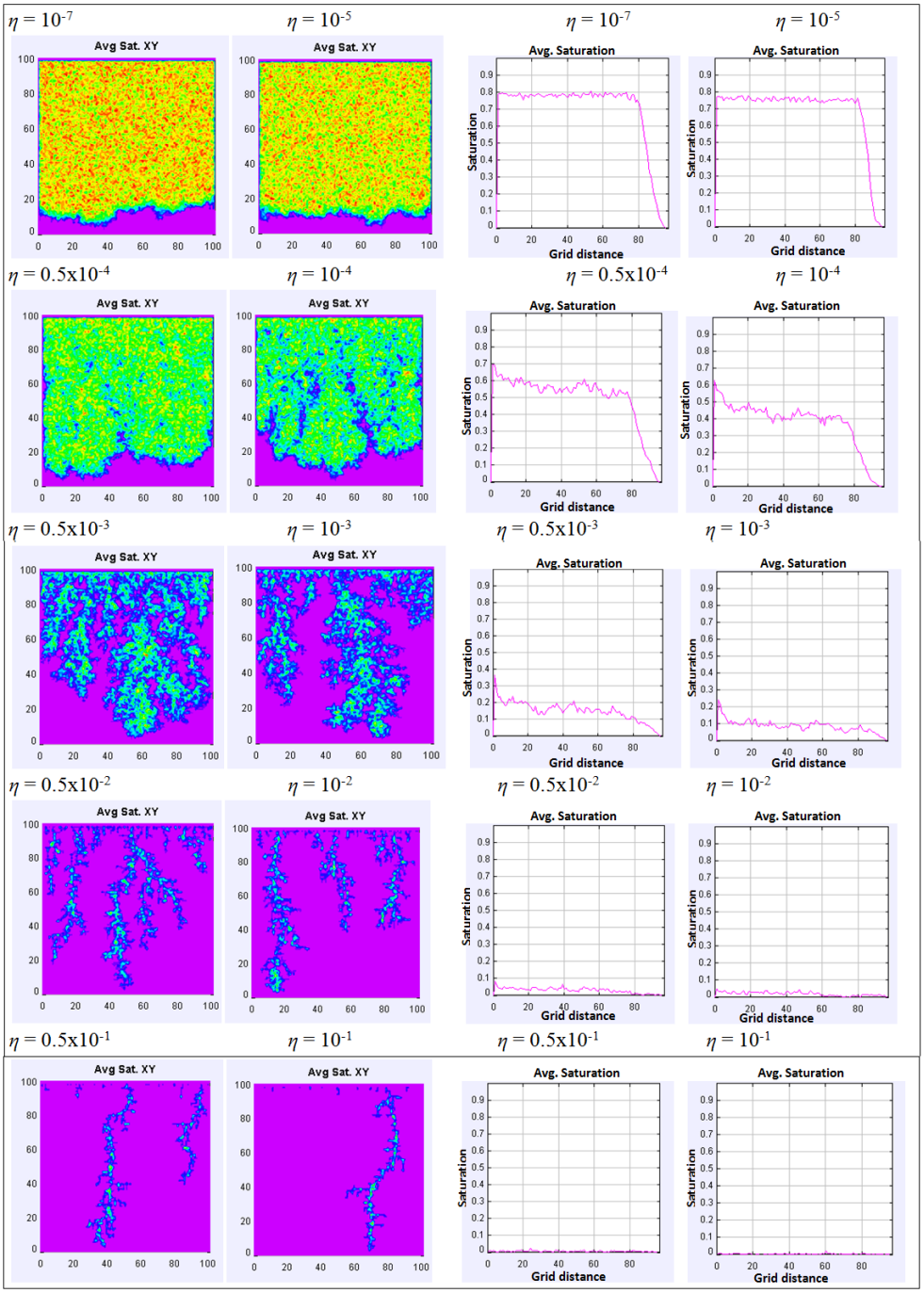

Figure 5.8: (a) Averaged water/oil distribution in XY plain (Avg Sat XY) for 3D simulation with different values of parameter η, (b) averaged water saturation distribution along the length of the matrix at the time of breakthrough

The trend observed in 3D simulations is similar to that observed in 2D simulations. The system evolves as a stable displacement at low values of η and as the value of η is increased to unity, the system transforms from thick fingers into DLA like fractals fingers. For all the finite values of η (up to 10^{-7}), the recovery efficiency is below 80%. This is consistent with the experiments and our 2D simulations. In Figure 5.6, recovery efficiency is plotted vs. power law index η for 3D simulations along with 2D results. The two curves for 2D and 3D simulations follow the same trend but they do not overlap. The curves are shifted by about an order of magnitude. On comparison, it appears that the η values for the same recovery efficiency in 3D and 2D simulations differ by a factor of approximately 15 which is also the number of grids in the z-direction. Figure 5.9 shows the two curves of Figure 5.6 after the parameter η of the 2D simulation has been scaled down by a factor of 15. This suggests that the correlation between η and μ_r, obtained from 2D analysis can also be scaled up for 3D. By this logic the new correlation for the 3D systems is,

$$\eta = 6.67 \text{ x } 10^{-7} \mu_r^{0.8775} \tag{5.11}$$

Figures 5.10 (c) and 5.10 (d) show the Xray radiograph images of water injection in Bentheimer slabs originally saturated with oils of viscosity 7000 and 2000 cP (Skauge et al., 2012). The slabs used in this study were about 12 X 12 X 1 inch in dimensions and therefore 100 X 100 X 8 gridding scheme was chosen for the simulation to maintain the 12:1 aspect ratio. The boundary conditions were similar to the experiments. In our simulation, we do not assign any pore size distribution explicitly. So the grid is homogeneous, as expected for a Bentheimer rock sample. Also, the details about the spatial distribution of porosity and permeability were not provided in the paper and were

therefore not modeled. The value of η for viscosity ratios of 2000 and 7000 can be calculated to be 3.16 x 10^{-3} and 1.05 x 10^{-3} for 2000 and 7000 cP oils, respectively. The results of the simulation in 3D for the two cases are shown in Figure 5.10(a) and (b). They are qualitatively very similar to Figure 5.10(c) and (d) of Skauge et al. (2012). More experimental data in 3D is needed to validate and fine tune the correlation for 3D systems

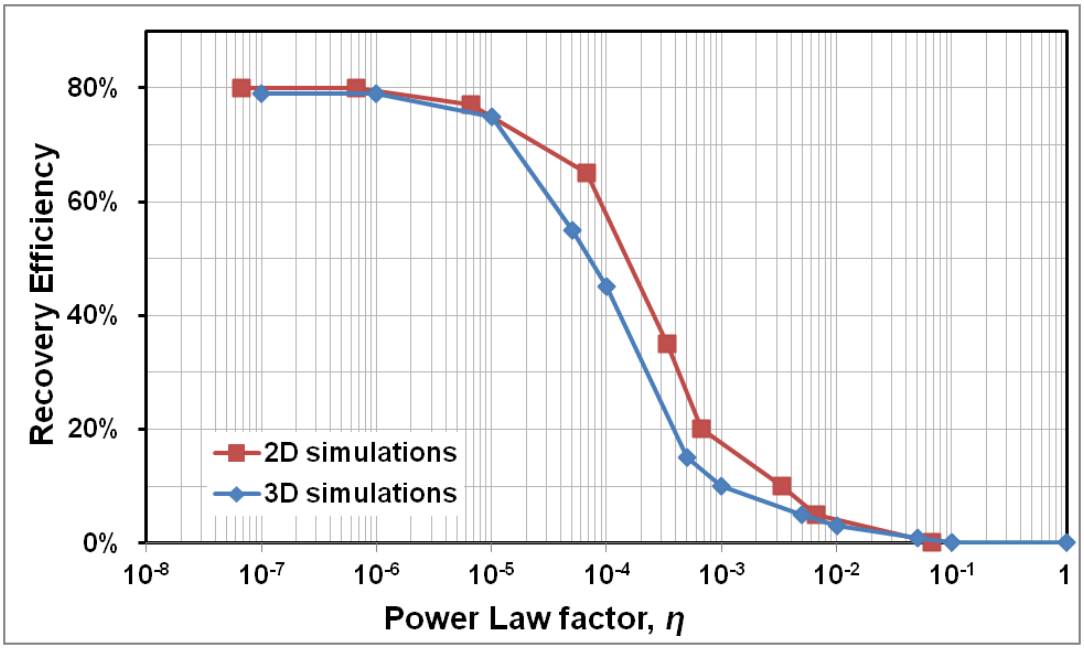

Figure 5.9: A plot showing that the recovery trends of 2D and 3D simulations are scalable.

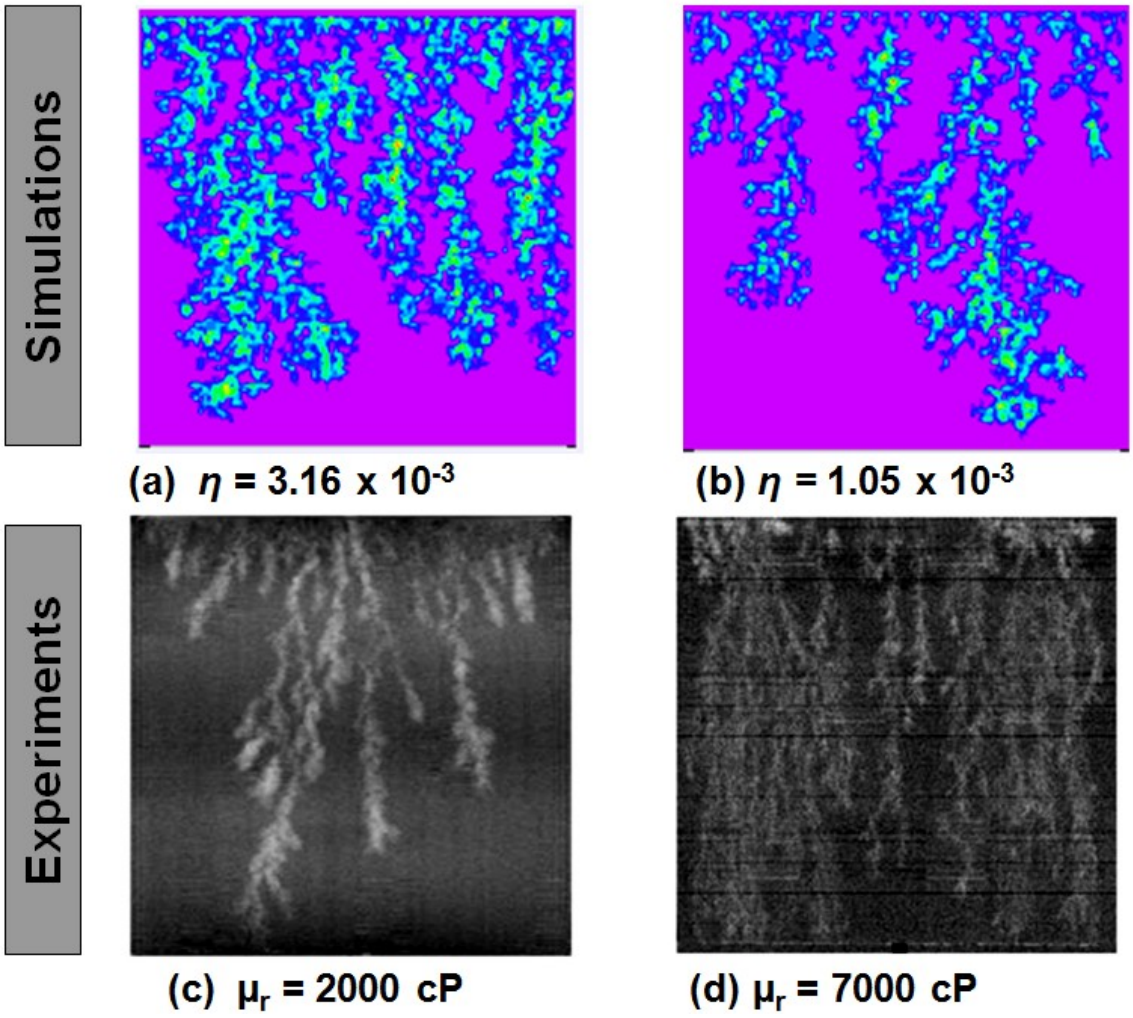

Figure 5.10: Simulations of oil displacement for η = 3.16 x 10^{-3} and 1.05 x 10^{-3} to simulate the 2000 and 7000 viscosity ratio displacement experiments in Bentheimer slabs presented by Skauge et al. (2012).

Effect of Domain Width

It is a well known fact that the viscous instabilities are also influenced by the system dimensions, especially the width. For a slim core, if the finger width is bigger than the core diameter the fluid will not finger through and the displacement will be stable in the core. It is tough to capture this effect through experiments as the experiments in the lab

scale are mostly restricted by the size of available core holders. The effect of system dimension was tested on our extended DBM. Figure 5.11 shows the images of the experiment conducted for three different values of η at aspect ratios of 10:1, 1:1 and 1:6. First row of the Figure 5.11 shows the results of the simulation set for $\eta = 10^{-4}$. It is clear that this displacement is relatively stable and is therefore not severely affected by the domain width or the aspect ratio. However, the next two rows ($\eta = 10^{-3}$ and 10^{-2}) portray unstable displacement. The results of the simulation show that the displacement is adversely influenced by the increase in domain width. At aspect ratio of 10:1, the width is much smaller than the length; hence, all three experiments look stable and the recovery is about the same. When the domain width is increased and the aspect ratio becomes 1:1; instability begins to set in for $\eta = 10^{-3}$ and the displacement at $\eta = 10^{-2}$ is clearly unstable while the displacement at $\eta = 10^{-4}$ remains stable. Further increasing the domain width adversely effects the unstable displacement and the instabilities become severe.

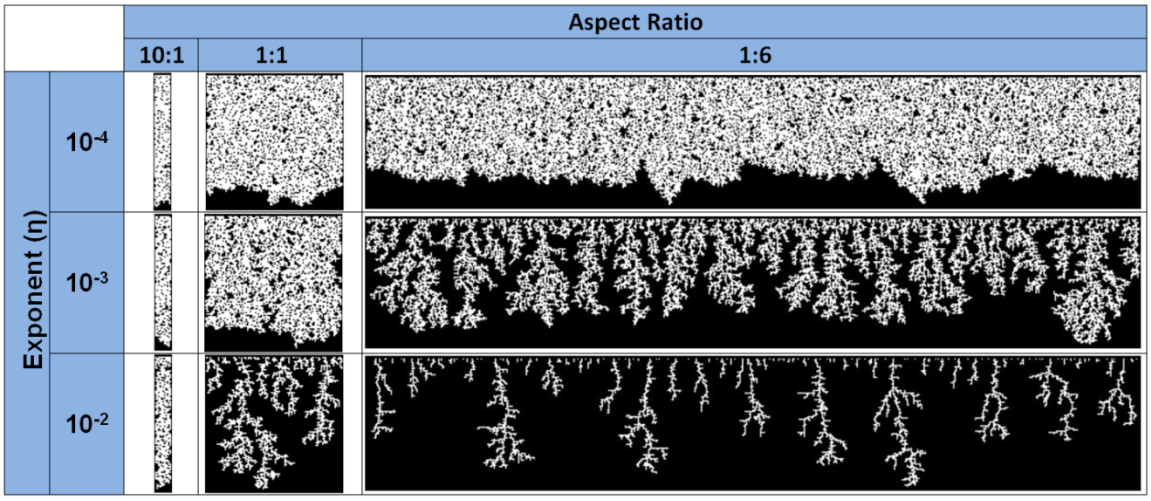

Figure 5.11: Results of extended DBM simulation that captures the effect of aspect ratio on displacement efficiency for stable and unstable displacements.

Figure 5.11 provides a qualitative idea of the effect of domain width on displacement. To better understand the relation between recovery and domain width a detailed study was also conducted at η of 10^{-4}, 10^{-3}, 10^{-2} and $5x10^{-2}$ for a wide range of domain widths. These simulations were conducted on a 100 x 100 grid scheme at the aspect ratio of 1:1. To vary the domain width, number of grids in the direction perpendicular to the flow were increased or decreased while the grids in the flow direction were kept constant at 100. For each simulation run the mean value of average recovery was also noted. The unstable and random nature of displacement yields a slightly different value of recovery in each run. Therefore the reported values are the mean recoveries for that simulation set. Figure 5.12-5.15 show the results of the simulations conducted for η of 10^{-4}, 10^{-3}, 10^{-2} and $5x10^{-2}$ respectively. The recovery data for each run is organized in Table 5.2. For calculation purposes the domain width at the aspect ratio of 10:1 was assumed to be 1 and all the other domain width were scaled accordingly.

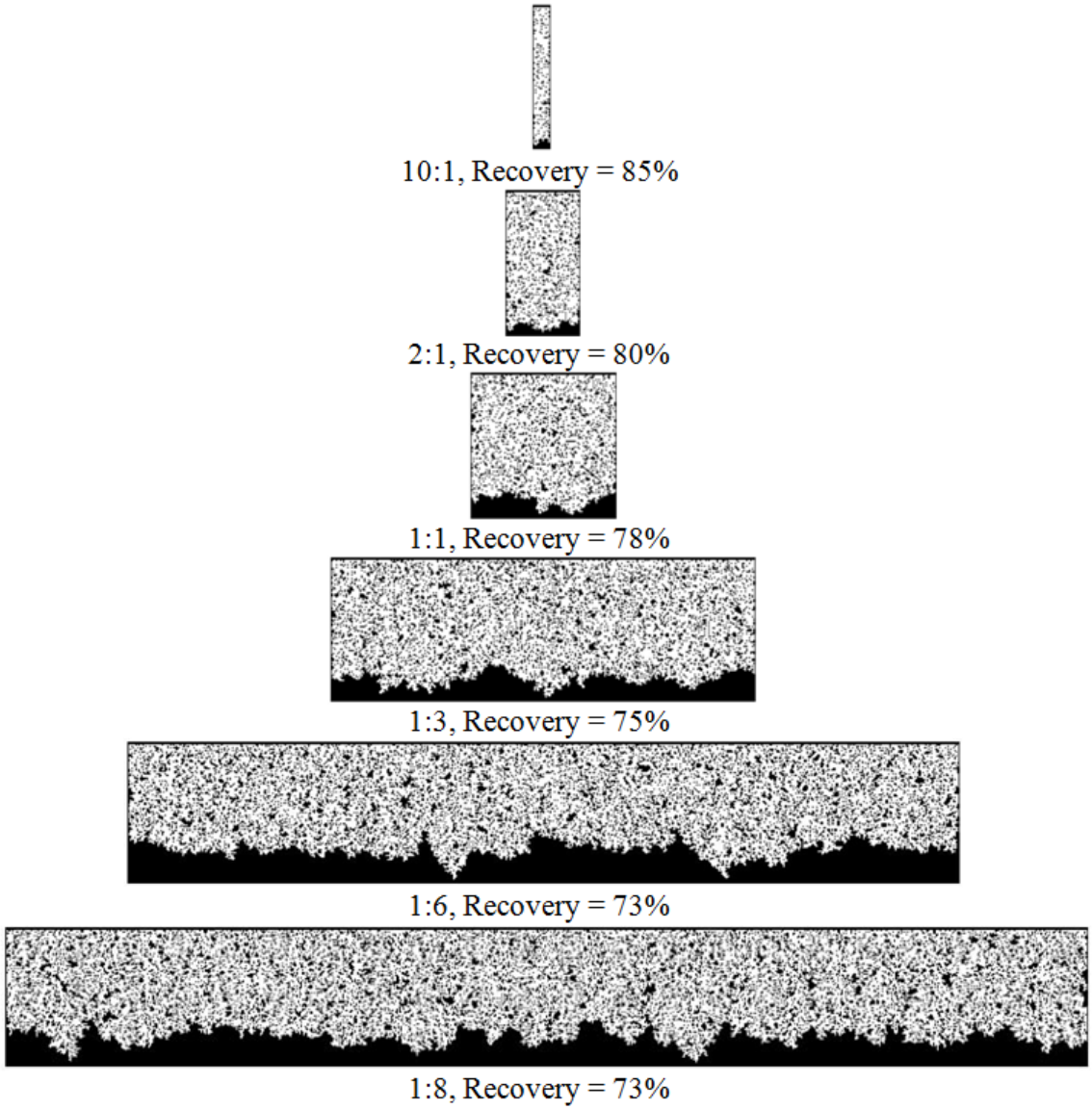

Figure 5.12: Results of the extended DBM simulation runs for $\eta = 10^{-4}$ at various aspect ratios

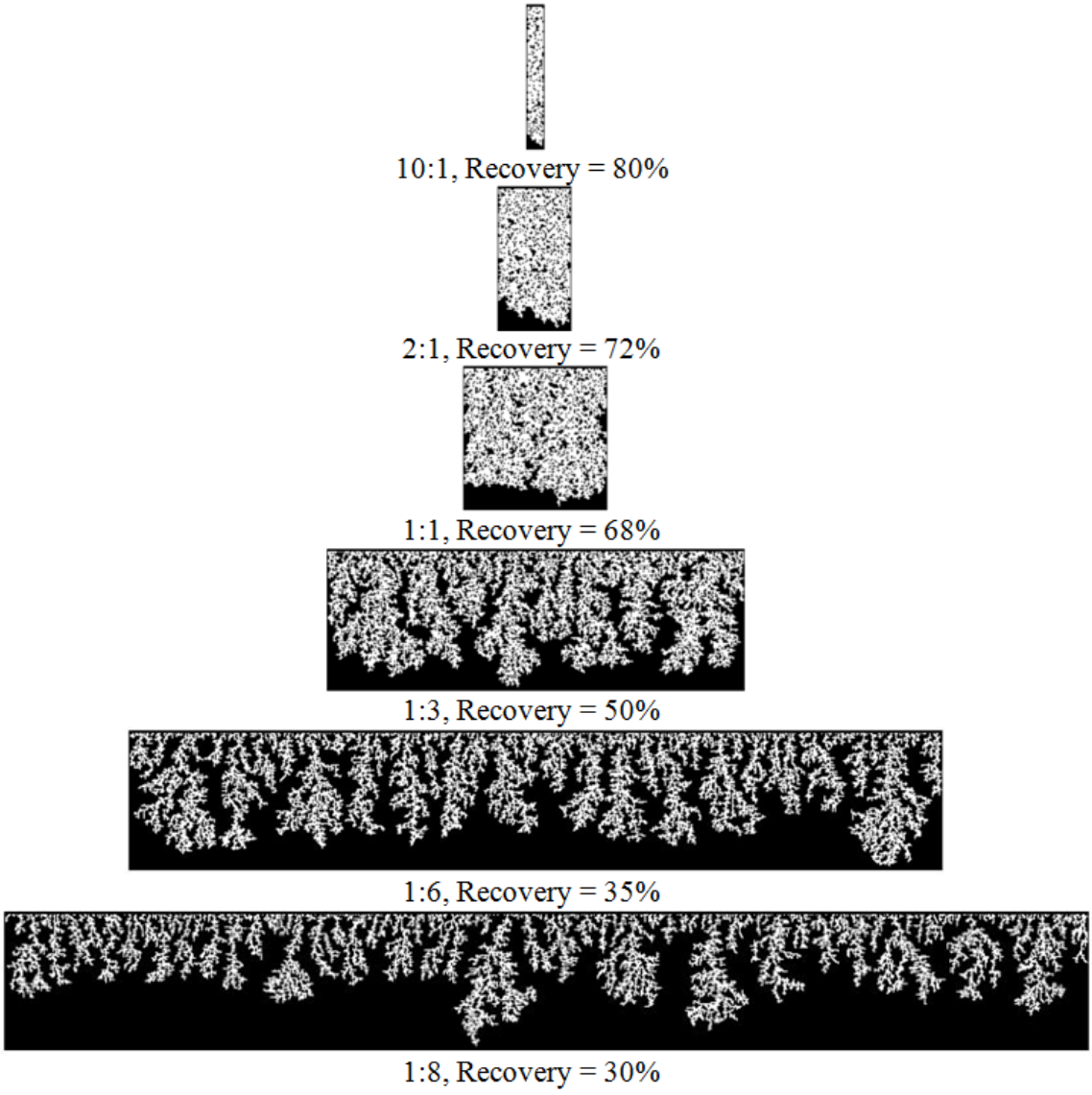

Figure 5.13: Results of the extended DBM simulation runs for $\eta = 10^{-3}$ at various aspect ratios

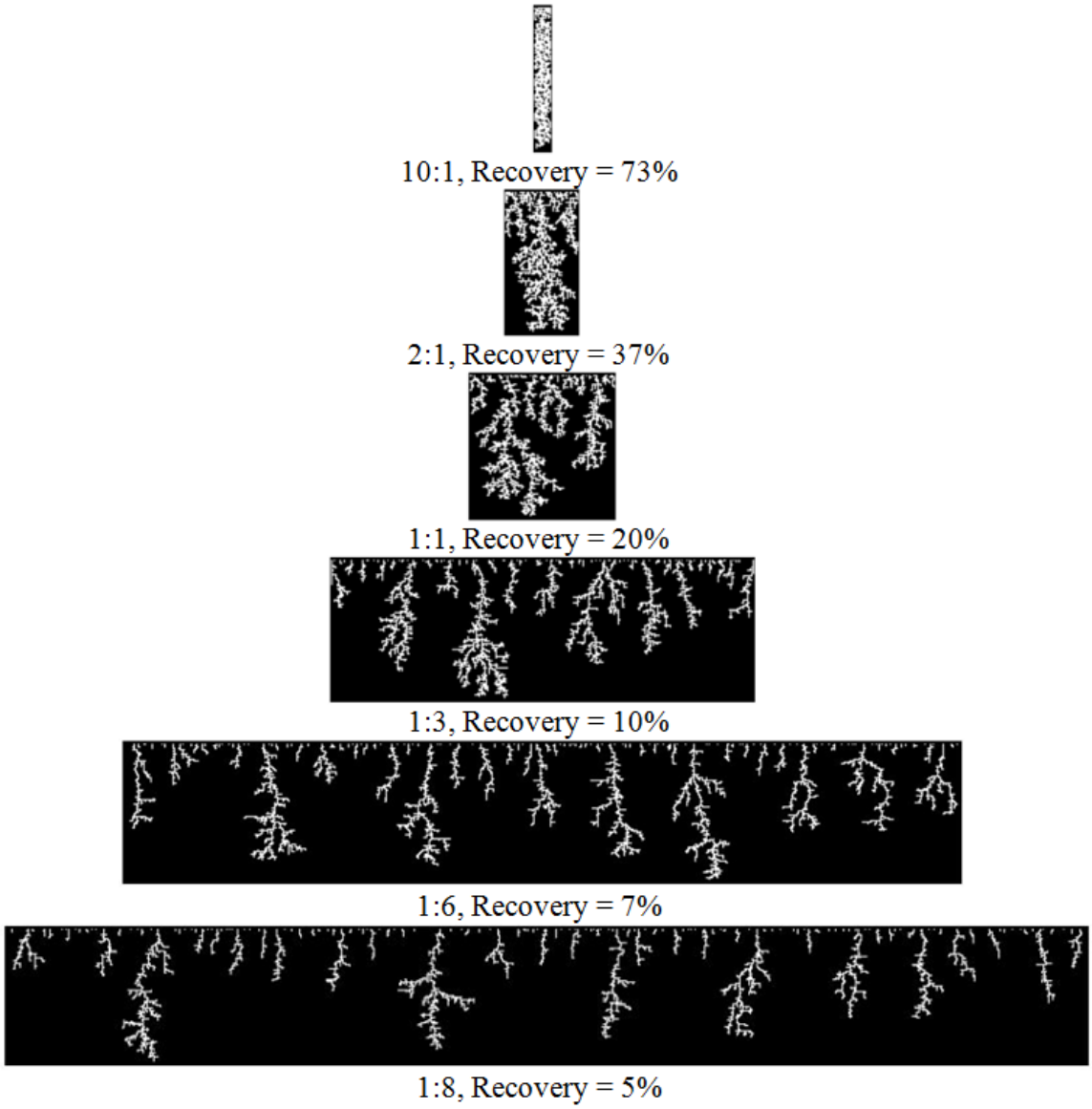

Figure 5.14: Results of the extended DBM simulation runs for $\eta = 10^{-2}$ at various aspect ratios

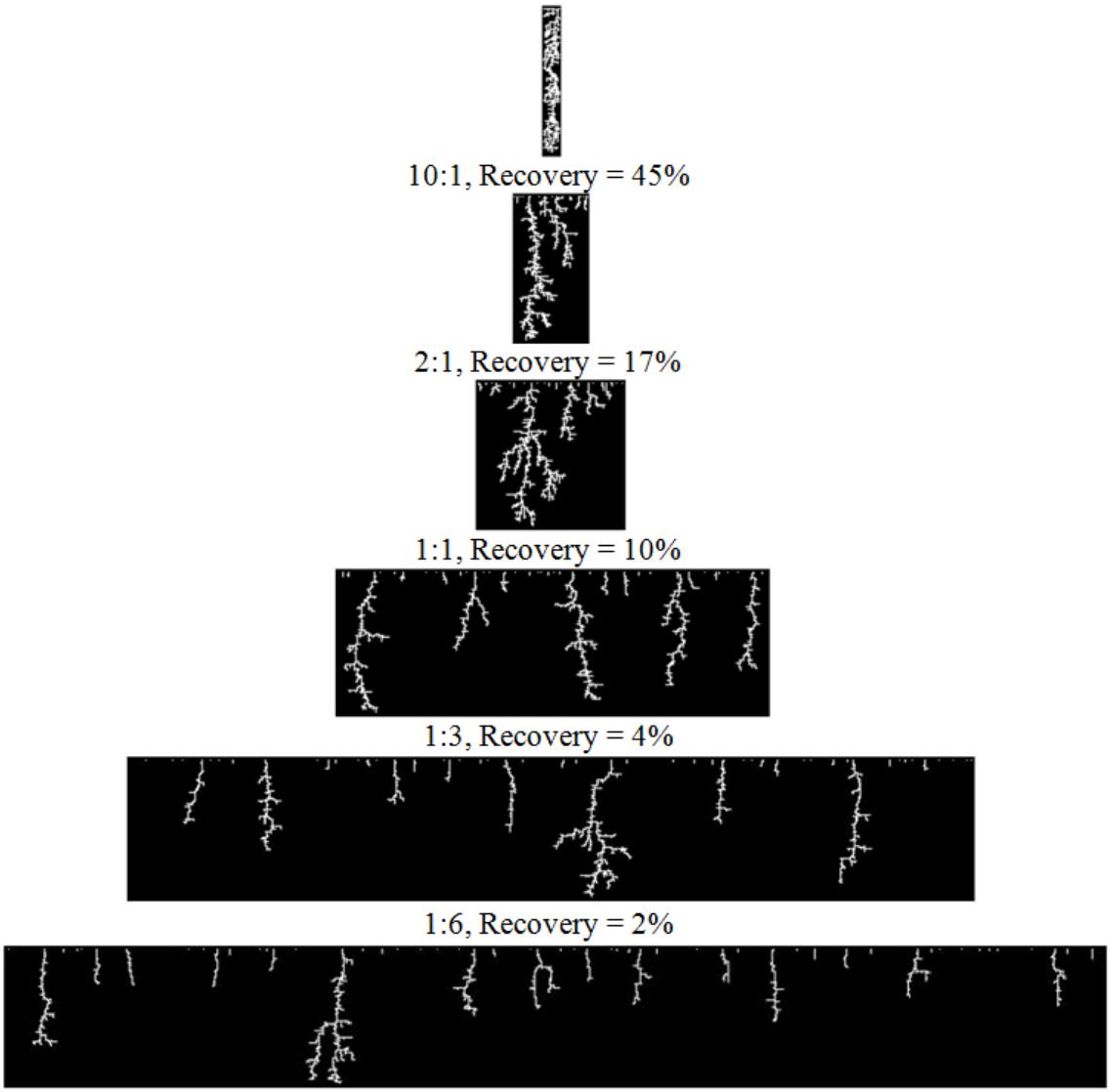

Figure 5.15: Results of the extended DBM simulation runs for η = 5 x 10^{-2} at various aspect ratios

	Aspect ratio	D	Mean recovery (%)
$\eta = 10^{-4}$	10:1	1	85
	2:1	5	80
	1:1	10	78
	1:3	30	75
	1:6	60	73
	1:8	80	73
$\eta = 10^{-3}$	10:1	1	80
	2:1	5	72
	1:1	10	68
	1:3	30	50
	1:6	60	35
	1:8	80	30
$\eta = 10^{-2}$	10:1	1	73
	2:1	5	37
	1:1	10	20
	1:3	30	10
	1:6	60	7
	1:8	80	5
$\eta = 5 \times 10^{-2}$	20:1	0.5	57
	10:1	1	45
	2:1	5	17
	1:1	10	10
	1:3	30	4
	1:6	60	2
	1:8	80	2

Table 5.2: Data of the extended DBM simulation for various values of η at different aspect ratios and the corresponding recovery for each run

Data from Table 5.2 shows that as the domain width (D) increased the recovery decreases for most cases. The decrease is much subtle for stable floods. From the correlation, $N_c \mu_r^2 \left(D^2 / K \right)$ developed in Chapter 4, the recovery is correlated with D^2. The simulated recovery from Table 5.2 was also plotted against the square of domain

width (D^2). Due to the statistical nature of the simulation the recovery of each simulation run is slightly different and varies around a certain average or mean value. The value of the recovery reported in Table 5.2, Figure 5.16 and Figure 5.17 are the average of three consecutive simulations runs. Figure 5.15 shows the plot of the mean simulated recovery versus D^2 for all the four simulated cases. The recovery for the stable displacement is almost unaffected by the domain width and is represented by an almost horizontal straight line. As the displacement gets unstable, the curve starts to deviate from the straight horizontal line and the recovery declines rapidly. Higher the instability, earlier the curve deviates from the straight line trend and faster is the decline in the recovery. For smaller diameters, all the curves tend to converge towards a same point.

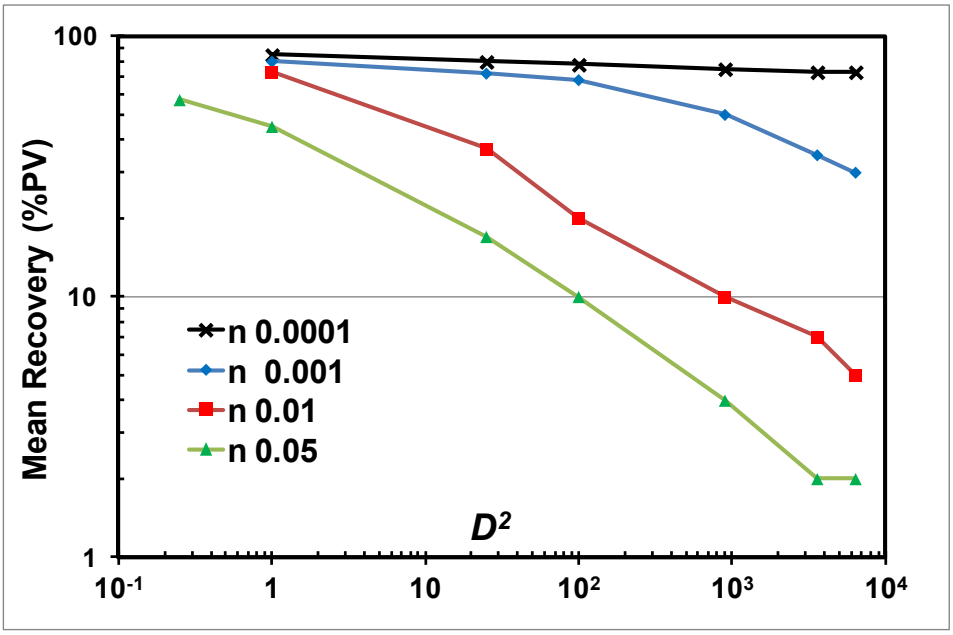

Figure 5.16: A plot of mean recovery derived from extended DBM simulations versus the square of domain width for 4 different values of exponent η (or viscosity ratios)

In chapter 4, a dimensionless scaling correlation ($N_c \mu_r^2 \left(D^2 / K \right)$) was developed. This correlation was tested against recovery data from 49 different experiments and the correlation showed a consistent and unique trend. As the simulated results of extended DBM show a variation with width or diameter; it was also tested against the $N_c \mu_r^2 \left(D^2 / K \right)$correlation. All the four set of simulations described in Table 5.2 were conducted at the same boundary conditions, so the injection velocity or the capillary number (N_c) is same for all the experiments. Average permeability will also not vary. Thus, viscosity ratio is the only other parameter that is variable. In the extended DBM simulations the change in viscosity ratio is induced by changing the value of the exponent η. In equation 5.10, a relation in between the η and viscosity ratio has already been developed. Using this correlation, a value of viscosity ratio (μ_r) corresponding to each simulation set can be obtained. Table 5.3 shows extension of Table 5.2, including the values the calculated viscosity ratios (using Eq. 5.10).

	Aspect ratio	D	Mean recovery (%)	$\eta = 10^{-5}\mu_r^{0.8775}$	$D^2\mu_r^2$
$\eta = 10^{-4}$	10:1	1	85	13.8	1.90×10^{2}
	2:1	5	80		4.75×10^{3}
	1:1	10	78		1.90×10^{4}
	1:3	30	75		1.71×10^{5}
	1:6	60	73		6.85×10^{5}
	1:8	80	73		1.22×10^{6}
$\eta = 10^{-3}$	10:1	1	80	190.2	3.62×10^{4}
	2:1	5	72		9.04×10^{5}
	1:1	10	68		3.62×10^{6}
	1:3	30	50		3.26×10^{7}
	1:6	60	35		1.30×10^{8}
	1:8	80	30		2.32×10^{8}
$\eta = 10^{-2}$	10:1	1	73	2623	6.88×10^{6}
	2:1	5	37		1.72×10^{8}
	1:1	10	20		6.88×10^{8}
	1:3	30	10		6.19×10^{9}
	1:6	60	7		2.48×10^{10}
	1:8	80	5		4.40×10^{10}
$\eta = 5 \times 10^{-2}$	20:1	0.5	57	16419	6.74×10^{7}
	10:1	1	45		2.70×10^{8}
	2:1	5	17		6.74×10^{9}
	1:1	10	10		2.70×10^{10}
	1:3	30	4		2.43×10^{11}
	1:6	60	2		9.71×10^{11}
	1:8	80	2		1.73×10^{12}

Table 5.3: Data of the extended DBM simulation of Table 5.2 along with the value of viscosity ratios corresponding to the power exponent η

Using the values of viscosity ratios calculated in Table 5.3, $D^2\mu_r^2$ can be calculated for each simulation run. As capillary number (Nc) and average permeability (K) are same for all the run, $D^2\mu_r^2$ should be as effective as the correlation $N_c\mu_r^2\left(D^2 / K\right)$. The same simulated recovery data was now plotted against $D^2\mu_r^2$; all the four curves of

Figure 5.16 collapse over each other. Figure 5.17 shows the plot of simulated recovery versus $D^2\mu_r^2$. This suggests that the scaling parameter developed in Chapter 4 not just captures the effect is viscosity ratios and flow rates. It also accurately captures the effect of domain width. As the experimental data for a wide range of core diameter was not available, the extended DBM model has helped in validating the correlation with respect to the different core diameters. In validating the $N_c\mu_r^2\left(D^2/K\right)$correlation, extended DBM has also validated itself as a useful tool for accurately simulating 2D unstable displacement.

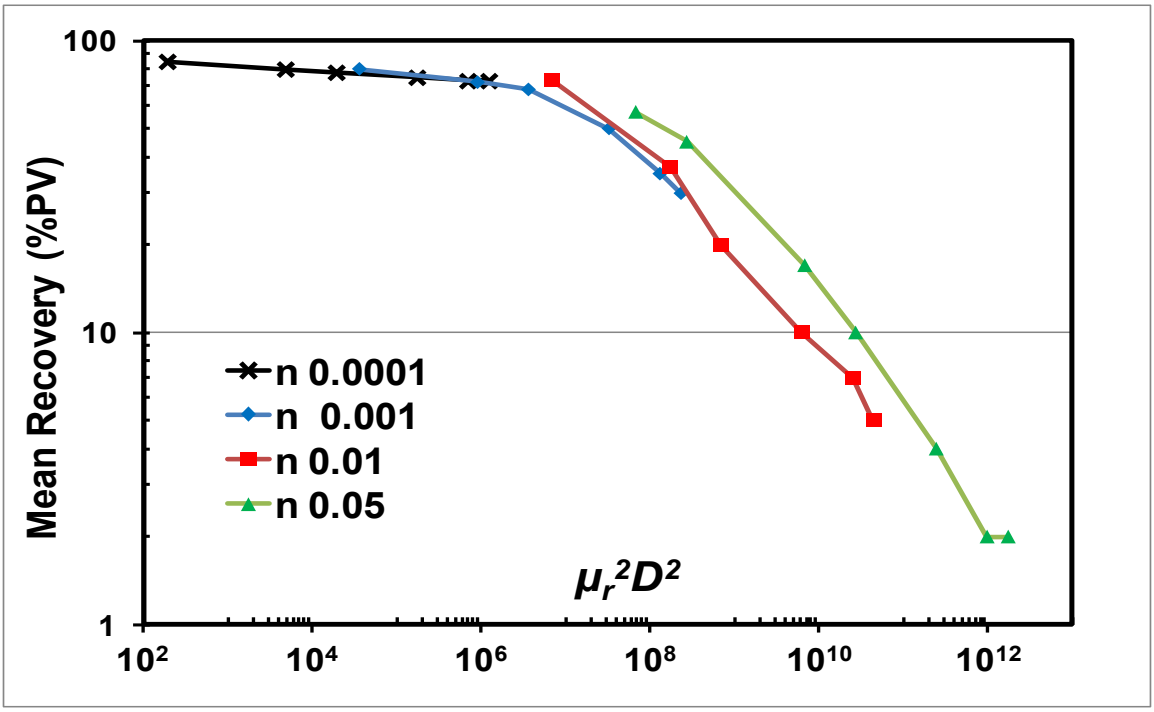

Figure 5.17: Plot of simulated recovery versus $\mu_r^2D^2$.

5.1.5 Extended DBM Summary

The extended dielectric breakdown model captures the pore level details and can be an effective tool to simulate smaller scale displacements in micromodels and some

core flood. The correlation between the parameter η and viscosity ratios enables us to perform simulations and get an accurate idea of recovery and finger structures without the need of conducting an experiment. The model also captures the effect of aspect ratio or system dimension on the recovery efficiency for stable and unstable viscosity ratios. If the displacement is stable, it is totally unaffected by the system dimensions; but the sweep in an unstable displacement is significantly dependent on the aspect ratio. The results of the extended DBM simulation also helped in validation the $N_c \mu_r^2 \left(D^2 / K \right)$ correlation developed in Chapter 4. Extended DBM is therefore an excellent tool to simulated unstable 2D displacement. The model can be a good substitute for micromodel experiments. However, for length scales larger than a couple of feet, the extended dielectric breakdown model will be computationally too expensive and will capture a lot of unnecessary pore level details. This makes the applicability of extended DBM at reservoir scales questionable. Reservoir scale simulations are conducted on large simulation grids and having very finer reservoir grids is not encouraged due to very large run times. With larger grids it is not possible to explicitly capture each and every finger as most fingers are smaller than the grid size. Therefore, a method that captures the effects of viscous fingering and flow rates (discussed in chapter 4) on the larger grid blocks without the necessity of fine grid detailed simulations is desirable from the reservoir engineering point of view. In the next section, a lumped model is proposed to history match all the core floods with different viscosity ratios and flow rate (Chapter 4, Table 4.8) using pseudo-relative permeabilities.

5.2 LUMPED FINGER MODEL

5.2.1 Proposed Model

In this section, a model is presented that can capture the effect of fingering without having to simulate each and every individual finger. From the experiments listed in Chapter 4, it is clear that fingers are often smaller than the size of a typical reservoir simulation grid cell. Therefore, in this model we propose to lump all the sub-grid fingers into one equivalent finger and then modify the multiphase flow equations to account for the presence of this lumped finger. The idea is graphically summarized in Figure 5.18. The green color represents oil phase, white is water fingering through the oil and dark green represents the isolated zone which comprises of the bypassed oil and λ is the width of the averaged finger.

The main assumptions of this model are:

1. All the sub-grid fingers can be represented by one equivalent finger.
2. As the fingers grow they leave behind bypassed pockets that cannot be swept (typically, a part of the region in between fingers). This region is lumped together into a region called the isolated zone (deep green in Figure 5.18, right panel). The region that is unswept but could be eventually swept by the finger at a later time is called the unswept zone (light green in Figure 5.18, right panel).
3. Two phase flow occurs only within the finger.
4. Single phase oil flow occurs in the unswept zone outside of the isolated zone.
5. No flow occurs in the isolated zone.

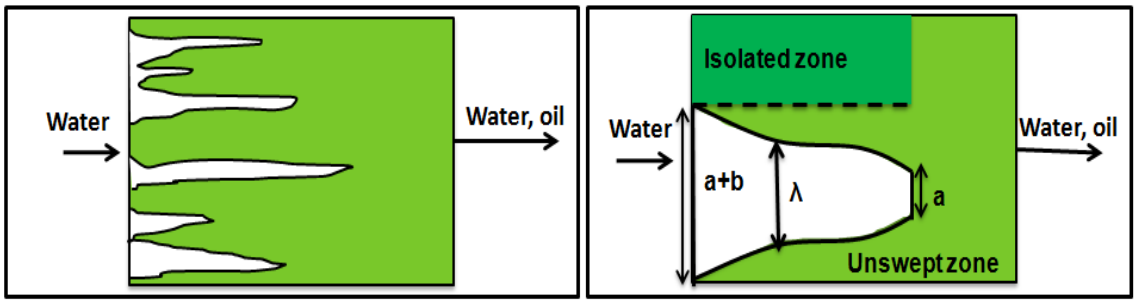

Figure 5.18: (left) Graphical representation of viscous fingering within a grid; (right) an equivalent averaged viscous finger of a fractional width λ that captures the physics of multiple sub-grid fingers.

A similar model to account for viscous fingering in miscible displacement was developed by Fayers (1988). They described their averaged finger width as a function of the concentration of the injected solvent and represented it by function $\boldsymbol{\lambda = a + bC^{\beta}}$, where $\boldsymbol{a}$, $\boldsymbol{b}$ and $\boldsymbol{\beta}$ are fitting parameters of the system and C is the normalized concentration of the injected solvent. The averaged finger width λ varies from $\boldsymbol{a}$ at C = 0 to $\boldsymbol{a+b}$ at C = 1. Parameter $\boldsymbol{a}$ can be called the head width of the finger and $\boldsymbol{a+b}$ is the final width of the finger. For a miscible displacement in a homogeneous rock, it is possible to recover 100% of the oil in place and hence, $\boldsymbol{a+b}$ = 1. In this study, the same function form of the averaged finger width is used, but C is replaced by normalized water saturation, $\boldsymbol{\overline{S_w}}$. For immiscible displacement, sweep is always less than 100%; therefore $\boldsymbol{a+b}$ < 1. In this case, $\boldsymbol{a+b}$ represents the maximum area swept by water injection and ($\boldsymbol{1-a-b}$) will be the isolated zone that was never contacted by water. Inclusion of this lumped finger within the grid changes the oil and water flow equations as shown in Eqs. 5.12 and 5.13. The area available for water to flow is now only a fraction of the cross-sectional area ($\boldsymbol{\lambda A}$) instead of the actual cross-section area $\boldsymbol{A}$. The water flow equation can now be written as;

$$q_w = -\frac{Kk_{rw}\lambda A}{\mu_w}\left(\frac{dp}{dx}\right) \tag{5.12}$$

Oil flows both in the finger and outside of the finger. The flow in the finger will be influenced by the relative permeability (K_{ro}) corresponding to the average water saturation at that cross-section. Outside of the finger, oil will flow at its end point relative permeability at irreducible water saturation (k_{ro}^0). The oil flow equation can be written as;

$$q_o = \underbrace{-\frac{Kk_{ro}\lambda A}{\mu_o}\left(\frac{dp}{dx}\right)}_{\text{Flow inside the finger}} \underbrace{-\frac{Kk_{ro}^0(a+b-\lambda)A}{\mu_o}\left(\frac{dp}{dx}\right)}_{\text{Flow outside the finger}} \tag{5.13}$$

K_{rw} and K_{ro} are the regular relative permeabilities for a stable displacement, K is the absolute permeability, λ is the fractional finger width and A is the cross-sectional area. On comparison with the standard oil-water flow equations, Eqs. 5.12 and 5.13 yield a set of modified or pseudo relative permeability functions for both water and oil, as shown in equations 5.14 and 5.15.

$$k_{rw,pseudo} = k_{rw}\lambda \tag{5.14}$$

$$k_{ro,pseudo} = k_{ro}\lambda + k_{ro}^0\left(a+b-\lambda\right) \tag{5.15}$$

The thickness of the isolated zone will depend on the thickness of the averaged finger width. As averaged finger width will change for every viscosity ratio the remaining oil saturation, S_{orem} *(different from* S_{or}*)* will also be different in each case. Therefore, the end-point water saturations of the new pseudo relative permeability curves are at S_{wi} and S_{wmax}, where

$$S_{wmax} = 1 - S_{orem} = [\underbrace{S_{wi}(1-a-b)}_{\text{Outside finger}} + \underbrace{(1-S_{or})(a+b)}_{\text{Inside finger}}]. \tag{5.16}$$

It should be noted that experimentally obtained S_{wi} reported in Chapter 4 were slightly different for different viscosity ratios, but for modeling purposes both the end points were shifted equally to keep the initial water saturation (S_{wi}) constant. This changes the initial oil in place, but the total oil recovery in terms of % pore volumes remains the same.

Expt.	μ_w	μ_o	μ_r	S_{wi}	S_{wmax}	Corrected S_{wi}	Corrected S_{wmax}	Recovery (%PV)
1	60	60	1	0.17	0.82	0.089	0.74	65
2	1	60	60	0.17	0.68	0.089	0.60	51
3	1	560	560	0.156	0.52	0.089	0.45	37
4	1	1440	1440	0.117	0.41	0.089	0.38	29
5	1	5200	5200	0.089	0.32	0.089	0.32	23
6	1	10500	10500	0.089	0.28	0.089	0.28	19
7	1	10500	10500	0.089	0.32	0.089	0.32	23
8	1	10500	10500	0.089	0.35	0.089	0.35	26

Table 5.4: Initial and final water saturation data of experiments listed in Table 4.8 along with the corrected saturation for simulations purposes

5.2.2 Model Results

The results of the core floods presented in Table 4.8 were used to validate the lumped finger model. The lumped finger model requires a set of base relative permeability curves for a stable displacement. These curves serve as the basic input to the model and are modified for different viscosity ratios using eq. 5.14 and eq. 5.15. However, the JBN analysis for the pressure and recovery data of experiment 1 does not yield much relative permeability data because of the low viscosity ratio. There was a large saturation shock in the displacement and hence no relative permeability data could be obtained for saturations before the shock. Therefore, unsteady state relative permeability was calculated from Exp. 2 (μ_r = 60) by the JBN method and model parameters were obtained

by fitting a Corey model to the relative permeability data for Exp. 2. Corey exponents for oil and water relative permeability curves were $n_o = 1$ and $n_w = 3$.

Figure 5.19 shows the JBN data for Exp. 2 and the fitting Corey relative permeabilities. The relative permeabilities generated using these exponents gave a good match with the experimental pressure and recovery data for experiment 1 as well (Figure 5.20(a)). These relative permeability curves with Corey exponent of 1 and 3 for oil and water respectively will be used as the base case relative permeability curves. Once the base relative permeability curves were fixed, the parameters *a, b* and *β* of the lumped model were assumed to estimate a pseudo relative permeability for each experiment. The coreflood was then simulated using this pseudo relative permeability in a 1D CMG-IMEX simulator. The predicted oil recovery and pressure drop were compared with the corresponding experimental data. The parameters *a, b* and *β* were varied until a reasonable match was obtained.

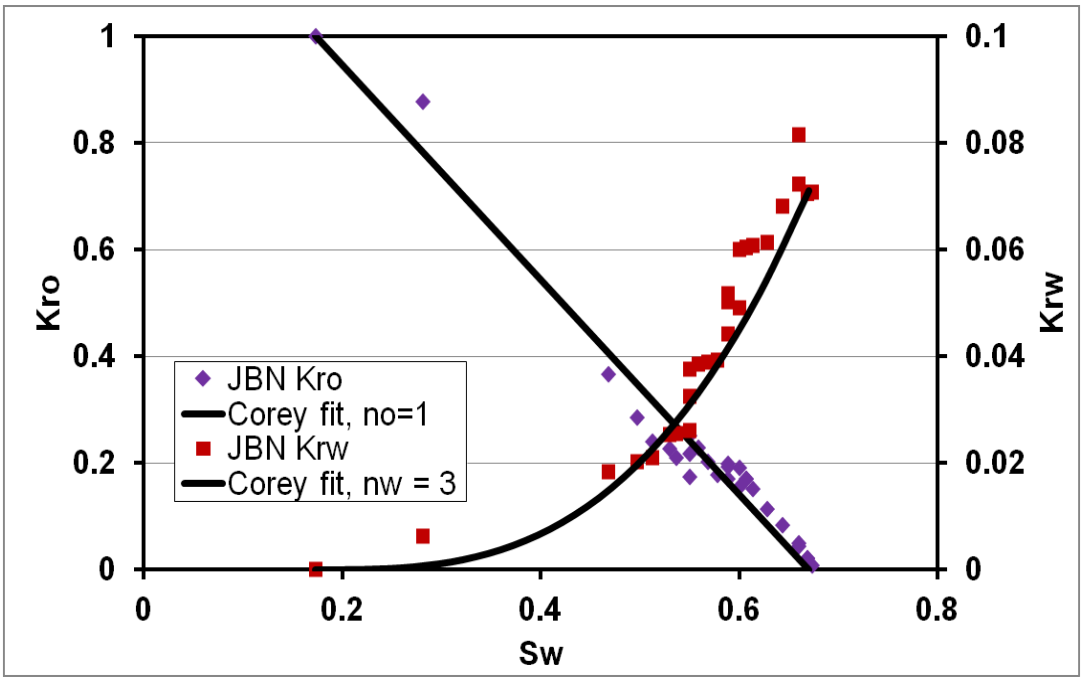

Figure 5.19: Relative permeabilities obtained by the JBN method for Exp. 2 and the corresponding Corey curves for $n_w = 3$ and $n_o = 1$

The results of the history match using the fingering function are shows in Figure 5.20 (b) – (h). The smooth curves are the simulated results and the dotted / wavy curves are experimentally collected data.

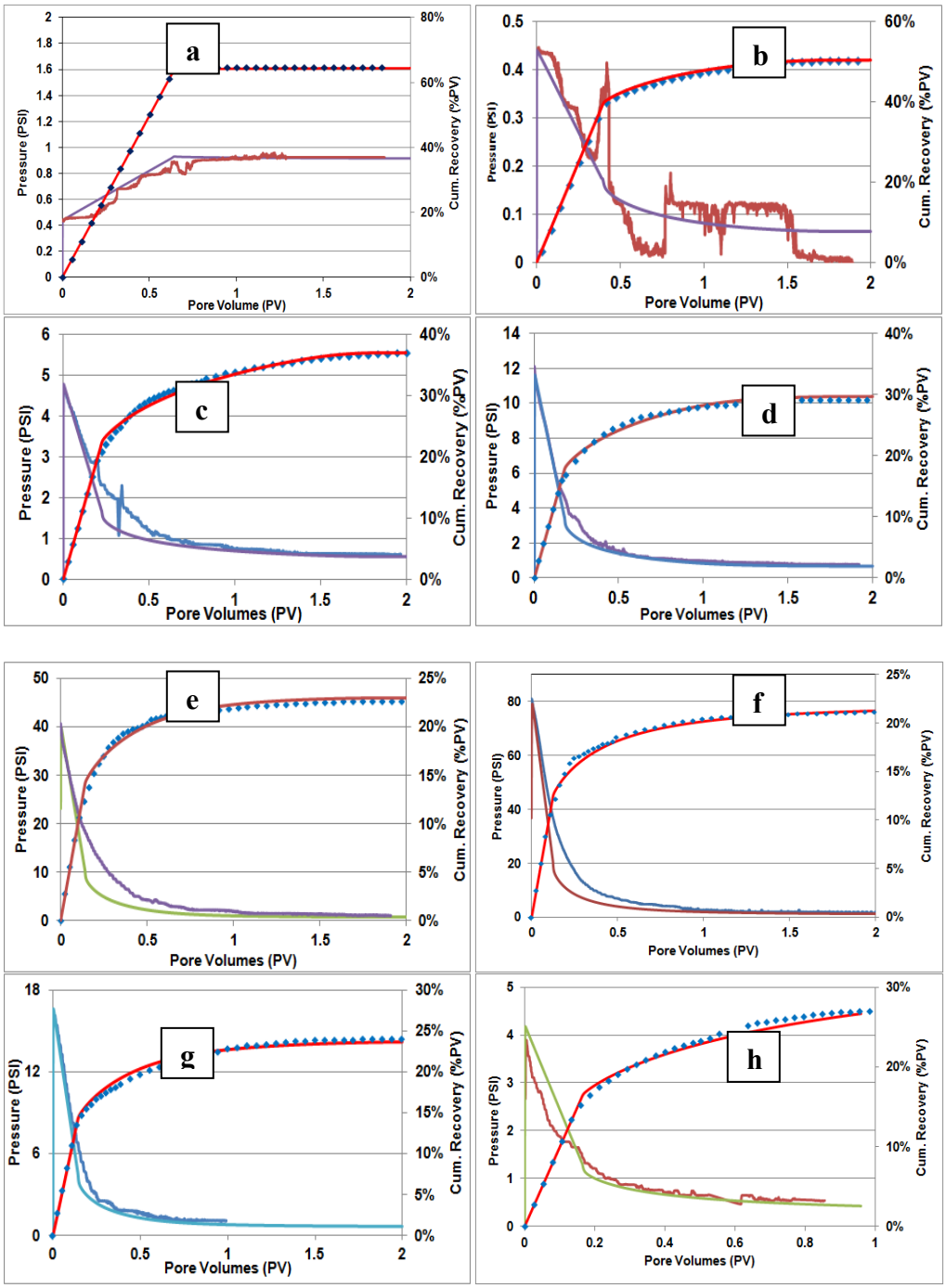

Figure 5.20: (a) Match of the unit viscosity ratio displacement (exp.1) and assumed relative permeability curve, (b-h) the match of the experimental data and simulations using the pseudo-relative permeability functions predicted by the proposed model.

Figures 5.21 and 5.22 show the oil-water pseudo relative permeability curves, respectively, for experiments 2-6 as predicted by the model using the base case relative permeability curves. The base case relative permeability curves of experiment 1 are shown by the dark black line. As the viscosity ratio is increased, the oil pseudo relative permeability curves drift towards left or towards a higher S_{or} (Figure 5.21). In the water pseudo relative permeability curve, the end point shift towards left and the curve in general shifts downwards (Figure 5.22). When the flowrate is decreased, the oil relative permeability curves drift back towards the stable case (Figure 5.23). This trend is not very prominent for water pseudo relative permeability as k_{rw}^{0} does not seem to increase with a decrease in flowrate or perhaps the change is unnoticeable experimentally (Figure 5.24).

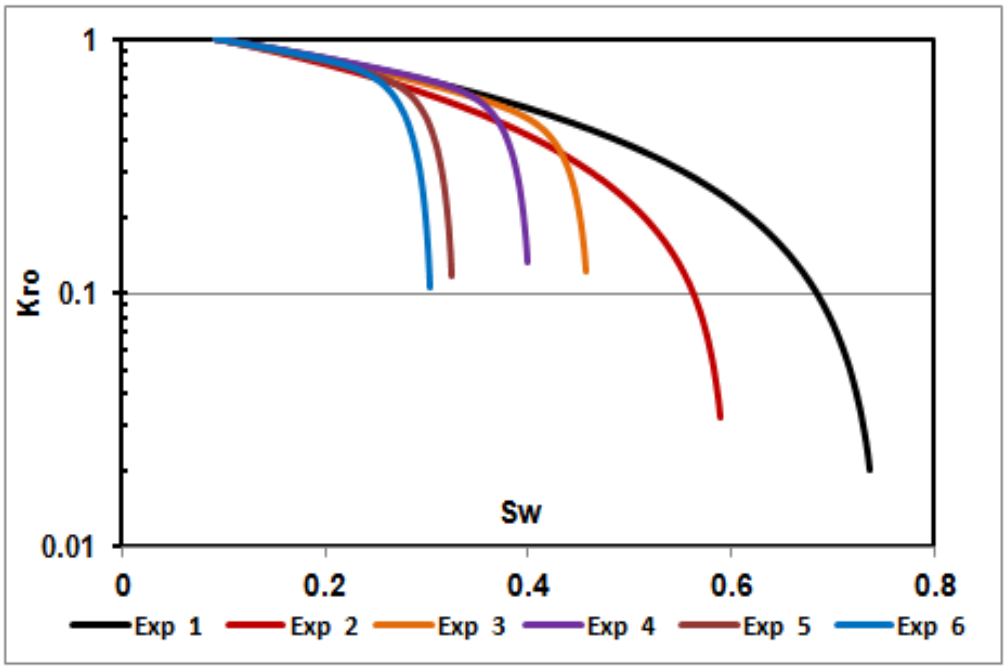

Figure 5.21: Pseudo relative permeability functions for oil phase predicted by the proposed model for different viscosity ratios

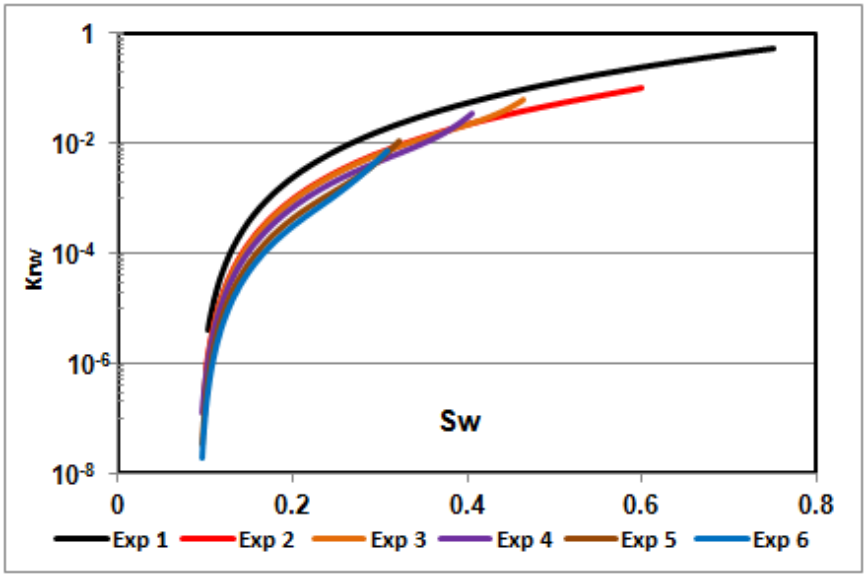

Figure 5.22: Pseudo relative permeability functions for water phase predicted by the proposed model for different viscosity ratios

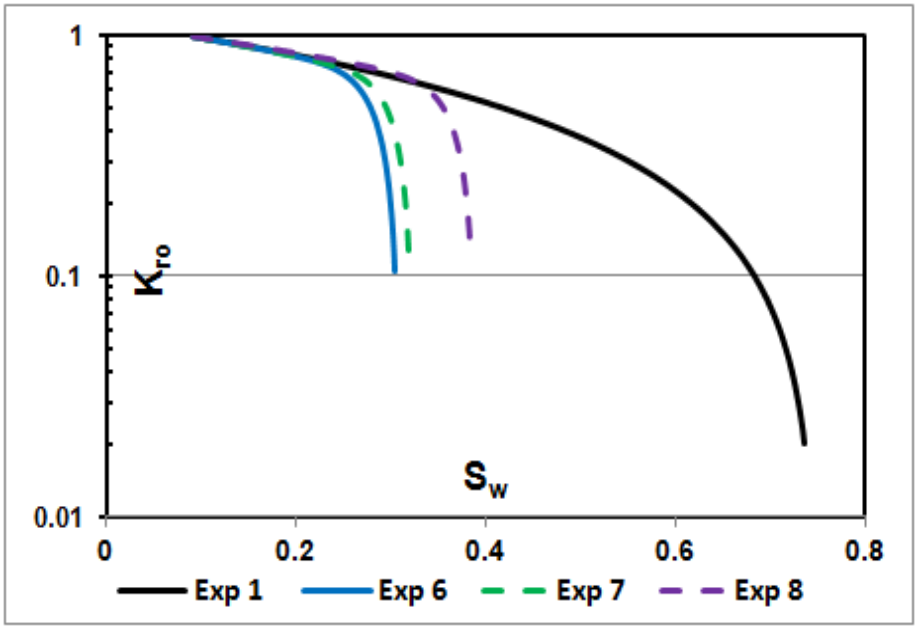

Figure 5.23: Pseudo relative permeability functions for oil phase predicted by the proposed model for different injection rates at a constant viscosity ratio of 10,500

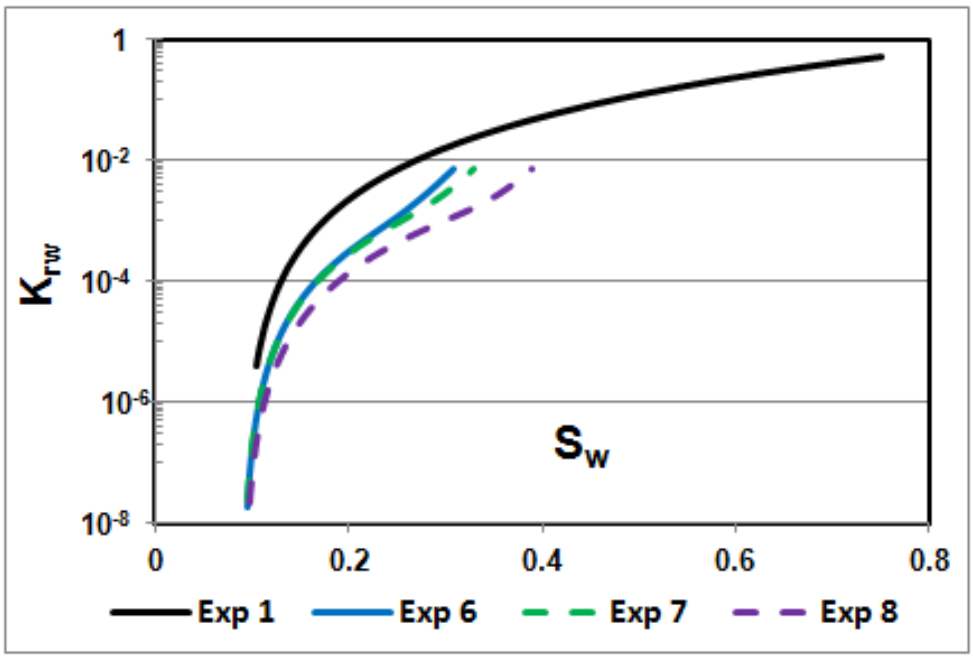

Figure 5.24: Pseudo relative permeability functions for water phase predicted by the proposed model for different injection rates at a constant viscosity ratio of 10,500

Table 5.4 shows the values of *a, b* and β that gave the best history match with the experimental results (Figure 5.20). Parameters *a, a+b* and β show a trend with both N_c and μ_r. As discussed earlier, the parameters *a* and *a+b* are essentially the initial and final widths of the lumped finger and they both decrease with the increase of viscosity ratios and increase with the decrease in flowrate. This trend is consistent with our observations in the micromodel.

	μ_r	K_{rw}^0	a	b	a+b	β	$N_C\mu_r^2$
Exp1	1	0.5	1	-	1	-	6.51E-06
Exp2	60	0.1	0.77	0.03	0.8	20	3.91E-04
Exp3	560	0.06	0.37	0.25	0.62	15	3.40E-02
Exp4	1440	0.035	0.25	0.29	0.54	12	0.225
Exp5	5200	0.011	0.16	0.27	0.43	9	2.934
Exp6	10500	0.007	0.14	0.27	0.41	7	11.963
Exp7	10500	0.007	0.18	0.26	0.44	9	2.393
Exp8	10500	0.007	0.21	0.31	0.52	11	0.598

Table 5.5: Values of lumped finger function parameter a, b and β for experiments 1 - 8

Just like the recoveries of experiment 1-8, the parameters *'a', 'a+b'* and *'β'* do not show any trend with only N_c or only μ_r. But when plotted against the dimensionless number $N_c\mu_r^2$ they show a consistent trend. Figures 5.25 – 5.27 show the fingering function parameters *'a', 'a+b'* and *'β'* with respect to $N_c\mu_r^2$. Parameters *'a'* and *'a+b'* show a power law relationship with $N_c\mu_r^2$ and *'β'* show a logarithmic fit with $N_c\mu_r^2$. K_{rw}^0 which was measured experimentally shows (Figure 5.28) a power law relation with only μ_r.

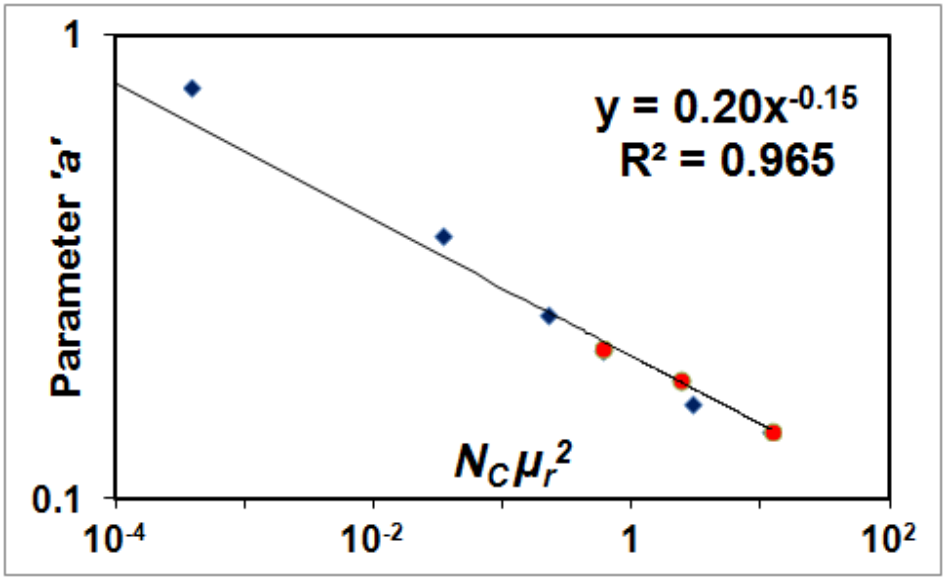

Figure 5.25: The parameter 'a' shows a power law trend with $N_c\mu_r^2$

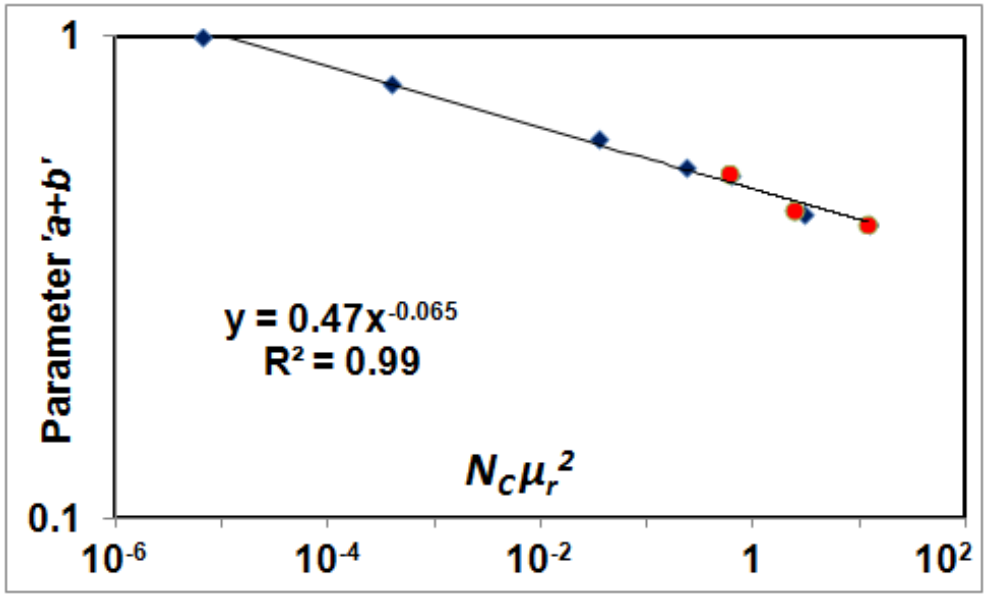

Figure 5.26: Parameter 'a+b', which is also the maximum area contacted by the water also shows a power law fit with $N_c\mu_r^2$

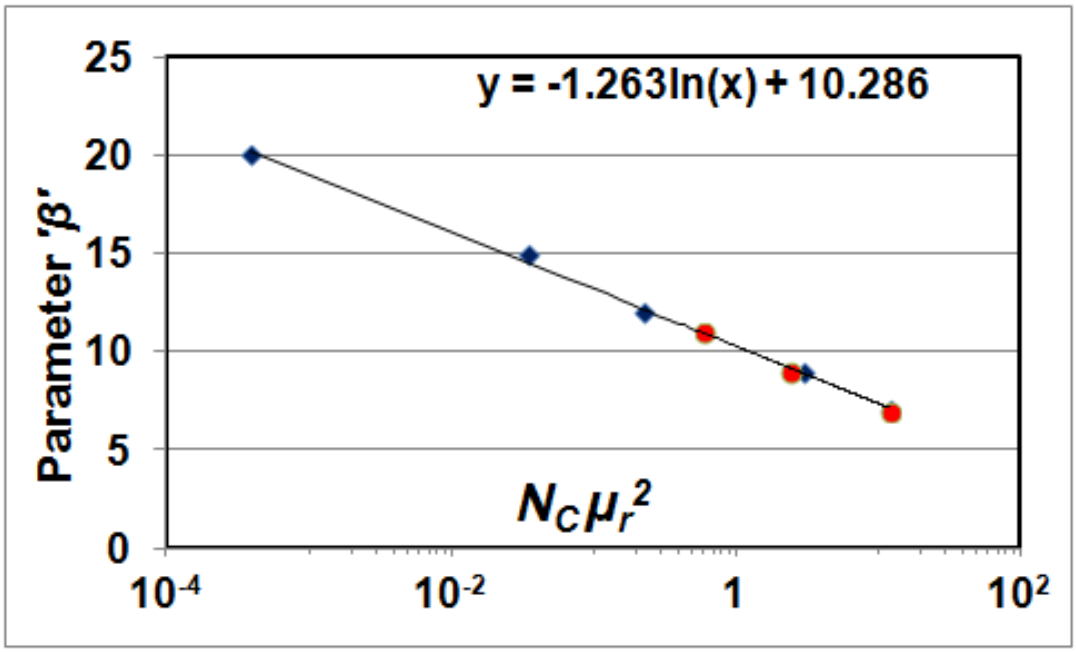

Figure 5.27: Exponent β shows a logarithmic relationship with $N_c\mu_r^2$

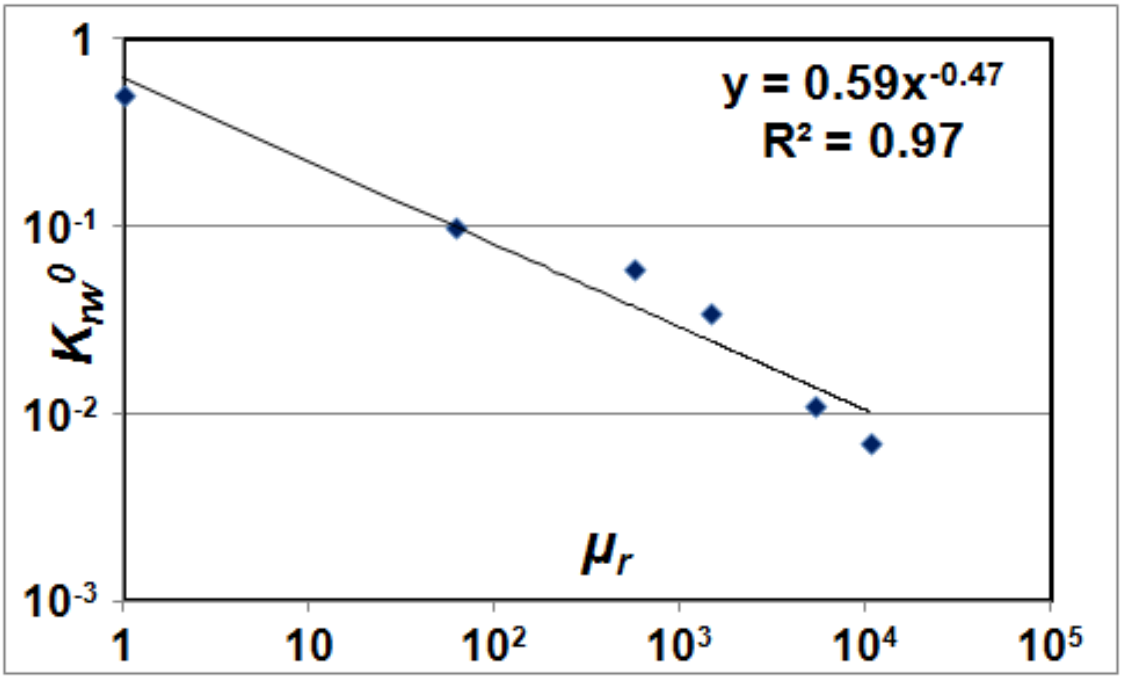

Figure 5.28: End point water relative permeability (K_{rw}^0) shows a power law trend with only viscosity ratio

This proves that the fingering function parameters *'a', 'a+b'* and *'β'* are not just random fitting parameters that are manipulated until a good history match with the experimental data is achieved. They are actually physical parameters that signify the shape of an averaged or lumped finger and therefore vary in a systematic manner showing a trend with $N_c\mu_r^2$. This implies that for a new system, parameters a, b and β can be interpolated or extrapolated to generate a new fingering function and a new set of pseudo-relative permeability curves. These pseudo-relative permeability curves would yield a more reliable pressure and recovery data.

5.2.3 Lumped Finger Model Summary

A model to predict the pseudo relative permeability for unstable displacement from a set of stable relative permeability curves has been developed. The model modifies the relative permeability based on the size of lumped finger width / cross-sectional area. Due to the physical nature of the model, the parameters governing the lumped finger are not just random fitting parameters, but are a function of $N_c\mu_r^2$. The model was not tested with experiments at different diameters but it is expected to be scalable with respect to $N_c\mu_r^2\left(D^2/K\right)$ as well. Several authors have experimentally observed the variation of heavy and viscous oils relative permeabilities with change in viscosity ratio, temperature and injection rate, but a reason or mechanism behind the observation was never explained. In this study we have not just described the mechanism for the observed pseudo trend, but have also developed model to predict it. Varying degree of instability causes this change in observed relative permeability. The dimensionless number $N_c\mu_r^2$ can be considered to be similar to the instability number proposed by Peters and Flock (1978). As our model just modifies the input to a conventional simulator, it can predict both expected recovery and pressure profiles accurately. This is an added advantage over

the Koval model or the modified Koval model that is often used to predict recovery trends for unstable immiscible floods (Jain & Lake, 2014), as the Koval theory does not predict the pressure trends.

This model can be useful in simulating the recovery of thermal displacement processes. During a thermal displacement a wide range of temperatures exist in the reservoir; different temperatures lead to different viscosity ratios and hence different recoveries. As our model already captures the effect of change in viscosity ratio it can be coupled with a function describing the change in viscosity ratio with temperature to include the thermal effect. The lumped fingering function can also be modified to include the effect of sub-grid heterogeneities if such data is available.

CHAPTER 6: CONCLUSIONS AND RECOMMENDATIONS

This chapter summarizes the major conclusions of this study. Both experiments and simulations were conducted in this research to better understand the unstable displacement in porous media and the phenomenon of viscous fingering. The conclusions of the experimental part of the study are discussed first, followed by the conclusions of modeling and simulation. Towards the end of the chapter some recommendations for future research have been suggested.

6.1 CONCLUSIONS OF EXPERIMENTAL STUDY

6.1.1 Conclusions of Polymer Flood for Viscous Oils in Carbonates

Based on the experiments conducted in the study following conclusions were made:

1) It was found that the timing of polymer flood is not very critical for a highly heterogeneous, preferentially water-wet reservoir with viscous oils in the range of 100 cp or above. The ultimate recovery was independent of polymer flood initiation time. There was no clear benefit of an early polymer flood.
2) Tertiary polymer floods conducted after waterfloods of viscous oils recovered more oil than secondary polymer floods in water-wet vuggy dolomite cores. This was also observed in mildly oil-wet dolomite cores although the difference was smaller.
3) The secondary polymer flood, of course, recovered the oil faster than tertiary polymer floods under constant injection rate conditions. This result may vary for a constant pressure injection condition.

4) In less water-wet cores, the tertiary oil recovery during polymer floods was lower and the recovery rate was slower as compared to water-wet cores. This was believed to be due to the slower imbibition rates in less water-wet cores.
5) In addition, spontaneous imbibition appeared to be slower for polymer solution than for water. Polymer took about thrice as long to produce same amount of oil in an imbibition experiment conducted on a water-wet Berea core.
6) Micromodel experiments proved to be useful to understand the interplay between viscous fingering, structural heterogeneity and wettability that lead to the higher ultimate oil recovery for a tertiary polymer flood in a water-flooded core.
7) Micromodel experiments showed that viscous fingering leaves behind mobile-connected oil in bypassed zones that can be recovered by a polymer flood. This mobile-connected oil is the reason for consistent tertiary oil recovery in all experiments. More oil is bypassed in a heterogeneous rock than in a homogeneous rock and hence, the potential for tertiary polymer flood is higher in a heterogeneous (carbonate) rock.
8) Micromodels replicated the trends of the coreflood experiments. They proved that the ultimate recovery is higher for tertiary polymer because the natural imbibition along high permeability channels makes more oils available to the tertiary polymer drive. However, natural imbibition is slower for polymer and hence the contacted oil is smaller and the final recovery is less.

6.1.2 Conclusions of Viscous Fingering in Porous media

Based on the experiments conducted in the study following conclusions were made:

1. In the micromodel experiments, it was observed that a flow pattern in two-phase displacement is dependent on both viscosity ratio and flow rate.

2. At low viscosity ratio the displacement is stable but as the viscosity ratios increases fingers become skinnier and the separation in between the fingers increase.
3. Fingers at viscosity ratios of around 10000 are highly fractal and resemble DLA like structures.
4. Lower injection rates make viscous fingers thicker and the displacement is more stable.
5. Coreflood experiments showed similar results. Oil recovery declined exponentially with increase in viscosity ratios and increased but at a slower rate during low rate water injection.
6. Effect of viscosity was found to be an order of magnitude higher than the effect of flow rate as both the breakthrough recovery and the overall recovery were scalable with respect to $N_c \mu_r^2$.
7. Scaling with respect to the system width can be introduced by multiplying with the dimensionless term of D^2/K. Under certain assumptions, the term $N_c \mu_r^2 \left(D^2 / K \right)$ was found to be similar to the instability number of Peters and Flock (1981).
8. The Peters and Flock (1981) instability number predicts a separate trend line for each viscosity ratio while $N_c \mu_r^2 \left(D^2 / K \right)$ predicts the same trend for all values of viscosity ratio and flow rate.
9. The dimensionless scaling number $N_c \mu_r^2 \left(D^2 / K \right)$ showed promising agreement with 8 experiments results from this study and 41 published results from the literature.

6.2 CONCLUSION OF MODELING AND SIMULATION

6.2.1 Conclusions of Extended DBM

Based on the similarities between dielectric breakdown and flow in porous medium, an extension of the existing DBM model was developed to predict viscous fingering patterns for all viscosity ratios. The major conclusions from the simulations conducted in the study are:

1. Extended DBM model was found to be a reliable model to simulate unstable displacement in two-dimension. It captures the different displacement regimes at different viscosity ratios and at different width.
2. The model is qualitatively consistent with the fingers observed in our 2D micromodel experiments and also with the published results for a larger 3D slab.
3. A correlation between the simulation parameter, η and viscosity ratio was developed for the 2D system by comparing simulations and micromodel results ($\eta = 10^{-5}\mu_r^{0.8775}$).
4. The model successfully captures the effect of aspect ratio on unstable displacement. A stable displacement is not at all affected by the variation in core diameter but the unstable displacement is adversely influenced by the increase in domain width.
5. The model helped in testing the dimensionless scaling term, $N_c\mu_r^2\left(D^2 / K\right)$ with respect to variation in domain width (D). The results of the simulations proved that the correlation $N_c\mu_r^2\left(D^2 / K\right)$ is consistent as the results of all the simulated recoveries at different viscosity ratio and different dimensions were scalable with respect to $N_c\mu_r^2\left(D^2 / K\right)$.

6.2.2 Conclusions of Lumped Finger Model

Capturing detailed fingering is not critical at field scale; an averaged model that mimics the effects of viscous fingering with a large grid size is technically more desirable at field scale. Lumped finger model was developed as one such model and the major conclusions of the model and its simulations are:

1. The lumped finger model modifies the standard relative permeabilities to develop a set of pseudo relative permeability functions that can capture the effect of viscous fingering in a 1D simulation.
2. The fingering function λ ($\lambda = a + b\bar{S}^{\beta}$) varies as function of both viscosity ratio and capillary number, i.e., the shape of the lumped finger is a function of viscosity ratio and capillary number.
3. The parameters of the fingering function, (a, b and β) were also found to be scalable with respect to $N_c \mu_r^2$. Although they were not tested, but it is hypothesized that they will be scalable with respect to $N_c \mu_r^2 \left(D^2 / K \right)$ as well.
4. The pseudo relative permeability curves predicted from the lumped finger model shows a good match with the experimental oil recovery and the pressure drop data.

The lumped finger model could be a useful model for capturing the effect of viscous fingering at a larger scale without the requirement of very fine grid simulations. Model can be useful in simulation thermal displacement of heavy oils if viscosity ratio as a function of temperature is known. Sub-grid heterogeneities can also be included in the model by introducing some change in the lumped fingering function. A correlation between sub-grid heterogeneity and the parameters of the lumped finger model needs to be developed in future.

6.3 RECOMMENDATIONS

Based on the experiences gained during this research some suggestions and recommendation are proposed for further research in this area:

1. Displacement of heavy oil in heterogeneous carbonates should also be conducted at constant pressure as the flow rates in the field are constrained by the allowable pressure and the observed field rates for viscous oils will be much less than 1 foot/day. Also, under constant pressure conditions polymer injection rate will be much slower than the injection rate of water. This may imply that above a critical polymer viscosity value polymer may not recover oil faster than water.
2. A secondary polymer flood with slowly increasing polymer concentration may provide both imbibition and mobility control benefits. This could be tested in an experiment and compared with secondary and tertiary polymer floods.
3. Visualizing the displacement in carbonate rock slabs was attempted (without any success) during this study. Scanning a core or a slab using a high resolution CT scanner or an X-Ray radiograph could yield results that are critical in further understanding the recovery mechanism.
4. Micromodels experiments should be conducted in longer micromodels to make sure that the results are not influenced by entrance and end effects.
5. Using a higher resolution imaging device for the micromodel experiments will help in getting pore level details and the full scan simultaneously. With the current imaging system, during full scan the pore level details are mostly lost.
6. Considering the small pore volume of the micromodels, system compressibility can lead to delayed flow response especially for heavy oils experiments that

requires high flow pressure. Use of metal tubing along with a hard plastic or metal syringe with a hard piston would reduce such problems.

7. All the eight unstable core-flood experiments during this research were conducted on a single water-wet core. Repeating these experiments on cores of different diameters will be helped in experimentally verifying the accuracy of the scaling parameter $N_c \mu_r^2 \left(D^2 / K \right)$. Core holders are available for cores up to 4 inch in diameter. For higher diameters, tightly packed sand packs will be a better alternative.
8. Repeating similar experiments on an oil-wet core and a mild water-wet core could help us understand the effect of wettability. A scaling term for wettability could also be added to the $N_c \mu_r^2 \left(D^2 / K \right)$ correlation.
9. Lumped finger model could be incorporated in a thermal simulator as it captures the effect of viscous fingering at different viscosity ratio.

APPENDIX A: MICROMODEL FABRICATION PROTOCOL

This section lists the materials required for micromodel fabrication and outlines the directions and safety methods to be enforced during the process. The fabrication procedure is similar to that followed by Seright et al. (1991). Table A.1 below shows the detailed list of solutions required during the fabrication process along with their purpose, composition and handling and storing instructions.

Purpose	Chemical/composition	Handling and storing
Mirror-backing strippers	Methylene chloride	(Store only in glass. Use only in a glass or steel pan.)
Copper stripper	60% Nitric acid 40% Distilled water or Copper etchant ($FeCl_3$)	Store in acid resist/spill container
Glass etcher	110 g Ammonium hydrogen difluoride 600 ml Distilled water 15 ml Sulfuric acid Bring up to 1 liter with distilled water	(Store and use only with fluorine-proof materials.)
Photo Resist	DuPont Riston Etchmaster EM 213 dryfilm photoresist.	Store in dark room.

Table A.1: List of chemicals required for micromodel fabrication

Glass micromodel fabrication involves the use of hazardous chemicals. Proper training in handling such chemicals and use of safety equipment is necessary. Commercially available mirror glass plates are preferably used in glass micromodels

fabrication. Mirror glass plates are preferred as the metallic coating (Cu and Ag) provided better adhesion with the photoresist and also serves as a second layer of defense against HF during the etching phase.

Mask

The first step in glass micromodel fabrication requires designing of the complex pore network pattern that needs to be etched on the micromodel. A detailed pore network pattern is designed digitally on a computer using commercial software like Adobe Illustrator or Auto-CAD. Illustrator or CAD formats are preferred as they are vector images and not graphic pixilated images. Vector images can be scaled up without any loss of resolution. The pattern is then printed onto a transparent mylar sheet using a high resolution laser printer. The print job was commissioned to CAD/Art Services, Inc. Bandon, Oregon. A printer of at least 4000 dpi is required to capture resolution of a few micrometers. Features lower than 10 microns cannot be captured in this printing. Figure A.1 shows an example of few basic mask patterns that can be used for micromodel fabrication. The masks were designed in Adobe illustrator. The essential feature of each of these masks is the fluid distribution ports that deliver the fluid into the pore network at the inlet and carry it away at the outlet.

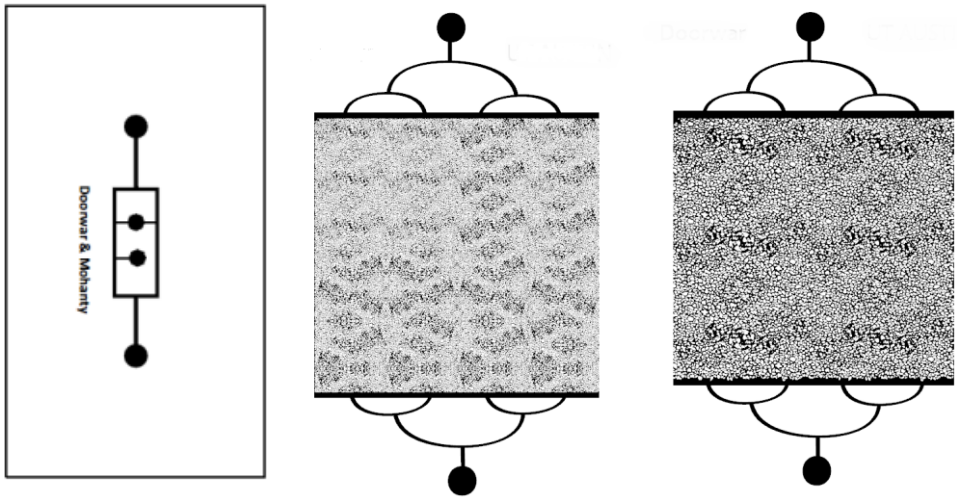

Figure A.1: Samples of the mask of the pore pattern

Photo-resist

Several different photo-resists are commercially available from several suppliers. The Du-Pont Etch-master thin film photoresist was used in this study. The Du-Pont Etch-master thin film photoresist is a negative acting photoresist; this means that the photoresist hardens when exposed to light and the unexposed part gets washed off by the developer solution. In our case, the black region in the mark will remain undeveloped and will get etched. If a positive acting resist is used then the polarity of the image must be reversed i.e. the black region in the mask should be white and vice-versa.

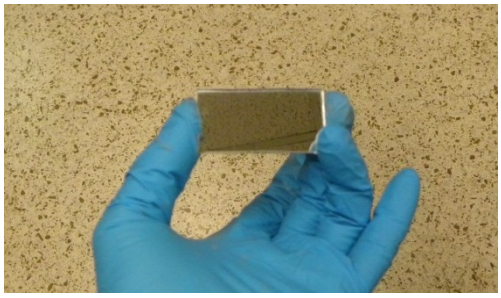

Figure A.2: A mirror piece cut to the desired size

Mirror tiles

The 12“X12“ mirror panels were bought from ERIASTM and were later cut into desired shapes at the glass workshop in the department of Chemistry at UT Austin. Commercial mirrors are sold with typically two layers of protective backings to guard the underlying reflective silver/copper layer. Generally there is a red layer of soft paint to prevent the silver against oxidization on exposure and a hard paint layer to protect the red paint. The hard paint layer is removed using Methylene chloride as the paint stripper. Methylene chloride is highly volatile and should only be used in a well ventilated fume hood.

PROCEDURE

Preparing the glass

Place the mirror in the solution with the backing side facing up and then pour enough stripper solution onto the mirror to submerge it. Use a glass or metal container as methylene chloride reacts with some plastics. It took about 5 to 10 minutes for the backing to soften and peel off with slight scrubbing. Scrubbing should be done with soft hands using a wooden stirrer. Some commercial mirrors have a hard paint backing that does not react with methylene chloride. In such cases, use a solution of sodium hydroxide and iso-propyl alcohol. When the hard paint backing is completely removed, the underlying red paint and silver layer are exposed. (Figure A.3).

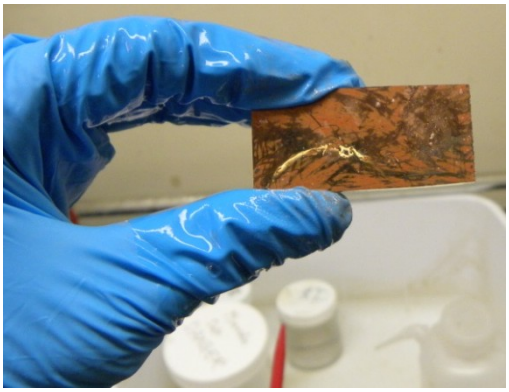

Figure A.3: The silver/cupper backing of the mirror along with some red backing

The red paint layer can be scrubbed off easily by rubbing with a cotton pad dipped in acetone. Use liberal amount of acetone to avoid hard scrubbing and scratching the silver layer. The shiny metal layer is now exposed. (Figure A.4). The plate should then be washed in running water with a non-abrasive soap and then air dried. Any visible traces of paint should be removed. A good test for cleanliness of a surface could be judged by pouring some water on it and allowing it to drain. If all the water drains, leaving no water beads, the surface is clean. If water sticks to the glass, rinse it again in acetone followed by soap water (Figure A.5).

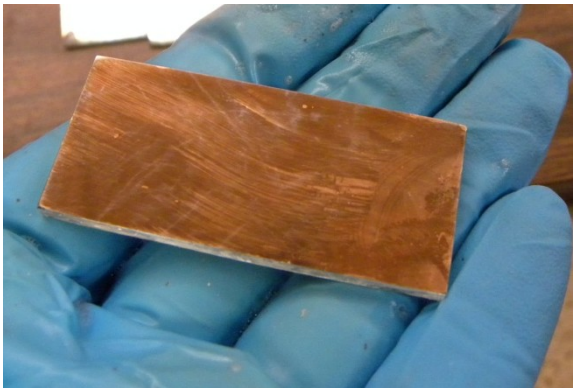

Figure A.4: A clean shiny silver surface of the mirror exposed after the paint removal.

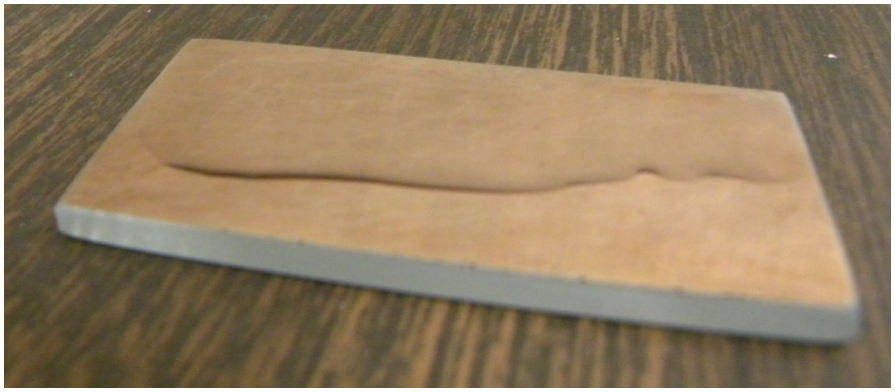

Figure A.5: A water film indicates that the silver backing of the glass is clear of impurities

It should be ensured that the cupper surface is not severely scratched. This can be done by quickly looking at a light source through the metal coated side. A badly scratched surface should either be discarded or used as the cover plate during the fusing step. It is a good idea to avoid using it for applying a photo-resist coating.

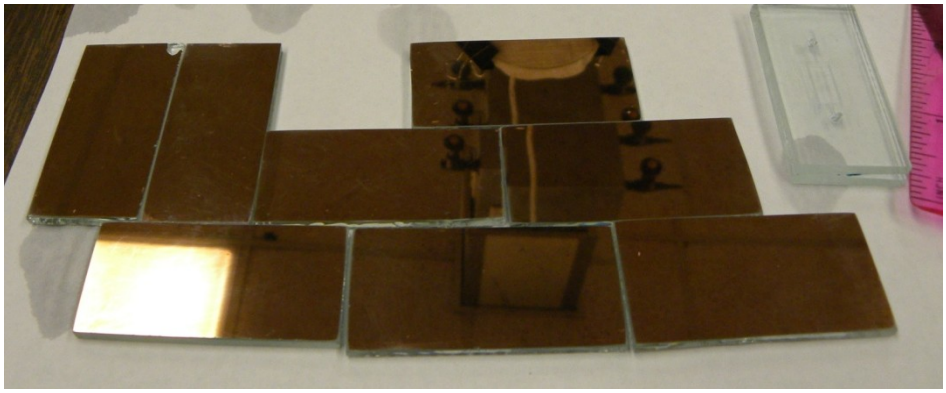

Figure A.6: Scratch free silver backing on several clean mirrors

Photo-lithography

This part of the study should be done in a dark room with yellow lights. The cleaned metal coated glass plates were laminated with the negative acting dry film

photoresist. DuPont's etchmaster photoresist is sold as a thin plastic sheet and the photo-active layer is sandwiched in between two protective plastic foils. The softer translucent plastic sheet should be peeled first to expose the photoresist layer. The photoresist layer is sticky and hence care should be taken to avoid any trapped air bubble in between the film and the plate. Wet lamination is more effective and produces a bubble-free laminated surface. For wet lamination, spray DI water over the metal coated side and slowly lower the photoresist film over the plate. Roll a soft rubber or plastic rod from one side to squeeze out the water layer as shown in Figure A.7.

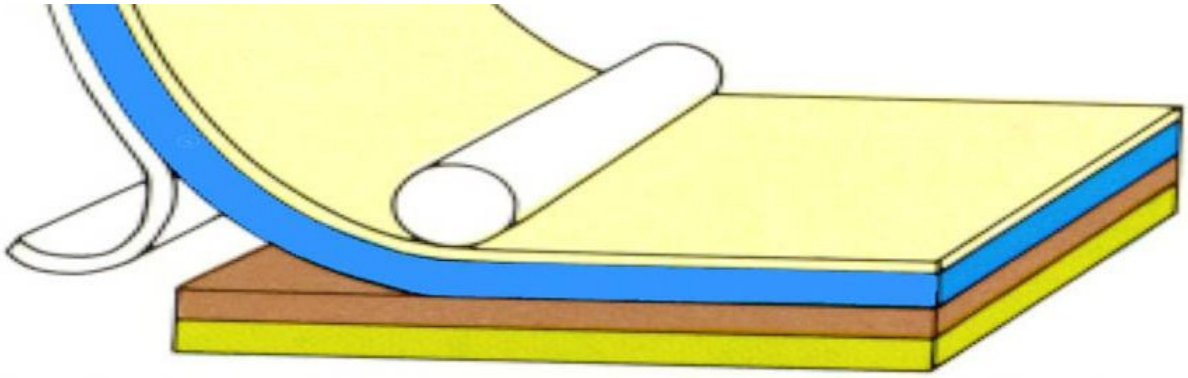

Figure A.7: A schematic showing the wet lamination technique using a soft roller

After lamination, wipe of the excess water from the glass chip. Heat makes the photoresist bond well with the glass. The glass plate was rolled under two layers of paper and gently pressed using a medium hot electrical iron for about 10-15 seconds. Allow the glass to cool down before initiating the next step. Place the transparent mask over the photoresist coated metal side with the emulsion side facing down. It is advised to have some text printed on the sheet along with the pore pattern. This helps as a marker for the emulsions side. Cover the mask with a clean glass panel to ensure prefect contact between the photoresist and the mask.

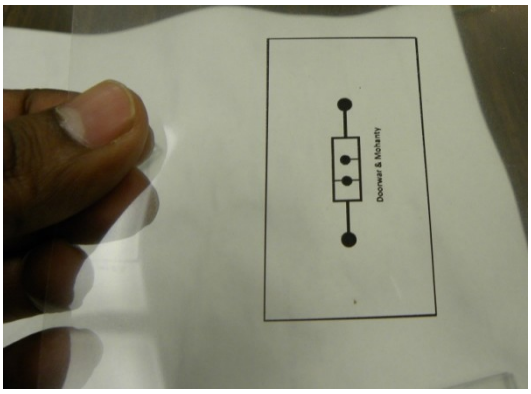

Figure A.8: A sample print mask on a transparent mylar sheet.

`The plate was then exposed with UV light. The UV light source used is a 6W Entela Model UVL-56, 365 nm long wave ultraviolet light source. The photoresist used is most sensitive to UV light in 365 nm wavelength. The time of exposure varies from pattern to pattern depending on the detailing in the printed mask. Some trial and error is required to get the exact time. If the photoresist is underexposed the print pattern will appear fuzzy and will be washed off. If the resist is overexposed the unexposed area will not be fully washed and etching will not be good. The Dupont riston dryfilm is light blue in color and changes to darker blue when exposed to UV. As a result, the unexposed region or the black area of the mask appears lighter over the copper coating. Once the exposure in complete, the mask can be removed and the other harder plastic cover over the photoresist can be peeled off. The glass slide can now be immersed in the developer solution for development. The developer solution recommended for Riston photoresist is 1% by weight solution of $NaHCO_3$ in DI water. The unexposed region of the micromodel gets washed off in 5 – 10 minutes and the underlying shiny copper surface is exposed (Figure A.9).

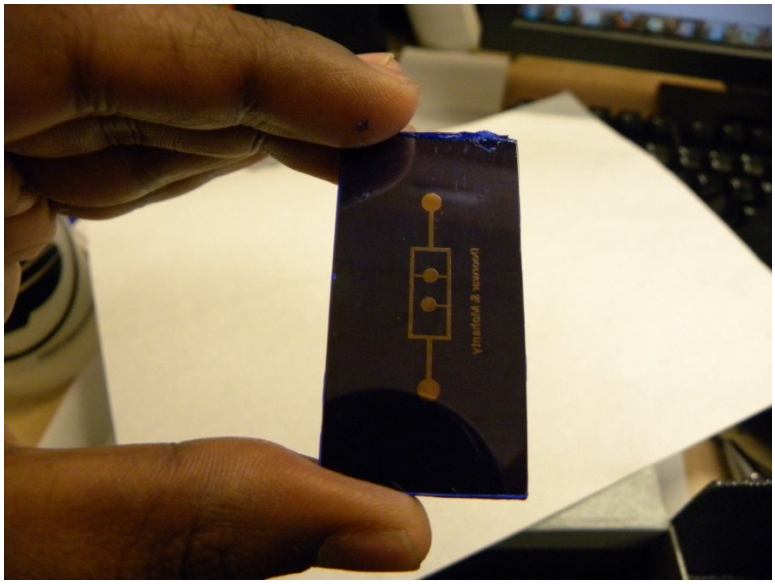

Figure A.9: A fully developed slide after photolithography step

Inspect for traces of unwashed/undeveloped photoresist before bringing the photoresist outside the dark room. The developed glass slide is washed under running tap water and dried in air. It is recommended that the holdup time after developing should not be more than couple of days. Before proceeding with etching the exposed metal layer has to be removed. This should be done by softly applying the copper etchant using a cotton swab. This removes all the Cu/Ag from the channels to be etched exposing the glass underneath. Nitric acid being a strong acid reacts with the photoresist causing loss of tiny details. Ferric chloride being a weaker copper etchant, slowly etches the copper without affecting the photoresist. Ferric chloride was purchased from Sigma Aldrich.

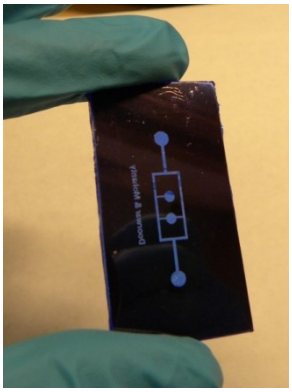

Figure A.10: Picture of the glass slide after nitric acid or copper etchant treatment. Printed channels now become transparent.

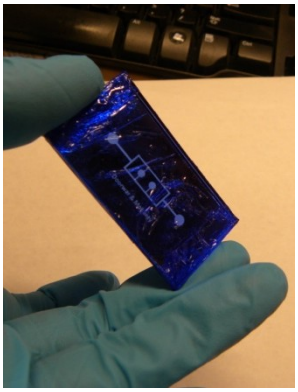

Figure A.11: Last step before etching, the glass slide completely wrapped in HF resistant tape or photoresist with only the etched section exposed.

Etching

Before immersing the slide in the HF solution ensure that only the glass surface that needed to be etched is exposed to HF. Rest of the glass can be protected by coating it with wax, electrical insulating tape or parafilm. The glass etchant solution described in the Table A.1 was prepared in a small glove box that was specially designed for storing HF and is constructed with fluoride resistant plastic. Figure A.12 shows the glove box used for synthesis, storage of HF. A demonstration of proper lab attire with all the

personal lab safety gears required while working with HF is shown in Figure A.13. A layer of short neoprene or nitrile gloves should be worn under a pair of long butyl gloves. A rubber apron should be worn over a full sleeve lab coat along with a face shield to cove the facial area. A calcium gluconate gel should be stored in the vicinity of the glove box to be use immediately after any skin contact.

Figure A.12: The HF resistant glove box used for synthesis, storage and etching using HF

Figure A.13: A demonstration of proper lab attire with all the personal lab safety gears required while working with HF

For the final glass etching, place the glass plate pattern side up in a tray filled with glass etcher for some calculated amount of time. For the concentration described in Table A.1, etch rate of about 1.5 micrometer per minute was observed. However, the rate slows down after 30 minutes due to build up of the reactants in the channels. This can be avoided by stirring or agitating the solution while etching. Agitation was avoided to prevent the risk of spilling the etching solution and scratching the resist while stirring.

At the end of the etching cycle, carefully lift the sample and dip it in a big container of water. The water in this container should be discarded in a liquid waste container and not in the drain. Use a forceps for transferring the plate in between the solutions, to avoid any contact with the acid. After 5 min. of soaking in water pull the

sample out and let it sit under running water for another 2 minutes. The photoresist and all the other protective coatings can now be removed to get the etched glass unless a second round of etching is desired. A second round of etching is typically used to introduce heterogeneities by etching a certain section of the micromodel deeper than the rest.

For a second-stage selective etching, molten wax was used to cover the rest of the micromodel leaving only a selected pattern exposed to HF for a second round of etching. The chip was then submerged again in the HF mixture for a set amount of time. After the second stage of etching, wash the chip as described earlier.

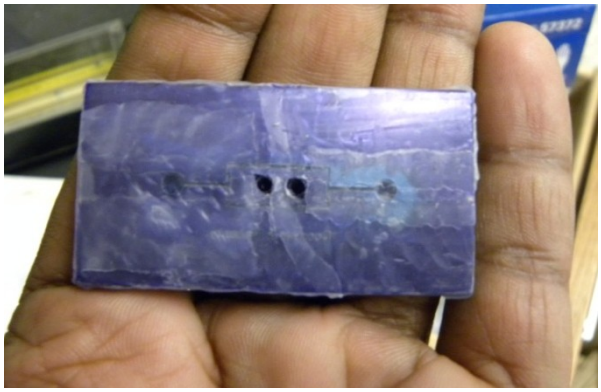

Figure A.14: A wax coated slide with only two exposed holes for the second round of selective etching

Preparing for fusing

At the end of etching, all the protective layers of material like electrical tape, wax, photoresist and copper need to be removed to get a clear etched glass. Wax can be washed off easily by soft scrubbing in hot water. DuPont EtchMaster resist is soluble in acetone and can be removed after 5 mins of immersion in acetone. The underlying Cu layer is exposed at the end and should be dissolved using the nitric acid or the copper

stripper. Inspect the clean glass under microscope to confirm that the pore pattern is uniformly and neatly etched. Also confirm the etch depth by using a stylus profiler. Before fusing, inlet and outlet hole will have to be drilled in the glass plate. Two 0.5 mm diameter holes were drilled using a diamond bit at the inlet and outlet ports of the etched plate. For each hole it is recommended to drill half way through from either side of the plate. This procedure will minimize the chances of cracking the glass while drilling. The ports were drilled by the professional technicians at UT glass workshop.

Fusing

The last step in the fabrication of the glass micromodel requires fusing of the etched plate and a cover plate. A cover plate of exactly the same dimensions as the etched plate is chosen and should be of the same material as the etched plate. If the composition of the two glasses is not the same the fusing will fail. This is because different glasses have different expansion and contraction coefficients, so after bonding at high temperature both the plates contract at a different rate which builds the stresses in the glass and it breaks. The etched plate and the cover glass plate are glued at the corners to prevent slipping. The glued plated are then placed on a flat borosilicate glass plate separated by a sheet of fire shelf paper. The borosilicate prevents the glass from coming in contact with the rugged surface of the furnace and fire-shelf paper prevents the glass from fusing with borosilicate glass. The softening temperature of a borosilicate glass is as high as 850^{o}C and is therefore a safe choice for fusing process below 800^{o}C. The fire shelf paper turns into a layer of white ash at the end of the process but gives a smooth and clear finish to the glass.

The plates were fused in a high temperature furnace and the routine shown in Table A.2 was followed. The step-wise heating cycle is used to prevent the glass from cracking due to a heat shock. Step 3 and 4 are the most critical steps of this 6 step cycle

and should be executed for at least the duration of time mentioned alongside in Table A.2. If steps 3 and 4 are rushed, the fusing will be patching and incomplete. At the end of the fusing step the micromodel will be ready for experiments.

	Furnace Temperature	**Duration**
1	200^{o}C	60 mins
2	400^{o}C	60 mins
3	545^{o}C	60 mins
4	690^{o}C	120 mins (at least)
5	545^{o}C	60 mins
6	25^{o}C	Overnight cooling, Furnace off.

Table A.2: The temperature cycle used in the furnace for glass fusion

APPENDIX-B PORE SCALE EXPLANATION OF $\mu_r^2 N_c \left(D^2/K\right)$

A more mechanistic explanation of the origin of the scaling factor, $\mu_r^2 N_c \left(D^2/K\right)$ term can be provided by comparing the capillary dominated and the viscous dominated flow at the pore scale.

A capillary pore doublet model is commonly used to explain the capillary de-saturation curve for the steady state for capillary driven displacement. Figure B-1 (a) shows a typical capillary doublet model. Let us assume that phase A (blue) is the wetting phase, phase B (red) is the non-wetting phase. The flow direction is from left to right. First, let us consider the capillary-driven displacement of light oil with water. The moment, water (phase A) reaches the doublet intersection. The capillary forces pull the water into the thinner throat much faster than it gets pulled into the other branch. As a result meniscus in the thinner branch will reach the exit junction faster and some oil (phase B) will be trapped in the wider branch of the doublet (Figure B-1 (b)). Now, if we increase the injection velocity such that the influx at the inlet junction is higher than what is satisfied by the capillary imbibition, water will be diverted into the wider branch of the doublet (path of least resistance). As a result at, Q_2 injection rate, the meniscus in the wider branch will move further into the capillary than before (Figure B-1 (c)). At one particular flow rate, both the menisci will reach the exit junction at the same time and the residual will be at its minimum Figure B-1 (d). So essentially, it is the ratio of time taken by each meniscus to move from the entry to the exit that determines the residual oil saturation. For light oils, it is fairly accurate to assume that all the capillary movements occur instantaneously and therefore the time is not an important factor, but the ratio of the forces driving the two menisci (capillary number) is considered a better predictor of the de-saturation trend. This may not be very effective for systems where equilibrium is not instantaneous.

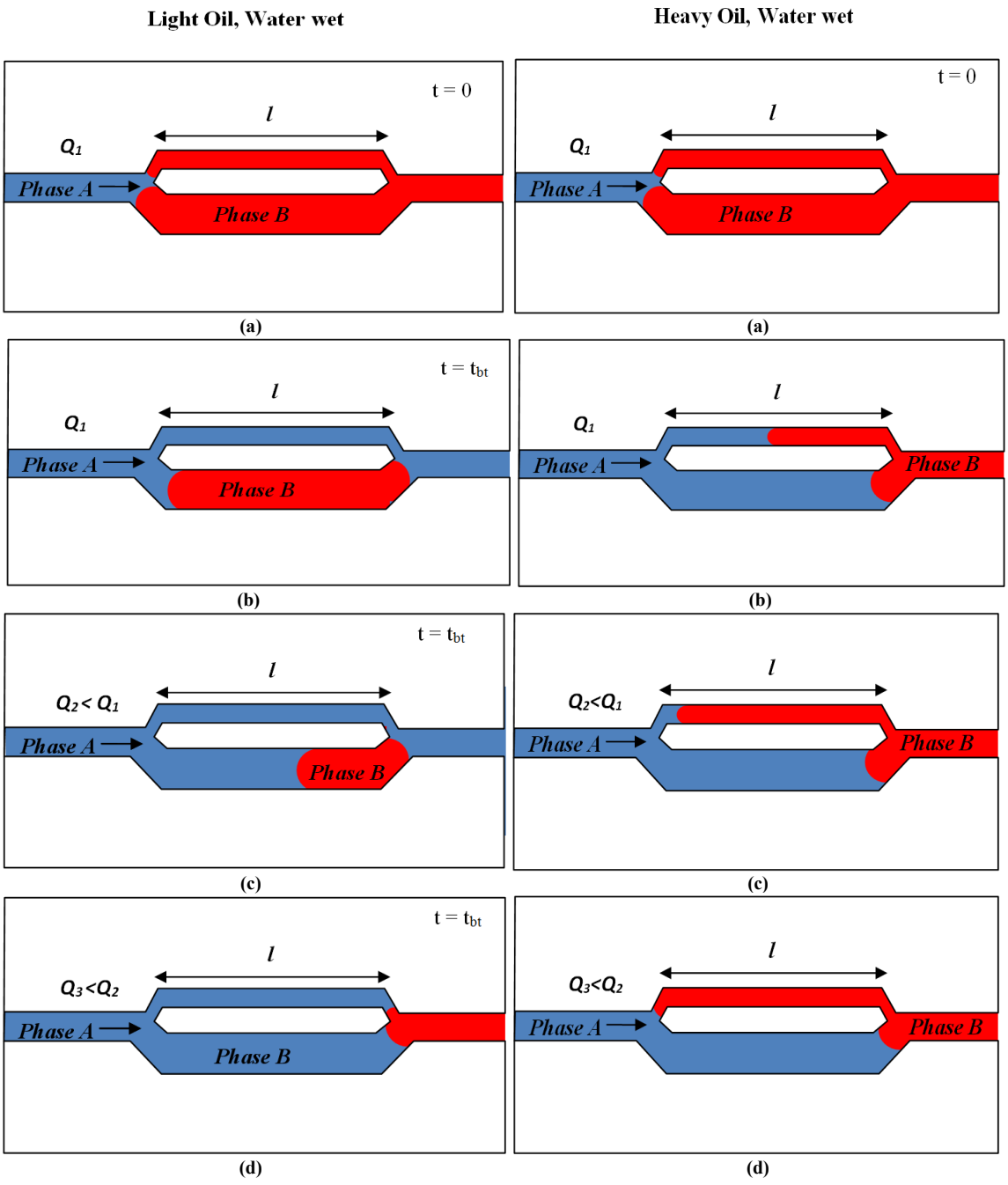

Figure B-1: Capillary de-saturation for light oils explained by the pore doublet model

Figure B-2: Capillary de-saturation for heavy oils explained by the pore doublet model

For the same doublet model, same wettability and surface tension; if the displaced phase B is replaced by viscous oil (say 1000 time higher viscosity), the pore level physics will change drastically. In this case, the capillary equilibrium will not be instantaneous as the fluid being displaced by the same amount of capillary force offers 1000 time higher resistance. As a result, at the same injection rate (Q1) as Figure B-1 (a and b) more flow will be diverted to the path of least resistance (wider branch). Figure B-2 (a) –(d) shows the pore doublet response to change in flowrate for viscous systems. At higher velocity, we are allowing less time for imbibition and therefore the meniscus in the slimmer throat will be further away from the exit junction. If we inject slower, we allow more time for imbibition and therefore we leave behind lesser residual. Clearly, for this case the relationship with flow rate is inverse. In this case, the competition between the time of imbibition and time of viscous flow will be a more consistent definition than the force competition.

Assuming a simple bundle of capillary tube system, the time of imbibition can be calculated by the Washburn's equation. According to Washburn's equation,

$$\text{Time of imbibition} = T_{imb} = \frac{4l^2\mu_o}{\sigma_{ow}d} \tag{4.14}$$

where, l is the length of the capillary, d is the diameter. Viscosity of the oil is used in the system as the more viscous phase will dictate the imbibition time. Time for viscous flow can be given by the ratio of length of the capillary over the interstitial velocity.

$$\text{Time of viscous flow} = T_{Visc} = \frac{l}{v_{\text{int}}} \tag{4.15}$$

Therefore, the new dimensionless ratio of time scales will be,

$$\frac{T_{imb}}{T_{visc}} = \frac{4l\mu_o v_{\text{int}}}{\sigma_{ow}d} \tag{4.16}$$

As defined earlier,

$$v_{\text{int}} = \frac{Q_w}{\phi A(S_{oi} - S_{or})} \tag{4.17}$$

and

$$v_w = \frac{Q_w}{\phi A} \tag{4.18}$$

hence,

$$\frac{T_{imb}}{T_{visc}} = \frac{4l\mu_o v_w}{\sigma_{ow} d(S_{oi} - S_{or})}, \tag{4.19}$$

by multiplying and dividing by $\mu_{w,}$ we get

$$\frac{T_{imb}}{T_{visc}} = \frac{4l\mu_o v_w}{\sigma_{ow} d(S_{oi} - S_{or})} \times \left(\frac{\mu_w}{\mu_w}\right) \tag{4.20}$$

Equation 4.20 can be rearranged in terms of N_c and μ_r

$$\frac{T_{imb}}{T_{visc}} = \frac{4l}{d} \times \left(\frac{v_w \mu_w}{\sigma_{ow}}\right)\left(\frac{\mu_o}{\mu_w}\right)\left(\frac{1}{S_{oi} - S_{or}}\right) = \frac{4l}{d} \times N_c \mu_r \times \left(\frac{1}{S_{oi} - S_{or}}\right) \tag{4.21}$$

The term S_{oi}-S_{or} is the area available for water to flow during a water flood. From our micromodel experiments it is known that this is not a constant but is critically dependent on the viscosity ratios (Figure 4.18). The difference S_{oi}-$S_{or,}$ is higher when the viscosity ratio is smaller and vice versa. Therefore, there is an inverse correlation between the two and can be expressed as,

$$S_{oi} - S_{or} = B\left(\frac{1}{\mu_r}\right)^{\psi} \tag{4.22}$$

where B is a proportionality constant and ψ is an exponent. Substituting 4.22 in 4.21, we get a new dimensionless number,

$$\frac{T_{imb}}{T_{visc}} = \frac{4l}{d} \times B \times N_c \mu_r^{1+\psi} \tag{4.23}$$

From equation 4, we see a correlation similar to $\mu_r^2 N_c$ for ψ = 1.

This new definition based on competition of time scale of imbibition and viscous flow is more robust. For low viscosity systems, as $\mu_w \rightarrow \mu_o$ the ratio $\mu_r^2 N_c$ converges to N_c, suggesting that for light oil only capillary number dominates the residual oil saturation.

NOMENCLATURE

a - Parameter of fractional finger width
A – Area of cross section. cm^2
b - Parameter of fractional finger width
B – Proportionality constant
C – Chouke's constant
C^* - Wettability number
C_f – Average solvent concentration
d - Diameter of a pore
D – Diameter of a core
E - Effective viscosity ratio for Koval theory
g – Gravitational acceleration
H – Heterogeneity constant for Koval Theory
I_{sc} – Instability number of Peter and Flock (1981)
K – Absolute permeability
k – Relative permeability
K_{rw} - Relative permeability of water
K_{ro} - Relative permeability of oil
K_{ro}^{0} – End point relative permeability of oil
K_{rw}^{0} - End point relative permeability of water
$K_{roPseudo}$ – Pseudo relative permeability of oil
$K_{rwPseudo}$ – Pseudo relative permeability of water
l – Length of a pore
L – Length of a core
L_x – Length of a block in x direction
L_y - Length of a block in y direction
M – Mobility ratio
n_o – Corey exponent for oil
n_w – Corey exponent for water
N_c – Capillary number ($v_w\mu_w/\sigma$)
N_{c_visc} – Modified capillary number ($v_w\mu_o/\sigma$)
N_g – Bond's number
P_{ij} – Growth Probability
Q – Volumetric injection rate
S_w – Water saturation
$\overline{S}_w$ – Cross-sectional averaged water saturation
S_{oi} – Initial oil saturation
S_{or} – Residual oil saturtion
S_{wmax} – Maximum water saturation at the end of a core flood
S_{wi} – Initial water saturation
T_{imb} – Time taken for imbibition in a pore
T_{visc} – Time for viscous flow in a pore

U - Superficial velocity (Q/A)
U_c – Critical superficial velocity
v *or* v_w – Interstitial velocity (Q/AΦ)
v_{int} – True interstitial velocity (Q/AΦ(S_{oi}-S_{or}))

Greek symbols

β – Exponent for fractional finger width
ψ - Exponent
η – Extended DBM exponent
ρ – Specific density
λ – Fractional finger width
μ - Viscosity
μ_o – Viscosity of oil
μ_w – Viscosity of water
μ_r – Relative viscosity (μo/ μw)
σ – Interfacial tension
σ_{ow} – Oil water interfacial tension
σ* - Effective interfacial tension in porous media
ϕ - Porosity

REFERENCES

Abrams, A. (1975, October 1). The Influence of Fluid Viscosity, Interfacial Tension, and Flow Velocity on Residual Oil Saturation Left by Waterflood. Society of Petroleum Engineers. doi:10.2118/5050-PA

Adkins S., Liyanage P., Pinnawala Arachchilage G. W. P., Mudiyanselage T., Weerasooriya U., and Pope G.. 2010. A New Process for Manufacturing and Stabilizing High-Performance EOR Surfactants at Low Cost for High-Temperature, High-Salinity Oil Reservoirs. Proceedings of SPE Improved Oil Recovery Symposium.

Akin, S., Castanier, L. M., & Brigham, W. E. 1998. Effect of Temperature on Heavy-Oil/Water Relative Permeabilities. Presented at SPE Annual Technical Conference and Exhibition, New Orleans, Louisiana, USA, 27-30 September. SPE 4902.

Alvarez, J., Han, S., (July 2013), Current Overview of Cyclic Steam Injection Process, Journal of Petroleum Science Research Volume 2 Issue 3, 116-127

Araktingi, U. G., & Orr Jr, F. M. (1993, April 1). Viscous Fingering in Heterogeneous Porous Media. Society of Petroleum Engineers. doi:10.2118/18095-PA

Ayasse, C., Bloomer, C., Lyngberg, E., Boddy, W., Donnelly, J., & Greaves, M. (2005, January 1). First Field Pilot of the THAI Process. Petroleum Society of Canada. doi:10.2118/2005-142

Baird,H. J. (1978) Waterflooding Behavior of Viscous Oils, M.Sc. Thesis, Univeristy of Alberta

Beskrovnyi, N.S., Gol'dberg, I.S., Makarov, K.K., Sobolev, V.S., and Taliev, S.D., 1975, Prirodnye tverdye bitumy v SSSR—vazhnyi syr'evoi rezerv narodnogo khoziaistva [Natural solid bitumens in the USSR—an important raw material reserve for the National economy]: Geologiia Nefti I Gaza, no. 4, 1975, p. 14-20. (Translation into

English by Dorothy B. Vitaliano, March, 1985, available for consultation only at the U.S Geological Survey Library, Reston, VA)

Blunt, M. J., & Christie, M. A. (1994, April 1). Theory of Viscous Fingering in Two Phase, Three Component Flow. Society of Petroleum Engineers. doi:10.2118/22613-PA

Bondino, I., Nguyen, R., Hamon, G., Ormehaug, P. A., Skauge, A., & Jouenne, S. (2011, September). Tertiary polymer flooding in extra-heavy oil: an investigation using 1D and 2D experiments, core scale simulation and pore-scale network models. In Paper SCA2011-A063 presented at the International Symposium of the Society of Core Analysts, Austin (pp. 18-21).

Bondino, I., Santanach-Carreras, E., Levitt, D., Jouenne, S., & Bourrel, M. (2013, July 2). Polymer Flooding of Heavy Oil Under Adverse Mobility Conditions. Society of Petroleum Engineers. doi:10.2118/165267-MS

Bondino I., Doorwar S., Ellouz R. and Hamon G., 2013. Visual Microscopic Investigations about the Role of pH, Salinity and Clay on Oil Adhesion and Recovery, reviewed proceedings for the 27th International Symposium of the Society of Core Analysts, Napa Valley, California, USA,

Brook, G., & Kantzas, A. (1998, January 1). Evaluation of Non-thermal EOR Techniques For Heavy Oil Production. Petroleum Society of Canada. doi:10.2118/98-45

Briggs, P. J., Baron, P. R., Fulleylove, R. J., & Wright, M. S. (1988, February 1). Development of Heavy-Oil Reservoirs. Society of Petroleum Engineers. doi:10.2118/15748-PA.

Briggs, P. J., Beck, D. L., Black, C. J. J., & Bissell, R. (1992, May 1). Heavy Oil From Fractured Carbonate Reservoirs. Society of Petroleum Engineers. doi:10.2118/19671-PA.

Bryan, J. and Kantzas, A. 2007. Enhanced Oil Recovery by Alkali-Surfactant Flooding. Paper SPE 110738 presented at the SPE Annual Technical Conference and Exhibition, Anaheim, CA USA, 11-14 November. doi: 10.2118/110738-MS.

Bryan, J., & Kantzas, A. (2009, February 1). Potential for Alkali-Surfactant Flooding in Heavy Oil Reservoirs Through Oil-in-Water Emulsification. Petroleum Society of Canada. doi:10.2118/09-02-37.

Bryan, J. L., Kantzas, A., Shamekhi, H., & Su, S. (2013, June 11). Insights into Heavy Oil Recovery by Surfactant, Polymer and ASP Flooding. Society of Petroleum Engineers. doi:10.2118/165440-MS.

Bryan, J. L., & Kantzas, A. (2014, June 10). Oil Recovery Mechanisms in Bitumen-Bearing Carbonate Rocks. Society of Petroleum Engineers. doi:10.2118/170079-MS.

Buchgraber, M., Clemens, T., Castanier, L.M. and Kovscek, A.R. 2011. A Microvisual Study of the Displacement of Viscous Oil by Polymer Solutions, SPE-122400-PA, SPE Res Eval & Eng 14 (3): 269-280.

Buckley, I.S. 1990 Multiphase Displacements in Micromodels, Chapter 5, in Interfacial Phenomena in Oil Recovery, N. R Morrow, ed..

Buckley, S. E., & Leverett, M. C. (1942, December 1). Mechanism of Fluid Displacement in Sands. Society of Petroleum Engineers. doi:10.2118/942107-G

Butler, R.M., Mcnab, G.S. and Lo, H.Y., Theoretical Studies on the Gravity Drainage of Heavy Oil During In Situ Steam Heating; Canadian Journal Chemical Engineering, 59, 455460, (1981).

Butler, R.M. and Stephens, D.J., The Gravity Drainage of Steam Heated Heavy Oil to Parallel Horizontal Wells; Journal of Canadian Petroleum Technology, 096, April,June, 1981.

Butler, R.M.; A Method for Continuously Producing Viscous Hydrocarbons by Gravity Drainage While Injecting Heated Fluids; UK Pat. Appl GB 2,053,328 (1980) also US 4,344,485 (1982) and Can. 1,130,201 (1982).

Buza, J. W. (2008, January 1). An Overview of Heavy and Extra Heavy Oil Carbonate Reservoirs in the Middle East. International Petroleum Technology Conference. doi:10.2523/12426-MS.

Campbell, B.T. 1982. Photofabrication of Porous Networks in Two-Dimensional Glass Plate Micromodels, PRRC Report No. 83-3, New Mexico Petroleum Recovery Research Center, Socorro, NM.

Chang, J. (2013, June 11). Understanding HW-CSS for Thin Heavy Oil Reservoir. Society of Petroleum Engineers. doi:10.2118/165386-MS.

Chatzis, I., 1982. Photofabrication Technique of 2-D Glass Micromodels, PRRC Report NO. 82-12, New Mexico Petroleum Recovery Research Center, Socorro, NM.

Chen, J. D., & Wilkinson, D. (1985). Pore-scale viscous fingering in porous media. Physical review letters, 55(18), 1892.

Chuoke, R.L., van Meurs, P., and van der Poel, C. "The Instability of Slow, Immiscible, Viscous Liquid-Liquid Displacments in Permeable Media," Aime 216, 1959.

Clemens, T., Tsikouris, K., Buchgraber, M., Castanier, L. M., & Kovscek, A. (2013, April 23). Pore-Scale Evaluation of Polymers Displacing Viscous Oil--Computational-Fluid-Dynamics Simulation of Micromodel Experiments. Society of Petroleum Engineers. doi:10.2118/154169-PA

Conrad, S. H., Wilson, J. L. Mason, W. R. and Peplinski, W. J. 1992. Visualization of residual organic liquid trapped in aquifers, Water Resour. Res., 28, 467-478.

Croissant, R. 1968. Developpement des Instabilites en milieu poreux-Influence de la Pression Capillaire. Presented at the 1968 111e Colloque de l'ARTFP (1968), Pau, France, Sept. 23-26 (in French).

Cueto-Felgueroso, L., & Juanes, R. (2008). Nonlocal interface dynamics and pattern formation in gravity-driven unsaturated flow through porous media. Physical review letters, 101(24), 244504.

Davidson, L. B.: "The Effect of Temperature on Relative Permeability Ratio of Different Fluid Pairs in Two Phase Systems," (1969), No.8, 1937.

Davidson, B. C., Dusseault, M. B., & Wang, J. (1999, January 1). Laboratory Experiments On Pressure Pulse Flow Enhancement In Porous Media. Petroleum Society of Canada. doi:10.2118/99-90

Davis, J. A. and Jones, S.C. 1968. Displacement mechanisms of micelle solutions, J. Pet. Technol., 20, 1415-1428.

De Haan, J. (1959, January 1). 25. Effect of Capillary Forces in the Water-Drive Process. World Petroleum Congress.

Delamaide, E., Bazin, B., Rousseau, D., & Degre, G. (2014, March 31). Chemical EOR for Heavy Oil: The Canadian Experience. Society of Petroleum Engineers. doi:10.2118/169715-MS

Delamaide, E. (2014, September 24). Polymer Flooding of Heavy Oil - From Screening to Full-Field Extension. Society of Petroleum Engineers. doi:10.2118/171105-MS

Denney, D. (2013, January 1). Polymer Flooding in a Large Field in South Oman - Results and Plans. Society of Petroleum Engineers. doi:10.2118/0113-0082-JPT

DOE Office of Petroleum Reserves-Strategic Unconventional Fuels, Fact Sheet: US Heavy Oil Resource Potential, June 2007.

Dusseault, M. B. (2003, January 1). New Oil Production Technologies. Society of Petroleum Engineers.

Dusseault, M.B. (12–14 June 2001). Comparing Venezuelan and Canadian Heavy Oil and Tar Sands (PDF). Calgary, Canada: Canadian International Petroleum Conference. Retrieved 5 May 2008.

Edmondson, T. A. 1965. Effect of Temperature on Waterflooding. Journal of Canadian Petroleum Technology 4(04), 236-242.

Element, D. J., Goodyear, S. G., Sargent, N. C., and Jayasekera, A. J. 2001. Comparison of polymer and waterflood residual oil saturations, in 11th Europeans Symp. on IOR, Amsterdam, Netherlands.

Engelberts, W. F., & Klinkenberg, L. J. (1951, May). Laboratory experiments on the displacement of oil by water from packs of granular material. In Proceedings 3rd World Petroleum Congress, The Hague (Vol. 2, pp. 544-554).

Fabbri, C., Cottin, C., Jimenez, J., Nguyen, M., Hourcq, S., Bourgeois, M., & Hamon, G. (2014, January 19). Secondary and Tertiary Polymer Flooding in Extra-Heavy Oil: Reservoir Conditions Measurements - Performance Comparison. International Petroleum Technology Conference. doi:10.2523/IPTC-17703-MS

Falls, A.H., Thigpen, D.R., Nelson, R.C., Ciaston, J.W., Lawson, J.B., Good, P.A., Ueber, R.C., Shahin, G.T. 1994. Field Test of Cosurfactant-Enhanced Alkaline Flooding. SPE Res Eng, 9(3): 217-223. SPE 24117-PA. doi: 10.2118/24117-PA

Feder, J., Hinrichsen, E. L., Måløy, K. J., & Jøssang, T. (1989). Geometrical crossover and self-similarity of DLA and viscous fingering clusters. Physica D: Nonlinear Phenomena, 38(1), 104-111.

Ferer M., Sams, W.N., Geidbrecht, R.A. and Smith, D.H. 1995. Fractal Nature of Viscous Fingering in Two Dimensional Pore Level Models. AICHE J. 41(4) 749-763

Fayers, F. J. (1988, May 1). An Approximate Model With Physically Interpretable Parameters for Representing Miscible Viscous Fingering. Society of Petroleum Engineers. doi:10.2118/13166-PA

Fayers, F. J., Blunt, M. J., & Christie, M. A. (1992, May 1). Comparisons of Empirical Viscous-Fingering Models and Their Calibration for Heterogeneous Problems. Society of Petroleum Engineers. doi:10.2118/22184-PA

Fortenberry, R., Kim, D. H., Nizamidin, N., Adkins, S., Arachchilage, G., Koh, H., Pope, G. A. (2015, April 1). Use of Cosolvents To Improve Alkaline/Polymer Flooding. Society of Petroleum Engineers. doi:10.2118/166478-PA

Greaves, M., Tuwil, A. A., & Bagci, A. S. (1993, April 1). Horizontal Producer Wells In In Situ Combustion (ISC) Processes. Petroleum Society of Canada. doi:10.2118/93-04-04

Greaves, M., & Al-Shamali, O. (1996, April 1). In Situ Combustion Isc Process Using Horizontal Wells. Petroleum Society of Canada. doi:10.2118/96-04-05

Greaves, M., Xia, T. X., Turta, A. T., & Ayasse, C. (2000, January 1). Recent Laboratory Results of THAI and Its Comparison with Other IOR Processes. Society of Petroleum Engineers. doi:10.2118/59334-MS

Greaves, M., Dong, L. L., & Rigby, S. (2011, January 1). Upscaling THAI: Experiment to Pilot. Society of Petroleum Engineers. doi:10.2118/148989-MS

Greaves, M., Dong, L. L., & Rigby, S. (2012, January 1). Determination of Limits to Production in THAI. Society of Petroleum Engineers. doi:10.2118/157817-MS

Haghighat, P., & Maini, B. B. (2010, March 1). Role of Asphaltene Precipitation in VAPEX Process. Society of Petroleum Engineers. doi:10.2118/134244-PA

Hagoort, J. (1974, February 1). Displacement Stability of Water Drives in Water-Wet Connate-Water-Bearing Reservoirs. Society of Petroleum Engineers. doi:10.2118/4268-PA

Hallam, R.J., Plekenbrock, E.J., Abou-Sayed, A.S., Garon, A.M., Putnam, T.W., Weggeland, M.C. & Webb, K.J. 1992. Resource Description and Development Potential of the Ugnu Reservoir, North Slope, Alaska. SPE Form Eval 7 (3): 211-218. SPE-21779-PA. doi: 10.2118/21779-PA.

Hocine, S., Magnan, A., Degre, G., Rousseau, N., & Rousseau, D. (2014, March 31). Alkaline-Free Surfactant Polymer Process for Heavy Oil. Society of Petroleum Engineers. doi:10.2118/169697-MS

Hubbert, M.K., 1956 Nuclear Energy and Fossil Fuels, Drilling and Production Practices Journal: 7-25.

Hughes, D. S., & Murphy, P. (1987, January 1). An Analytical Model Of Unstable Immiscible Flow. Society of Petroleum Engineers.

Hughes, D. S., & Murphy, P. (1988, November 1). Use of a Monte Carlo Method to Simulate Unstable Miscible and Immiscible Flow Through Porous Media. Society of Petroleum Engineers. doi:10.2118/17474-PA

Huh, C., and Pope, G. A. 2008. Residual Oil Saturation from Polymer Floods: Laboratory Measurements and Theoretical Interpretation, Society of Petroleum Engineers. doi:10.2118/113417-MS

Hussain, A, *et al*. 2006 Highlighting heavy oil-World Oil Review, 34-56.

Jain, L., & Lake, L. W. (2013, September 30). Upscaling of Miscible Floods: An Extension to Koval Theory. Society of Petroleum Engineers. doi:10.2118/166400-MS

James, L. A., Rezaei, N., & Chatzis, I. (2008, April 1). VAPEX, Warm VAPEX and Hybrid VAPEX - The State of Enhanced Oil Recovery for In Situ Heavy Oils in Canada. Petroleum Society of Canada. doi:10.2118/08-04-12-TB

Jaspers, H. F., Al-Amri, M. S., Al-Saqri, K. A., Zuhaimi, K., Al-hashmi Khalid Hamad, & Thakuria, C. (2013, July 2). Performance Review of Polymer Flooding in a Major Brown Oil Field of Sultanate of Oman. Society of Petroleum Engineers. doi:10.2118/165262-MS

Jennings, H. Y. Jr., Johnson, C. E. Jr., and McAuliffe, C. D., 1974. A Caustic Waterflooding Process for Heavy Oils, J. Pet. Tech., 1344–1352.

Kang, X., Zhang, J., Sun, F., Zhang, F., Feng, G., Yang, J., … Xiang, W. (2011, January 1). A Review of Polymer EOR on Offshore Heavy Oil Field in Bohai Bay, China. Society of Petroleum Engineers. doi:10.2118/144932-M

King, M. J., & Scher, H. (1985, January 1). Probabilistic Stability Analysis of Multiphase Flow in Porous Media. Society of Petroleum Engineers. doi:10.2118/14366-MS

King, M. J. (1987, January 1). Viscous Fingering Utilizing Probabilistic Simulation. Society of Petroleum Engineers. doi:10.2118/16708-MS

Kloepfer, J.G. (1975) Viscous fingering in uncolsolidated cores, M.Sc. Thesis, Univeristy of Alberta

Knizikevičius, R., 2009. Simulations of Si and SiO2 etching in SF6 +O2 plasma, Vacuum, Volume 83, Issue 6, Pages 953-957. Park, J. H., Lee, N. E., Lee, J., Park, J. S. and Park, H. D. 2005. Deep dry etching of borosilicate glass using SF6and SF6/Ar inductively coupled plasmas, Microelectronic engineering, 82(2), 119-128.

Koh H., (2015) Experimental Investigation of the Effect of Polymers on Residual Oil Saturation, PhD Dissertation, University of Texas at Austin

Koval, E. J. (1963, June 1). A Method for Predicting the Performance of Unstable Miscible Displacement in Heterogeneous Media. Society of Petroleum Engineers. doi:10.2118/450-PA

Kucheryavski, S., Belyaev I.: Classification and analysis of non-isotropic images by Angle Measure Technique (AMT) with contour unfolding, Analytica Chimica Acta (2008)

Kumar, M., Inouye, T. A. (1994). Low-Temperature Analogs of High-Temperature Water/Oil Relative Permeabilities. Presented at SPE Annual Technical Conference and Exhibition, New Orleans, USA, 25-28 September. SPE 28616.

Kumar, R., Dao, E., & Mohanty, K. (2012, June 1). Heavy-Oil Recovery by In-Situ Emulsion Formation. Society of Petroleum Engineers. doi:10.2118/129914-PA.

Kumar R., (2013) Enhanced Oil Recovery of Heavy Oils by Non-Thermal Chemical Methods, PhD Dissertation, University of Texas, Austin

Lake, L. 1989. Enhanced Oil Recovery. Englewood Cliffs, New Jersey: Prentice Hall

Lefebvre de Prey, E.J.: "Factors Affecting Liquid-Liquid Relative Permeabilities of a Consolidated Porous Medium," SPEJ (Feb. 1973) 39-47

Lenormand, R., & Zarcone, C. (1985). Invasion percolation in an etched network: measurement of a fractal dimension. Physical review letters, 54(20), 2226.

Lenormand, R., Touboul, E., & Zarcone, C. (1988). Numerical models and experiments on immiscible displacements in porous media. Journal of Fluid Mechanics, 189, 165-187.

Levitt, D., Bourrel, M., Bondino, I., Jouenne, S., & Gingras, J.-P. (2011, January 1). The Interpretation of Polymer Coreflood Results for Heavy Oil. Society of Petroleum Engineers. doi:10.2118/150566-MS

Li, X., Abe, T. and Esashi, M. (2000). Deep reactive ion etching of Pyrex glass, Micro Electro Mechanical Systems, 2000. MEMS 2000. in the Thirteenth Annual International Conference, vol., no., pp.271,276.

Li, Y. and Wardlaw, N. C., (1986). The influence of wettability and critical pore-throat size ratio on snap-off, J. Colloid Interface Sci., 109, 461-472.

Liyanage, P. J., Solairaj, S., Pinnawala Arachchilage, G., Linnemeyer, H. C., Kim, D. H., Weerasooriya, U., & Pope, G. A. (2012, January 1). Alkaline Surfactant Polymer Flooding using a Novel Class of Large Hydrophobe Surfactants. Society of Petroleum Engineers. doi:10.2118/154274-MS

Lo, H. Y., & Mungan, N. (1973). Effect of Temperature on Water-Oil Relative Permeabilities in Oil-Wet and Water-Wet Systems, Presented at Fall Meeting of the Society of Petroleum Engineers of AIME, Las Vegas, Nevada, USA, 30 September-3 October. SPE 4505.

Lu, J., Pope, G. A., & Weerasooriya, U. P. (2013, April 8). Stability Investigation in Low-Tension Surfactant Floods. Society of Petroleum Engineers. doi:10.2118/164090-MS

Lu, J., Weerasooriya, U. P., & Pope, G. A. (2014). Investigation of gravity-stable surfactant floods. Fuel, 124, 76-84.

Mai, A., & Kantzas, A. (2009, March 1). Heavy Oil Waterflooding: Effects of Flow Rate and Oil Viscosity. Petroleum Society of Canada. doi:10.2118/09-03-42

Mai, A., Bryan, J., Goodarzi, N., & Kantzas, A. (2009, March 1). Insights Into Non-Thermal Recovery of Heavy Oil. Petroleum Society of Canada. doi:10.2118

Mai, A., & Kantzas, A. (2010, March 1). Mechanisms of Heavy Oil Recovery by Low Rate Waterflooding. Society of Petroleum Engineers. doi:10.2118/134247-PA/09-03-27

Maini, B. B., & Batycky, J. P. (1985, August 1). Effect of Temperature on Heavy-Oil/Water Relative Permeabilities in Horizontally and Vertically Drilled Core Plugs. Society of Petroleum Engineers. doi:10.2118/12115-PA

Måløy, K. J., Feder, J., & Jøssang, T. (1985). Viscous fingering fractals in porous media. Physical review letters, 55(24), 2688.

Mandelbrot, B. B. (1967). How long is the coast of Britain. Science, 156(3775), 636-638.

Marques, C., Castanier, L.M., and Kovscek, A.R. (2009). Thaw Front Dynamics and Super Insulated Wells for Thermal Recovery in Cold Environments. Paper SPE 121059 presented at the SPE Western Regional Meeting, San Jose, California, 24-26 March. doi: 10.2118/121059-MS.

Mattax, C. C. and Kyte, J. R. (1961). Ever see a water flood? Oil & Gas Journal, 59, 115-128.

McFadyen, D. (2012). Water disposal limits and reporting requirements for thermal in-situ oil sands schemes, Alberta Energy Regulator Publication, https://www.aer.ca/documents/directives/Directive081.pdf

McInnis, L. E., Ellis-Toddington, T. T., Hunter, K. D., & Grawbarger, D. J. (2013, July 2). Case Study of the Taber Mannville B ASP Flood. Society of Petroleum Engineers. doi:10.2118/165264-MS

McKellar, M. and Wardlaw, N.C. (1982). A Method of Making Two-Dimensional Glass Micromodels of Pore Systems, Tech. note, J. Canadian Pet. Tech., 21, 39-41.

Meakin, P. (1991). Fractal aggregates in geophysics. Reviews of Geophysics, 29(3), 317-354.

Meyer, R.F., Attanasi, E.D.. "Heavy Oil and Natural Bitumen—Strategic Petroleum Resources," USGS Fact Sheet PS-070-03, August 2003.

Miller, M. A., & Ramey, H. J. (1985). Effect of Temperature on Oil/Water Relative Permeabilities of Unconsolidated and Consolidated Sands. Journal of Petroleum Technology, 25(06), 945-953.

Moe Soe Let, K. P., Manichand, R. N., & Seright, R. S. (2012, January 1). Polymer Flooding a ~500-cp Oil. Society of Petroleum Engineers. doi:10.2118/154567-MS

Mosavat, N, Zarivnyy, O., & Torabi, F. (2013). Developing New Corey-Based Water/Oil Relative Permeability Correlations for Heavy Oil Systems. Presented at SPE Heavy Oil Conference-Canada, 2013, Calgary, Alberta, Canada, 11-13 June. SPE 165445.

Mostaghimi, P., Kamali, F., Jackson, M. D., Muggeridge, A. H., & Pain, C. C. (2015, February 23). A Dynamic Mesh Approach for Simulation of Immiscible Viscous Fingering. Society of Petroleum Engineers. doi:10.2118/173281-MS

Nakornthap, K., & Evans, R. D. (1986, May 1). Temperature-Dependent Relative Permeability and Its Effect on Oil Displacement by Thermal Methods. Society of Petroleum Engineers. doi:10.2118/11217-PA

Niemeyer, L., Pietronero, L., & Wiesmann, H. J. (1984). Fractal dimension of dielectric breakdown. Physical Review Letters, 52(12), 1033-1036.

Nittman, J., Daccord, G., & Stanley, M. C. (1985). Fractal growth of viscous fingers: quantitative characterizations of a fluid instability phenomenon. Nature,314, 391.

Odeh, A. S. (1959). Effect of Viscosity Ratio on Relative Permeability. Trans. AIME, 216, 346-352.

Osoba, J.S., Richardson, J.G., Kerver, J.K., Hafford, J.A. and Blair, P.M. (1951). Laboratory Measurements of Relative Permeability. J of Petr. Tech. 3(2).

Paterson, L. (1984). Diffusion-limited aggregation and two-fluid displacements in porous media. Physical review letters, 52(18), 1621.

Pavone, D. (1992). Observations and correlations for immiscible viscous-fingering experiments. SPE Reservoir Engineering 7(2), 187-194. SPE 19670-PA.

Perkins, T. K., Johnston, O. C., & Hoffman, R. N. (1965, December 1). Mechanics of Viscous Fingering in Miscible Systems. Society of Petroleum Engineers. doi:10.2118/1229-PA

Perkins, T. K., & Johnston, O. C. (1969, March 1). A Study of Immiscible Fingering in Linear Models. Society of Petroleum Engineers. doi:10.2118/2230-PA

Peters, E. J., (1979) Stability Theory and Viscous Fingering in Porous Media, PhD Dissertation, University of Alberta

Peters, E. J., & Flock, D. L. (1981, April 1). The Onset of Instability During Two-Phase Immiscible Displacement in Porous Media. Society of Petroleum Engineers. doi:10.2118/8371-PA

Peters, E.J., Khatanair, S. (1987) The effect of instability on relative permeability curves obtained by the dynamic displacement method. SPE Formation Evaluation 2(4).

Peyton, H.R. (1970). Arctic Engineering. J. Pet. Tech. 22 (9): 1076-1082. SPE-2701-PA. doi:10.2118/2701-PA.

Pietronero, L., & Wiesmann, H. J. (1988). From physical dielectric breakdown to the stochastic fractal model. Zeitschrift für Physik B Condensed Matter,70(1), 87-93.

Poston, S. W., Ysrael, S., Hossain, A. K. M. S *et al.* (1970). The Effect of Temperature on Irreducible Water Saturation and Relative Permeability of Unconsolidated Sands. Society of Petroleum Engineers Journal, 10(02), 171 – 180. SPE-1897-PA.

Pye, D. J., (1964). Improved secondary recovery by control of water mobility, *J. Pet. Tech*., **16** (8), 911−916.

Rachford, H. H. (1964, June 1). Instability in Water Flooding Oil from Water -Wet Porous Media Containing Connate Water. Society of Petroleum Engineers. doi:10.2118/684-PA

Reppert, T. R., Bragg, J. R., Wilkinson, J. R., Snow, T. M., Maer, N. K., & Gale, W. W. (1990, January 1). Second Ripley Surfactant Flood Pilot Test. Society of Petroleum Engineers. doi:10.2118/20219-MS

Rezaei, N., & Chatzis, I. (2007, January 1). Incorporation of Heat in the VAPEX Process: Warm VAPEX. Petroleum Society of Canada. doi:10.2118/2007-133-EA

Riaz, A., & Tchelepi, H. A. (2006). Numerical simulation of immiscible two-phase flow in porous media. Physics of Fluids (1994-present), 18(1), 014104.

Saffman, P.G. and Taylor, G. (1958). The Penetration of a Fluid into a Porous Medium or Hele-Shaw Cell Containing a More Viscous Liquid. Proc. R. Soc. Lond. 245 312-329.

Sandberg, C.R., Gourney, L.S. and Sippel, R.F. (1958). Effect of Fluid flow rate and viscosity on Laboratory determinations of oil water relative permeabilities. Trans AIME 213, 36-43.

Salter, S. J. and Mohanty, K. K. (1982). Multiphase Flow in Porous Media: I. Macroscopic Observations and Modeling, Society of Petroleum Engineers. doi:10.2118/11017-MS

Sandiford, B. B.,(1964). Laboratory and field studies of water floods using polymer solutions to increase oil recoveries, *J. Pet. Tech*., **16** (8), 917−922.

Shamekhi, H., Kantzas, A., Bryan, J. L., & Su, S. (2013, June 11). Insights into Heavy Oil Recovery by Surfactant, Polymer and ASP Flooding. Society of Petroleum Engineers. doi:10.2118/165440-MS

Sharma, H., Weerasooriya, U., Pope, G. A., & Mohanty, K. K. (2014, October 27). Ammonia-Based ASP Processes for Gypsum-Containing Reservoirs. Society of Petroleum Engineers. doi:10.2118/170825-MS.

Sharma, J., Inwood, S. B. and Kovscek, A. R. (2012). Experiments and Analysis of Multiscale Viscous Fingering During Forced Imbibition, SPE Journal, 17(4) 1142-1159.

Sherwood, J. D., & Nittmann, J. (1986). Gradient governed growth: the effect of viscosity ratio on stochastic simulations of the Saffman-Taylor instability.Journal de Physique, 47(1), 15-22.

Shutang, G., Qiang, G., Lin, J. (2010). Recent Progress and Evaluation of ASP Flooding for EOR in Daqing Oil Field. Paper presented at the SPE EOR conference at Oil and Gas West Asia, Muscat, Oman, 11-13 April. doi: 10.2118/127714-MS

Sigmund, P., Sharma, H., Sheldon, D., & Aziz, K. (1988, May 1). Rate Dependence of Unstable Waterfloods. Society of Petroleum Engineers. doi:10.2118/14368-PA

Skauge, A., Ormehaug, P. A., Gurholt, T., Vik, B., Bondino, I., & Hamon, G. (2012, January 1). 2-D Visualisation of Unstable Waterflood and Polymer Flood for Displacement of Heavy Oil. Society of Petroleum Engineers. doi:10.2118/154292-MS

Skauge, T., Vik, B. F., Ormehaug, P. A., Jatten, B. K., Kippe, V., Skjevrak, I., … Skauge, A. (2014, March 31). Polymer Flood at Adverse Mobility Ratio in 2D Flow by X-ray Visualization. Society of Petroleum Engineers. doi:10.2118/169740-MS

Skaugen, E.: (1985) “Analytical Model of Viscous Fingering Including Buckley-Leverett Type Displacement” Proc of the 3rd European Meeting on Improved Oil Recovery, Rome, April..

Southwick, J. G., van den Pol, E., van Rijn, C. H. T., van Batenburg, D. W., Boersma, D. M., Svec, Y., Raney, K. (2014, April 12). Ammonia As Alkali For ASP Floods - Comparison to Sodium Carbonate. Society of Petroleum Engineers. doi:10.2118/169057-MS.

Stegemeier, G.L. (1977). Mechanism of Entrapment and Mobilization of Oil in Porous Media. New York City: Academic Press.

Stokes, J. P., Weitz, D. A., Gollub, J. P. *et al.* (1986). Interfacial stability of immiscible displacement in a porous medium. Physical review letters 57(14), 1718.

Subkow, P. (1942). Process for the Removal of Bitumen from Bituminous Deposits. U.S Patent No. 2,288,857.

Sufi, A. H., Ramey, H. J., & Brigham, W. E. (1982). Temperature Effects on Relative Permeabilities of Oil-Water Systems. Presented at 57th Annul Technical Conference and Exhibition, New Orleans, Louisiana USA, 26-29 September. SPE 11071.

Taghavifar, M., Fortenberry, R. P., De Rouffignac, E., Sepehrnoori, K., & Pope, G. A. (2014, June 10). Hybrid Thermal-Chemical Processes (HTCP) for Heavy-Oil and Oil-Sand Recovery. Society of Petroleum Engineers. doi:10.2118/170161-MS

Tavassoli, S., Lu, J., Pope, G. A., & Sepehrnoori, K. (2014, October 1). Investigation of the Critical Velocity Required for a Gravity-Stable Surfactant Flood. Society of Petroleum Engineers. doi:10.2118/163624-PA

Tavassoli, S., Pope, G., & Sepehrnoori, K. (2014, Nov. 1). Frontal-Stability Analysis of Surfactant Floods. Society of Petroleum Engineers. doi:10.2118/169118-PA

Todd, M. R., & Longstaff, W. J. (1972, July 1). The Development, Testing, and Application Of a Numerical Simulator for Predicting Miscible Flood Performance. Society of Petroleum Engineers. doi:10.2118/3484-PA

Van Meurs, P. (1957, January 1). The Use of Transparent Three-Dimensional Models for Studying the Mechanism of Flow Processes in Oil Reservoirs. Society of Petroleum Engineers.

Van Meurs, P., & van der Poel, C. (1958, January 1). A Theoretical Description of Water-Drive Processes Involving Viscous Fingering. Society of Petroleum Engineers.

Vermolen, E. C. M., van Haasterecht, M. J. T., & Masalmeh, S. K. (2014, March 31). A Systematic Study of the Polymer Visco-Elastic Effect on Residual Oil Saturation by Core Flooding. Society of Petroleum Engineers. doi:10.2118/169681-MS

Vicsek, T. (1984). Pattern formation in diffusion-limited aggregation. Physical Review Letters, 53(24), 2281.

Wan J., Tokunaga, T.K., Tsang, C.F. and Bodvarsson, G.S. (1996). Improved glass micromodel methods for studies of flow and transport in fractured porous media, Water Resources Research, 32(7) 1955-1964.

Wang, D., Cheng, J., Yang, Q., Wenchao, G., Qun, L., and Chen, F. (2000). Viscous-Elastic Polymer Can Increase Microscale Displacement Efficiency in Cores, Society of Petroleum Engineers. doi:10.2118/63227-MS

Wang, J., Dong, M., & Asghari, K. (2006). Effect of Oil Viscosity on Heavy Oil-Water Relative Permeability Curves. Presented at SPE/DOE Symposium on Improved Oil Recovery, 2006, Tulsa, Oklahoma, USA, 22-26 April. SPE 99763.

Wiborg, R. (1976) Frontal instabilities when waterflooding at unstable viscosity ratios Viscous, M.Sc. Thesis, Univeristy of Alberta

Wilkinson, D., & Willemsen, J. F. (1983). Invasion percolation: a new form of percolation theory. Journal of Physics A: Mathematical and General, 16(14), 3365.

Wilson, J. W. (1965): "Determination of Relative Permeability under Simulated Reservoir Conditions," AIChE J. 2, No.1, 94.

Wilson, E.D. (1972). Some Aspects of Arctic Oil Pipe Line Research. Paper SPE 1972-061 presented at the SPE Annual Technical Meeting, Calgary, Alberta, 16–19 May. doi:10.2118/1972-061.

Witten Jr, T. A., & Sander, L. M. (1981). Diffusion-limited aggregation, a kinetic critical phenomenon. Physical review letters, 47(19), 1400.

Witten Jr, T. A., & Meakin, P. (1983). Diffusion-limited aggregation at multiple growth sites. Physical Review B, 28(10), 5632.

World Energy Scenarios: Composing energy futures to 2050, October 2013.

Wreath, D.G. 1989. A study of polymer flooding residual oil saturation. MS Thesis, University of Texas at Austin.

Xia, T., Greaves, B., Werfilli, M. S., & Rathbone, R. R. (2002, January 1). THAI Process-Effect of Oil Layer Thickness on Heavy Oil Recovery. Petroleum Society of Canada. doi:10.2118/2002-027

Yang, H., Britton, C., Liyanage, P.M., Solairaj, S., Kim, D.H., Nguyen, Q., Weerasooriya, U., Pope, G.A. (2010). Low-Cost, High-Performance Chemicals for Enhanced Oil Recovery. Paper presented at the SPE Improved Oil Recovery Symposium, Tulsa, Oklahoma, 24-28 April. doi: 10.2118/129978-MS